Unveiling Hidden Mergers: Quantifying Merger Prevalence in Post-starburst Galaxies and the Efficacy of Common Merger Identification Techniques

by

Scott J. Wilkinson
B.Sc., University of Victoria, 2021

A Thesis Submitted in Partial Fulfillment of the
Requirements for the Degree of

MASTER OF SCIENCE

in the Department of Physics and Astronomy

Unveiling Hidden Mergers: Quantifying Merger Prevalence in Post-starburst Galaxies and the Efficacy of Common Merger Identification Techniques

by

Scott J. Wilkinson
B.Sc., University of Victoria, 2021

Supervisory Committee

Dr. Sara L. Ellison, Supervisor
(Department of Physics and Astronomy)

Dr. Alan McConnachie, Departmental Member
(Department of Physics and Astronomy)

ABSTRACT

Numerical simulations and observations agree that galaxies tend to evolve from star-forming spiral galaxies to quiescent ellipticals. Post-starburst (PSB) galaxies, defined as having experienced a recent burst of star formation, followed by a prompt truncation in further activity, are thought to be observed whilst rapidly transitioning from star-forming to quiescence. Thus, identifying the mechanism(s) causing a galaxy to experience a post-starburst phase provides integral insight into the causes of rapid quenching. Galaxy mergers have long been proposed as a possible post-starburst trigger. Effectively testing this hypothesis requires a large spectroscopic galaxy survey to identify the rare PSBs as well as high quality imaging and robust morphology metrics to identify mergers. In this work, I bring together these critical elements by selecting PSBs from the overlap of the Sloan Digital Sky Survey and the Canada-France Imaging Survey and applying a suite of classification methods including non-parametric morphology metrics such as asymmetry and Gini-M_{20}, a convolutional neural network (CNN) trained to identify post-merger galaxies, and visual classification. This work therefore includes the largest and most comprehensive assessment of the merger fraction of PSBs to date. I find that the merger fraction of PSBs ranges from 19% to 42% depending on the merger identification method and details of the PSB sample selection. These merger fractions represent an excess of 3-46× relative to non-PSB control samples. My results demonstrate that mergers play a significant role in generating PSBs, but that other mechanisms are also required.

Critical to the interpretation of the observed merger fraction of PSBs in this work is quantifying the efficacy of the merger identification methods employed. To test this, 2,119 known recent mergers ($t_{postmerger} \lesssim 200$ Myr) are drawn from the IllustrisTNG100 cosmological simulation, where assembly history and properties of the merger are known with certainty and devoid of observational impairment. Synthetic r-band images of the mergers are generated directly from the simulation particle data and degraded to various image qualities, adding observational effects such as sky noise and atmospheric blurring. The efficacy of the non-parametric merger identification methods is quantified using the completeness of recovered mergers, which is shown to increase from as low as 1% to as high as 37% as sky noise and atmospheric blurring decrease, but also depends on the morphology statistic considered. However, even in idealized imaging, free from atmospheric blurring and with minimal sky noise, the maximum completeness achieved is 39% indicating that reliable merger detection may be limited by the viewing angle at which it is observed. Future work will assess if CNN and visual inspection methods can identify mergers more reliably and thus allow for a more accurate quantification of the number of mergers in post-starburst galaxies and other galaxy samples, moving forward.

Contents

List of Tables

List of Figures

Acknowledgements

I would like to thank:

Dr. Sara Ellison, for her excellent supervision and guidance over several years, which has challenged me to continuously hone my research skills. Her contributions to this work and my personal development are immeasurable.

Dr. Alan McConnachie, for his support and encouragement throughout my research journey, and for his role as a member of my supervisory committee.

Dr. Dave Patton, Dr. Mallory Thorp, Bobby Bickley, Shoshannah Byrne-Mamahit, and Dr. Leonardo de Albernaz Ferreira for their regular scientific discourse, which challenged and inspired me and was integral to the development of this work.

Drs. Connor Bottrell, Maan Hani, and Salvatore Quai, for their mentorship, which helped me navigate the challenges of transitioning to graduate school and helped me grow personally and professionally.

My officemates, for their daily support and camaraderie, which made the journey more enjoyable and helped me stay motivated.

My family and friends, for constructing a personal support network as wide and deep as the Canada France Imaging Survey. Your encouragement has been a consistent source of strength for me along my journey.

I respectfully acknowledge that the sites on which this thesis was written are the ancestral territories of Indigenous peoples, specifically the Lekwungen, Songhees, Esquimalt and WSÁNEĆ peoples whose historical relationships with the land continue to this day. As I explore the shared sky, I acknowledge my responsibility to honour those who were here before me. I strive for respectful relationships and partnerships with all the peoples of these lands as we move forward together towards reconciliation and decolonization.

I acknowledge the support of the Natural Sciences and Engineering Research Council of Canada (NSERC), [funding reference number 601036-2022].

Dedication

This work is dedicated to my grandparents Fran & Wayne Roberts and Alan & Trudie Wilkinson. Thank you for your unwavering support.

Chapter 1

An Introduction to the Rapid Evolution of Galaxies From Star-Forming to Quiescence

One hundred and three years ago, Heber Curtis and Harlow Shapley presented opposing theories about the scale of the Universe and engaged in what is now known as the "Great Debate." The crux of the tension between the two theories was the nature of what they called "spiral nebulae." Shapley believed that the spiral nebulae, including Andromeda, were internal to the Milky Way, while Curtis believed them to be extragalactic entities and that the scale of the Universe is much larger than the Milky Way (Shapley 1919; Curtis 1920). We now know that Curtis's interpretation of the available data at the time was more accurate and that the "spiral nebulae" are indeed other galaxies much like the Milky Way itself. This revelation is often accredited to the work done a few years later by Edwin Hubble who measured the distance to Andromeda more accurately using Cepheid variable stars (Hubble 1925), confirming the extragalactic status of these objects.

In the year 1926, Hubble presented work wherein galaxies (deemed "extra-galactic nebulae" at the time) are broadly classified based on their observed shape and structure (Hubble 1926). From a sample of $\sim$400 galaxies, Hubble identified two main classes of "regular" galaxies: elliptical and spiral. Elliptical galaxies have smooth (void of any internal substructure) ellipsoidal morphologies that are brightest in the centre and gradually get dimmer towards the outskirts (Hubble 1926; de Vaucouleurs 1948; Sérsic 1963). Elliptical galaxies are further specified by how ellipsoidal they appear, quantified from 0 to 7 by the relative size of the semi-major and semi-minor axes (Hubble 1926). Spiral galaxies, however, have highly elongated shapes when viewed edge-on (i.e. disks) and have light profiles that decrease exponentially away from the centre with internal spiral structure when viewed face-on (Sérsic 1963). Spiral galaxies are divided into two subclasses depending on the presence or lack of a central bar and are further specified (from a through c) by the size of their central bulge and how tightly wound the spiral structure appears (Hubble 1926). Hubble intuited that spirals, ellipticals, and the subclasses therein, exist along a morphology sequence, which we now refer to as the Hubble tuning fork[1]. An example of a Hubble tuning fork diagram is presented in Figure 1.1. While Hubble did not propose a theory that would explain how such a sequence may have originated, asserting that these profoundly different objects are similar entities existing along a sequence was a remarkable leap in understanding that should not be taken for granted.

Modern sky surveys, such as the Sloan Digital Sky Survey (SDSS; York et al. 2000), have provided a detailed statistical sampling of galaxies that allows for conclusions to be drawn about galaxy populations as a whole. Indeed, the bimodality of galaxy morphology observed by Hubble has only been strengthened by large statistical studies (e.g. Strateva et al. 2001; Driver et al. 2006; Lintott et al. 2008, 2011; Nair and Abraham 2010; Wuyts et al. 2011). In addition to morphology, observations have shown that the bimodality of galaxies exists in other properties as well including colour (Strateva et al. 2001; Baldry et al. 2004; Driver et al. 2006), star formation rate (SFR; Wuyts et al. 2011), and gas content (Catinella et al. 2010; Saintonge et al. 2011). The bimodal properties tend to be correlated such that, generally speaking, spiral galaxies are bluer, gas-rich and actively forming stars and elliptical galaxies are redder, gas-poor and passively evolving (Driver et al. 2006; Catinella et al. 2010; Wuyts et al. 2011; Saintonge et al. 2011).

In Figure 1.2, I present the work done by Wuyts et al. (2011) which shows the location of galaxies in the SFR-mass plane and their associated morphologies as quantified by their Sérsic indices (see Appendix A.1 and Sérsic 1963, for more details). Figure 1.2 demonstrates three important points about galaxy properties. First, that star-forming galaxies typically have star-formation rates that correlate with their stellar mass (see also Brinchmann et al. 2004; Whitaker et al. 2012). This linear correlation is a byproduct of the Schmidt-Kennicut relation (Schmidt 1959; Kennicutt

---

[1] Galaxies with morphologies that did not exhibit elliptical or spiral morphologies were deemed "irregular" galaxies, which made up ∼3% of Hubble's sample.

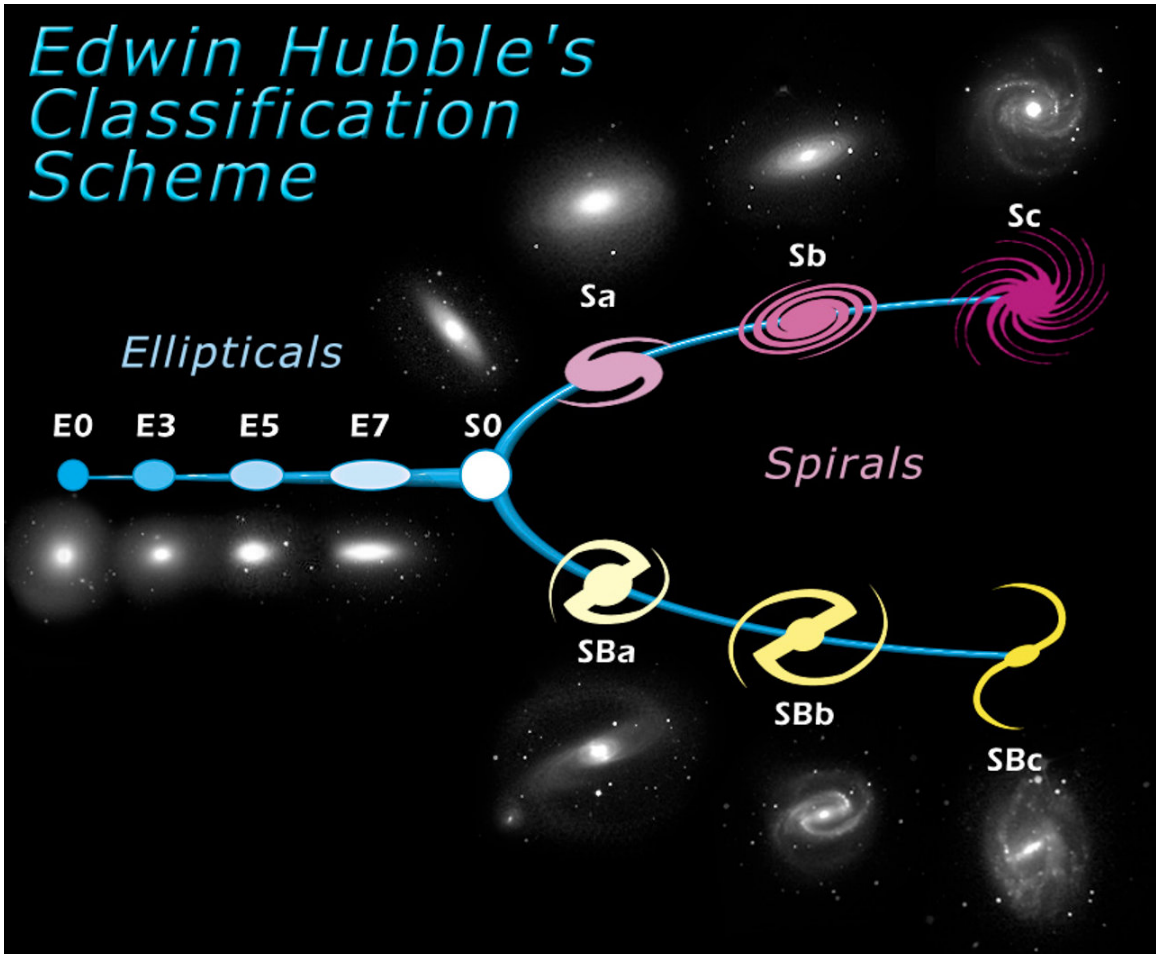

Figure 1.1: A Hubble tuning fork diagram presented by NASA/ESA. On the left are elliptical galaxies which become more elliptical from E0 to E7. On the right are spiral disks which are subdivided in to a,b and c depending on how tightly wound the spiral arms and how small the central bulges appear. The diagram bifurcates at the junction between ellipticals and spirals to account for spirals with and without bars.

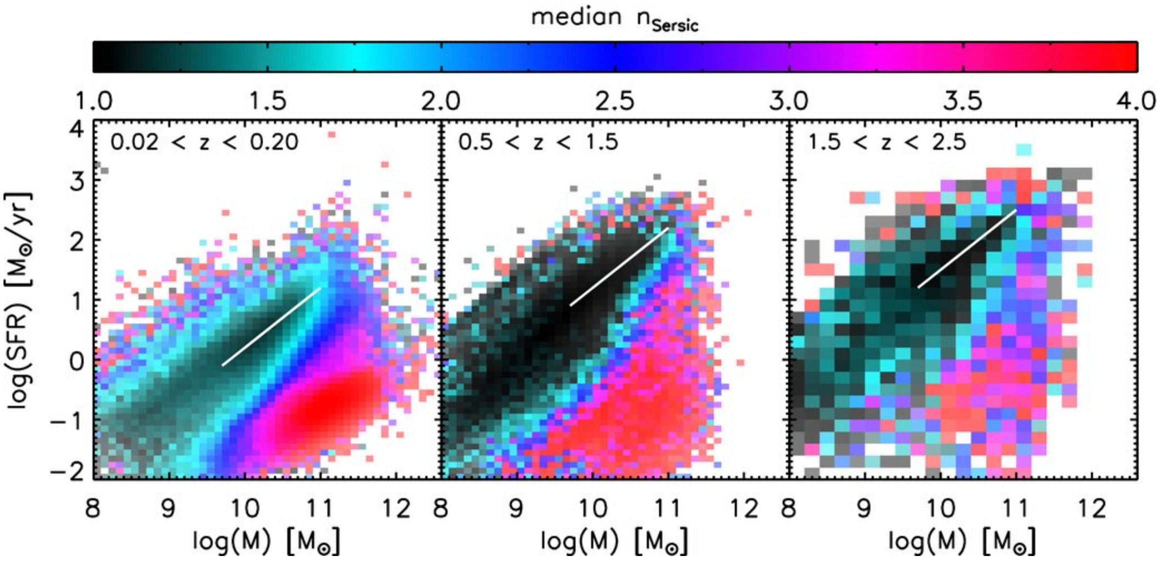

Figure 1.2: Surface brightness profile shape in the SFR–mass diagram. A "structural main sequence" is clearly present at all observed epochs, and well approximated by a constant slope of 1 and a zero point that increases with lookback time (white line). While star-forming galaxies on the SFMS are well characterized by exponential disks, quiescent galaxies at all epochs are better described by de Vaucouleurs profiles. Those galaxies that occupy the tip and upper envelope of the SFMS also have cuspier light profiles, intermediate between SFMS galaxies and red and dead systems. This figure and caption are taken from Wuyts et al. (2011).

1998) and the molecular gas main sequence (Lin et al. 2019) which allows for more star-formation to occur when there is more star-forming fuel, generally found regions of higher stellar density (Lin et al. 2019; Baker et al. 2022). The line along which star-forming galaxies lie in this plane is known as the star-forming main sequence (SFMS). Secondly, there is a strong correlation between galaxy morphology and star-formation. Lastly, the correlation between morphology and star-formation rate has existed for at least ∼11 Gyr (i.e. z∼2.5) and persists to the low-redshift Universe.

The focus of many modern studies has been to understand how galaxy bimodality comes to be. Studying the properties of galaxies at higher redshifts (i.e. further away and further back in time, see Hubble 1929), it has become apparent that the relative number of spiral, elliptical and peculiar morphology galaxies has evolved over time. In Figure 1.3, I show the work done by Buitrago et al. (2013) and presented in Conselice (2014) that shows how the number of disk-like versus spheroid-like galaxies and spiral (late-type), elliptical (early-type) and peculiar galaxies has changed since the Universe was only ∼2 Gyr old (i.e. z∼3). The important takeaway from Figure

1.3 is that at early times, disk-like spiral galaxies were more numerous than elliptical galaxies and since then, the number of spirals has decreased proportionally to the increase in the number of ellipticals. The exchange of disk-like spirals for spheroidal ellipticals suggests that the evolutionary sequence of galaxies is from star-forming, gas-rich, blue spiral disks to quiescent, gas-poor, red spheroidal ellipticals.

Galaxy mergers represent a logical mechanism for the transformation of spirals into ellipticals. Hierarchical galaxy assembly through mergers is a natural consequence of the leading cosmological paradigm: cold dark matter (CDM) with a dark energy term (Λ), ΛCDM (White and Rees 1978; Blumenthal et al. 1984; Davis et al. 1985; Cole et al. 2000). Theory demonstrates that galaxies emerge from overdense regions of the early universe and accrue matter by either accreting gas from the immediate surroundings and forming stars *in-situ* or through repeated mergers with other galaxies. Thus, it is thought that virtually all modern day massive galaxies are the assembly of many smaller galaxies. Tracing this process though time reveals what is known as a merger tree, an example of which from De Lucia and Blaizot (2007) is presented in Figure 1.4. In addition to the growth of mass, the merger tree in Figure 1.4 demonstrates that galaxies tend towards redder colours after successive mergers. This would indicate mergers play a role in ceasing the formation of new stars and thus the evolution of galaxies from star-forming to quiescence. Indeed, the merger sequence and its transformative effect on galaxy properties has been well studied by both numerical simulations and observations.

Numerical simulations allow for a detailed analysis of the effects of mergers over the span of billions of years. An example of a numerical simulation of the merger sequence is presented in Figure 1.5 from Hopkins et al. (2006). Each panel of Figure 1.5 shows a different snapshot of time of a galaxy merger with brightness representing stellar density and colour representing the gas content. 0.21 Gyr into the merger sequence, two spiral galaxies are well separated and as such, exhibit very "normal" features such as symmetric spiral structure and high gas fraction. Since the two galaxies are bound by gravity, they orbit each other having a first pericentric passage at around 0.39 Gyr, in this case. The close interaction leads to tidal gravitational forces which cause several features to appear including the unraveling of the spiral arms, asymmetric tidal tails and stellar bridges between the two galaxies (Toomre and Toomre 1972). Due to dynamical friction between the dark matter halos of the two galaxies (see Chandrasekhar 1943; Lacey and Cole 1993; Boylan-Kolchin et al. 2008; Benson 2010), the orbits of the two galaxies degrade and the two galaxies merge

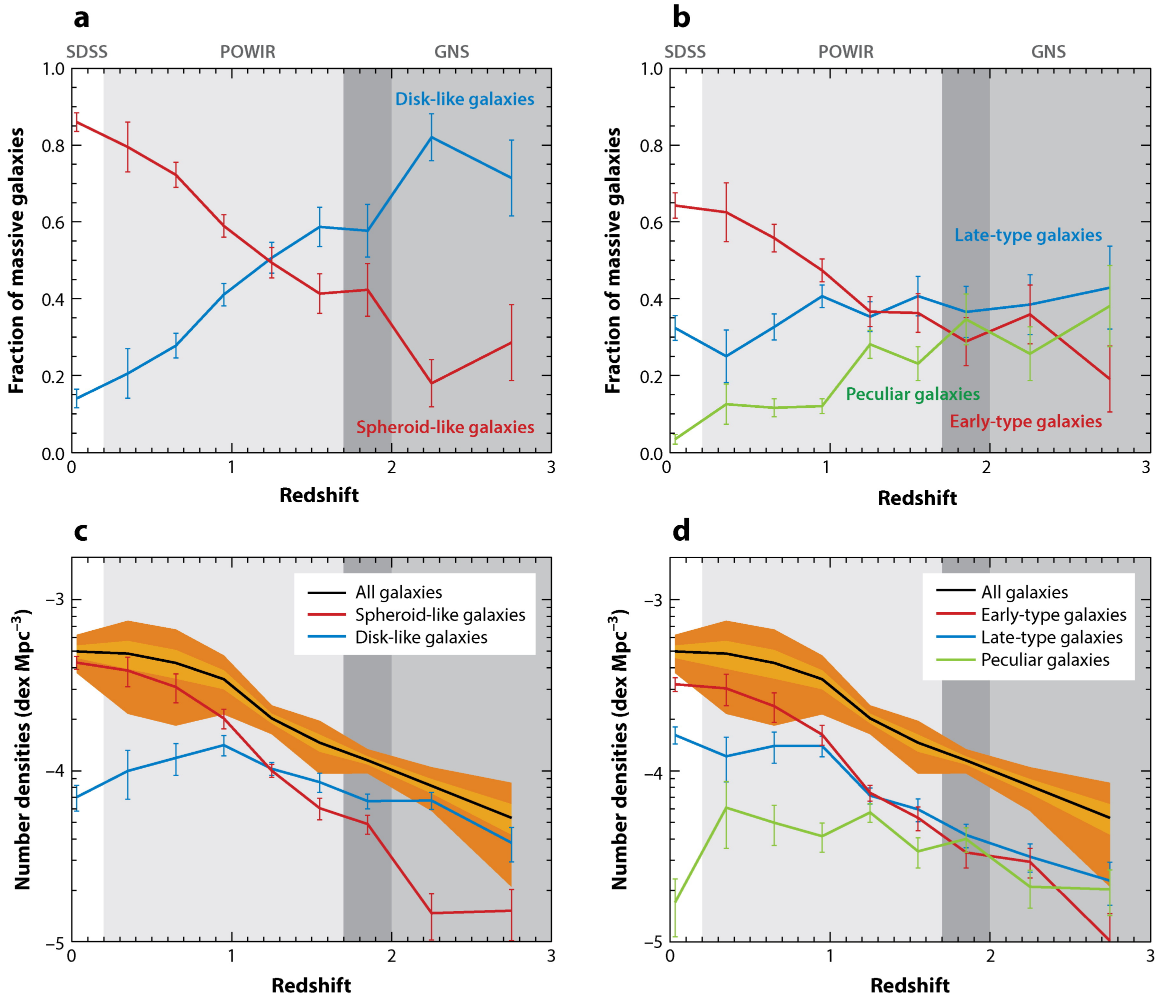

Conselice CJ. 2014.
Annu. Rev. Astron. Astrophys. 52:291–337

Figure 1.3: The evolution of apparent morphology and Sérsic-index-based classifications for massive galaxies with $M_\star > 10^{11} M_\odot$ from Buitrago et al. (2013). Shown are the morphologies and structures derived from three different surveys—the Sloan Digital Sky Survey (SDSS) for nearby galaxies, the Palomar Observatory WideField Infrared (POWIR) survey (Conselice et al. 2007) for systems up to $z\sim2$, and the Great Observatories Origins Deep Survey NICMOS survey (GNS) for systems at $z\sim1.8$-3. (a) In this plot, disk-like galaxies are those with Sérsic indices $n<2.5$, and spheroid-like galaxies are for those with $n>2.5$. (b) The morphological evolution as judged from visual estimates. Plotted here are both the fraction of types and the number density evolution. (c,d) The orange shading gives the total number density of all galaxies as a function of redshift up to $z\sim3$. As can be seen, there is a gradual transition from galaxies that appear peculiar and "disk-like" in their Sérsic indices at high redshifts $z>1.5$, which gradually transform into early types today. This figure and caption are taken from Conselice (2014).

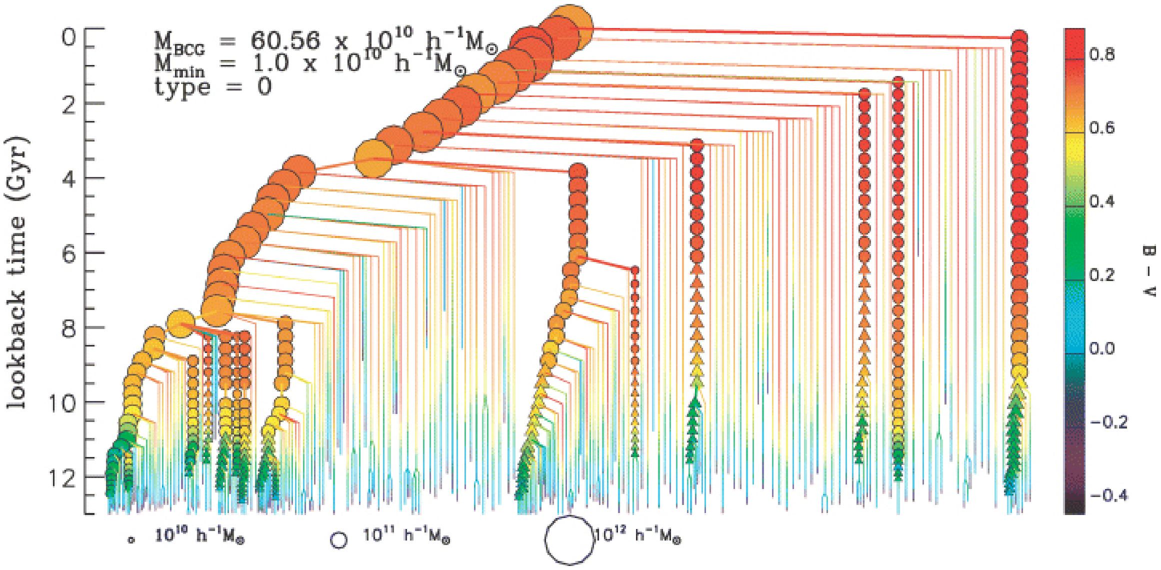

Figure 1.4: A schematic representation of a "merger tree" depicting the growth of a brightest cluster galaxy (BCG) as the result of a series of mergers. Symbols are colour-coded as a function of B−V colour and their area scales with the stellar mass. Only progenitors more massive than 10^10 M$_\odot$ are shown with symbols. Circles are used for galaxies that reside in the group inhabited by the main branch. Triangles show galaxies that have not yet joined this group. This figure and caption are taken from De Lucia and Blaizot (2007).

into one and coalesce ~ 1.5 Gyr into the simulation. After coalescence, several types of perturbations in the stellar distribution of the remnant galaxy (henceforth referred to as merger features) persist for several 100 Myr including asymmetric features, tidal tails, and shells (see Toomre and Toomre 1972). Throughout the merger sequence, the growth of non-axisymmetric structures results in gravitational torques that cause gas to lose angular momentum and fall towards the centre of the galaxy (Toomre and Toomre 1972; Barnes and Hernquist 1991; Iono et al. 2004; Blumenthal and Barnes 2018). The flow of gas to the centre of the galaxy initiates a period of enhanced star-formation (i.e. a central starburst; Kapferer et al. 2005; Di Matteo et al. 2007; Cox et al. 2008; Moreno et al. 2015; Hani et al. 2020). Additionally, the increase in gas around the nucleus of the galaxy causes an enhancement in the accretion rate (Capelo et al. 2015; Byrne-Mamahit et al. 2023) and thus often triggers an active galactic nucleus (Keel et al. 1985; Di Matteo et al. 2005; Hopkins et al. 2006, 2008). AGN can eject gas from the system, energize the remaining gas in the galaxy such that it can no longer form stars, and prevent any further accretion of star-forming gas from cosmic filaments, sealing the fate of galaxies as they transition to quiescence (Davies et al. 2022).

Observationally, studying the merger sequence is challenging due to the timescales on which these systems evolve. Nonetheless, detailed studies of galaxies in the pair and post-merger phases of the merger sequence broadly support the findings from numerical simulations. For example, studies of galaxies undergoing a pair-phase interaction have shown disturbed morphologies (e.g. Patton et al. 2016), coincident with enhanced star-formation rates (e.g. Barton et al. 2000; Lambas et al. 2003; Kewley et al. 2006; Ellison et al. 2008; Woods et al. 2010; Scudder et al. 2012; Patton et al. 2013; Knapen et al. 2015; Shah et al. 2022) and suppressed metallicities (Kewley et al. 2006; Scudder et al. 2012) which demonstrate tidal gravitational forces produce non-axisymmetric structures and torques that drive gas towards the centre of the galaxy. Recent post-merger galaxies (identified by their disturbed morphologies, see Section 1.2) also exhibit enhanced star-formation (Bridge et al. 2010; Ellison et al. 2013; Thorp et al. 2019; Pearson et al. 2019a; Bickley et al. 2022; Shah et al. 2022), suppressed metallicities (Ellison et al. 2013; Thorp et al. 2019), and an enhanced frequency of AGN (Ellison et al. 2013, 2019; Bickley et al. 2023).

In addition to mergers, many other mechanisms are capable of causing galaxies to transition from star-forming spirals to quiescent ellipticals which generally involve gravitational interactions with other galaxies and/or the depletion of star-forming gas

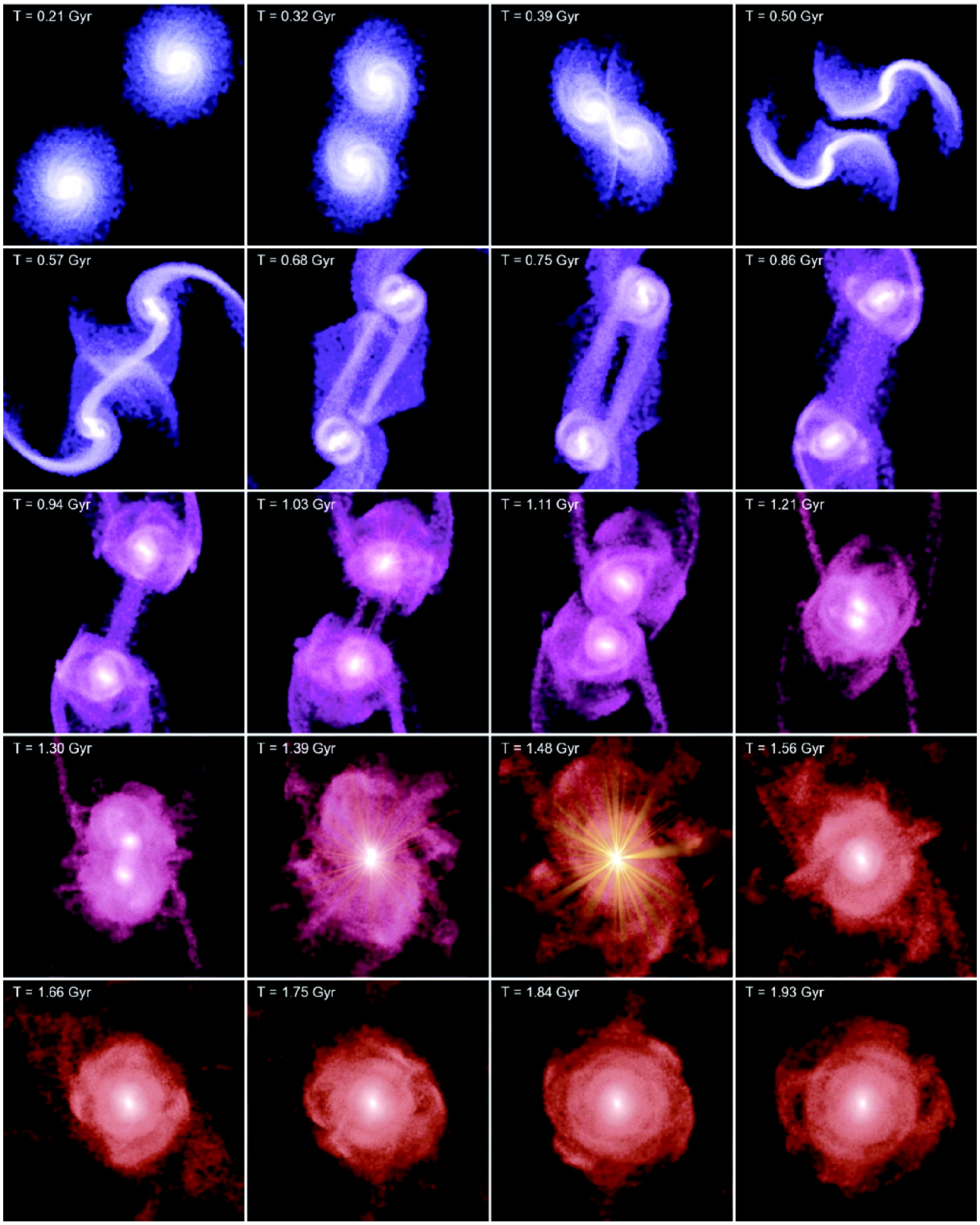

Figure 1.5: Time sequence from one of the merger simulations ($V_{\rm vir} = 160 {\rm km} s^{-1}$, initial gas fraction 20%) in Hopkins et al. (2006). Each panel is $80{\rm h}^{-1}$kpc on a side and shows the simulation time in the upper left corner. Brightness of individual pixels gives the logarithm of the projected stellar mass density, while color hue indicates the baryonic gas fraction, from 20% (blue) to less than 5% (red). At T = 1.03, 1.39 and 1.48 Gyr, when the black hole could be seen as an optical quasar, nuclear point sources are shown, providing a representation of the relative luminosities of stars and the quasar at these times. This figure and caption are taken from Hopkins et al. (2006).

in the system. A non-exhaustive list of evolution mechanisms includes harassment (Moore et al. 1996, 1998), ram pressure stripping (Gunn and Gott 1972; Roberts et al. 2021, 2022; Boselli et al. 2022), AGN feedback (Hopkins et al. 2006, 2008; Cicone et al. 2014), stellar winds and supernova feedback (Heckman et al. 1990; Mac Low and Ferrara 1999), and ionizing winds from the cosmic microwave background (Brown et al. 2014). These processes are not exclusive; many different physical processes may be involved in a given galaxy's transition from star-forming to quiescence.

Vital to our understanding of how galaxies quench their star-formation and transform other properties is the contribution of galaxy mergers relative to other causal mechanisms. There are two important factors needed to effectively study the contribution of galaxy mergers to rapid quenching. First, a sample of galaxies currently or very recently transitioning from star-forming to quiescence. Second, a method to reliably infer that the mechanism contributing to or causing the transition is a recent merger or interaction with another galaxy. In the following two subsections, I introduce my approach to each of these important factors.

1.1 Recently and Rapidly Quenched Post-starburst Galaxies

Identifying a population of galaxies that are actively transitioning from star-forming to quiescence allows us to study the mechanisms driving the transformation process. Post-starburst galaxies (PSBs) offer such an opportunity. Originally, PSBs were known as "E+A" or "K+A" galaxies due to having spectra typical for red ("K," as in red K-type stars), quiescent elliptical ("E") galaxies but with the unusual superposition of the spectral features of A-type stars ("+A") (Dressler and Gunn 1983; Couch and Sharples 1987). PSBs are now more broadly characterized as galaxies with spectra that indicate the presence of recently formed stars in a period of elevated star formation, yet no ongoing star formation at the time of observation.

Traditionally, E+A post-starburst galaxies are selected on the basis of strong higher order Balmer absorption lines (such as Hδ and Hγ) and weak nebular emission lines (such as Hα and [OII]) (e.g., Zabludoff et al. 1996; Blake et al. 2004; Goto 2005, 2007). Strong Balmer absorption is indicative of significant light contributions from A- and F-type stars. A-type stars have a lifetime of $\sim$1 Gyr and so their presence implies recent star formation. On the other hand, Hα and [OII] are emitted by regions

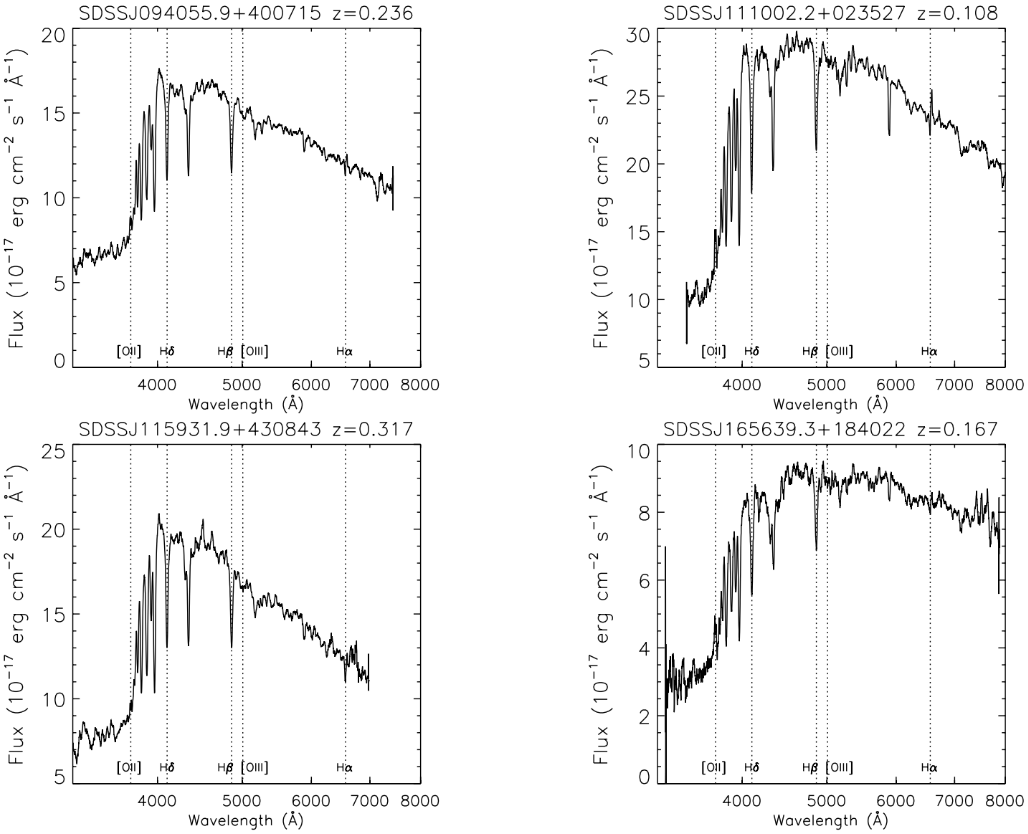

Figure 1.6: Example spectra of four E+A galaxies with largest Hδ equivalent widths of 8.62–9.27 Å. Each spectrum is shifted to the rest-frame wavelength and smoothed using a 20-Å box. This figure and caption are taken from Goto (2005).

of active star formation. Thus, their absence implies that there is no ongoing star formation at the time of observation. Together, these spectroscopic indicators describe a galaxy that had a recent burst in star formation that has subsequently ceased quite rapidly. Four examples of E+A spectra from Goto (2005) that demonstrate these characteristics are shown in Figure 1.6.

The traditional selection of PSBs requires strict cuts in nebular emission lines that excludes galaxies with some ongoing star formation as well as galaxies with other ionization methods such as active galactic nuclei (AGN) and shocks. Moreover, galaxies that have recently started to quench their star formation may have some remnant star formation occurring and should be included. Furthermore, both AGN and shocked emission have been shown to be present in significant numbers of PSBs (Tremonti et al. 2007; Wild et al. 2007; Yesuf et al. 2014; Alatalo et al. 2016a,b; Sazonova et al. 2021). Principle component analysis (PCA) methods have proven

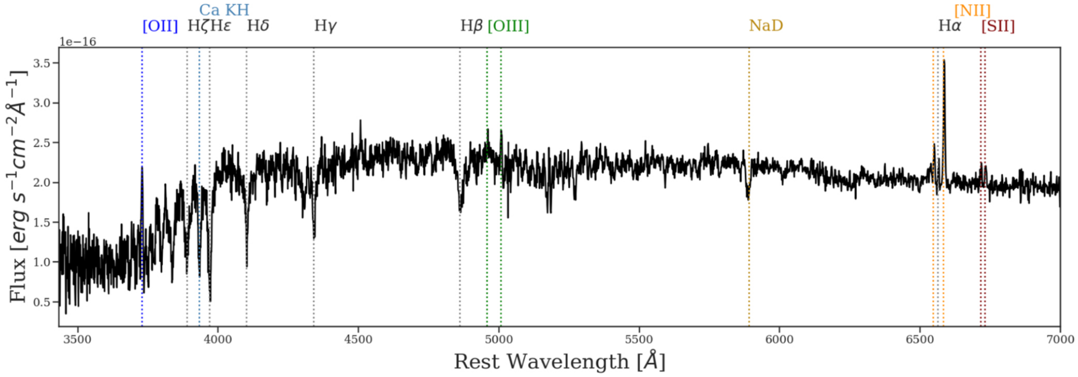

Figure 1.7: Example spectrum of a post-starburst galaxy from the SDSS (spec-0524-52027-0492). This galaxy was selected by all three of the Wild et al. (2007), Alatalo et al. (2016b), and French et al. (2018) selection methods. This galaxy has strong Balmer absorption and weak emission lines that are more consistent with shock or AGN-dominated ionization than ionization from star formation. In this spectrum, the Hϵ line is blended with the Ca H line, resulting in stronger emission than Ca K, a quick visual diagnostic for post-starburst spectra. This figure and caption are taken from French (2021).

capable of selecting PSBs without strict cuts in nebular emission which allow for the inclusion of PSBs with AGN, shocks, and residual star formation (Wild et al. 2007; Pawlik et al. 2016, 2018). A PSB with Hα emission selected by Wild et al. (2007), Alatalo et al. (2016b), and French et al. (2018) is presented in Figure 1.7.

The juxtaposition between recently formed stars and a lack of ongoing star formation inferred from the spectra of PSBs indicates a rapid truncation in star formation. Additionally, their diverse morphologies (Yang et al. 2008; Meusinger et al. 2017; Pawlik et al. 2018) and kinematic structure (Pracy et al. 2009, 2013; Chen et al. 2019) indicate that the rapid change in the star-formation of PSBs is coincident with a rapid change in the global properties of the galaxy. Thus, PSBs are viewed as an integral probe of rapid galaxy evolution.

Cosmological simulations (e.g. Davis et al. 2019; Pawlik et al. 2019) show that a variety of mechanisms can cause galaxies to rapidly quench and become PSBs including ram pressure stripping and outbursts from AGN. However, both major and minor mergers have been shown to be the most frequent cause of PSBs in simulations (Davis et al. 2019; Lotz et al. 2021). Furthermore, hydrodynamical simulations of individual galaxy mergers show that mergers can induce a burst in star formation followed by rapid quenching into a post-starburst phase, eventually progressing to become quiescent ellipticals (Wild et al. 2009; Snyder et al. 2011; Zheng et al. 2020). While not all mergers go through a post-starburst phase, mergers with higher mass ratios, higher initial gas contents and prograde orbital configurations have been shown to induce stronger and longer lasting PSB signatures (Bekki et al. 2005; Wild et al. 2009; Snyder et al. 2011; Pawlik et al. 2018; Zheng et al. 2020). Indeed, observationally, it is the most asymmetric mergers that exhibit the highest PSB fractions (Rowlands et al. 2018; Ellison et al. 2022).

Observationally, PSBs have been shown to be present in dense clusters and caused by ram pressure stripping (Werle et al. 2022). However, PSBs at low redshift are found predominantly in the field rather than in clusters (Zabludoff et al. 1996; Quintero et al. 2004; Blake et al. 2004; Goto 2005; Hogg et al. 2006; Wild et al. 2009; Yan et al. 2009; Rowlands et al. 2015) indicating that environmental quenching mechanisms like ram pressure stripping are unlikely to be the dominant cause of PSBs. Some PSBs are observed to have AGN (Goto 2006; Tremonti et al. 2007; Wild et al. 2007, 2010; Yesuf et al. 2014) and AGN have been found to be more prevalent in interacting pairs and recent post-mergers (e.g. Ellison et al. 2019; Bickley et al. 2023). Significant fractions of PSBs are found to have irregular and disturbed morphologies indicative of a recent merger or major gravitational interaction with another galaxy (Zabludoff et al. 1996; Blake et al. 2004; Goto 2005; Yang et al. 2008; Pracy et al. 2009; Alatalo et al. 2016b; Pawlik et al. 2016, 2018; Meusinger et al. 2017; Sazonova et al. 2021). Quantitatively, the merger fraction of post-starbursts has been determined to be anywhere from 13% (Blake et al. 2004) to 60% (Pracy et al. 2009). However, numerous factors will impact the the merger fraction of the PSB population, including the precise definition of a "PSB" and how a merger is identified.

The observed morphology of a galaxy merger is highly sensitive to the image quality, particularly the depth and resolution of the image (Lotz et al. 2004; Pawlik et al. 2016; Bottrell et al. 2019). In some cases, galaxy merger features may persist for up to ∼1 Gyr, but regularly begin to settle and become fainter on the order of ∼200 Myr after coalescence (Mihos 1995; Lotz et al. 2008; Bottrell et al. 2022). Considering that PSBs are typically 0.5 to 1 Gyr removed from the onset of the burst (Wild et al. 2010; Wild et al. 2020), the information regarding a PSB's (non-)merger history may have already faded beyond detection. Specifically, Pawlik et al. (2016) found that the observed merger fraction of young PSBs is reduced from 43% ($<$ 300 Myr after starburst) to 21% ($>$300 Myr after starburst) as the PSBs age. Due to the rapidly fading morphological information, the reported merger fractions of PSB samples are likely lower limits of the true fraction of recent mergers and interactions.

Deeper imaging enhances low surface brightness features such as fading tidal tails and higher spatial resolution imaging allows for internal disturbances to be resolved (Sazonova et al. 2021). Thus, higher quality imaging should allow for more mergers to be detected, approaching the true value of recent mergers. For example, when Yang et al. (2008) revisited the same galaxies from Zabludoff et al. (1996) with deeper and higher resolution imaging from the Hubble Space Telescope, the detection of merger features increased from 5/21 (24%) to 11/20 (55%).

The diversity of PSB merger fractions reported in the literature is demonstrated in Figure 1.8. Merger fractions of post-starburst galaxies from eight previous studies and the work presented in this thesis are plotted against the pixel scale resolution of the imaging used to detect the mergers[2]. Circles, squares and diamonds indicate merger fractions determined using visual identification, shape asymmetry and a convolutional neural network, repsectively, and their relative sizes indicate the size of the PSB samples. There is a decreasing trend in merger fraction with increasing on-sky pixel size, but more important is the significant vertical scatter at fixed pixel scale. The vertical scatter, and therefore the wide range of reported PSB merger fractions, is caused by a heterogeneous selection of PSBs across different studies, small samples of PSBs, and differing merger identification methods (including the quality of imaging used). By selecting PSBs using different techniques, these studies are identifying slightly different populations for which the merger fraction may be different (see Fig. 14 in Meusinger et al. 2017). Additionally, PSB merger fractions estimated from small samples (most previous studies contain only a few tens of objects) are subject to statistical error which contributes to the spread in reported values. Finally, visual identification of mergers is a subjective process and depends strongly on the quality of the imaging. Both the biases of the different classifiers and variation in the quality of imaging can be addressed if the merger identification methods are also applied to a robust control sample. Unfortunately, direct comparison to a control sample has not been commonly implemented. In Chapter 2, I will show definitively that the diversity of PSB merger fractions reported in the literature and thus the elusiveness of understanding the importance of mergers to rapid galaxy evolution are a result of the variable PSB selection techniques, variable merger identification methods, and variable image qualities combined with the small sample statistics and lack of control samples in previous works. I will do this by using 1) two large samples of PSBs with different selection methods, 2) both low and high quality imaging, 3) a robust

---

[2] Pixel scale resolution is the only ubiquitously reported image quality metric available.

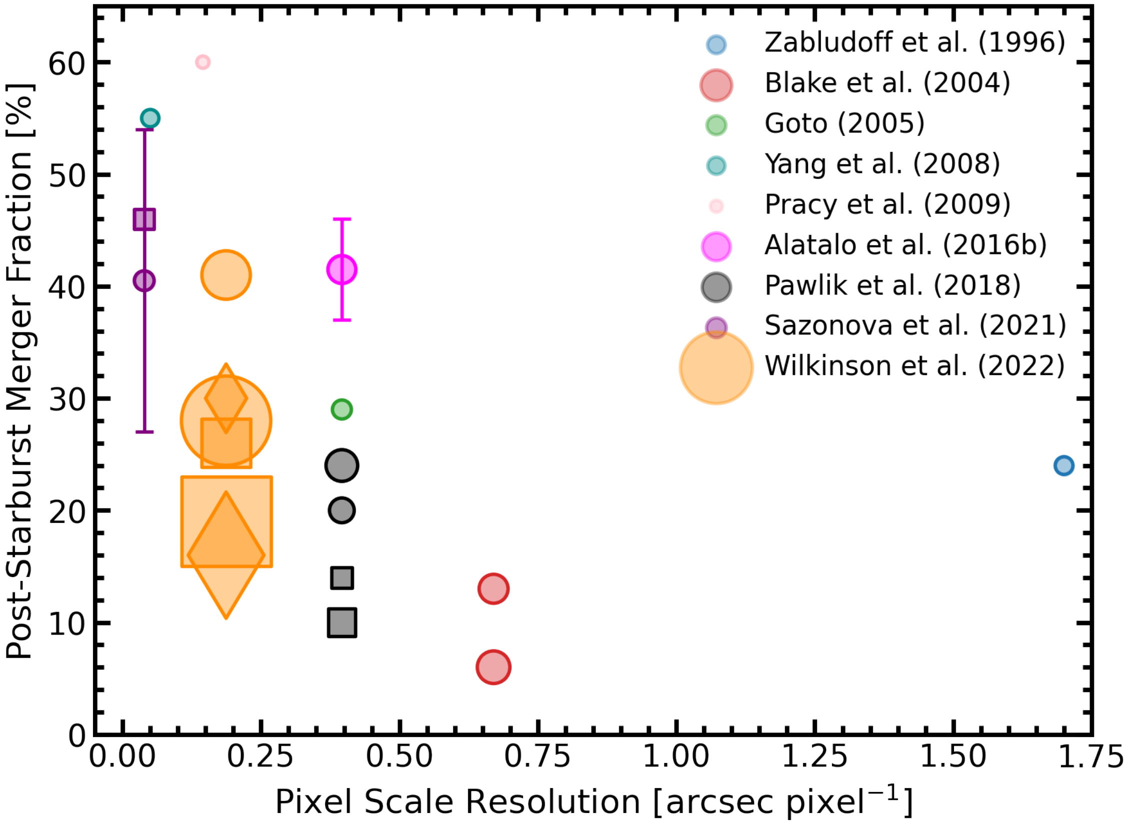

Figure 1.8: The merger fraction of post-starburst galaxies reported by previous studies, plotted as a function of the pixel scale resolution of the imaging used to identify the mergers. Pixel scale resolution is the only metric reported ubiquitously and with consistent units and is used here as a proxy for image quality. Colours of the points are representative of the study from which the merger fraction is derived. Symbols represent the merger identification technique: visual inspection (circles), shape asymmetry greater than 0.4 (squares), or convolutional neural network prediction (diamonds). The sizes of points correlate linearly with the size of the post-merger sample and range from 10 galaxies (Pracy et al. 2009) to 533 (Wilkinson et al. 2022). Merger fractions reported as ranges are conveyed by error bars. In general, each study uses different PSB selection criteria and in some instances, studies use multiple selection methods which contributes to the spread in merger fractions. Note that the shape asymmetry merger fraction for Sazonova et al. (2021) was calculated for the purposes of this figure from data made publicly available by the authors.

control sample, and 4) a broad suite of morphology metrics and merger identification methods.

1.2 The Identification of Galaxy Mergers

The human brain is naturally skilled at categorization, pattern recognition, and, importantly, identifying objects or features of objects that deviate from those expected (Mattson 2014). For this reason, many previous works have used visual inspection of galaxy images to deduce galaxy morphology and merger status (e.g. Couch et al. 1994; Zabludoff et al. 1996; Brinchmann et al. 1998; Bundy et al. 2005; Goto 2005; Bridge et al. 2010; Nair and Abraham 2010; Sheen et al. 2012; Hung et al. 2013; Atkinson et al. 2013; Kartaltepe et al. 2015; Ellison et al. 2019; Bílek et al. 2020). The process of identifying galaxies in this way is very simple: generally speaking, the photometric (and in some cases, multi-band colour) image of a galaxy is inspected by a human classifier who synthesizes prior knowledge based on theory or experience to assert if the observed galaxy morphology is the result of a merger or otherwise.

However, visual identification of galaxy mergers suffers from two specific and acute drawbacks. First, the prior knowledge available to a given classifier and the way in which it is synthesized and applied to a given galaxy is an inherently subjective process. Additional layers of variance include whether or not a classifier is optimizing their decision process for high completeness or high purity of a merger sample or if classifications include discussion and deliberation amongst other classifiers. This causes varying results between classifications (for example, see Fig. 19 in Bickley et al. 2021), making it difficult to compare results reliably between studies. Secondly, visual inspection by humans takes a significant amount of time. In the era of digitized sky surveys, datasets are often much larger than what can feasibly be classified by a single classifier.

One method used to overcome the subjectivity and prohibitive time requirement of visual classification of galaxy mergers is crowd-sourcing the classification process using citizen science programs. Citizen science programs are generally built upon a web-based infrastructure that welcomes volunteers from all levels of expertise to classify galaxies as a hobby. The benefit of this method is threefold: the time required to classify large datasets is distributed across a larger number of classifiers, the biases of individual classifiers are averaged out over many classifiers, and, as an added bonus, it increases community engagement with science, bolstering dissemination efforts of scientific results. A notably successful implementation of this method is GalaxyZoo (Lintott et al. 2008, 2011; Willett et al. 2013; Simmons et al. 2017) from which the public classifications of galaxies have been used in a variety of science cases (e.g. Cardamone et al. 2009; Amorín et al. 2010; Darg et al. 2010a,b; Finkelman et al. 2012; Willett et al. 2015) and as a benchmark for validating new galaxy classification methods (e.g. Banerji et al. 2010; Huertas-Company et al. 2011; Casteels et al. 2013; Dieleman et al. 2015; Walmsley et al. 2020). Another alternative to visual classification is automating the classification using computer programming. Two types of automated methods, non-parametric morphology statistics and machine learning techniques, are introduced in detail in the following two subsections.

1.2.1 Non-parametric Morphology Statistics

Non-parametric morphology statistics of galaxies encompass any calculation regarding the shape of the galaxy light profile that does not assume any prior knowledge of the galaxy shape (for this reason, the term "non-parametric" can be equivalently thought of as "model-independent"). There are many such non-parametric morphology statistics ranging from a measures of concentration (e.g. Abraham et al. 1994; Conselice 2003) to non-radially constant structure, spirality (Ferrari et al. 2015). A small fraction of these non-parametric morphology statistics were either designed for the purpose of, or later adopted for the use of, identifying mergers.

In general, non-parametric morphology statistics take on values along a gradual continuum. Therefore, if a statistic is to be used as a merger detection method, a threshold must be set that separates mergers from non-mergers. When a new non-parametric morphology statistic is introduced in the literature for the purpose of identifying mergers, it is generally paired with a suggested threshold above which galaxies are to be considered mergers. However, galaxy morphology is known to differ in different wavelengths (e.g. Kelvin et al. 2012; Vika et al. 2013; Häußler et al. 2013; Baes et al. 2020) and in different image qualities (e.g. Lotz et al. 2004; Lisker 2008) and thus, the optimal threshold for separating mergers from non-mergers may differ between datasets. Furthermore, as in the case of visual classification, the boundary above which you consider a galaxy a merger might depend on if you are optimizing for purity or completeness of detected mergers. In this work, I will at times explore how my results would differ if a different threshold were used to identify mergers. For this reason, I refer to the threshold used widely in the literature as either the "suggested threshold" or the "default threshold" throughout.

Although all of the non-parametric morphology metrics used in this work are well established in the literature, for completeness I briefly review the definitions of the metrics relevant for identifying mergers used herein and provide references for readers desiring more detailed descriptions.

Asymmetry

Asymmetry (Abraham et al. 1996; Conselice et al. 2000), A, quantifies the azimuthal asymmetry of a galaxy's light profile. To extract this information, the image is rotated by 180°, subtracted from the original image and normalized by the total flux. To account for contributions to the asymmetry from the background noise, the average asymmetry of the background is subtracted from the total:

$$A = \frac{\Sigma|I_0 - I_{180}|}{\Sigma|I_0|} - A_{\mathrm{bgr}}, \tag{1.1}$$

where I_0 is the flux of a pixel in the original image, I_{180} is the flux of the same pixel after the image has been rotated by 180° about the centre of the galaxy, determined by minimizing the value of A, and A_{bgr} is the average asymmetry of the background. The sum is carried out over all pixels within a circular aperture with radius of 1.5 Petrosian radii.

The method by which the asymmetry of the background noise is measured and rectified can greatly affect the accuracy of the asymmetry measurement (Thorp et al. 2021). There are several ways to measure the average asymmetry of the background noise (e.g. Conselice et al. 2000; Curtis-Lake et al. 2016; Wen and Zheng 2016; Tohill et al. 2021). In this work, I use the a morphology code, `statmorph` from Rodriguez-Gomez et al. (2019) (see Section 2.2.1 for more details), which determines A_{bgr} by first calculating the sum of the absolute difference between a square portion of sky and its 180°-rotated counterpart. That sum is normalized by the number of pixels in that "skybox" to determine an average and then multiplied by the number of pixels present in the 1.5 Petrosian radii aperture used to determine the asymmetry of the target galaxy. This quantity is normalized by the absolute sum of the unrotated image. The `statmorph` determination of A_{bgr} can be represented as:

$$A_{\mathrm{bgr}} = \frac{\Sigma|B_0 - B_{180}| \times \frac{a_{1.5r_p}}{a_{\mathrm{skybox}}}}{\Sigma|I_0|}, \tag{1.2}$$

where B_0 and B_{180} represents the unrotated and rotated skybox, respectively, a_{skybox} is the area (in pixels) of the skybox, and $a_{1.5r_p}$ is the area (in pixels) over which the asymmetry of the galaxy is calculated, in this case the area within the circular aperture with a radius of 1.5 Petrosian radii.

Low values of asymmetry indicate the galaxy is very azimuthally symmetric, a common feature of early-type galaxies with spheroidal morphologies (Conselice 2003). Spiral galaxies inherently have slightly elevated asymmetries due to naturally occurring asymmetric features like dust lanes and clumpy star formation (Conselice 2003). Higher asymmetry values are common amongst galaxies exhibiting strong merger and post-merger signatures; Conselice (2003) suggest galaxy mergers are those with $A > 0.35$.

Outer Asymmetry

Outer asymmetry (Wen and Zheng 2016), A_O, is defined in the same way as asymmetry (see Equation 1.1) but the sum is computed over an annulus aperture rather than a circular aperture with a radius of 1.5 Petrosian radii. The annulus over which the sum is computed has an inner boundary equal to an ellipse within which 50% of the total light of the galaxy is contained and an outer boundary which is determined by the maximum radius of a pixel belonging to the galaxy. Since the central region of a galaxy is often bright and symmetric, excluding the central region from the asymmetry sum allows for A_O to be more sensitive to faint and asymmetric tidal features. Wen and Zheng (2016) note that most galaxies have $A_O < 0.6$, suggesting that galaxies above this threshold are mostly merging galaxies. However, the method by which sky noise is accounted in Wen and Zheng (2016) is different from the Rodriguez-Gomez et al. (2019) approach used in this work, which ultimately changes its normalization (see Appendix A of Wen and Zheng 2016). To compare outer asymmetry directly to the asymmetry statistic from Conselice et al. (2000) which has a near-identical calculation except for the exclusion of the central region, I assume the default threshold to be $A_O > 0.35$.

Shape Asymmetry

Shape asymmetry (Pawlik et al. 2016), A_S, is also defined in the same way as asymmetry (see Equation 1.1) but instead of each pixel having an intensity, I, each pixel is given a binary value: 1 if the pixel belongs to the galaxy, 0 otherwise. The binary mask used to measure shape asymmetry is distinct from the binary segmentation map provided to `statmorph` as input and is generated internally by `statmorph` following the method described in Pawlik et al. (2016). The point around which the image is rotated is the same as the point in the asymmetry measurement which minimizes the light-weighted asymmetry.

By calculating the asymmetry of the binary mask rather than the flux of the image itself, equal weight is given to pixels belonging to both the faint and bright regions of the galaxy. Comparatively, standard light-weighted asymmetry weights the central region of a given galaxy proportionally to its flux relative to the faint tidal features around it, which often differ by several orders of magnitude. Hence, the shape asymmetry statistic is more sensitive to low surface brightness features, such as faint tidal streams. This is of particular importance since faint tidal features may be key to identifying late-stage mergers expected in the PSB samples.

Pawlik et al. (2016) suggest that a threshold value of $A_S \geq 0.2$ can be used to reliably identify mergers in SDSS. It is important to note that the definition of shape asymmetry given in Pawlik et al. (2016) has an additional factor of 1/2 compared to the definition of Conselice et al. (2000) and, importantly, Rodriguez-Gomez et al. (2019). When the factor of 1/2 is accounted for, the Pawlik et al. (2016) recommended merger threshold becomes $A_S \geq 0.4$. For reference, the equation used in Pawlik et al. (2016) for both asymmetry and shape asymmetry is:

$$A = \frac{\Sigma|I_0 - I_{180}|}{2\Sigma|I_0|} - A_{\mathrm{bgr}}, \tag{1.3}$$

Gini-M$_{20}$

The Gini coefficent (Lotz et al. 2004), G, is defined as the mean of the absolute difference of the light curve from a uniform distribution where the variable X describes the flux in each pixel and is ordered from lowest to highest flux:

$$\mathrm{G} = \frac{1}{\overline{X}n(n-1)}\sum_{i}^{n}(2i-n-1)|X_i|, \tag{1.4}$$

where n is the number of pixels associated with the galaxy and $\overline{X}$ is the mean of flux of the pixels belonging to the galaxy.

The Gini coefficient is independent of the location of the brightest pixel and tends towards unity if the light from the galaxy is concentrated in a small number of pixels.

If all of the galaxy's light were to come from a single pixel, G = 1, and if the light is evenly distributed across every pixel in the galaxy, G = 0. For a galaxy with a recent burst of star formation in the central regions, one might expect an increase in the Gini coefficient.

Before defining M_{20}, I first introduce the second moment of the total light distribution, $\mathrm{M}_{\mathrm{tot}}$. The second moment of the light distribution, related to the spatial variance of the light distribution, is the summation of the flux of each pixel f_i multiplied by the squared distance from the centre:

$$\mathrm{M}_{\mathrm{tot}} = \sum_i^n \mathrm{M}_i = \sum_i^n f_i \left[(x_i - x_c)^2 + (y_i - y_c)^2 \right], \tag{1.5}$$

where x_c and y_c are x- and y-coordinates of the centre, determined by selecting the x- and y-coordinates that minimize $\mathrm{M}_{\mathrm{tot}}$.

M_{20}, then, is defined as the second moment of the brightest pixels that produce 20% of the galaxy's light, normalized by the total second moment of the galaxy. If pixels are ordered from highest to lowest flux, M_{20} is calculated as:

$$\mathrm{M}_{20} = \log_{10}\left(\frac{\sum_i \mathrm{M}_i}{\mathrm{M}_{\mathrm{tot}}} \right), \text{while} \sum_i f_i < 0.2 f_{\mathrm{tot}}. \tag{1.6}$$

In tandem, the Gini coefficient and M_{20} can be used to identify galaxies with large portions of the total light profile contained within a small number of spatially separated pixels. Lotz et al. (2008) suggest that at low-redshift ($z < 1.2$), galaxy mergers have Gini and M_{20} values such that meet the following equation:

$$G > -0.14\mathrm{M}_{20} + 0.33. \tag{1.7}$$

Figure 1.9, taken from Bignone et al. (2020), demonstrates the typical morphologies of galaxies in the Gini-M_{20} plane. Equation 1.7 is represented by the white dashed line, above which galaxies are considered mergers. While not all galaxies above the line appear as mergers (suggesting possible contamination using this method), there does seem to be an abundance of irregular morphologies relative to those below the line. The dotted line is commonly used to separate spiral disks from (below) elliptical galaxies (above).

Rather than relying on the rigid and empirically derived merger regime in the Gini-M_{20} plane defined by the green line in Figure 1.9, it is desirable to have a continuous statistic that builds off of the same principal. For this, Snyder et al. (2015) define

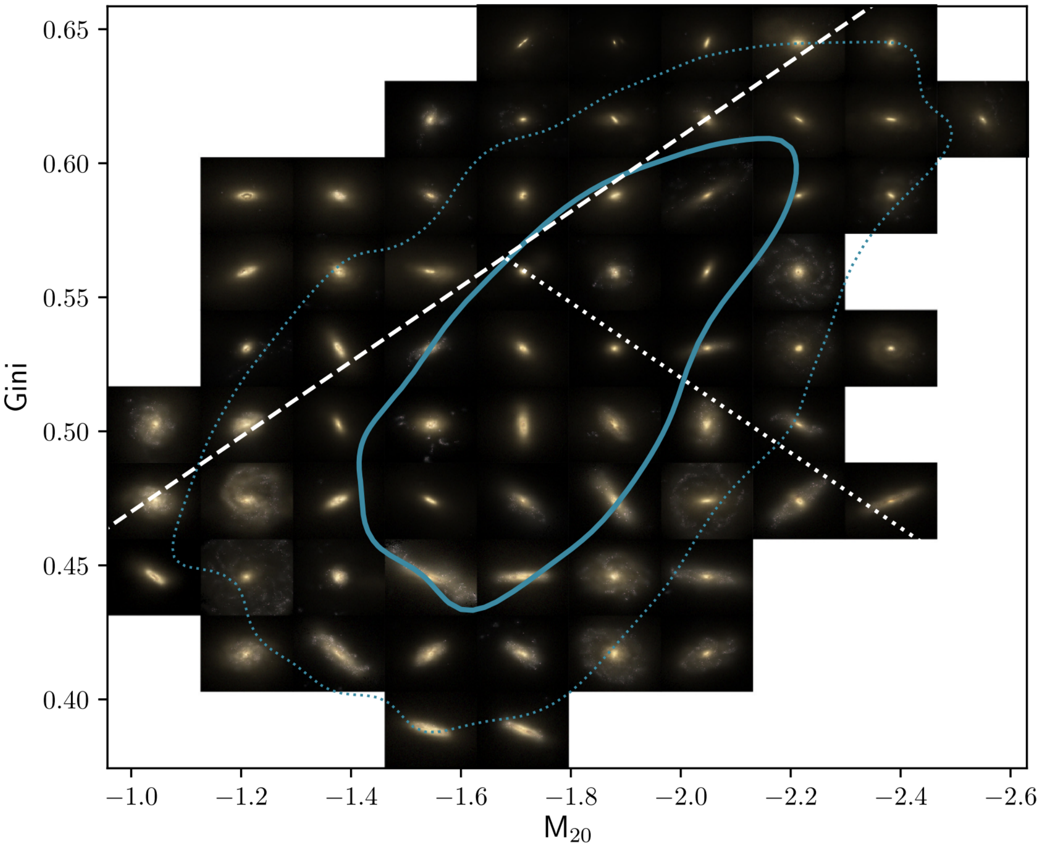

Figure 1.9: Mock gri-SDSS colour composite images of galaxies in the Ref-100 sample from the EAGLE simulation (Schaye et al. 2015) arranged according to their G and M_{20} values. Solid (dotted) contours represent the region containing 68 (95) per cent of all objects. The white dashed and dotted lines separate the subspace into regions for mergers, late types, and early types according to Lotz et al. (2008). In accordance with observational trends, prevailing morphologies at the top right of the diagram are of the early type, while galaxies at the lower left are late type. Signs of disturbed morphologies can be found above the dashed line for some galaxies. This figure and caption are taken from Bignone et al. (2020).

the Gini-M_{20} merger statistic, S(G, M_{20}), as the distance of a galaxy in the Gini-M_{20} plane from the merger cutoff line defined by Equation 1.7. Explicitly, in this work it is calculated following Rodriguez-Gomez et al. (2019) using the following equation:

$$S(G, M_{20}) = 0.139\mathrm{M}_{20} + 0.990G - 0.327 \tag{1.8}$$

By this equation, mergers are defined by having S(G, M_{20}) > 0 and thus I take this to be the default threshold in this work.

1.2.2 Machine Learning Techniques

Non-parametric morphology statistics take the two-dimensional spatial coordinates and measured flux of each pixel in a galaxy image and reduce it to a single dimension, conceivably carrying sufficient information to identify galaxy mergers. While this process can be automated and thus applied to large datasets, non-parametric morphology statistics contain less information and nuance than a human could extract from the original image. For example, bursty star-formation, foreground star contamination, and dust obscuration can all produce similar non-parametric morphology statistics as a bona fide merger, but could easily be differentiated by simply looking at the original image.

Recent advancements in machine learning techniques have allowed for a new method to automate galaxy classifications with human-like nuance. Broadly speaking, machine learning programs "learn" how to classify galaxies accurately by synthesizing the information from many examples of galaxies and their correct classifications. Machine learning programs applicable to galaxy classifications come in many forms including both classical methods such as random forest classifiers (e.g. Beck et al. 2018; Sreejith et al. 2018; Snyder et al. 2019; Guzmán-Ortega et al. 2023; Rose et al. 2023) and support vector machines (e.g. Huertas-Company et al. 2008, 2011; Sreejith et al. 2018), and deep-learning techniques (e.g. Hocking et al. 2018; Martin et al. 2020; Cheng et al. 2021b; Tohill et al. 2021; Bottrell et al. 2022). In particular, convolutional neural networks (CNNs) have become very popular due to their particular emphasis on identifying spatially cohesive structures and relatively high accuracy compared to other algorithms (Cheng et al. 2020; Ćiprijanović et al. 2020). CNNs have been used to classify galaxies by morphological type (Cheng et al. 2021a; Huertas-Company et al. 2015) and also to identify galaxy mergers (Bottrell et al. 2019, 2022; Ćiprijanović et al. 2020; Ferreira et al. 2020a, 2022; Bickley et al. 2021) with very high accuracy (up to ∼98% in the case of morphological types and ∼90% for galaxy mergers). Due to both the popularity and success of CNNs, it is the machine learning technique of choice in this work.

Machine learning techniques, such as CNNs, come with their own challenges too. Most inhibiting is the need for very large (on the order of thousands to millions of images) collections of pre-existing galaxy images and their correct classifications in order to adequately train a CNN. Another limitation is the difficulty of interpreting what the machine is learning. “Attention maps” can be used to identify which regions of a galaxy image were more important to the classification (e.g. Ćiprijanović et al. 2020), but the use of the information in important regions by the network is open to interpretation. Lastly, the applicability of a single CNN across datasets is very poor. Since the performance of CNNs drops significantly as general properties of the images change (such as sky noise, pixel scale, and atmospheric blurring), a single neural network cannot be used out-of-the-box on a given dataset the way the non-parametric morphology statistics can (Bottrell et al. 2019). This means that using CNNs to identify mergers in a new dataset requires both the expertise to build and train one, but also a pre-existing training set for which the classifications are known. Despite their challenges, CNNs are an exciting new tool for identifying galaxy mergers with very high accuracy.

1.2.3 Merger Properties That Affect Morphology and Detection

Several properties of the merger, including the total stellar mass of the system, the mass ratio of the two merging galaxies and the gas content of the galaxies, can effect both the degree of transition and morphological disturbance (e.g. Bendo and Barnes 2000; Naab and Burkert 2003; Bournaud et al. 2004, 2005; Bell et al. 2006; Lotz et al. 2010a,b; Nevin et al. 2019; Snyder et al. 2019). The total stellar mass of the system, $M_\star$, has been shown to have an effect on the completeness and purity of recovered mergers (Snyder et al. 2019). In this work, it is measured immediately following coalescence such that the two merging galaxies have become one entity. Even though most of a galaxy’s mass is in the form of dark matter (Moster et al. 2010b), in this work, I focus on the total *stellar* mass of galaxies since it can be directly measured at optical wavelengths.

A primary driving factor of induced impact from a galaxy merger is the mass ratio of the two merging progenitors (Bendo and Barnes 2000; Naab and Burkert 2003;

Bournaud et al. 2004, 2005). Numerical simulations have shown that the relative masses of the two progenitors dictate both the degree of morphological disturbance (e.g. Lotz et al. 2010b; Ji et al. 2014; Nevin et al. 2019) and other factors such as the strength of the ensuing starburst, for example (e.g. Cox et al. 2008; Hani et al. 2020). Observationally, interacting pairs with more lopsided mass ratios experience stronger morphological disturbance (e.g. Casteels et al. 2014a) and star formation enhancements (e.g. Scudder et al. 2012). In this work, I quantify the post-merger mass ratio, μ, as the ratio of the stellar mass of the smaller of the two progenitors, $\mathrm{M}_{\star,\ \mathrm{smaller}}$ to that that of the larger of the two, $\mathrm{M}_{\star,\ \mathrm{larger}}$:

$$\mu = \frac{M_{\star,\ \mathrm{smaller}}}{M_{\star,\ \mathrm{larger}}}. \tag{1.9}$$

Another driving property of galaxy morphology and evolution is the availability of star-forming gas (Bell et al. 2006; Lotz et al. 2010a). Star-forming gas content is measured here using the gas fraction, f_{gas}. The gas fraction is defined as the total mass of gas, $\mathrm{M}_{\mathrm{gas}}$ divided by the total baryonic mass (gas and stellar mass) within the same radius:

$$f_{\mathrm{gas}} = \frac{M_{\mathrm{gas}}}{M_{\mathrm{gas}} + M_{*}}. \tag{1.10}$$

Gas content of the progenitors can have a significant effect on the outcome of the merger (Hopkins et al. 2009a,b). High gas content can induce a stronger burst of star-formation (e.g. Cox et al. 2008) and can be critical to the survival or re-establishment of the disk (Hopkins et al. 2009a; Moster et al. 2010a). From an observational standpoint, higher gas fraction mergers have been shown to exhibit stronger and longer lasting merger features (e.g. Bell et al. 2006; Lotz et al. 2010a).

1.2.4 Observational Challenges Impeding Merger Detection

Aside from the inherent physical properties of the mergers, there are three key observational challenges that limit our ability to detect mergers in photometric imaging. First is the signal to noise, or depth, of the imaging. Since merger features, such as tidal tails or shells, are often diffuse, extended features (Toomre and Toomre 1972; Malin and Carter 1983; Quinn 1984; Johnston et al. 2002; Wang et al. 2012; Amorisco 2015; Vera-Casanova et al. 2022), deep imaging is required to assess their presence (Johnston et al. 2008; Ji et al. 2014; Duc et al. 2015; Martin et al. 2022). Several works have shown that observed morphology is not robust in shallow imaging and as a result, fewer mergers are detected (Lotz et al. 2004; Lisker 2008). The second limitation is the resolution of the imaging, as quantified by the full width at half maximum (FWHM) of the point spread function (PSF). Lower resolution imaging blurs out morphology details important for classification and thus classification accuracy decreases in lower resolution imaging (e.g. Moore et al. 2006; Reichard et al. 2008; Martin et al. 2022). Lastly, morphological disturbance has been shown to be most extreme at or near the time of coalescence and slowly fade over time (Lotz et al. 2008; Lotz et al. 2010a,b; Nevin et al. 2019; McElroy et al. 2022). As a result, fewer mergers are detected at increasing time after coalescence.

As a result of these effects, it has been shown that common merger identification techniques are not identifying mergers in their totality (Kampczyk et al. 2007; Bignone et al. 2017; Abruzzo et al. 2018; Blumenthal et al. 2020; Lambrides et al. 2021; McElroy et al. 2022; Rose et al. 2023). Specifically, Blumenthal et al. (2020) show that visual identification of mergers in SDSS-quality imaging recovers only 45% of interacting galaxies. Other works have shown similar levels of completeness using non-parametric morphology statistics; for example, Rose et al. (2023) find that Gini-M_{20} recovers 48% of mergers and Bignone et al. (2017) find that 45% of major mergers satisfy $A > 0.35$ in SDSS-like imaging.

While several previous works have quantified the individual effects of depth, resolution, and time since coalescence on observed morphology and merger detection, no one has quantified their combined effect. In Chapter 3, I assess the completeness of recovered recent mergers as function of resolution and depth, individually and in tandem, using a large sample of simulated galaxy mergers which are robustly sampled in terms of total stellar mass, mass ratio, and gas fraction. In Chapter 4, I discuss future work that will include an assessment of the completeness of detected mergers as a function of time after coalescence and its interplay with the depth and resolution of the imaging.

1.3 Thesis Outline

The thesis is constructed as follows. Chapter 1 introduced the methods of identifying post-starburst galaxies and the techniques used to identify recent mergers for the purpose of better understanding the role mergers play in causing galaxies to rapidly evolve in the local Universe. Chapter 2 presents an analysis of the incidence of mergers in two samples post-starburst galaxies. Chapter 3 quantifies the efficacy of non-parametric morphology merger identification techniques. Finally, Chapter 4 discusses future directions of the work and provides a summary of the work presented. Throughout, I assume a standard ΛCDM cosmology with $\Omega_{\mathrm{M}} = 0.3$, $\Omega_{\Lambda} = 0.7$, and $\mathrm{H}_0 = h100$ km s^{-1} Mpc^{-1} where $h = 0.7$.

Chapter 2

The Merger Fraction of Post-starburst Galaxies

Post-starburst galaxies are thought to be in the process of rapidly transitioning from star-forming to quiescence. Precisely quantifying the fraction of PSBs that have recently undergone a merger with another galaxy will allow for a better understanding of how galaxies rapidly evolve in the low-redshift universe. The work presented in this chapter seeks to quantify the merger fraction of galaxies more precisely than previous studies by using 1) a large sample of PSBs, 2) high quality imaging, 3) a robust control sample, and 4) a broad suite of morphology metrics and merger identification methods. To address the differences that may incur from different selection methods, I study two samples of PSBs with differing selection criteria in tandem. In this work, I use the Canada France Imaging Survey (CFIS) which offers deep and high-resolution imaging and has a large overlap with the Sloan Digital Sky Survey (SDSS) which offers optical spectra of sufficient quality for PSB selection. It is this novel combination that allows for a detailed morphological study with a large sample of PSBs of which I take advantage to quantify a robust merger fraction of PSBs. A majority of the work presented in this chapter has been peer-reviewed and published in Wilkinson et al. (2022).

2.1 Data

Post-starburst galaxies are selected based on the star-formation histories inferred from their spectral properties, while mergers are identified by their stellar light dis-

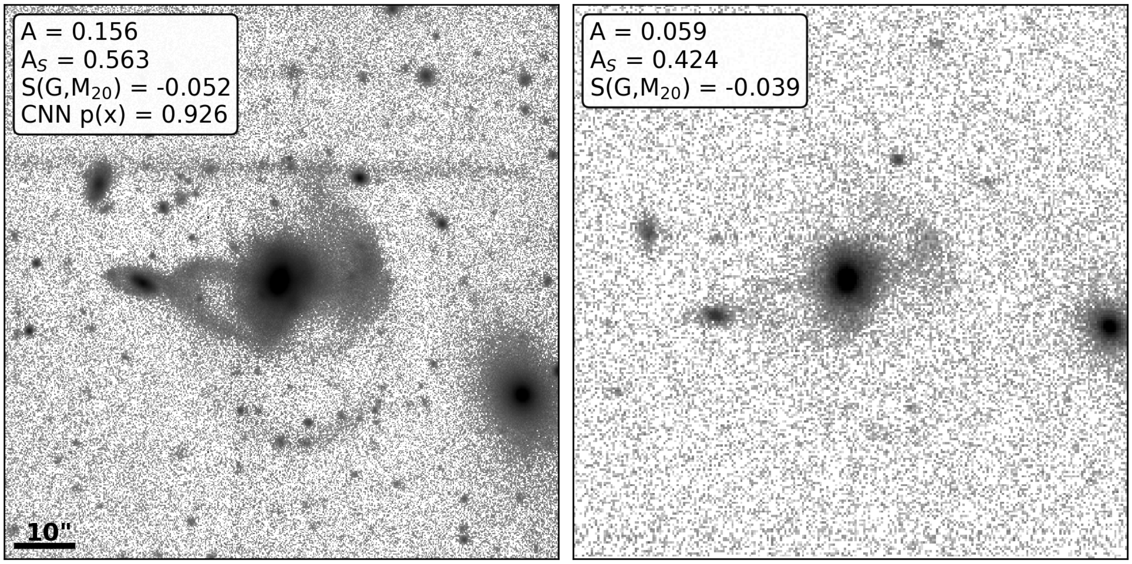

Figure 2.1: An example of a post-starburst galaxy with faint merger features as imaged by CFIS and SDSS. The images are normalized and displayed on equivalent logarithmic scales. Relevant morphology parameters (see Section 2.2) for merger classification are shown in the top left corners of each image. Although the merger features are much more evident in the CFIS image, based on the non-parametric morphology metrics both surveys would reach the same qualitative result: shape asymmetry identifies this as a merger while asymmetry and the Gini-M_{20} merger statistic do not.

tributions. Therefore, to conduct an analysis of the merger fraction of post-starburst galaxies, both spectroscopic and photometric imaging data are required.

2.1.1 SDSS Imaging, Spectroscopy, and Ancillary Data Products

The SDSS is constructed using a dedicated 2.5 m telescope located at the Apache Point Observatory in New Mexico. It is equipped with a mosaic charged-coupled device (CCD) camera to obtain images in five optical bands, and two fibre-fed optical spectrographs to obtain spectra (York et al. 2000). The seventh data release of the SDSS (DR7; Abazajian et al. 2009) includes optical spectra and u-, g-, r-, i-, and z-band images for over 900,000 galaxies[1]. In the work presented here, I make use of SDSS spectra and r-band imaging.

SDSS spectra have a spectral resolution of R $= \lambda/\Delta\lambda \sim$ 800-2200 over the wavelength range 3800-9200 Å and are collected from optical fibres which have an on-sky

---

[1] https://classic.sdss.org/dr7/

aperture of three arcseconds. Thus, the spectra only include light from the central ∼500 pc for lower-redshift ($z \sim 0.025$) galaxies and from the central ∼4 kpc for higher-redshift ($z \sim 0.25$) galaxies in the survey. SDSS r-band imaging has a pixel scale resolution of 0.396 arcsec/pixel, a median seeing of 1.4 arcsec, and a 1-σ sky noise (i.e. depth) of 24.3 mag/arcsec^2.

The SDSS has been widely used to study galaxies in large statistical samples and for many science initiatives. As a result, the value of the survey has grown through the production of ancillary data products. In particular, the Max-Planck-Institute for Astrophysics–John Hopkins University (MPA-JHU) data catalogues[2] provide flux measurements of up to 12 emission lines, photometric stellar mass estimates following the methods of Kauffmann et al. (2003b) and Salim et al. (2007), and star-formation rates (SFRs) based on Brinchmann et al. (2004). Details regarding these data products are as follows:

- *Emission line flux measurements* are taken directly from the public MPA-JHU raw data catalogue[3]. Fluxes in the catalogue are corrected for foreground Galactic reddening following O'Donnell (1994). However, an additional correction to the emmission line fluxes in the catalogue was applied by a previous member of my research group, Dr. Jillian Scudder (see Scudder et al. 2012), accounting for the internal galactic reddening of the target galaxy using the Small Magellanic Cloud (SMC) extinction curve presented in Pei (1992).

- *Stellar mass estimates* are determined by Kauffmann et al. (2003b), who use the best-fit model spectrum from Bruzual and Charlot (2003) to estimate the mass-to-light ratio (among other properties) of each galaxy. The stellar mass is estimated by multiplying the mass-to-light ratio by the total luminosity from the photometric data. Multiplying by the total luminosity from the photometric data accounts for the fact that the aperture of the fibre from which the spectrum of each galaxy is extracted is often smaller than the total extent of the galaxy. However, using this method assumes that the mass-to-light ratio measured within the fibre aperture is constant throughout the galaxy. The estimated masses have a 95% confidence interval of a factor of ∼2.

- *Star formation rates* of star-forming galaxies, measured by Brinchmann et al. (2004), are constrained by many emission lines, with the greatest weight carried

---

[2] https://wwwmpa.mpa-garching.mpg.de/SDSS/DR7/

[3] https://wwwmpa.mpa-garching.mpg.de/SDSS/DR7/raw_data.html

> by Hα. For cases where there is no Hα emission or when there is AGN contamination, SFRs are derived from the 4000 Å break, calibrated using the Hα SFR estimates of star-forming galaxies. SFRs are aperture-corrected according to the colour and magnitude of the galaxy outside of the fibre. For most PSBs, the SFR is measured using the 4000 Å break method since their SFR is minimal by definition. Due to the rapidly changing SFR of PSBs and the relatively long timescale of 4000Å break sensitivity to SFR, the 4000Å break-calibrated SFRs are likely overestimating the instantaneous SFR in PSBs. However, since SFRs are used to primarily select star-forming control galaxies and only to provide context to the PSBs, any overestimation of PSB SFRs has no impact on my analysis.

In total, there are 674,448 galaxies in SDSS DR7 with the ancillary data described above.

2.1.2 CFIS Imaging

The Ultraviolet Near Infrared Optical Northern Survey[4] (UNIONS) is a collaboration of wide field imaging surveys of the northern hemisphere. UNIONS consists of the Canada-France Imaging Survey (CFIS), conducted at the 3.6-metre Canada France Hawaii Telescope (CFHT) on Maunakea, members of the Pan-STARRS team, and the Wide Imaging with Subaru HyperSuprime-Cam of the Euclid Sky (WISHES) team. Together, UNIONS will assemble deep imaging of the Northern sky in the u-, r-, i- and z-bands. In the work presented here, I use the CFIS r-band imaging only.

The second CFIS data release (CFIS DR2), which includes all data collected before February 2020, has r-band images of over 373 million sources spread over $\sim$ 2,700 deg^2 of northern sky. Upon completion, CFIS r-band will cover at total of 4,800 deg^2. In Figure 2.2, I present a figure generated by the CFIS collaboration which showcases the CFIS DR2 coverage (green shading) and the planned final coverage (red outline) with respect to the Galactic plane (blue shading) in equatorial coordinates.

The science-ready CFIS imaging provided by the UNIONS collaboration is a manifestation of 1-3 exposures from the MegaCam instrument on CFHT. The exposures are combined and calibrated following the methods outlined in (Gwyn 2008). The resulting CFIS imaging offers superior depth and resolution relative to that of SDSS. CFIS has a pixel scale resolution of 0.187 arcsec/pixel and in the r-band it has a

---

[4] https://www.skysurvey.cc/

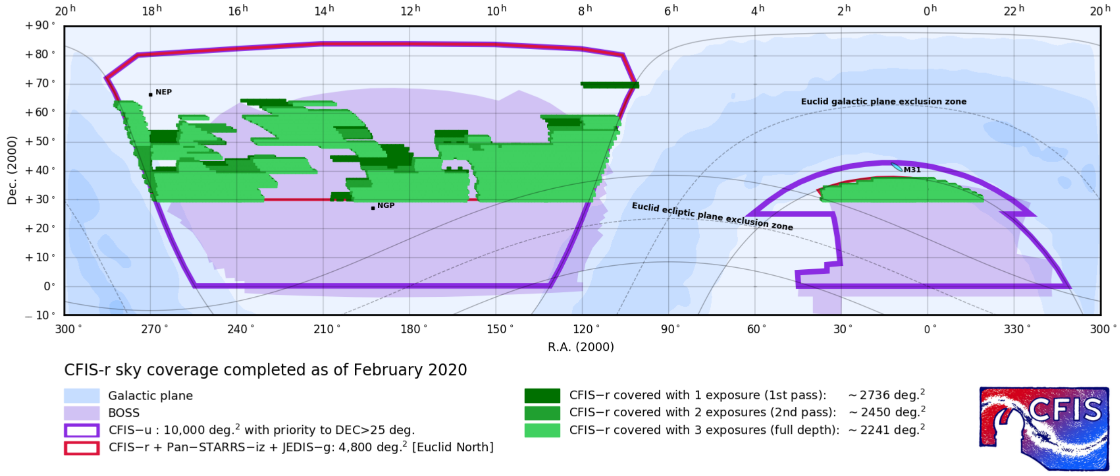

Figure 2.2: CFIS DR2 r-band coverage in equatorial coordinates. Green regions denote the sky area with at least one exposure in CFIS DR2. The red outline is the expected final 4,800 deg^2 coverage of UNIONS. Blue shaded regions indicate sky area in which extinction in visible wavelengths caused by the Galactic plane is significant. Finally, the purple shaded region shows the survey footprint of the Baryon Oscillation Spectroscopic Survey, indicating the level of overlap between CFIS r-band photometry and SDSS spectroscopy. Image credit: UNIONS Collaboration, J.-C. Cuillandre.

median seeing of 0.69 arcsec and a 1-σ sky noise of 25.4 mag/arcsec^2. The superior depth of CFIS images allows for the observation of low surface brightness features that would be undetectable in SDSS imaging. To exemplify the difference CFIS imaging makes, I present both the CFIS (left) and SDSS (right) r-band image of a post-starburst galaxy that happens to have faint merger features in Figure 2.1.

In order to study PSBs with high-quality CFIS imaging, I need spectra with which I can identify PSBs. Fortunately, CFIS DR2 has a large overlap with SDSS DR7 (see purple shading in Figure 2.2) which provides optical spectra with which PSBs can be selected. Thus, galaxies in CFIS DR2 and SDSS DR7 are matched using their on-sky positions with a matching tolerance of three arcseconds (the fibre aperture of SDSS spectroscopy). Of the 674,448 galaxies in SDSS DR7, there are 168,477 galaxies with CFIS DR2 r-band imaging.

2.2 Merger Identification Methods

2.2.1 Non-parametric Morphologies with `statmorph`

Several previous works have produced morphology catalogues for SDSS galaxies (e.g., Simard et al. 2011; Mendel et al. 2014). Here, I extend these past efforts in two ways. First, I determine quantitative morphologies for a broad range of metrics that are developed for the identification of mergers. Second, I determine these metrics in a homogeneous and reproducible way using deep and high resolution CFIS imaging.

To meet these objectives, quantitative morphologies for each galaxy are computed using the Python package `statmorph` (Rodriguez-Gomez et al. 2019). `statmorph` takes the background-subtracted image of the galaxy, binary segmentation map identifying pixels belonging to the target galaxy, a point spread function (PSF), and a weightmap (see Section 2.2.1 for more details) and returns 43 non-parametric morphological statistics and the seven parametric quantities needed to construct a single 2-D Sérsic profile (Sérsic 1963). In this work, I use the four non-parametric morphologies commonly used to identify mergers introduced in Section 1.2.1.

In order to compute quantitative morphologies for a galaxy with `statmorph`, several inputs are required.

- *Image*: Each galaxy's image is a 100"×100" cutout from a CFIS tile. The selected 100"×100" field of view ensures that, for even the largest, low-redshift galaxies, the entire stellar light profile including all potential extraneous low surface brightness features are contained entirely within the image with ample surrounding sky for robust sky statistics to be determined.

- *Binary Segmentation Map*: The segmentation map is generated using `sep` (Barbary 2016), the Python implementation of Source Extractor (Bertin and Arnouts 1996). I tune the input parameters of `sep` such that identified sources must have a minimum of five contiguous pixels with values greater than 1.5× that of the fiducial background noise. Nearby sources, particularly foreground stars and close pairs, are deblended internally by Source Extractor[5]. Sources identified that are not the primary target are included in the mask.

- *Mask*: `statmorph` interprets the mask as pixels the user wishes to be ignored from the morphology calculations. The mask for each galaxy includes the pixels belonging to sources identified by Source Extractor that are not the primary target but still in the field of view, pixels with flux values lower than -50, and pixels with values of exactly 0. The latter two specifically mask out chip gaps and other survey artefacts.

- *Weightmap*: The weightmap provided to `statmorph` is the map of inverse variance generated by the CFIS calibration pipeline for the same region of sky, converted to a standard deviation weightmap.

- *Point Spread Function*: The PSF is approximated as a 2-D Gaussian profile with a full-width at half-maximum (FWHM) specific to the atmospheric seeing experienced by each galaxy and in accordance with its region within the CFIS tile. The PSF is only used by `statmorph` when computing the best-fit Sérsic profile.

Two examples of the input data to `statmorph` are presented in Figure 2.3. From left to right, Figure 2.3 shows the CFIS image, segmentation map, mask, weightmap, and PSF for two galaxies (SDSS object IDs 587725469589307489 and 587725469589307491 in the top and bottom rows, respectively) likely undergoing a pair-phase interaction with a foreground star nearby in the field of view. In addition to showing examples of the data products input to `statmorph`, Figure 2.3 demonstrates how well the Source Extractor code, tuned specifically for the properties of CFIS images, can identify the extent of the science target for which the morphology measurements are desired and

---

[5] Implemented with input parameters `deblend_nthresh` = 32 and `deblend_cont` = 0.05.

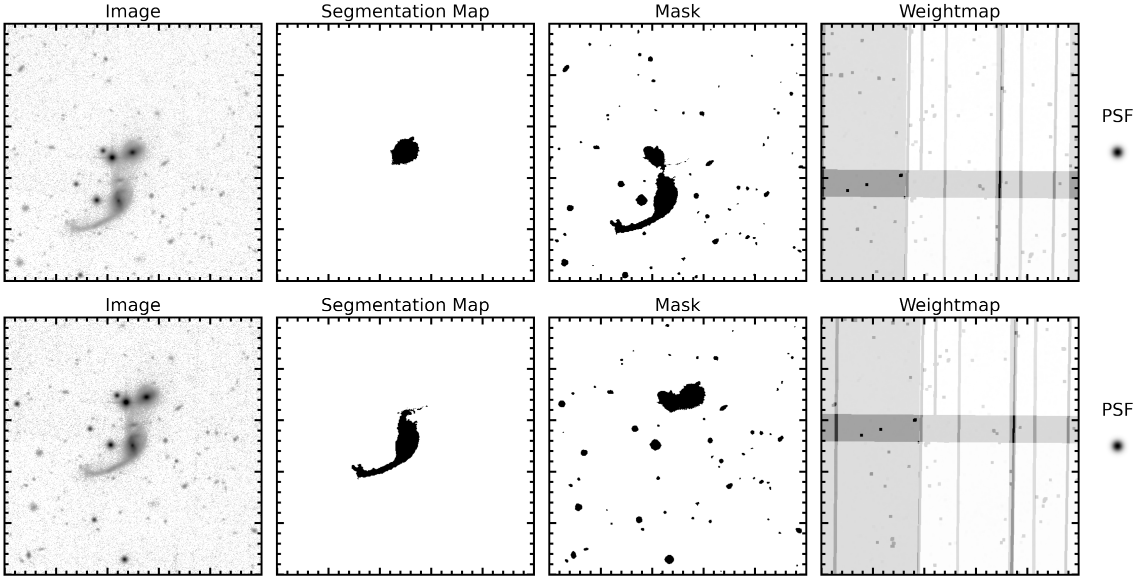

Figure 2.3: A visual summary of the five data products passed to `statmorph` as input. From left to right, the data products are the CFIS image of the target galaxy, Source Extractor segmentation map which informs `statmorph` on the extent of the target galaxy, the mask which informs `statmorph` on the pixels to be excluded from the morphology calculations, the standard deviation weightmap which quantifies the uncertainty in pixel values, and the point spread function. The top and bottom rows are of two example galaxies (SDSS object IDs 587725469589307489 and 587725469589307491) which seem to be undergoing a pair-phase interaction.

mask out nearby galaxies and foreground stars that would otherwise contaminate the morphology results.

A unique galaxy cutout, weightmap, segmentation map and point spread function are generated for each galaxy in the overlap of CFIS DR2 and SDSS DR7 and passed to `statmorph`. 2.8% of galaxies did not have successful `statmorph` fits, often due to incomplete imaging at the edge of CFIS coverage. An additional 8.5% of the remaining galaxies raise a general morphology flag. Since the flag cannot be traced back to determine which morphology calculation caused the problem, I discard all morphology parameters for any galaxy with such a flag. This leaves us with 149,923 galaxies with trustworthy CFIS morphology measurements and complementary SDSS spectroscopic data products. The 149,923 galaxies represent the parent sample from which I will later select my PSBs and controls.

2.2.2 Convolutional Neural Network Post-Merger Classification

In addition to the non-parametric morphologies described in Section 2.2.1, I make use of recent advances in machine learning that have developed artificial neural networks for the purposes identifying galaxy mergers (e.g., Pearson et al. 2019b; Ferreira et al. 2020b, 2022; Bottrell et al. 2022). Accounting for observational effects in the training of the neural network has proved crucial to a network's performance (Bottrell et al. 2019; Ćiprijanović et al. 2021). Hence, I utilize a convolutional neural network (CNN) trained to identify mergers specifically in CFIS from Bickley et al. (2021).

The CNN is capable of detecting mergers in CFIS by learning and synthesizing morphological features indicative of recent mergers from the 100-1 run of the IllustrisTNG cosmological simulation (Springel et al. 2017; Nelson et al. 2018a; Pillepich et al. 2018; Marinacci et al. 2018; Naiman et al. 2018). The CNN learns from post-mergers identified using the merger trees created by `SUBLINK` (Rodriguez-Gomez et al. 2015), following the methodology of Hani et al. (2020). The merging galaxies must have had their subhalos coalesce within the timeframe of one snapshot in the simulation ($t_{\text{post-merger}} \lesssim 162$ Myr; Patton et al. 2020), occurred at a time where $z \leq 1$, and have stellar mass ratios $\mu \geq 0.1$. Furthermore, their merger remnants must have a total stellar mass between 10^{10} $\mathrm{M}_{\odot}$ and 10^{12} $\mathrm{M}_{\odot}$. The post-merger and non-post-merger training samples naturally include a range of early- and late-type morphologies and star-formation histories. Realistic survey effects are integrated into the training of the CNN using the `RealSim-CFIS` code[6], a version of `RealSim`[7] (Bottrell et al. 2019) with specifications unique to CFIS. For further details regarding the CNN's construction, training, and validation, I refer the reader to Bickley et al. (2021).

The CNN is trained to classify galaxies as post-mergers or non-post-mergers using the simulated CFIS-realistic image of the galaxy only; no additional information such as photometry data or star-formation history of the galaxy is provided to the CNN. For each galaxy image, the network returns a floating point prediction, $p(x)$, between 0 and 1, quantifying the certainty in its post-merger prediction. Traditionally, $p(x) > 0.5$ is interpreted as a positive prediction (in this case, a positive post-merger prediction) and $p(x) < 0.5$ is interpreted as a negative result (in this case, a non-post-merger prediction). However, this threshold can be raised to enhance the purity of the post-merger sample (e.g., Bickley et al. 2021). While some previous works have used CNNs to classify galaxies into their morphological types (e.g., Dieleman et al.

---

[6] github.com/cbottrell/RealSimCFIS

[7] github.com/cbottrell/RealSim

2015; Huertas-Company et al. 2015), this CNN is designed to predict whether a given galaxy is a post-merger or non-post-merger only.

When tested on synthetic images of IllustrisTNG galaxies with CFIS realism applied, the CNN achieves a success rate of post-merger identification of ∼89% with no significant dependence of the recovery rate on galaxy properties such as mass ratio (Bickley et al. 2021). Furthermore, approximately half of the false-positive post-mergers are pre-coalescence interacting galaxies that go on to merge within 500 Myr. For the purposes of connecting PSBs to merger and interaction origins, contamination from pre-coalescence merging galaxies is not an issue.

Bickley et al. (2022) have applied the neural network to the 168,477 galaxies in the overlap of CFIS DR2 and SDSS DR7, generating floating point post-merger predictions for each galaxy. The authors of Bickley et al. (2022) further distilled 2000 galaxies with floating point predictions $p \gtrsim 0.75$ into a pure sample of 699 visually-confirmed post-mergers. Using the raw floating point predictions allows us to identify mergers with high completeness, whilst using the visually-confirmed sample of post-mergers allows us to identify mergers with high purity. Hence, both the $p(x)$ values and the visually confirmed sample are used in Section 2.4.2 to compute a merger fraction of PSBs.

2.2.3 Visual Classification

Due to the vast and ever-increasing amount of available astronomical data and the variability of human classification leading to a lack of reproducibility, the field is moving away from visual classification as a core analysis method. Yet, my two PSB samples (consisting of 157 and 533 galaxies, respectively, and the selection of which is described in the following section) are still small enough that visual classification of the entire sample is a reasonable endeavour. The identification of mergers from the sample by-eye can then be compared to the various automated results as well as provide a more consistent comparison to many previous works (e.g., Zabludoff et al. 1996; Blake et al. 2004; Goto 2005; Yang et al. 2008).

For this analysis, I classified each galaxy as either (1) a single galaxy with a disturbed morphology indicative recent merger or interaction, (2) a galaxy with a clear ongoing interaction with a companion galaxy, or (3) possessing no clear merger features. Galaxies classified as non-mergers may include isolated galaxies, galaxies with a companion in the frame but with no obvious interaction features (possibly due to either projection effects or a pre-pericentric companion), as well as galaxies for which the correct classification is unclear. The visual classification of post-starbursts and controls (the selection of which is described in the following section) is done in a randomized order, so as to remove any subconscious bias. When visually classifying the galaxies, I allow myself to freely adjust the scaling and orientation of the r-band image cutout, but no additional information such as mass, colour or redshift is made available to assist in classification.

2.3 The Selection of Post-Starburst Galaxies

2.3.1 PSBs from Traditional Selection Methods

In order to assemble a sample of PSBs using a more traditional selection method, I draw from a pre-existing catalogue[8] of "E+A" PSBs in SDSS DR7 generated by Goto (2007). The catalogue uses the following criteria to classify 816 galaxies as PSBs:

EW(Hδ) > 5.0Å

EW([OII]) > -2.5Å[9]

EW(Hα) > -3.0Å

r-band S/N > 10

For the purposes of my morphology analysis, I further require that the PSBs drawn from this catalogue have mass and redshift measurements from SDSS and CFIS imaging with flag-free `statmorph` morphologies, of which there are 169.

In Section 2.4, I will quantify the fraction of PSBs that are classified as mergers (using the metrics defined in Section 2.2). In order to contextualize the PSB merger fraction, it is necessary to also assess the merger fraction in a non-PSB control sample. If PSBs are triggered by mergers, I expect to see an elevated merger fraction in the PSB sample compared with the control sample.

The control sample should represent the progenitors of the PSB sample. In this way, I can fairly compare the merger fraction of the pre-starburst event to the post-starburst remnant. Therefore, the pool from which I select star-forming controls is

---

[8] Accessed at http://www.phys.nthu.edu.tw/∼tomo/cv/index.html

[9] Convention dictates that emission lines have negative equivalent widths while absorption lines are positive.

defined as being within ±1σ (~0.24 dex) of the SFR-$M_\star$ star-forming main sequence, excluding galaxies with emission lines indicative of AGN or LINERs as governed by the Kauffmann et al. (2003a) parameterization. It is expected that the number of identified mergers in this star-forming control sample will be quite low. Thus, it is imperative that the control sample has ample size for robust conclusions despite the difficulty of counting statistics of rare events. Therefore, each PSB is matched to ten star-forming galaxies of approximately equal stellar mass and redshift. This is done by iterating ten times through the PSB sample, each time selecting the closest match in $\log(M_\star)$-$\log(z)$ space from the pool of controls. If in any of the ten iterations a PSB does not have a matched control within the matching tolerance of 0.2 dex in mass and 0.02 in redshift, that PSB is removed from my final sample and its previously matched controls are returned to the pool. There are 157 PSBs that successfully match ten controls which typically differ by much less than the maximum tolerance; the average absolute difference between the PSBs and their controls is $\Delta M_\star = 0.011$ dex and $\Delta z = 0.003$. The positions of these PSBs and their controls in relation to the star-forming main sequence are shown in Figure 2.4 and the resulting stellar mass and redshift distributions are shown in Figure 2.5. Henceforth, I will refer to the sample selected in this way as E+A PSBs.

2.3.2 PSBs from Principal Component Analysis

PCA is a technique wherein a 1-dimensional spectrum with n data points is represented as a single point in n-dimensional space. A large sample of spectra such as SDSS DR7 becomes a cloud of points in n-dimensional space and orthogonal lines of greatest variance are considered eigenspectra onto which all other SDSS DR7 spectra are projected. The eigenspectra are numbered in order of the amount of variance each contributes to all spectra in SDSS. The projections onto the 1^{st} and 2^{nd} eigenspectra give values for principle components 1 and 2 (PC1 and PC2). The first two principle components carry enough information such that the evolutionary state of a galaxy can be roughly determined from only two components. PC1 captures very similar information as the 4000Å-break strength (D_n4000) and conveys information about the age of the galaxy's stellar population while PC2 is approximately equivalent to a measure of *excess* Balmer absorption given the age of the stellar population and, as such, can be used to differentiate PSBs from the broader population.

To construct a more inclusive sample of PSBs (i.e. allows for some Hα emission

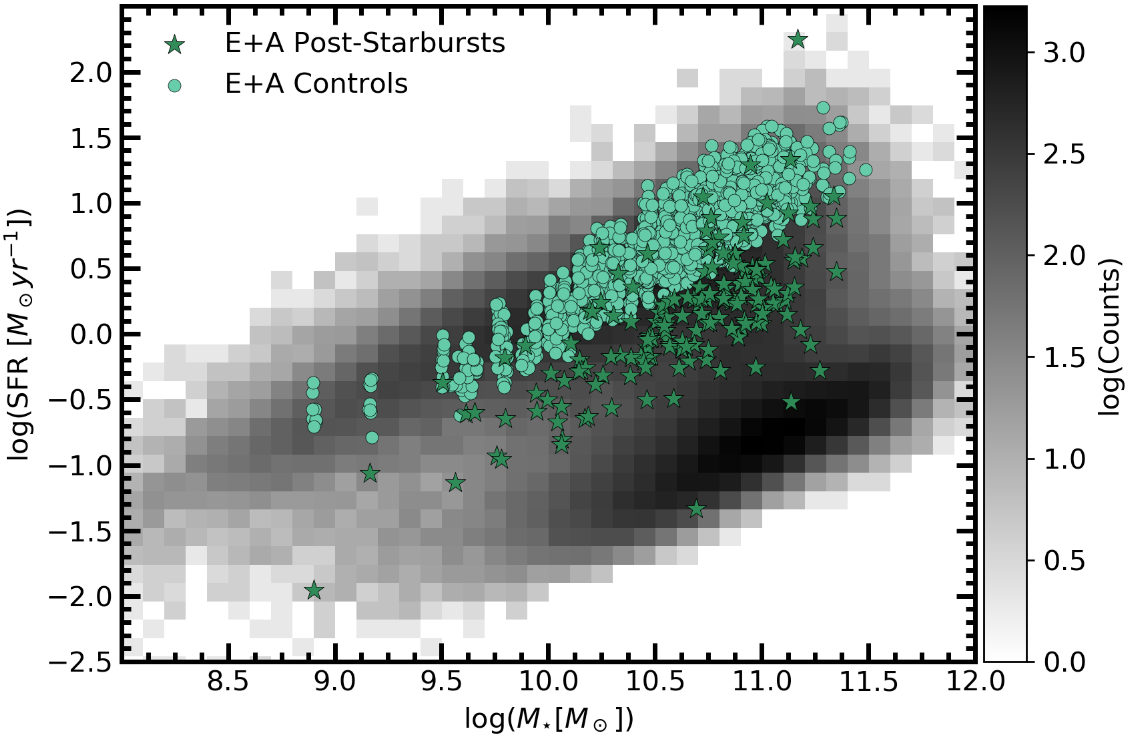

Figure 2.4: The location of the E+A PSBs (green stars) and their star-forming controls (light green circles) in the context of the star forming main sequence. The parent sample of ∼ 150,000 galaxies (with SDSS data products and flag-free CFIS morphologies) is shown as a 2-D histogram where the grey scale represents the number of galaxies in each bin.

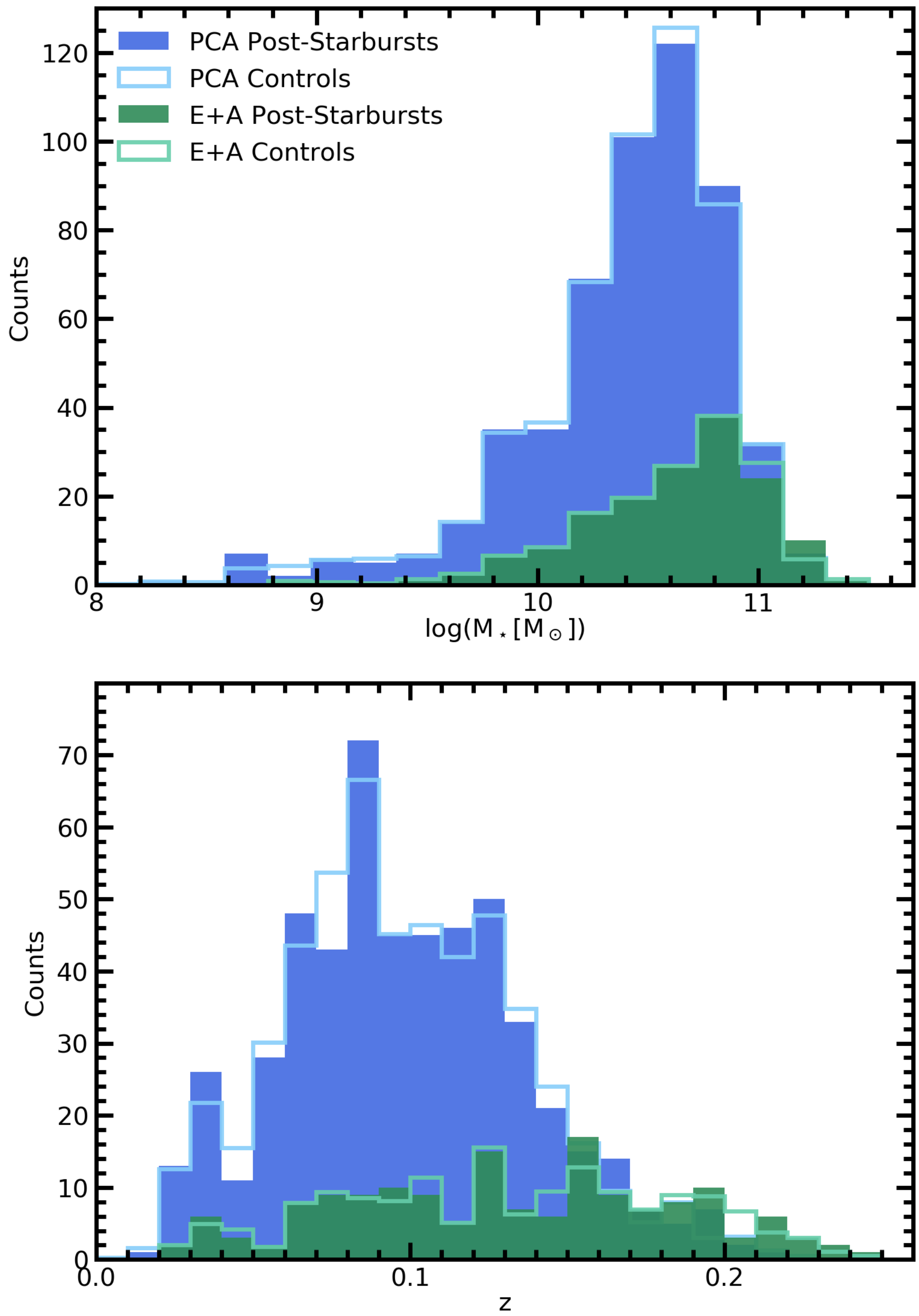

Figure 2.5: The stellar mass (top panel) and redshift (bottom panel) distributions of the PCA PSBs (blue), PCA star-forming controls (light blue lines), E+A PSBs (green), and E+A controls (light green lines). Note that since there are ten controls for each post-starburst, the histograms of the controls are weighted by a factor of 1/10 so they can be compared directly to the post-starburst distributions.

from AGN or shocks) than is afforded by traditional (no emission line) methods, I utilize the PCA catalogue[10] of SDSS DR7 spectra from Wild et al. (2007). In order for the PCA to be reliable, the spectra require a g-band S/N > 8 (Wild et al. 2007; Pawlik et al. 2018). Hence, I only consider galaxies above that threshold. To select PSBs, I employ the same cut as in Pawlik et al. (2018):

$$PC2 - PC2_{\mathrm{err}} > 0.0,$$

where $\mathrm{PC2}_{\mathrm{err}}$ is the error on the PC2 measurement of a given galaxy.

Using only this cut, however, includes a significant amount of quiescent galaxies with high values of PC1 in my PSB sample. While these galaxies may have excess Balmer absorption given the age of their stellar population, the high stellar population age indicates that these galaxies have quenched their star formation long ago. This is not the population that I wish to study and so I make an additional cut:

$$PC1 + PC1_{\mathrm{err}} < -1.5.$$

There is uncertainty in the existing literature about whether post-starbursts with high dust contents are truly post-starbursts or star-bursting galaxies with light from O- and B-type stars being preferentially obscured by dust (Smail et al. 1999; Poggianti and Wu 2000; Miller and Owen 2001; Goto 2004; Wild et al. 2007; Yesuf et al. 2014; Pawlik et al. 2018). Nielsen et al. (2012) has shown that this is not a problem for the selection method used in Goto (2005) but Pawlik et al. (2018) found that, based on SDSS imaging, the morphologies of PCA-selected "dusty PSBs" were consistent with their star-forming controls. Hence, I must recognize that the population of dusty PSBs studied by Pawlik et al. (2018) is too ambiguous to be included in my sample and must be removed.

I quantify the dust content in a galaxy using its Balmer decrement. The Balmer decrement is the ratio between the strength of the redder Hα emission line to the bluer Hβ. Since dust preferentially scatters shorter wavelengths, galaxies with Balmer decrements higher than the natural ratio of 2.86 have more dust (Osterbrock and Ferland 2006). The signal to noise of the Balmer decrement is defined as:

$$S/N = \frac{1}{\sqrt{(1/(S/N)_{H\alpha})^2 + (1/(S/N)_{H\beta})^2}}. \tag{2.1}$$

---

[10] Accessed at http://www-star.st-and.ac.uk/ vw8/downloads/DR7PCA.html

Following Pawlik et al. (2018), I require PSBs with nebular emission (which I define as having Balmer S/N > 3) to meet the following criteria:

$H\alpha/H\beta < 6.6$ if $\mathrm{M}_\star > 3 \times 10^{10} M_\odot$, or

$H\alpha/H\beta < 5.2$ if $\mathrm{M}_\star < 3 \times 10^{10} M_\odot$.

As for the E+A PSBs, I must compile a control sample of star-forming non-PSBs for the PCA sample. Since the PCA PSBs are defined in PC1-PC2 space, I also draw controls from the PC1-PC2 plane. Following the method employed by Pawlik et al. (2018) but with different bounds[11], the pool from which the PCA controls are drawn is restricted to the following regime of the PC1-PC2 plane:

$PC1 - PC1_{\mathrm{err}} > -5.0$

$PC1 + PC1_{\mathrm{err}} < -2.0$

$PC2 - PC2_{\mathrm{err}} > -1.0$

$PC2 + PC2_{\mathrm{err}} < 0.0.$

Each PCA-selected PSB is matched in stellar mass and redshift to ten star-forming controls using the same method outlined in the previous subsection. 533 PCA PSBs are successfully matched to ten controls. The average absolute difference between the PSBs and their controls is $\Delta M_\star = 0.017$ dex and $\Delta z = 0.003$. The redshift and stellar mass distributions of the matched samples are shown in Figure 2.5 and their locations in the PC1-PC2 plane are shown in Figure 2.6. Henceforth, I will refer to the sample of PSBs selected in this way as PCA PSBs.

2.4 Results: Quantifying the Merger Prevalence in Post-Starburst Galaxies

The primary objective of the work presented here is to assess the fraction of mergers in the PSB samples and to quantify whether this fraction is in excess of expectations given the matched control samples. The merger fraction of each sample is assessed

---

[11] The bounds in Pawlik et al. (2018) and described here a designed to sample galaxies from the region dominated by star-forming galaxies defined in Wild et al. (2007).

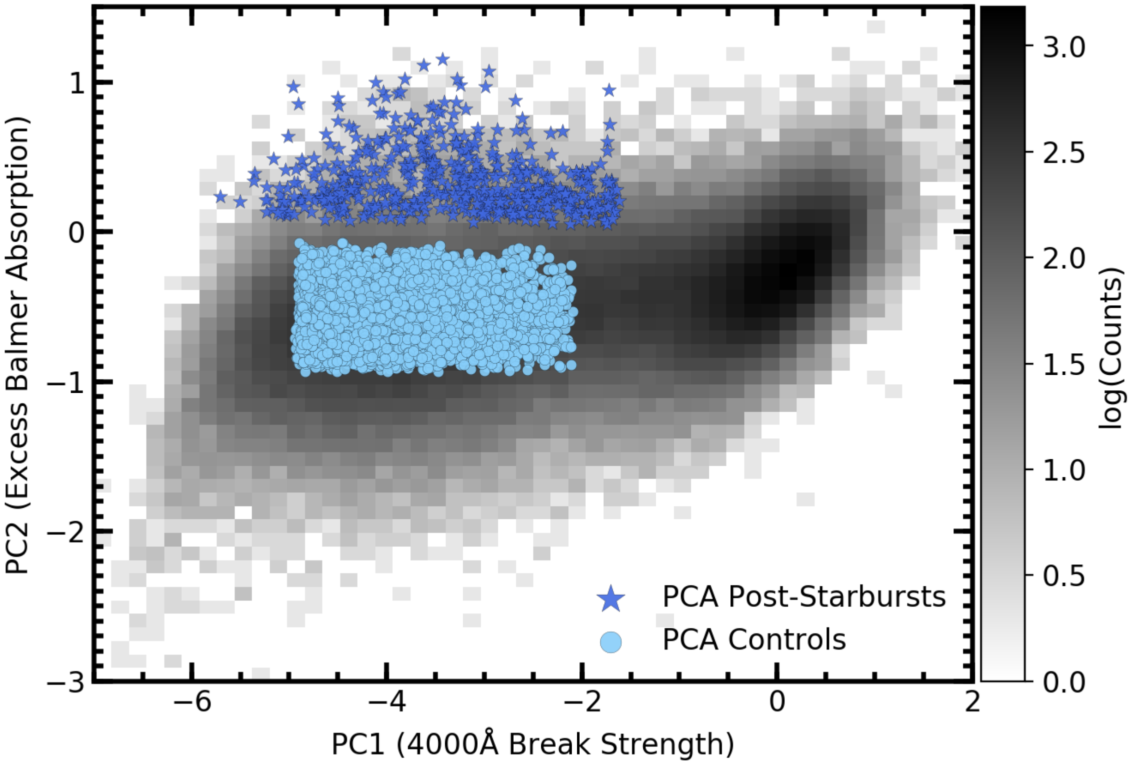

Figure 2.6: The location of the PCA PSBs (blue stars) and their star-forming controls (light blue circles) in the PC1-PC2 plane. The parent sample from which they are selected is shown as a 2-D histogram where the grey scale represents the number of galaxies in each bin. To the right of the figure, at high values of PC1, galaxies are typically quiescent ellipticals and in the bottom left corner, galaxies are typically recent starbursts (Wild et al. 2007).

with three approaches: quantitative morphologies computed with `statmorph` (Section 2.4.1), CNN post-merger predictions (Section 2.4.2), and visual classification (Section 2.4.3).

To quantitatively compare PSBs to their controls, I use the merger fraction, f, and excess disturbance frequency, Q. For a given continuous morphology metric, X, that I wish to use as a merger indicator, a threshold, T, must be set beyond which galaxies are considered to be a merger. Hence, the merger fraction, f, is defined as:

$$f_X = \frac{N(X > T)}{N}. \tag{2.2}$$

Merger fractions calculated this way are likely to be an incomplete assessment of the merger fraction and additionally may have some contamination from non-mergers (see Bickley et al. 2021). Thus, a more robust metric to measure the causal importance of mergers to PSBs is the excess merger fraction relative to the star-forming controls, Q, defined as the ratio between the merger fraction of the PSBs and the merger fraction of the star-forming control sample:

$$Q_X = \frac{f_{X,\text{ PSBs}}}{f_{X,\text{ Controls}}}. \tag{2.3}$$

The errors on the merger fractions, Δf, are calculated using the binomial error in the median:

$$\Delta f = \sqrt{\frac{f(1-f)}{N}}, \tag{2.4}$$

and are propagated through the division in Equation 2.3 to estimate the error on the excess mergers in the PSB samples.

2.4.1 Quantitative Morphologies

In Figure 2.7, I present a summary of the `statmorph`-derived morphologies of the PSB and control samples for metrics commonly used to identify mergers. In each panel, the distribution of the PCA PSBs and the E+A PSBs are shown with blue and green filled histograms, respectively. The distribution of their controls are shown as unfilled histograms of the corresponding lighter colours. Since the controls outnumber the PSBs by a factor of ten, the counts of the controls are weighted by a factor of 1/10. Presenting the data in this way preserves the relative size of the PCA and E+A PSB samples while also allowing for direct comparison between the distributions of

Sample	A	A_S	G	M_{20}	S(G, M_{20})	CNN p
PCA PSBs	$0.06^{+0.08}_{-0.03}$	$0.25^{+0.18}_{-0.09}$	$0.56^{+0.04}_{-0.04}$	$-1.94^{+0.20}_{-0.18}$	$-0.05^{+0.03}_{-0.02}$	$0.05^{+0.43}_{-0.05}$
PCA Controls	$0.11^{+0.08}_{-0.06}$	$0.22^{+0.11}_{-0.06}$	$0.50^{+0.05}_{-0.05}$	$-1.82^{+0.17}_{-0.18}$	$-0.08^{+0.04}_{-0.04}$	$0.01^{+0.09}_{-0.01}$
E+A PSBs	$0.05^{+0.06}_{-0.02}$	$0.27^{+0.26}_{-0.09}$	$0.57^{+0.03}_{-0.03}$	$-1.94^{+0.13}_{-0.18}$	$-0.04^{+0.02}_{-0.02}$	$0.14^{+0.64}_{-0.13}$
E+A Controls	$0.13^{+0.09}_{-0.06}$	$0.23^{+0.12}_{-0.07}$	$0.50^{+0.05}_{-0.05}$	$-1.80^{+0.20}_{-0.18}$	$-0.08^{+0.04}_{-0.04}$	$0.00^{+0.09}_{-0.00}$

Table 2.1: The median value of several morphology parameters for each of the samples derived from CFIS imaging. The lower and upper errors on each median are calculated using the 16th and 84th percentiles, respectively.

the PSB samples and their controls. Vertical dashed lines indicate the medians of the distributions for which exact values can be found in Table 2.1. A more detailed description of each panel is described in the subsections that follow.

Gini-M_{20} Merger Statistic

In the lower left panel of Figure 2.7, I show histogram distributions of the Gini-M_{20} merger statistic for the PSB samples (solid histograms) and their respective controls (open histograms). Looking first at the results from the PCA-selected samples, I find that the PCA PSBs have elevated values of the Gini-M_{20} merger statistic relative to their star-forming controls. However, at the merger threshold of S(G, M_{20}) > 0, the merger fraction of the PCA PSBs is only $f_{\text{G-M}_{20}} = (7.5 \pm 1.1)\%$, at least a factor of 2 lower than expected based on previous studies (see Figure 1.8 for references). Nonetheless, the PCA PSBs have a higher merger fraction than that of their controls which have a merger fraction of $f_{\text{G-M}_{20}} = (4.2 \pm 0.3)\%$. This translates to an excess over the controls of $Q_{\text{G-M}_{20}} = 1.8 \pm 0.3$ for PCA PSBs.

The result is much the same for the E+A PSBs for which the default Gini-M_{20} threshold gives $f_{\text{G-M}_{20}} = (7.0 \pm 2.0)\%$ with an excess over the controls of $Q_{\text{G-M}_{20}} = 1.4 \pm 0.4$. The excess of mergers in the E+A PSBs over their controls is consistent with one, in part due to the statistical uncertainty that comes with a smaller sample size. Therefore, at the default threshold, the Gini-M_{20} merger statistic does not seem to identify a statistically significant surplus of mergers in the E+A sample of PSBs.

In theory, it is possible to explore the potential merger excess in the PSB sample using a more strict Gini-M_{20} cut (i.e. larger values of S(G, M_{20})). Indeed, with the other statistics (A, A_O, A_S, and the CNN prediction) I will perform such a test.

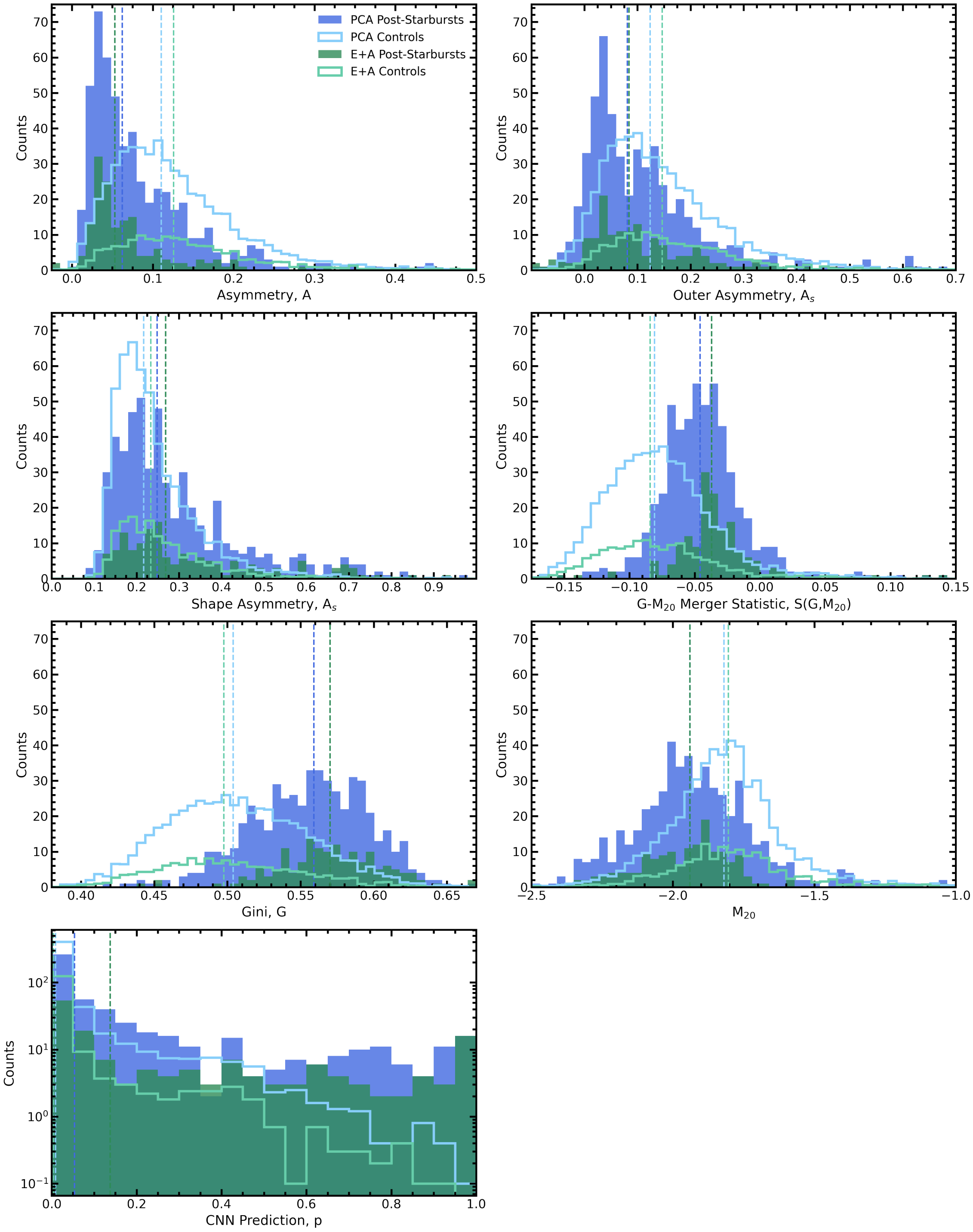

Figure 2.7: The distributions of four morphology parameters relevant to identifying mergers for the PCA PSBs (blue), PCA-controls (light blue), traditionally selected PSBs (green) and their controls (light green). In each figure, the medians of each population are plotted as vertical dashed lines and the values of those medians can be found in Table 2.1. Note that since there are ten controls for each post-starburst, the histograms of the controls are weighted by a factor of 1/10 so they can be compared directly to the post-starburst distributions.

However, the number of galaxies in any of the PSB or control samples with S(G, M_{20}) > 0 is quite small and so no statistically robust conclusions can be drawn. Furthermore, galaxies contaminated by a foreground star near its nucleus have highly concentrated and spatially separated light distributions that artificially enhance S(G, M_{20}), sometimes causing false-positive merger identifications. These cases are difficult to deblend or flag as doing so would also remove double-nuclei pre-coalescence merging galaxies and galaxies with clumpy star formation from my morphology catalogue. Foreground star contamination affects each population equally which is, in part, driving the excess to unity.

From hydrodynamical simulations of individual galaxy mergers, Lotz et al. (2008) find the Gini-M_{20} merger indicator fades more rapidly than other morphology metrics. Thus, S(G, M_{20}) seems to identify ongoing mergers and interactions more effectively than late-stage post-mergers (this is discussed further in Section 2.5.3). For PSBs, which are expected to be several 100 Myr removed from the starburst event, S(G, M_{20}) does not seem to be a particularly salient merger indicator.

Asymmetry

Significant fractions of galaxies with moderate asymmetries in the control samples is to be expected; both late-type disks (A = 0.15 ± 0.06; Conselice 2003) and edge-on disks (A = 0.17 ± 0.11; Conselice 2003) will contribute a number of moderately high asymmetry measurements due to clumpy star formation and the edge-on view of dust lanes in disks. However, the asymmetry distributions presented in the top left panel of Figure 2.7 show that both samples of PSBs tend to have lower asymmetry measurements than their star-forming controls. So, relative to their star-forming controls, PSBs actually have *suppressed* asymmetries, and even more dramatically so in the case of E+A PSBs.

Adopting a threshold of $A > 0.35$ to discriminate mergers from the sample gives a merger fraction of $f_A = (1.9 \pm 0.6)\%$ for the PCA PSBs, translating to an excess over their controls of $Q_A = 0.9 \pm 0.3$. Thus, the number of identified mergers in the PCA PSBs is consistent with no change from their star-forming controls. The merger fraction of the E+A PSBs is even lower at $f_A = (1.3 \pm 0.9)\%$. In fact, there are fewer mergers in the E+A PSB sample than in their star-forming controls with a excess below one of $Q_A = 0.4 \pm 0.3$.

In Figure 2.8, I explore how my results are affected by the asymmetry threshold used to define a merger. In the top panel I present the merger fraction of the PCA and E+A PSBs as a function of the asymmetry threshold used to define a merger with solid blue and green curves, respectively. For comparison, I show on the same panel the merger fraction of the PCA controls (light blue) and E+A controls (light green). Shaded areas around the curves represent the binomial error of the merger fraction (see Equation 2.4) which are propagated into the lower panel. In the lower panel, I show the excess of mergers in the PSBs over their controls for the PCA PSBs (dark blue) and E+A PSBs (dark green). In this case, I find that there is an excess number of galaxies with very high asymmetries ($A \gtrsim 0.5$) in both PSB samples but equal or fewer mergers in the PSB samples than their star-forming controls ($Q_A \lesssim 1$) for all other considered merger thresholds.

The suppressed asymmetries of the PSB samples cause the merger fractions determined using asymmetry to be significantly lower than previous studies would suggest (see Figure 1.8 for references) and lower than those identified using the Gini-M_{20} merger statistic in Section 2.4.1. However, there is an additional nuance not previously considered: PSBs selected on the basis of SDSS centrally-located optical fibres would, by definition, have had a recent burst in star formation in the central region of the galaxy. It is likely that the central burst in star formation would produce a very bright, azimuthally symmetric light profile at the centre of the galaxy which would increase the denominator of Equation 1.1 with negligible change to the numerator, systematically driving down the asymmetry calculation of each post-starburst galaxy (see Appendix A.1 for a more detailed discussion).

If PSBs are expected to have bright, concentrated, azimuthally symmetric cores, ordinary asymmetry may not be the best metric to derive a merger fraction of PSBs as these bright, symmetric centres are weighted much more heavily than any faint, asymmetric tidal features. Perhaps other statistics such as outer asymmetry and shape asymmetry, which distribute more statistical weight to faint tidal features, will be more applicable to identifying mergers in the PSB populations.

Outer Asymmetry

Since outer asymmetry does not a have a widely adopted threshold above which galaxies are to be considered mergers, I adopt the same default threshold as asymmetry. Therefore, using outer asymmetry, mergers are defined as those with $A_O > 0.35$. Outer asymmetry excludes the central region from the asymmetry calculation and

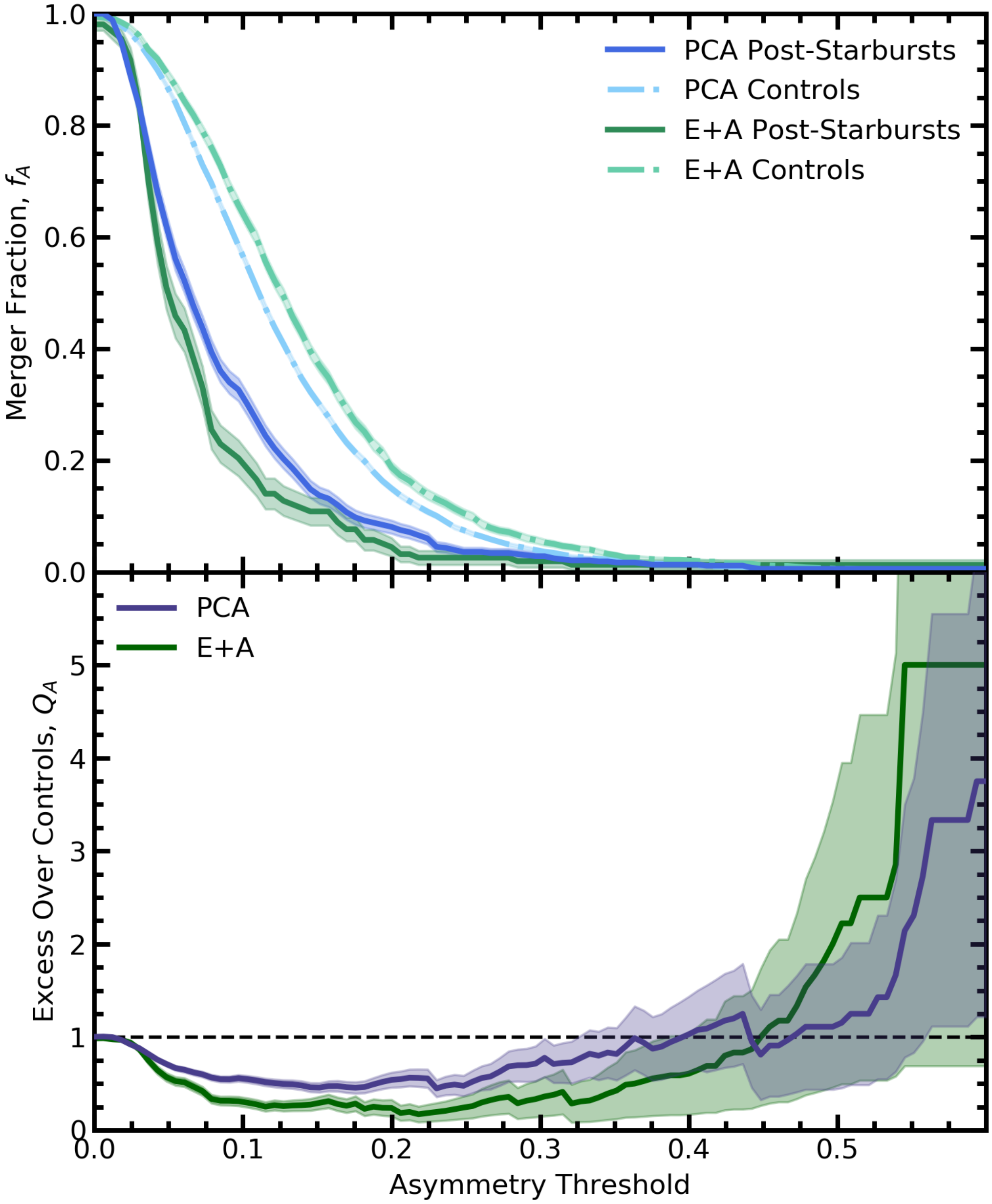

Figure 2.8: *Top*: The merger fraction of PCA PSBs (blue line) and E+A PSBs (green line) compared to their star-forming controls (dotted lines) as a function of the threshold above which a galaxy would be considered a merger. For example, using a threshold of $A > 0.1$ to identify mergers results in ∼20% of E+A PSBs being classified as mergers. Since all galaxies typically have a positive asymmetry, 100% of galaxies in all samples would be classified as mergers if a $A > 0$ threshold were imposed. *Bottom*: The excess fraction of mergers in each sample relative to their star-forming controls as a function of the asymmetry threshold used to identify mergers based on the asymmetry of their light profiles. The black dashed line represents the line of equality between the merger fraction of the PSBs and their controls.

therefore provides more statistical weight to the faint exterior regions of the galaxy.

Using $A_O > 0.35$ to identify mergers, the merger fraction of the PCA PSBs is found to be $f_{A_O} = (4.6 \pm 0.9)\%$ with an excess over the star-forming control sample of $Q_{A_O} = 0.8 \pm 0.2$. Similarly, for the E+A PSBs, the merger fraction is $f_{A_O} = (4 \pm 2)\%$, giving an excess over the controls of $Q_{A_O} = 0.6 \pm 0.2$. It is worth noting that both the merger fractions and excess over the controls of the PCA and E+A PSB samples measured with outer asymmetry are equal within error to those measured with regular asymmetry.

To explore the effect of the outer asymmetry threshold used to classify a galaxy as a merger, I calculate f_{A_O} and Q_{A_O} for a range of possible thresholds, which are presented in Figure 2.9. The green and blue curves in the top panel of Figure 2.9 show that, regardless of the outer asymmetry threshold adopted, the merger fraction of the PSB samples is less than or equal to (within error) the merger fraction of the star-forming control sample. This result is echoed by the dark blue and green curves in the bottom panel of Figure 2.9 which show the excess with respect to the controls is always less than or consistent with unity. As with the merger fractions and excesses at the default threshold, the relationship between merger threshold and merger fraction and excess is roughly equivalent to that of regular asymmetry.

While, in theory, outer asymmetry seems more applicable to identifying merger features in PSBs than regular asymmetry, in practice, the two metrics produce equivalent results. Therefore, for the remainder of the analysis presented in this chapter, I will only include asymmetry for brevity. The utility of asymmetry and outer asymmetry will be revisited in Chapter 3.

Shape Asymmetry

Pawlik et al. (2016) suggest a threshold of $A_S > 0.2$ is appropriate for the identification of mergers from SDSS imaging. However, as noted in Section 1.2.1, a factor of 2 difference in the definition of A_S translates this to a threshold of 0.4 for the `statmorph` measurements. From a visual inspection of the CFIS images, I also confirm that this is an appropriate threshold for my sample. Adopting a threshold of $A_S > 0.4$, I find that the merger fraction for the PCA PSBs is $f_{A_S} = (19 \pm 2)\%$ with an excess over their controls of $Q_{A_S} = 2.6 \pm 0.3$. At the same threshold, the merger fraction of the E+A PSBs is $f_{A_S} = (26 \pm 3)\%$ which is significantly higher than that of the PCA PSBs, yet the excess over their controls is the same within statistical uncertainty at

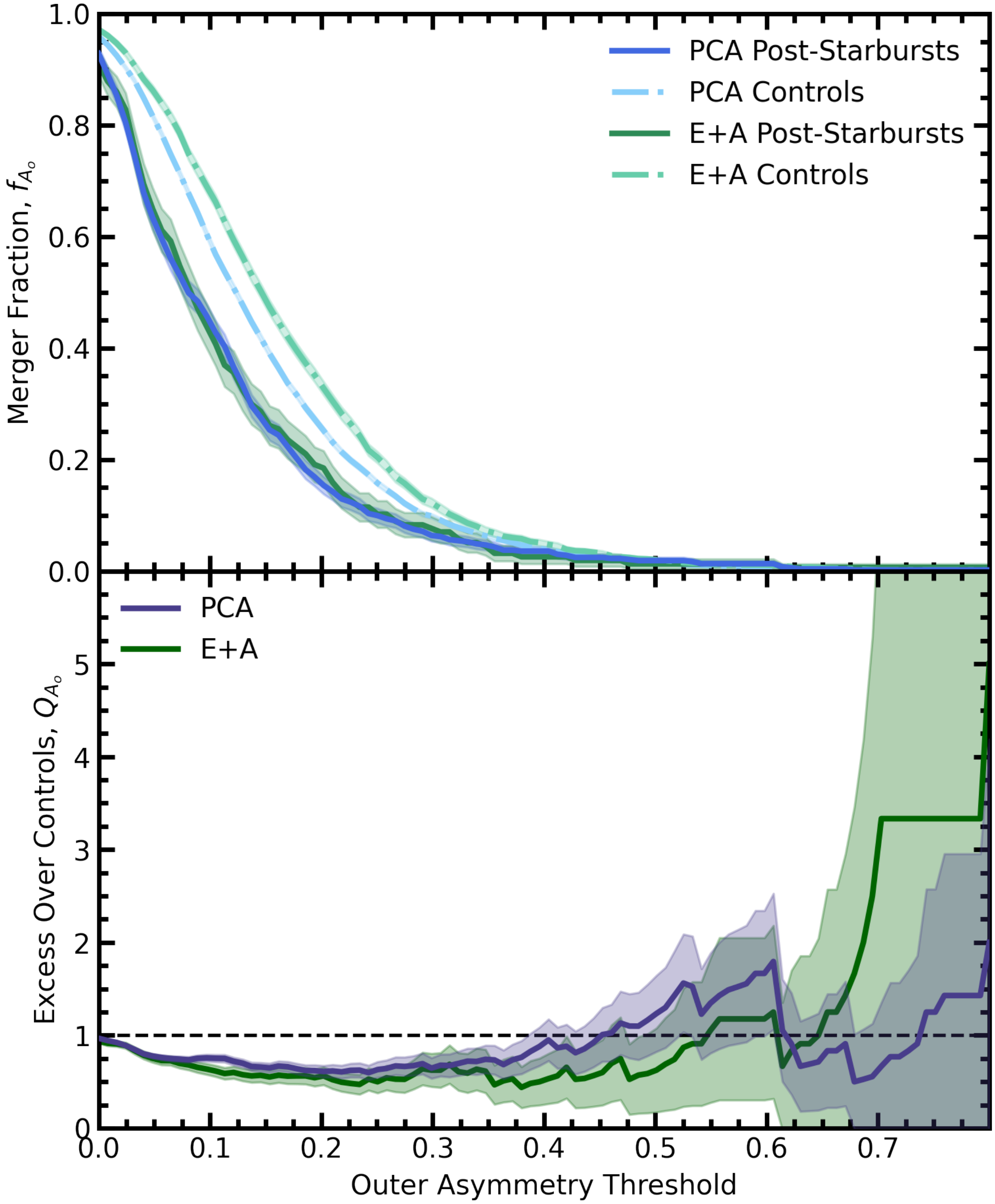

Figure 2.9: Same as Figure 2.8 but considering outer asymmetry.

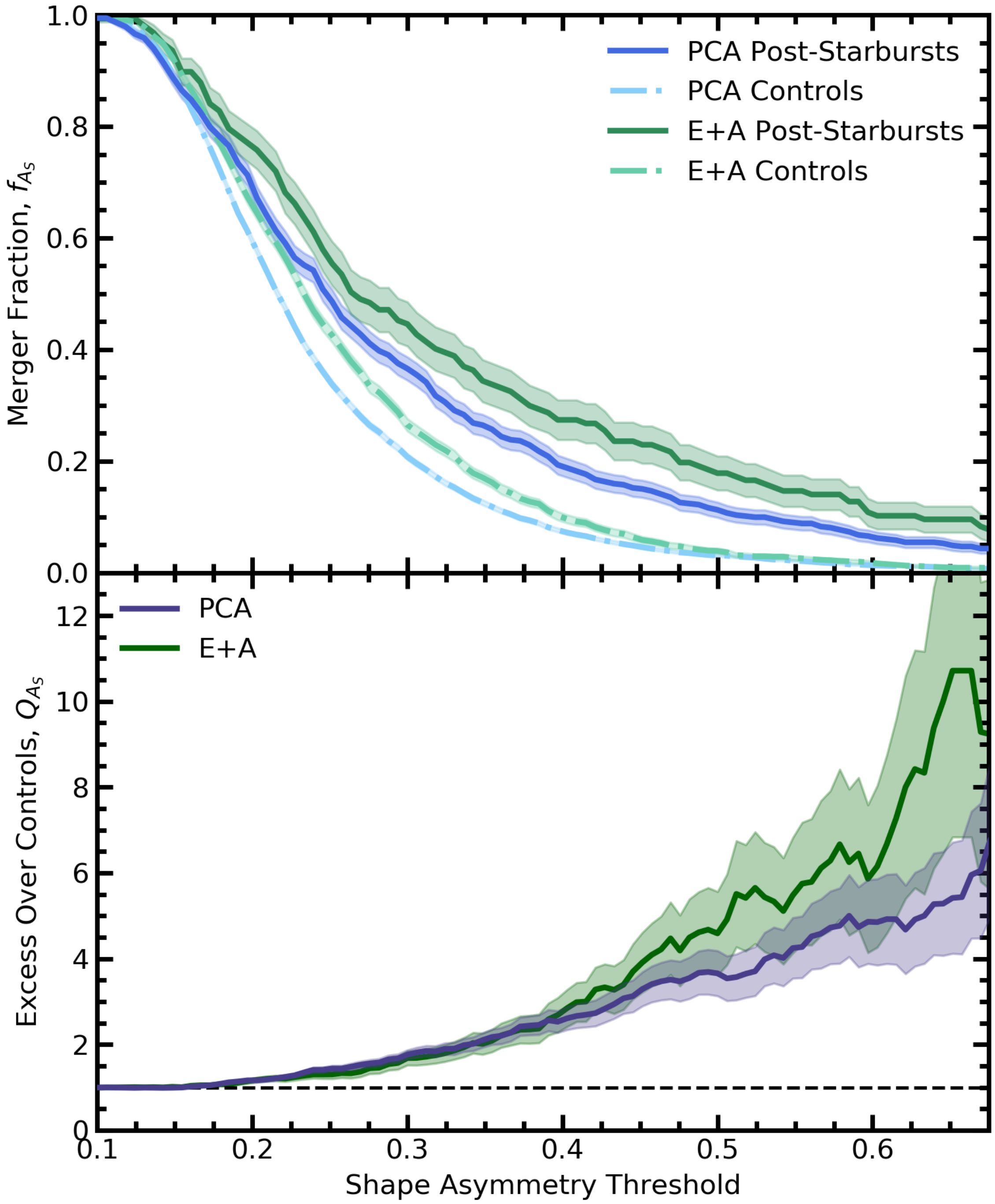

Figure 2.10: Same as Figure 2.8 but considering shape asymmetry.

$Q_{A_S} = 2.8 \pm 0.4$.

As was done previously for asymmetry and outer asymmetry to explore the effect of the threshold used to classify a galaxy as a merger, I calculate f_{A_S} and Q_{A_S} for a range of possible thresholds. The green and blue curves in the top panel of Figure 2.10 show that, regardless of my selected threshold, both samples of PSBs exhibit higher fractions of asymmetric low surface brightness tidal features than their controls (light blue and green dotted lines). Furthermore, the excess disturbance frequency is greater than one for both samples at all considered thresholds and the values of Q_{A_S} for both samples steadily increase as the threshold is increased. This indicates that the fraction of very highly disturbed PSBs ($A_S > 0.6$) is in excess over the controls by a factor of $Q \sim 5$. Due to the sensitivity of shape asymmetry to faint tidal features expected for PSBs and the agreement of the shape asymmetry merger fraction with previous studies, shape asymmetry seems to be a more reliable automated merger detection method than using Gini-M_{20} or asymmetry (see Section 2.5.3 for a more detailed discussion).

2.4.2 CNN Post-Merger Prediction

In the bottom right panel of Figure 2.7, I show the distributions of the floating point post-merger predictions assigned to each sample by the CNN. Typically in machine learning binary classification problems, the default threshold above which the output is considered a positive prediction is $p > 0.5$. The CNN finds that a majority of PSBs are assigned a floating point prediction less than 0.5 and therefore are not recent post-mergers. The distributions are so strongly clustered around the non-post-merger prediction (0) that I choose to display the distributions in log-scale so that differences between the samples at higher values of p can be seen.

At the default threshold of $p > 0.5$, the PCA PSBs have a merger fraction of $f_{\mathrm{CNN}} = (16 \pm 2)\%$ and an excess over their controls of $Q_{\mathrm{CNN}} = 8 \pm 1$. In contrast, at the default threshold of $p > 0.5$, the E+A PSBs have a merger fraction of $f_{\mathrm{CNN}} = (30 \pm 4)\%$, in excess over their controls by a factor of $Q_{\mathrm{CNN}} = 16 \pm 4$. These fractions indicate that post-merger galaxies are approximately twice as abundant in the E+A PSBs than in the PCA PSBs.

Although a $p > 0.5$ is a standard decision threshold in machine learning and despite the high performance of the CNN, Bickley et al. (2021) discuss how the application of this cut for a general dataset of galaxies is expected to lead to a merger sample that is only 6% pure (see also Bottrell et al. 2022). The degree of impurity is likely to be less extreme for my sample which are expected to have an excess of mergers. I improve my assessment of the CNN merger fraction in two ways. First, in Figure 2.11 I explore how the value of f_{CNN} would differ over a range of potential merger thresholds wherein higher values of p indicate higher confidence in the post-merger prediction from the CNN leading to a more pure sample of post-mergers. Second, by counting only visually confirmed post-mergers with $p > 0.75$ as identified post-mergers I distill a pure sample of post-mergers albeit one that is incomplete.

The top panel of Figure 2.11 shows that regardless of the CNN prediction threshold used, the merger fraction of PSBs galaxies is significantly higher than that of their star-forming controls and even higher for the E+A PSBs. The merger fraction in both samples decreases gradually as the threshold increases. This signifies a gradual exchange of completeness for purity when progressively higher decision thresholds are used. Thus, using any choice of threshold above which galaxies will be considered mergers will be somewhat arbitrary.

Using thresholds higher than $p > 0.5$ to classify galaxies as mergers increases the excess over the controls significantly. At very high thresholds ($p \gtrsim 0.85$) where the CNN has given galaxies a very high probability of being a post-merger, very few control galaxies are classified as post-mergers with this high confidence and as a result the excess of post-merger galaxies in both samples of PSBs is on the order of $Q \sim 100$ (± 70).

The shaded area of Figure 2.11 indicates the number of visually confirmed mergers from Bickley et al. (2022). This represents my purest sample of mergers, but is still a lower limit of the total post-mergers in the populations for two reasons. First, only galaxies assigned a post-merger probability of $p > 0.75$ were visually inspected and there may be some true post-merger galaxies that did not meet that threshold from the CNN. Second, the quality of imaging, orientation of the galaxy, and timescale of the merger features relative to that of post-starburst features may also cause galaxy mergers to be missed (this is discussed in more detail in Section 2.5 and Chapter 3). However, the latter would affect the classification of mergers in both the PSB and control samples proportionally. Thus, while the merger fractions may be lower limits, the excess over the controls is more robust. With this in mind, the visually-confirmed CNN-predicted merger fraction of PCA PSBs is $f_{\mathrm{CNN,\ VC}} = (7 \pm 1)\%$ with an excess over their controls of $Q_{\mathrm{CNN,\ VC}} = 29 \pm 9$. Comparatively, the merger fraction of the E+A PSBs is $f_{\mathrm{CNN,\ VC}} = (15 \pm 3)\%$ with an excess over their controls of

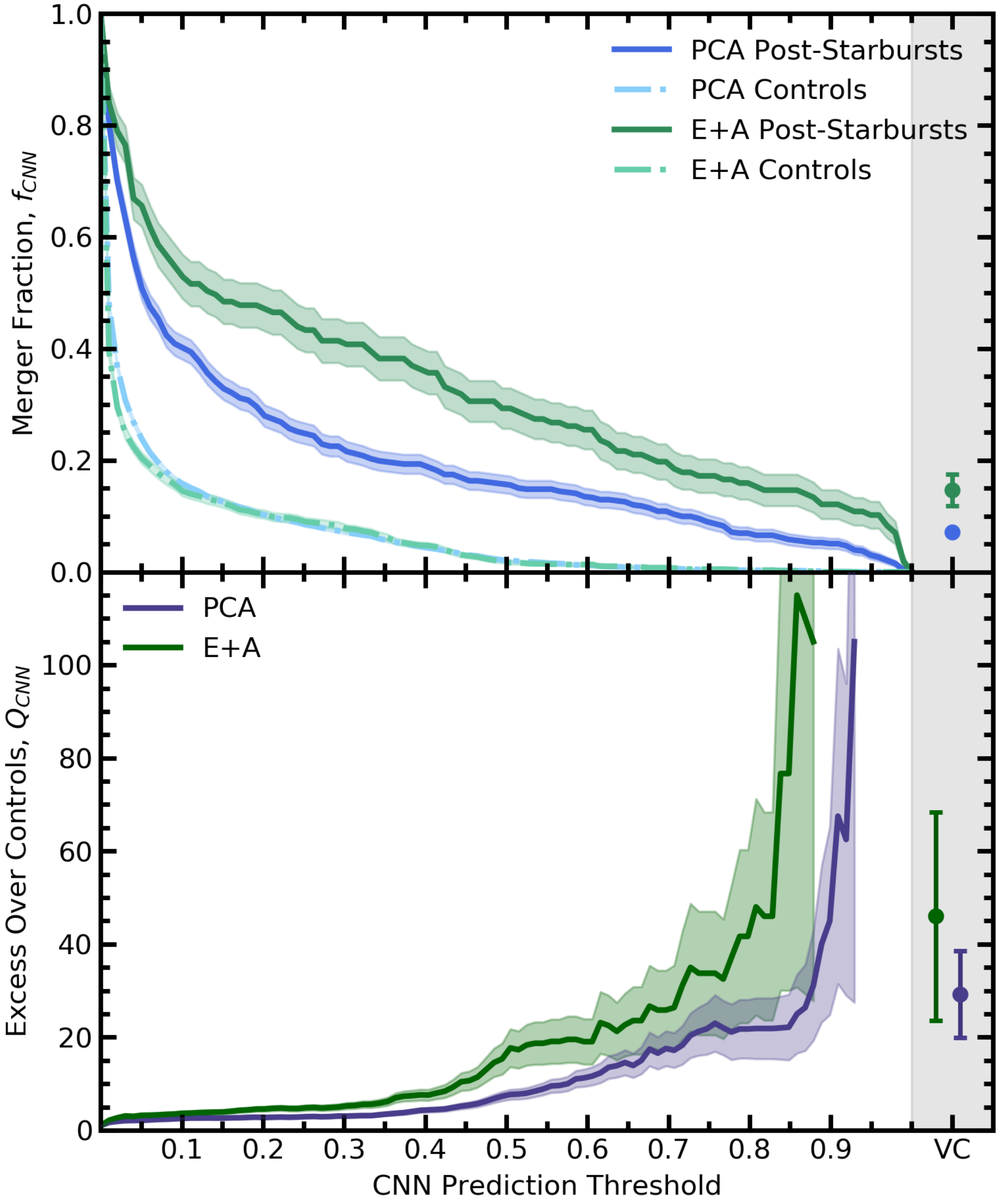

Figure 2.11: Same as Figure 2.8 but considering the CNN post-merger predictions. Predictions closer to 1 are more likely to be mergers and predictions closer to 0 are more likely to be isolated galaxies. The shaded region of the plot is distinct and represents the number of galaxies with $p \gtrsim 0.75$ that were visually confirmed (VC) by Bickley et al. (2022) to be post-merger galaxies.

$Q_{\text{CNN, VC}} = 46 \pm 22$.

2.4.3 Visual Classification

The identification of mergers by visual classification is not infallible and certainly subjective, but still provides a good comparison to previous studies and a sanity check for my other metrics. Hence, both the E+A and PCA PSB samples in their entirety were visually classified following the strategy outlined in Section 2.2.3. Because the control samples are ten times larger than the PSB samples only the best-matched control of each PSB are classified for comparison. 147 of the 533 PCA PSBs are visually classified as having disturbed morphologies indicative of a recent merger or interaction giving a merger fraction of $f_{\text{VC}} = (28 \pm 2)\%$. In contrast, only 16 of the 533 best-match star-forming controls are identified as mergers, translating to an excess in the PCA PSBs of $Q_{\text{VC}} = 9.6 \pm 0.3$. On the other hand, 66/157 ($42\% \pm 4\%$) E+A PSBs are identified as post-merger galaxies, in excess of their controls by a factor of $Q_{\text{VC}} = 9.9 \pm 0.4$. Thus, from directly inspecting the galaxy images of the PSB and control samples I find a significantly higher fraction of recent mergers in the E+A PSBs than in the PCA PSBs but when compared to their respective control samples, their excesses are statistically equivalent. This result is consistent with the findings from the non-parametric morphology methods (see Section 2.4.1) and from the CNN post-merger classifications (see Section 2.4.2) and therefore insensitive to the merger identification method.

2.5 Discussion of Results

2.5.1 A Morphological Comparison Between CFIS and SDSS

Previous works have shown that non-parametric morphology statistics are sensitive to the quality of imaging (Lotz et al. 2004; Pawlik et al. 2016; Bottrell et al. 2019). Since many previous works (e.g., Goto 2005; Alatalo et al. 2016b; Pawlik et al. 2018) have used SDSS imaging to quantify the merger fraction of PSBs, it is worth exploring how the improved quality of CFIS imaging has benefited our analysis. In this section, I will present a comparison between the non-parametric morphology statistics used for identifying mergers for all galaxies in the overlap of CFIS DR2 and SDSS DR7.

The 168,477 galaxies in CFIS DR2 and SDSS DR7 were processed with `statmorph` a second time but with SDSS r-band images instead of CFIS. The implementation is identical to the description in Section 2.2.1 except for minor changes to the treatment of the weightmap and segmentation map. Weightmaps are not available for SDSS images as they are for CFIS, so a gain is provided to `statmorph` instead. Using a gain or weightmap does not have any effect on the non-parametric morphologies computed by `statmorph`. The segmentation map was generated the same way but in some cases the target galaxy was too faint in SDSS to be detected by Source Extractor. In such cases, the detection threshold was reduced from 1.5σ to 1.1σ, and if the galaxy was still too faint to be detected, it was discarded from the catalogue.

In Figure 2.12, I present the difference between the non-parametric morphology statistics used in this work as derived using CFIS and SDSS imaging on a galaxy-by-galaxy basis. For each galaxy, the difference between a non-parametric morphology statistic X as measured in CFIS and SDSS is quantified as $\Delta X = X_{\mathrm{CFIS}} - X_{\mathrm{SDSS}}$. Looking first at the difference between S(G, M_{20}) in CFIS and SDSS shown in the top panel of Figure 2.12, the vast majority (∼95%) of galaxies differ between the two surveys by less than 0.05 and the scatter is symmetric about 0. By visually inspecting the images of the small number of cases ($< 1\%$) in the top right corner of this panel where S(G, M_{20}) > 0 in CFIS and the difference between the two surveys is large ($\Delta S > 0.1$), I find they are caused by foreground stars and close pairs that are not deblended from the target galaxy in CFIS because of an extended diffuse stellar halo but are deblended in SDSS, leading to a lower value of S(G, M_{20}). Galaxies found in the bottom left of this plot have the inverse deblending issue where objects are not deblended in SDSS because of PSF blurring.

The middle panel of Figure 2.12 shows that most galaxies have low values of asymmetry in both surveys, but those with high asymmetry in CFIS are higher in CFIS than SDSS. The small number of galaxies ($< 1\%$) with $\Delta A < -0.1$ are caused by close pairs and foreground stars that are successfully deblended from the galaxy in CFIS but not in SDSS.

Finally, I explore the difference in shape asymmetry between the two surveys. At high values of A_S in CFIS, the values are consistently higher in CFIS than in SDSS since low surface brightness azimuthally asymmetric features are more likely to be detected in the deeper survey. However, there are a significant number of galaxies with higher shape asymmetries in SDSS than in CFIS which are often caused by deblending errors but many of which are bona fide mergers. In some cases, the shape asymmetry will actually be lower when using deeper imaging if there is a diffuse stellar halo that is more symmetric than the slightly brighter tidal tails. In such a case, the binary mask

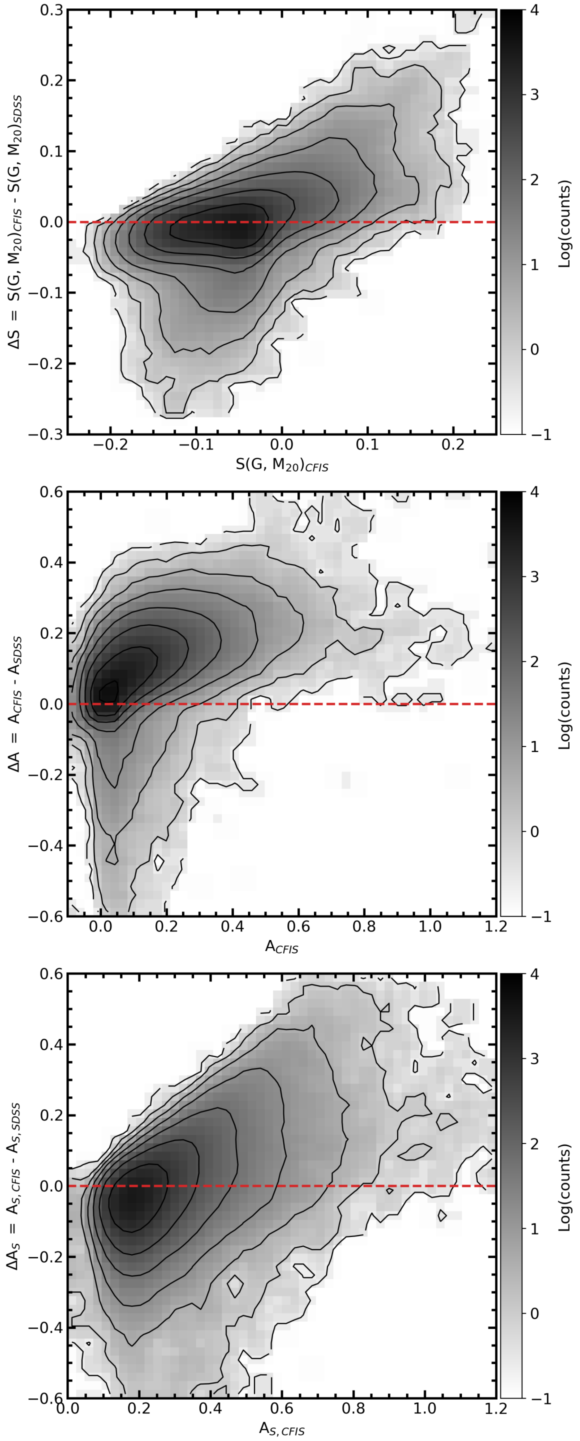

Figure 2.12: The differences between non-parametric morphologies as computed on a galaxy-by-galaxy basis using CFIS and SDSS r-band imaging. The dashed red red line denotes the line of equality between the two surveys and the colour gradient of the histogram denotes the number of galaxies in each bin in log scale. The histogram and contours are smoothed by a 3×3 kernel.

in SDSS includes only the asymmetric tidal tails, while in CFIS, the binary mask includes the faint and symmetric diffuse stellar halo. Another difference in the shape asymmetry measurements between the surveys is that inherently symmetric galaxies are assigned a higher shape asymmetry in SDSS than in CFIS. This is caused by the lower resolution of the imaging creating a more pixelated binary mask which has a higher probability of having asymmetric pixels.

2.5.2 The Difference in PSB Merger Fraction in CFIS and SDSS

Figure 2.12 demonstrates that the quality of imaging used to assess a galaxy's morphology can have a significant impact on the results. To explore how this would impact the number of mergers identified in my post-starburst samples, I now repeat the analysis in Section 2.4 using SDSS imaging to understand how the improved image quality offered by CFIS alters the PSB merger fraction results. In this section, I re-analyze the merger fraction of PSBs with the three non-parametric morphology metrics derived from SDSS and by visual classification of the SDSS images. Retraining and re-running a CNN to identify mergers in SDSS would be a significant undertaking that is outside the scope of this work (the prospect of which is discussed in Chapter 4). Furthermore, I restrict my analysis here to only the PCA PSBs since it is my intention to compare the effect of image quality on my results, not PSB selection strategy. I use the PCA PSB sample instead of the E+A PSB sample simply because it is larger and allows for more statistically robust conclusions to be drawn. When selecting the PSB and control samples in Section 2.3, I required galaxies to have flag-free CFIS morphologies. For a fair comparison between CFIS and SDSS galaxies, I require that every PSB and its controls have both flag-free CFIS and SDSS morphologies. This limits the PCA PSB sample size to 488.

Recall that in Section 2.4.1, I found that the S(G, M_{20})-derived merger fraction for the full sample of 533 PSBs was (8±1)%, a factor of 1.8±0.3 over their controls. Once the PSBs and their controls with SDSS morphology flags are removed, the merger fraction of the 488 remaining PSBs with CFIS imaging changes to (7±1)%, a factor of 2.3±0.7 more than their controls. Using SDSS imaging to determine the merger fraction of the same 488 PSBs reduces the merger fraction to (6±1)%, but still a factor of 1.7±0.4 more than their controls. Thus, fewer mergers are identified in the same sample but within statistical error the same S(G, M_{20}) results derived using CFIS imaging would be recovered using SDSS imaging.

In general, the asymmetry of galaxies in CFIS tend to be higher than in SDSS (see Figure 2.12). For the sample of 488 PSBs, CFIS imaging gives a merger fraction of (1.8±0.6)%, translating to an excess of (0.9±0.3) over their controls at a threshold of $A > 0.35$. In SDSS, the merger fraction of PSBs is (0.6±0.4)%, three times less than in CFIS but translating to a statistically equivalent excess over their controls of (1.2±0.7). In Figure 2.13, I test how the merger fraction and excess would change in CFIS and SDSS using various asymmetry thresholds to identify mergers. The top panel of Figure 2.13 shows that regardless of the asymmetry threshold used, there are fewer identified mergers in SDSS than in CFIS. While in CFIS PSBs have reduced asymmetries and thus fewer identified mergers than their controls at intermediate asymmetry thresholds, the same is not true for SDSS because the poorer image quality already dictates lower asymmetries in both samples. This drives the excess in SDSS to unity for almost all considered thresholds. In CFIS, there are a small number of galaxies with very high asymmetries ($A > 0.5$) which generate an excess at high thresholds. These are not present in the SDSS sample and since there are no galaxies in either the PSB or control samples with high asymmetries, the excess becomes incalculable.

Adopting a merger threshold of $A_S > 0.4$, the CFIS merger fraction is (19±2)%, a factor of 2.6±0.3 over the controls. In SDSS, the merger fraction is only marginally lower at (16±2)%, in excess of their controls by a factor of 2.3±0.3. Thus, at the default merger threshold, the same conclusion would be drawn using either survey. It is only at higher and lower merger thresholds that the difference in quality of imaging offered by each survey makes a difference in the conclusion, as shown in Figure 2.14. At lower thresholds, the merger fraction is higher in SDSS because galaxies with inherently low asymmetry have higher shape asymmetry in SDSS than CFIS due to noise and resolution effects (see Figure 2.12). The noise and resolution affect PSBs and controls equally and so there is no difference between the excess merger fraction at low thresholds. At higher merger thresholds, the excess over the controls in CFIS continues to increase to $Q \sim 8$. In SDSS, the shallower imaging causes fewer PSBs to have very high shape asymmetries and thus the excess over the controls stagnates at $Q \sim 2$. Therefore, whilst the merger excesses are similar for SDSS and CFIS images when asymmetry is used (Figure 2.13), shape asymmetry finds a higher merger excess in the deeper imaging.

Each PSB and best-match star-forming control were classified by eye as outlined in Section 2.2.3. Since visual classification does not rely on `statmorph` morphologies,

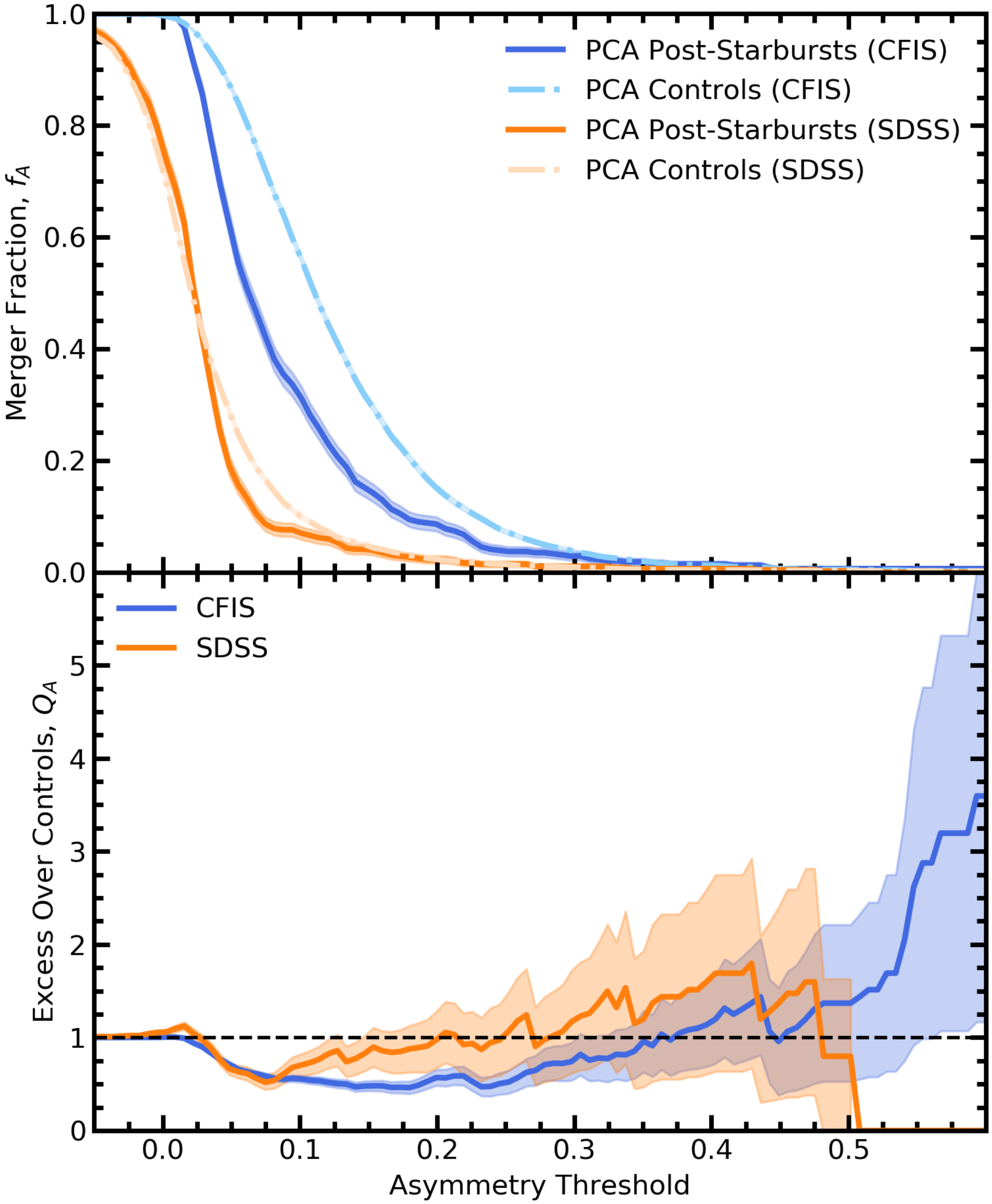

Figure 2.13: The same as Figure 2.8 but considering a subset of the PCA PSBs and their star-forming controls defined by each PSB and its matched control having flag-free morphologies for both CFIS and SDSS imaging. The orange curves show how my results would differ if I were to use SDSS imaging instead of CFIS.

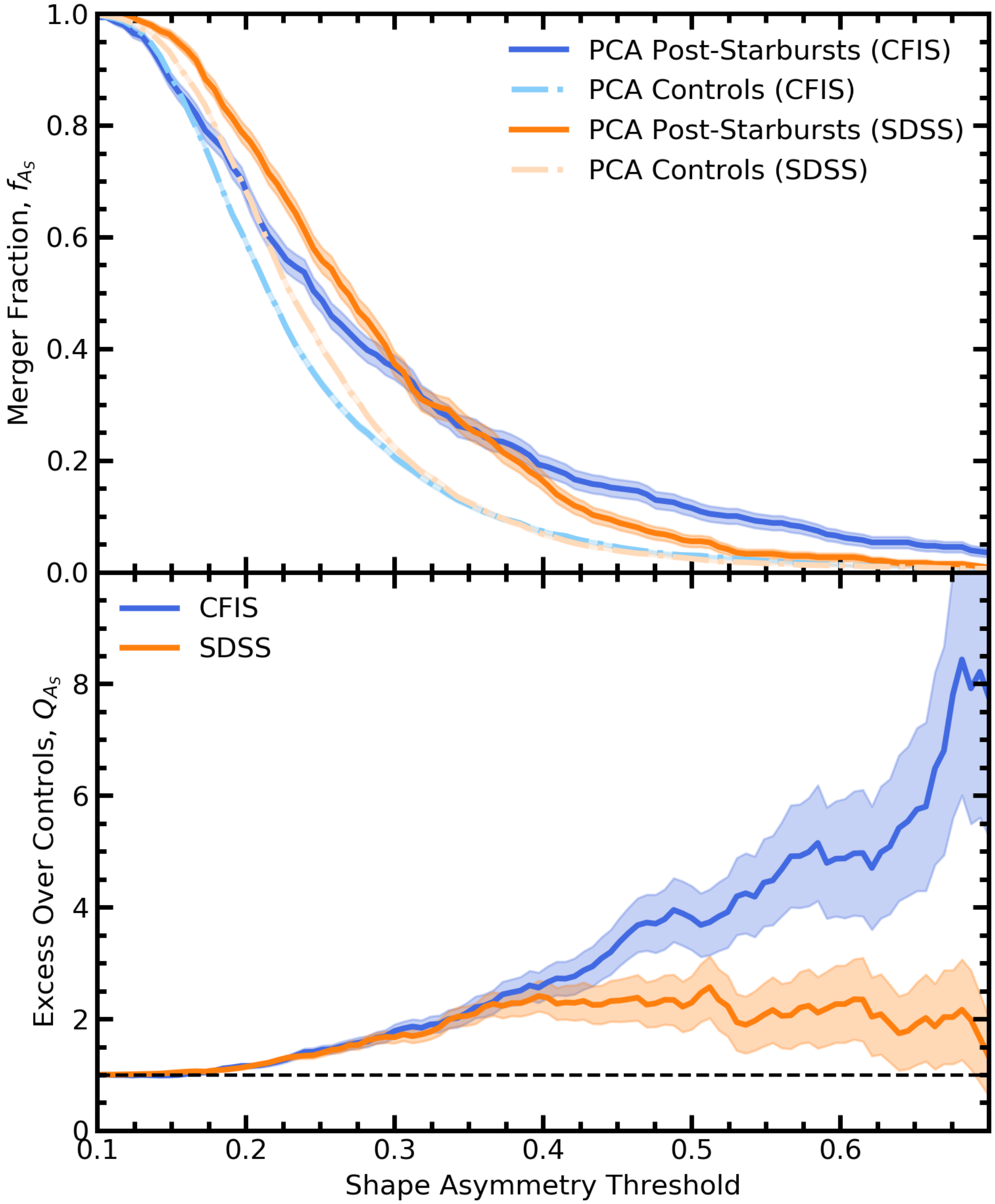

Figure 2.14: The same as Figure 2.10 but considering a subset of the PCA PSBs and their star-forming controls defined by each PSB and its matched control having flag-free morphologies for both CFIS and SDSS imaging. The orange curves show how my results would differ if I were to use SDSS imaging instead of CFIS.

I return to the full sample of 533 PCA PSBs. Recall from Section 2.4.3 that the visual classification of the PCA PSBs with CFIS images gave a merger fraction of $(28 \pm 2)\%$ with an excess over their controls of $Q_{\rm VC} = 9.6 \pm 0.3$. Since SDSS has shallower and lower resolution imaging, there are many cases where merger features are too faint to be seen. As a result, classification with SDSS imaging truncates the number of identified mergers resulting in a merger fraction of $(17 \pm 2)\%$ and an excess of 5.7 ± 0.3

This section has demonstrated that more mergers are detected in the PSB samples when using higher quality imaging, but that the degree to which the improved imaging affects the number of mergers detected depends on the metric used to identify the mergers. These factors are likely to be one of the main reasons for the diversity of results quoted in the literature (see Table 1.8). The use of CFIS imaging allows us to identify a more reliable merger fraction than previous studies that use SDSS imaging. However, my results also indicate that even higher quality imaging than CFIS would extend the number of identifiable mergers. The merger fractions derived from CFIS imaging are therefore likely to be a lower limit of the true merger fraction of PSBs.

2.5.3 Discussion of PSB and Merger Timescales

In Section 2.4, I quantified the merger fraction of PSBs using a variety of merger identification methods, each with varying minimum thresholds above which a galaxy is classified as a merger. I have often referred to the fact that if the initial starburst was caused by a merger, then its post-merger features will fade (perhaps beyond detection) by the time the galaxy becomes a post-starburst. However, my analysis uses strict post-starburst definitions and thus does not provide any insight into how the number of identified mergers would change in an evolutionary epoch after the initial starburst but before the galaxy becomes a post-starburst by my definitions. Since both the strength of PSB indicators in the spectra (Snyder et al. 2011) and the strength of merger features in the images (Lotz et al. 2008; Lotz et al. 2010a,b; Nevin et al. 2019) will both vary in time (and due to merger progenitor properties), it is worth understanding how many mergers may be identified outside the confines of the strict PSB defintions described in Section 2.3. In Figure 2.15, I present a retrospective assessment of the merger fractions computed using the default thresholds of several merger identification metrics throughout the entire PC1-PC2 plane. To provide context for the evolution of a (post-)starburst galaxy through the plane, I have overlaid a

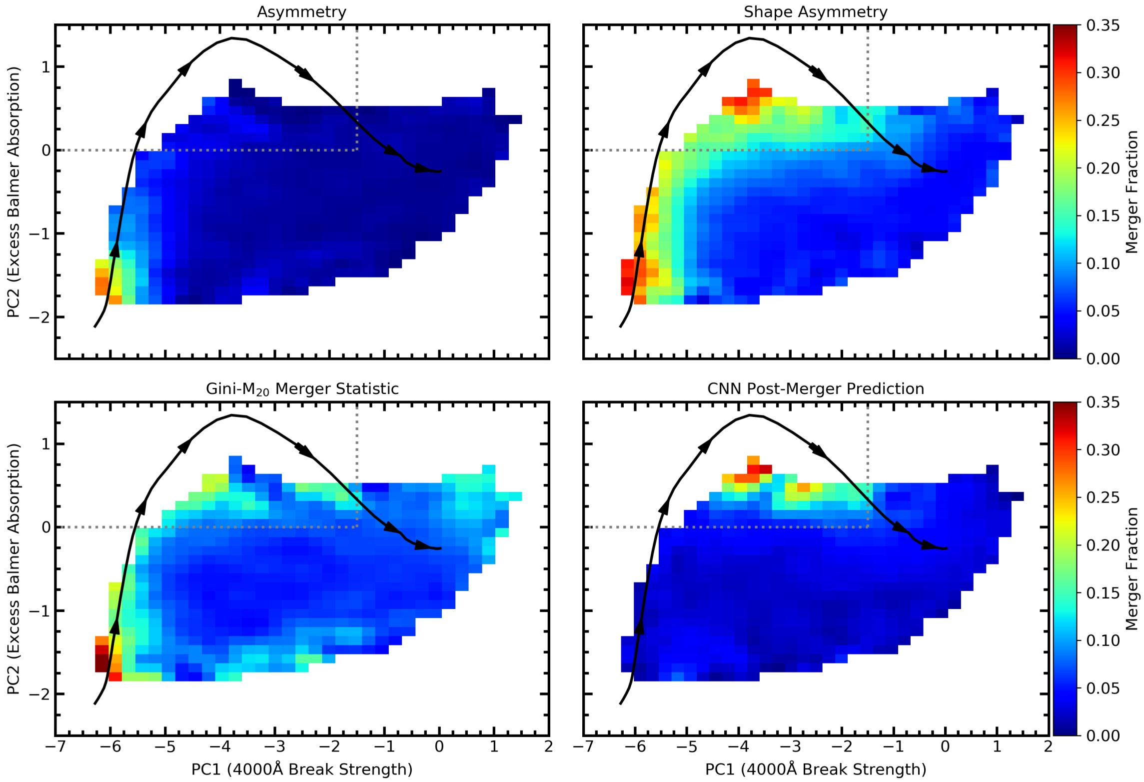

Figure 2.15: The merger fraction, as determined using the default threshold of four merger identification metrics, throughout the entire PC1-PC2 plane. The merger fraction is determined in each bin and then smoothed by a 3×3 kernel. The colour-merger fraction relationship is equal for each of the four panels, as quantified by the colour bar on the right. Over-plotted in black is a model evolutionary track of a tophat starburst of 0.03 Gyr duration and burst mass fraction of 3% from Wild et al. (2007). The track begins 35 Myr after the onset of the starburst (5 Myr after it ends) and the arrows are placed 0.05, 0.1, 0.2, 0.5, 1 and 2 Gyr after the onset of the burst. The dotted grey line indicates the PCA PSB selection region described in Section 2.3.

model evolutionary track of a starburst of 0.03 Gyr duration and burst mass fraction of 3% ($\mathrm{SFR}_{\mathrm{burst}} = 43\ \mathrm{M}_{\odot}/\mathrm{yr}$) superimposed upon a quiescent galaxy spectrum from Wild et al. (2007).

With the additional context of the PC1-PC2 plane, the merger fractions from Section 2.4 and the efficacy of each merger identification method used to assess the merger fraction of PSBs can be better understood. Asymmetry (top left panel of Figure 2.15) identifies significant numbers of starburst galaxies (located in the lower left corner of the plane, where the starburst track begins) as mergers. However, the number of identified mergers using asymmetry decreases rapidly as the starburst evolves and the merger features begin to fade. By the time a starburst galaxy reaches the post-starburst phase, as indicated by the region bounded by the grey dotted lines, very few galaxies remain detectable as mergers based on their asymmetry calculation, consistent with the low merger fraction measured in Section 2.4.1.

The Gini-M_{20} merger statistic (lower left panel of Figure 2.15) behaves very similarly but persists further into the post-starburst phase than asymmetry. However, it should also be noted that the merger fraction remains at $\sim$5%-10% throughout the PC1-PC2 plane indicating a significant number of false-positive merger predictions. Both observations of the Gini-M_{20} merger fractions in the PC1-PC2 plane are consistent with the results found in Section 2.4.1. Furthermore, both asymmetry and the Gini-M_{20} merger statistic are confirmed to be most effective at identifying interacting or very recent post-merger galaxies, but less so for the late-stage post-mergers expected in the post-starburst phase.

Shape asymmetry (top right panel of Figure 2.15) identifies significant fractions of mergers in recent starbursts but, unlike asymmetry, the information persists well into the post-starburst phase. However, shape asymmetry at its default threshold identifies $\sim$5% of galaxies as mergers throughout the PC1-PC2 plane, perhaps indicating a large number of false-positive contamination.

The CNN (lower right panel of Figure 2.15) does not predict a high merger fraction in the starburst region of the PC1-PC2 plane because it was trained to specifically find post-merger galaxies and to exclude interacting galaxies and ongoing pre-coalescence mergers. The region where the CNN predicts a fraction of post-merger galaxies $\gtrsim$10% is approximately the same as the region from which I selected my PSBs. Remarkably, this is the only region in the plane where this is the case indicating that a very significant fraction of CNN-predicted post-mergers in the overlap of CFIS and SDSS are post-starburst galaxies (see Ellison et al. 2022).

The panels in Figure 2.15 that use non-parametric morphology statistics as merger indicators suggest that the recovered merger fraction immediately after the starburst event may be as high as $\sim$30%. This merger fraction decreases significantly in the cases of asymmetry and the Gini-M_{20} merger statistic as the model post-starburst track progresses and merger features fade. However, shape asymmetry and the CNN post-merger prediction maintain a merger fraction as high as $\sim$30% in several bins within the post-starburst regime, indicating they are the more reliable merger identification methods within the context of PSBs.

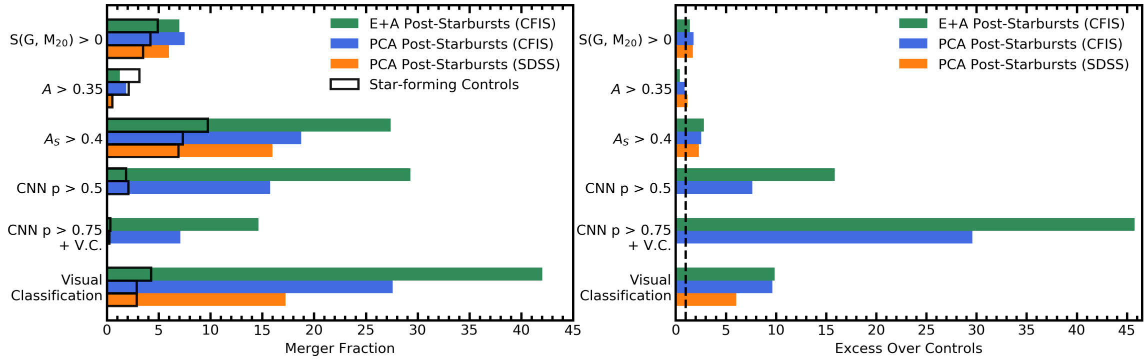

Figure 2.16: *Left*: A visual summary of the calculated merger fractions for a range of merger definitions, PSB selection methods, and image quality. While each coloured bar represents the PSB merger fraction, the black line gives the merger fraction of the matched star-forming controls. *Right*: A visual summary of the excess merger fraction in the PSB samples over their star-forming controls for a range of merger definitions, PSB selection methods, and image quality. The dashed black line indicates proportional mergers in the PSBs and their controls. *Both*: Each merger identification method is subject to a different interpretation: S(G, M_{20}) is best for identifying only very recent mergers and has a significant non-merger contamination; asymmetry is not sensitive to faint asymmetric features and is thus only sensitive to recent and extreme mergers; shape asymmetry is more sensitive to faint asymmetric features and thus detects more mergers in the PSB sample than standard asymmetry; the default CNN threshold identifies a more reliable sample of post-mergers with fewer non-merger contaminants than other automated methods; the visually confirmed CNN sample has near-perfect purity but only identifies a subset of all mergers; visual classification may be the truest representation of the merger fraction of these samples but is a subjective process that will not be applicable to large datasets.

2.6 Chapter Summary

Previous studies have found that significant fractions of post-starburst galaxies have disturbed morphologies indicative of a recent merger or interaction with another galaxy (e.g. Zabludoff et al. 1996; Blake et al. 2004; Yang et al. 2008; Pawlik et al. 2018). However, poor sample statistics, low quality imaging, and inconsistent methods of both selecting PSBs and identifying mergers contribute to a wide spread of reported merger fractions (see Table 1.8) and restrict the field from converging on a quantitative understanding of the importance of galaxy mergers to rapid quenching. In this chapter, I have presented my work which has addressed these issues by assembling two large samples of PSBs using an “E+A” selection technique (Goto 2005) and a PCA selection technique (Wild et al. 2007) from the overlap of SDSS

DR7 (which offers spectra for identifying PSBs) and CFIS DR2 (which offers deeper and higher resolution imaging than SDSS). I have assessed the merger fraction of the two samples of PSBs using three merger identification strategies: non-parametric morphology statistics (Rodriguez-Gomez et al. 2019), a CNN trained to identify post-merger galaxies in CFIS (Bickley et al. 2021), and by visual inspection of the galaxy images. In Figure 2.16, I present a visual summary of my main conclusions:

- **The merger fraction of a given sample of post-starburst galaxies is subject to change when different merger identification methods are applied.** I find that the merger fraction of PCA PSBs vary from 19% using shape asymmetry, to 16% using the CNN, to 28% when visually classified (see Section 2.4 and Figures 2.10-2.11).

- **The merger fraction of a given sample of post-starburst galaxies is subject to change when a different post-starburst selection strategy is implemented, but the excess number of mergers compared to the control sample remains the same.** This conclusion is ubiquitous for the E+A and PCA PSBs across all three merger identification strategies implemented (see Section 2.4 and Figures 2.8-2.11).

- **The merger fraction of a given sample of post-starburst galaxies is subject to change when different quality of imaging is used.** For example, the visually classified merger fraction of PCA PSBs is 28% when using deep and higher resolution CFIS imaging and only 17% when using lower quality SDSS imaging (see Section 2.5.2 and Figures 2.13-2.14).

- There is a clear excess of mergers in the two samples of post-starbursts studied in this work indicating **post-starbursts are often caused by mergers** (see Section 2.4 and Figures 2.8-2.11). Since the merger fraction is not 100%, other mechanisms may be causing galaxies to become post-starbursts. However, the tests described in Section 2.5 indicate that many PSBs may be recent mergers but are not detected as such due to the quality of the imaging and the timescale of merger features and PSB detection.

Chapter 3

Quantifying the Efficacy of Merger Identification Methods with IllustrisTNG

In Chapter 2, I assessed the merger prevalence in post-starburst galaxies and highlighted how different quality of imaging and different merger identification methods can yield different quantitative results. Observational limitations due to image quality can be quantified through controlled experiments with simulated galaxy mergers designed to replicate the physics of the Universe. Unlike real data, data from simulated mergers allows information regarding the morphology, star-formation rate, gas content, and merger history to be known with certainty. In this chapter, I will discuss the pipeline I have developed to take data from simulated galaxy mergers and generate realistic images according to any quality of imaging. The pipeline takes into account realistic effects such as transmission curves of telescope filters, sky noise, camera resolution effects, and atmospheric blurring. With observationally-realistic synthetic data, we can assess our merger identification techniques as a function of various properties of the imaging and the individual galaxies.

The chapter is constructed as follows. First, I will introduce the IllustrisTNG simulation from which simulated galaxy mergers will be drawn in Section 3.1. In Section 3.2, I will discuss the pipeline by which I generate synthetic images of varying quality and viewing angles from the IllustrisTNG simulation. The synthetic images are processed with the automated morphology code introduced in Section 2.2.1. Using the non-parametric morphology statistics derived from the synthetic images of galaxy mergers, I will assess what fraction of mergers are detected by these methods as a function of image quality in Section 3.3 and as a function of properties of the mergers themselves in Section 3.4. I discuss these results further, including a statistical assessment of the effect of viewing angle on merger detectability, in Section 3.5 and present a summary of my findings in Section 3.6.

3.1 Introduction to IllustrisTNG

Numerical simulations have been used to strengthen our understanding of galaxy evolution and study the properties of galaxy mergers for many decades (e.g. White 1978; Gerhard 1981; Davis et al. 1985; Katz 1992; Hernquist 1992; Mihos 1995; Mihos and Hernquist 1996; Springel et al. 2005; Hopkins et al. 2006; Cox et al. 2006; Di Matteo et al. 2007; Boylan-Kolchin et al. 2008; Moreno et al. 2015, 2019; Hani et al. 2020; Davies et al. 2022; Byrne-Mamahit et al. 2023). Over time, the simulations have become more advanced, as (access to) computational power has continued to increase and the community has developed a more sophisticated understanding of the underlying physics governing galaxy evolution. Most modern state-of-the-art numerical simulations with which galaxy mergers are studied, broadly speaking, come in one of three types: (1) smoothed particle hydrodynamical simulations of isolated mergers without cosmological context (i.e. a cosmic web of surrounding gas and galaxies which may be accreted over cosmic time), (2) zoom-in simulations of individual mergers within a large cosmological context, and (3) large-box cosmological simulations where initial conditions of a large-volume box are set according to observed cosmological constraints and the entire box is simulated forward in time according to our present understanding of the underlying physics of the Universe. Each category of numerical simulations has its own advantages and disadvantages in terms of computation time and resources, sample size, number of mergers simulated and layers of physics involved. Therefore, the type of simulation used will depend on the science question you seek to answer. For this work, I will be using a large-box cosmological simulation from IllustrisTNG.

The IllustrisTNG project is a suite of magneto-hydrodynamical large-box cosmological simulations with a range of box volumes and particle resolutions (Springel et al. 2017; Nelson et al. 2018a; Pillepich et al. 2018; Marinacci et al. 2018; Naiman et al. 2018). Each simulation includes dark and baryonic matter divided into four particle types each with differing properties: dark matter, star, gas and black hole particles.

The particles interact with each other according to gravitational and hydrodynamic equations which, in IllustrisTNG, are solved using the AREPO code (Springel 2010). The AREPO code carries out gravitational interactions by solving either the integral or differential form of Poisson's equation in a efficiency-motivated hybrid fashion, a Tree and Particle-Mesh (TreePM) algorithm (see Somerville and Davé 2015; Vogelsberger et al. 2020, for more details and context amongst other codes used by the community). The TreePM method solves short-range gravitational forces via the integral form of Poisson's equation by direct summation on a particle-by-particle basis using a tree approach to reduce computational cost (see Somerville and Davé 2015; Vogelsberger et al. 2020, for more details). The long-range forces are estimated using mesh-based solutions to the differential form of Poisson's equation, solved most efficiently in Fourier space (Somerville and Davé 2015; Vogelsberger et al. 2020). For baryonic matter, AREPO solves the equations of hydrodynamics on a moving unstructured mesh, which is re-generated at each time step using Voronoi tessellation (Springel 2010).

Many physical processes that are important for galaxy evolution are too small to be resolved by individual particles in the simulation. Thus, the hydrodynamics equations dictating interactions between baryonic matter must be supplemented with prescribed so-called sub-grid models that approximate the effect of the ongoing unresolved physics. These sub-grid models include unresolved processes such as stellar formation in the dense interstellar medium, galactic-scale outflows from stellar feedback, the formation, mergers and accretion around black holes, and multi-mode AGN feedback (Nelson et al. 2018b).

The IllustrisTNG suite of simulations is comprised of three different box sizes: (51.7 cMpc)^3, (110.7 cMpc)^3, and (302.6 cMpc)^3 (Pillepich et al. 2019). Simulation runs are named according to their box size: IllustrisTNG50, IllustrisTNG100, and IllustrisTNG300. Due to limited computational power, the mass-resolution of the simulations scales according to their box sizes, making IllustrisTNG50 the highest resolution and IllustrisTNG300 the lowest resolution[1]. Thus, there is a trade-off between volume of the simulation (and therefore number of galaxies and statistical

---

[1] Indeed, each box size is has several runs of varying resolutions, typically denoted by an additional "-N" where a lower number (N) indicates a higher resolution run at a given box size (e.g. IllustrisTNG100-2, is the second-highest resolution run at the 100 Mpc box size). Implicit in this introduction is the fact that I'm considering and discussing the highest resolution runs (and thus flagship simulations) of each box size. These are the most widely used runs in the community since they maximize the resolution-statistical sampling trade off.

sampling of various galaxy properties) and resolution of the simulated galaxies. For the experiments presented in this section, I choose to use IllustrisTNG100 as it sufficiently resolves galaxies above $M_\star > 10^{10}$ $M_\odot$ (consisting of at least ~ 7100 particles) and statistically samples galaxies of various masses and environments such that rare galaxies such as mergers can be robustly divided in to bins along different properties (see Section 3.4). IllustrisTNG100 has a baryonic mass resolution (i.e. mass of each particle) of 1.4×10^6 $M_\odot$ and a dark matter mass resolution of 7.5×10^6 $M_\odot$ which correspond to an approximate spatial resolution of 0.19 kpc and 0.74 kpc, respectively (Springel et al. 2018; Vogelsberger et al. 2020). Data are saved in coarse time steps called snapshots which vary in temporal size according to the redshift of the simulation at the time. The average time between snapshots at $z < 1$ of the simulation is 162 Myr.

While the IllustrisTNG simulations are tuned to approximately reproduce certain characteristics of the observable universe such as the galaxy mass function and sizes at $z = 0$, the simulations have not been tuned to reproduce observed galaxy morphologies. However, the ability to translate the conclusions drawn from the analysis presented in this chapter to the real Universe is ultimately dependent upon the simulation's ability to reproduce and represent the morphologies of galaxies in the real Universe. Recent works have shown that galaxy morphology is well replicated by the IllustrisTNG100 simulation, despite it not being tuned to do so (Rodriguez-Gomez et al. 2019; Tacchella et al. 2019). In Figures 3.1 and 3.2, I show work done by Rodriguez-Gomez et al. (2019) that demonstrates the morphologies of galaxies in IllustrisTNG100 are statistically consistent with galaxies observed with the Panoramic Survey Telescope and Rapid Response System (Pan-STARRS; Chambers et al. 2016). Each panel in Figures 3.1 and 3.2 shows the median trend of a given morphology statistic as a function of stellar mass of the galaxy for real data in black and simulated galaxies in coloured lines. The red lines represent the morphology of galaxies from the original Illustris simulation (Vogelsberger et al. 2014; Genel et al. 2014) which was a precursor to IllustrisTNG but with less advanced and realistic subgrid physics. The blue curves represent galaxy morphologies of galaxies drawn from IllustrisTNG100. The solid, dashed and dotted lines represent morphologies derived from the same galaxy images but generated with synthetic imaging pipelines with full radiative transfer, unresolved dust treatment, and no dust attenuation, respectively. In general, the median trends from IllustrisTNG100 are similar to that of galaxies in the real Universe and treatment of dust does not make a significant change to the median distribution of galaxy morphologies. Thus, Figures 3.1 and 3.2 indicate that, broadly speaking, the morphology results presented in Sections 3.3 and 3.4 are representative of results for galaxies in the real Universe.

3.1.1 Merger Selection

Individual galaxies in IllustrisTNG have been previously identified following the methods of Rodriguez-Gomez et al. (2015) and made public in the IllustrisTNG catalogues[2]. First the dark matter halos are identified by applying a friends-of-friends algorithm (Davis et al. 1985) on the dark matter particles, requiring a minimum of 32 particles to constitute a halo. After dark matter halos have been established, gas and star particles are assigned to the halo to which the nearest dark matter particle belongs. Substructure within the halo (i.e. subhalos) are identified using an extension of the `SUBFIND` algorithm (Springel et al. 2001; Dolag et al. 2009) and temporally connected through snapshots of the simulation using the `SUBLINK` algorithm. A natural consequence of hierarchical growth of galaxies and tracing galaxies through cosmological time with `SUBLINK` is the generation of merger trees. Merger trees identify when two subhalos become one and allow you to trace back the progenitor galaxies to understand their individual properties. From the legacy efforts of previous members of my research group, namely Drs. Maan Hani and Salvatore Quai, all of the mergers in IllustrisTNG100 have been identified and assembled along with properties of the post-merger and progenitors of the merger in a tabulated and documented format local to the University of Victoria. It is from these tables that I will construct a merger sample. For more details on the creation of the mergers trees via the application of the `SUBFIND` and `SUBLINK` algorithms, I direct readers to Rodriguez-Gomez et al. (2015). For more information on how the merger trees are parsed and assembled into our local tables, please see Hani et al. (2020) and Quai et al. (2023).

From the local catalogue of mergers in IllustrisTNG100, I construct a sample of mergers that meet the following requirements:

- The merger must have occurred within the preceding snapshot of the simulation (i.e. $\lesssim$160 Myr). The temporal resolution of IllustrisTNG100 is too coarse for a detailed study of how merger features fade over time. For now, I restrict my analysis to the most recent mergers in the simulation to assess the best-case-scenario for merger detection.

---

[2] https://www.tng-project.org/data/docs/specifications/

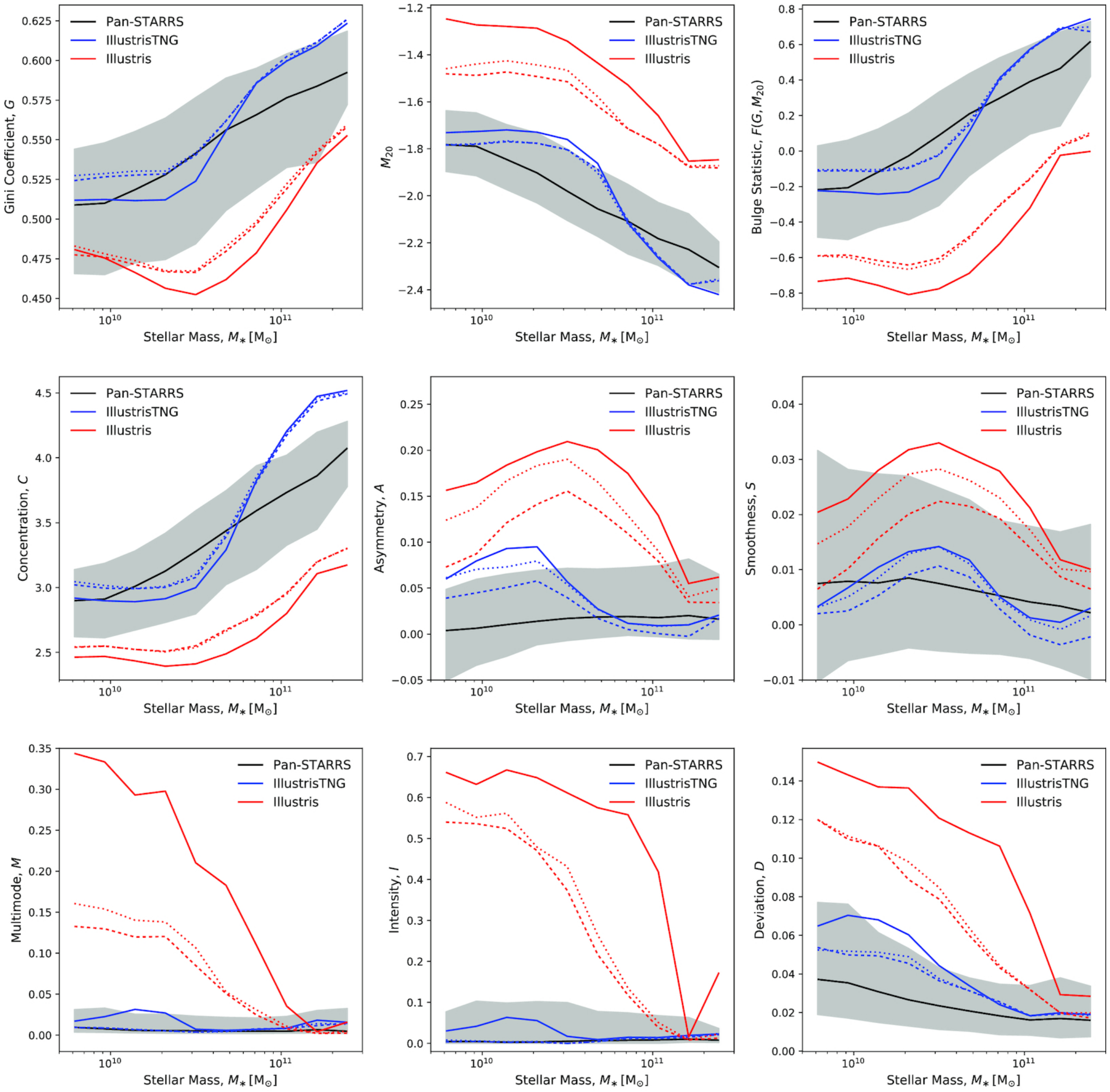

Figure 3.1: Median trends of various morphological parameters, as indicated in the y-axis labels, as a function of stellar mass. The top, middle, and bottom rows show the Gini–M_{20}, CAS, and MID statistics, respectively. In each panel, the black line shows the median trend for the observational Pan-STARRS sample, while the grey shaded region indicates the 16th to 84th percentile range of the same data. The blue and red lines show results from the IllustrisTNG and original Illustris simulations, respectively, with different line styles indicating model variations: the solid lines show results obtained with the SKIRT radiative transfer code including full dust modelling, while the dashed and dotted lines represent simpler models with an unresolved dust distribution and without dust, respectively. This figure shows that the optical morphologies of IllustrisTNG galaxies are in better overall agreement with observations than those of the original Illustris simulation. This figure is drawn from Rodriguez-Gomez et al. (2019). While MID statistics are not introduced or used in this work, further details regarding MID statistics can be found in Freeman et al. (2013).

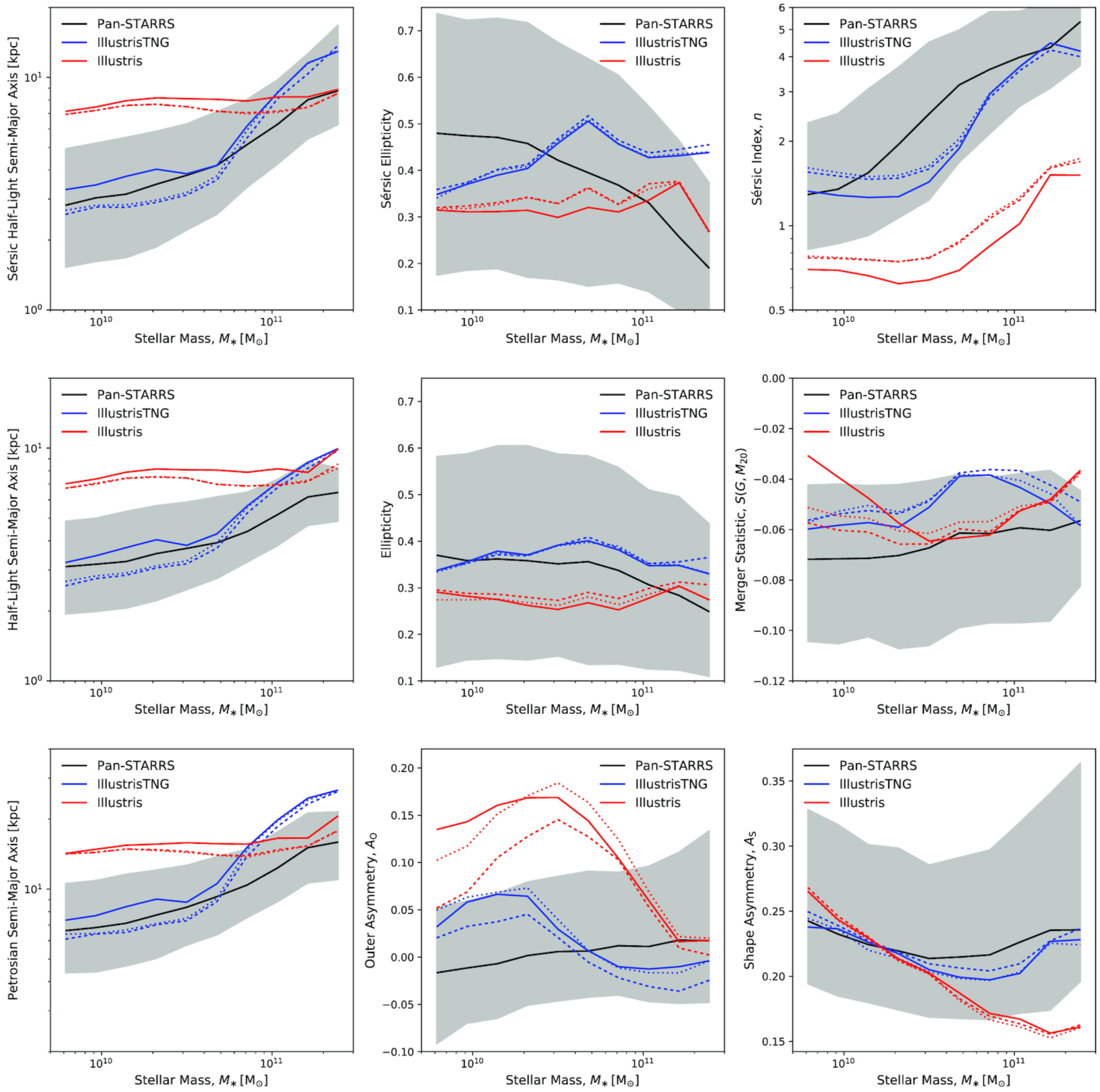

Figure 3.2: Same as Figure 3.1, but this time showing Sérsic parameters (top row), size measurements (left-hand column), shape measurements (top centre and middle panels), the Gini–M_{20} merger statistic (centre right-hand panel), and alternative definitions of the asymmetry index (bottom centre and bottom right-hand panels). This figure is drawn from Rodriguez-Gomez et al. (2019) and I refer readers to that paper and Appendix 2.5.1 of this thesis for detailed descriptions of morphology statistics not introduced herein.

- The mergers must occur at $z < 1$ of the simulation. The increased frequency of mergers in the simulation prior to this redshift threshold exacerbates issues such as numerical stripping and subhalo switching which makes reliable merger identification more challenging (for more details see Rodriguez-Gomez et al. 2015).
- The post-merger remnants must have a total stellar mass greater than 10^{10} $\mathrm{M}_{\odot}$. This mass ensures the merger remnant and both progenitors are well resolved, as long as a minimum mass ratio between the progenitors is required.
- The two progenitors of the post-mergers must have a mass-ratio greater than 1:10 ($\mu > 0.1$). This ensures the smallest progenitor would have at least 700 star particles, which is considered sufficiently resolved.

The number of mergers that meet these requirements is 2119. The distributions of total stellar mass and mass ratios of the mergers and the relationship (or lack thereof) between the two properties are shown in Figure 3.3. No strong trend between the total stellar mass and mass ratio of the mergers is evident. However, it is worth noting that the bottom left panel of Figure 3.3 indicates there is an overdensity of low-mass ratio and low-mass mergers in the merger sample and a dearth of high-mass and high mass ratio mergers. This is because both high mass ratio mergers and high stellar mass galaxies are rare, thus the likelihood of a high-mass major merger is very low. It may also be worth noting that the gas fraction, represented by the colour of the points, is generally higher in lower mass mergers than in higher mass mergers.

3.2 Synthetic Imaging Pipeline

Synthetic images are derived from the three-dimensional (3-D) stellar mass distributions of galaxies drawn from the IllustrisTNG100 simulation. For a given galaxy, the 3-D mass distribution is projected into two dimensions along four independent viewing angles, located at the vertices of a tetrahedron aligned with the cosmological box and not any specific property of the galaxy[3]. Projecting the stellar mass distributions along multiple viewing angles is a common way to increase the size of your sample of synthetic observations (e.g. Bottrell et al. 2019, 2022; Bickley et al. 2021;

---

[3] This is done with code adapted from Dr. Maan Hani's original code, which uses the `py-sphviewer` Python package (Benitez-Llambay 2015)

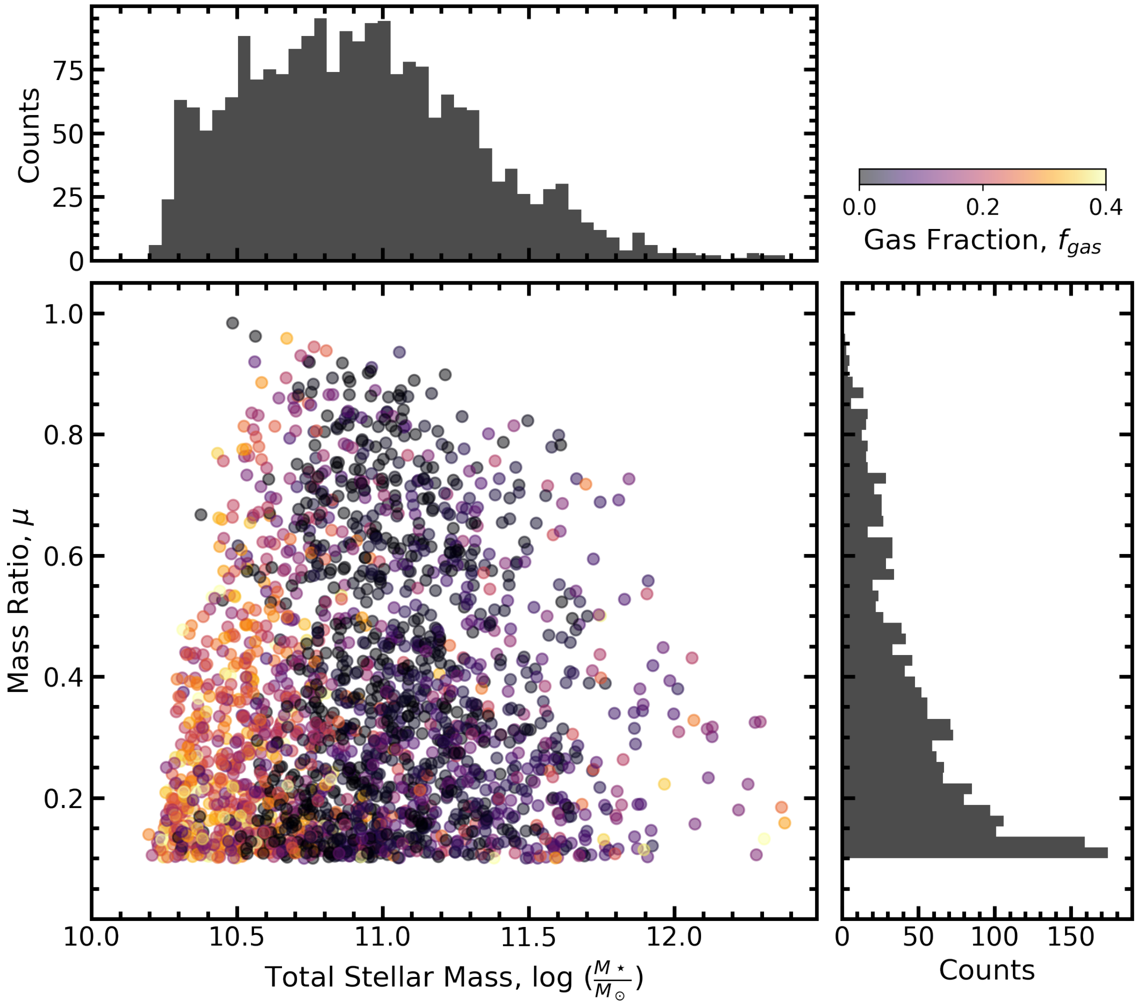

Figure 3.3: The distributions of the IllustrisTNG100 merger sample in total stellar mass and mass ratio. The top and right panels show the one-dimensional distribution of total stellar mass and mass ratio, respectively, as histograms. The central panel shows how the two properties relate to each other; no strong trend is observed, except for the dearth of high mass ratio mergers at high stellar mass. The colour of the points corresponds to the gas fraction of the merger remnant according to the colourbar shown in the top right corner.

Rodriguez-Gomez et al. 2019; Guzmán-Ortega et al. 2023). Each resulting 2-D stellar mass profile is used in this analysis as a proxy for the idealized (free from noise and resolution degradation) visible light profile along a given line of sight.

Using the 2-D projection of the stellar mass distribution as a proxy for the galaxy's light profile implicitly assumes that the galaxy has a mass-to-light ratio (M/L) equal to one, regardless of the age and metallicity (among other properties) of the stellar populations and the gas and dust distributions within the galaxy. These assumptions indeed may have an effect on the measured morphology of the galaxies, particularly in the case of mergers. Mergers often have enhanced star-formation rates (Darg et al. 2010a; Thorp et al. 2019; Bickley et al. 2022) and starburst stellar populations are known to be more commonly concentrated and with high Sersic indices (Wuyts et al. 2011). Visible light is attenuated by dust along the line of sight; in mergers, dust that is typically concentrated in disks, may be disrupted and attenuate light in more extant regions and from more viewing angles potentially affecting the measured morphologies (see Fig. 9 in Lotz et al. 2008). Furthermore, it has been shown that using radiative transfer simulation code such as SKIRT (Baes et al. 2011; Camps and Baes 2015) to generate synthetic light distributions of galaxies that better approximates the non-parametric morphology statistics of galaxies seen in real data (Rodriguez-Gomez et al. 2019; Guzmán-Ortega et al. 2023). However, it has also been shown that for merger identification purposes (albeit with machine learning methods rather than classical non-parametric methods), the degree of observational realism added to the images is a more important feature for classification performance than the use of radiative transfer simulations (Bottrell et al. 2019). Indeed, perhaps radiative transfer is not particularly important for identifying mergers due to the importance of features like shells, tidal tails and asymmetries of diffuse stellar halos which are largely unaffected by starbursts and dust attenuation. For the work presented here, I elect to not use radiative transfer, because the computational time required was incompatible with the timeline of the thesis. However, in future work I will be implementing this additional step as discussed in Section 4.2.

The 2-D stellar mass distributions (henceforth referred to as mass maps) are generated to be 1024×1024 pixels across and have a field of view of 92 kpc. The redshift of the synthetic images are fixed to z=0.1, giving an on-sky FOV of 50 arcsec. The images are then down-sampled to 250×250 pixels giving a pixel scale resolution of 0.2 arcsec / pix following the methods of the `RealSim`[4] code (Bottrell et al. 2019).

---

[4] github.com/cbottrell/RealSim

The absolute magnitudes of the galaxies are taken from the IllustrisTNG catalogues[5] (Nelson et al. 2019). The absolute magnitude of a given galaxy in the catalogue is calculated from a spectrum fit to each star particle, according to the age and metallicity of the stars within, using the Bruzual and Charlot (2003) models. r-band absolute magnitudes are generated by integrating that spectrum over the SDSS r-band filter response curve. The total flux according to a galaxy's r-band absolute magnitudes is distributed across the galaxy according to its 2-D stellar mass distribution. The surface brightness of the images are dimmed by a factor of $(1+z)^{-5}$, following the methods of the `RealSim` code (Bottrell et al. 2019). A factor of $(1+z)^{-4}$ comes from surface brightness dimming of the bolometric luminosity and an additional $(1+z)^{-1}$ comes from the loss of light in a particular photometric pass band.

To emulate the effect of atmospheric blurring, the redshift-corrected surface brightness profile of the galaxy is convolved with a PSF. PSFs, in general, account for all abberations of the light including those caused by the atmosphere but also the instrumentation itself. The intent of this work is to generalize beyond any specific instrument. Therefore, I use a simple 2-D Gaussian profile to model the blurring caused by the atmosphere and neglect contributions from instrumentation. The degree to which the image is blurred is dictated by the FWHM of the Gaussian profile.

After applying a PSF, the image is then co-added with a 250×250 pixel FOV of Gaussian sky noise. The sky flux in each pixel is drawn from a Gaussian profile with a mean of 0 (i.e. the image is sky subtracted) and a standard deviation according to a pre-determined depth (e.g. 26 mag arcsec^{-2}). Of course, Gaussian sky noise does not encompass all the complexities of real skies, particularly those in surveys which may have correlated noise due to the survey observation patterns and the data reduction pipeline. Real skies can't be drawn from surveys as is done in other works (e.g. Bottrell et al. 2019; Bickley et al. 2021; Ferreira et al. 2022) since the experiment requires full and individual control over both the depth and the resolution of the synthetic images. Nonetheless, my image construction serves as an example set from which the trends in PSF and sky noise on merger classification can be investigated.

For the experiment at hand, I degrade the idealized image of each galaxy viewing angle to a 6×6 grid of varying image qualities spanning six depths from 23-28 mag arcsec^{-2} and six PSFs with FWHMs ranging from 0.25-1.5 arcsec. For one example of a post-merger drawn from IllustrisTNG100-1 (snapshot 50, subhalo 222023) which has

---

[5] IllustrisTNG catalogues are documented here: https://www.tng-project.org/data/docs/specifications

a total stellar mass of $7.4\times10^{10}M_{\odot}$ and a mass ratio of 0.4, I present an example grid of all 36 degraded images in Figure 3.4. In addition to the 6×6 grid of image qualities, I generate an "ideal" image for each galaxy which has no atmospheric blurring effects and 30 mag arcsec^{-2} sky noise (some detectable level of sky noise must be added to avoid causing catastrophic `statmorph` errors.). The same example galaxy as in Figure 3.4 is shown with this ideal imaging in Figure 3.5.

3.3 How Image Quality Affects the Completeness of Recovered Mergers

The purpose of the experiments in this chapter are to understand and quantify the factors affecting one's ability to identify mergers in a given sample. This will be tested by measuring the non-parametric morphology statistics useful for identifying mergers for the sample of recent post-merger galaxies drawn from IllustrisTNG (as discussed in Section 3.1.1) which intrinsically have a range of galaxy merger properties such as final stellar mass of the system and mass ratio of the progenitors. The ability of a given non-parametric morphology statistic to identify mergers will be quantified using the completeness statistic (equivalently known as true positive rate, recovery fraction, recall, and sensitivity). Completeness is measured as the number of true mergers identified as mergers, $N_{\text{detected mergers}}$, by the statistic divided by the number of galaxies in the total merger sample, $N_{\text{total mergers}}$:

$$\text{Completeness} = \frac{N_{\text{detected mergers}}}{N_{\text{total mergers}}}. \tag{3.1}$$

Another common and useful metric to assess a sample of detected mergers is the purity of the detected merger sample. Purity is defined as the ratio of the number of true positive mergers to the total number of detected "mergers". Purity is important to merger identification because mergers are so rare, particularly in the low-redshift universe (Lotz et al. 2011). Since most galaxies observed are non-mergers, even if a statistic used for identifying mergers has a very low rate of false positives, the total number of false positives can dominate the sample of detected "mergers" (Bickley et al. 2021). To make an assessment of the purity of the merger samples at different image qualities, I would need to construct a realistic survey-like sample of mergers and non-mergers which will depend on the redshift (and redshift distribution, related to the depth and magnitude limit of imaging). Furthermore, such an analysis would not

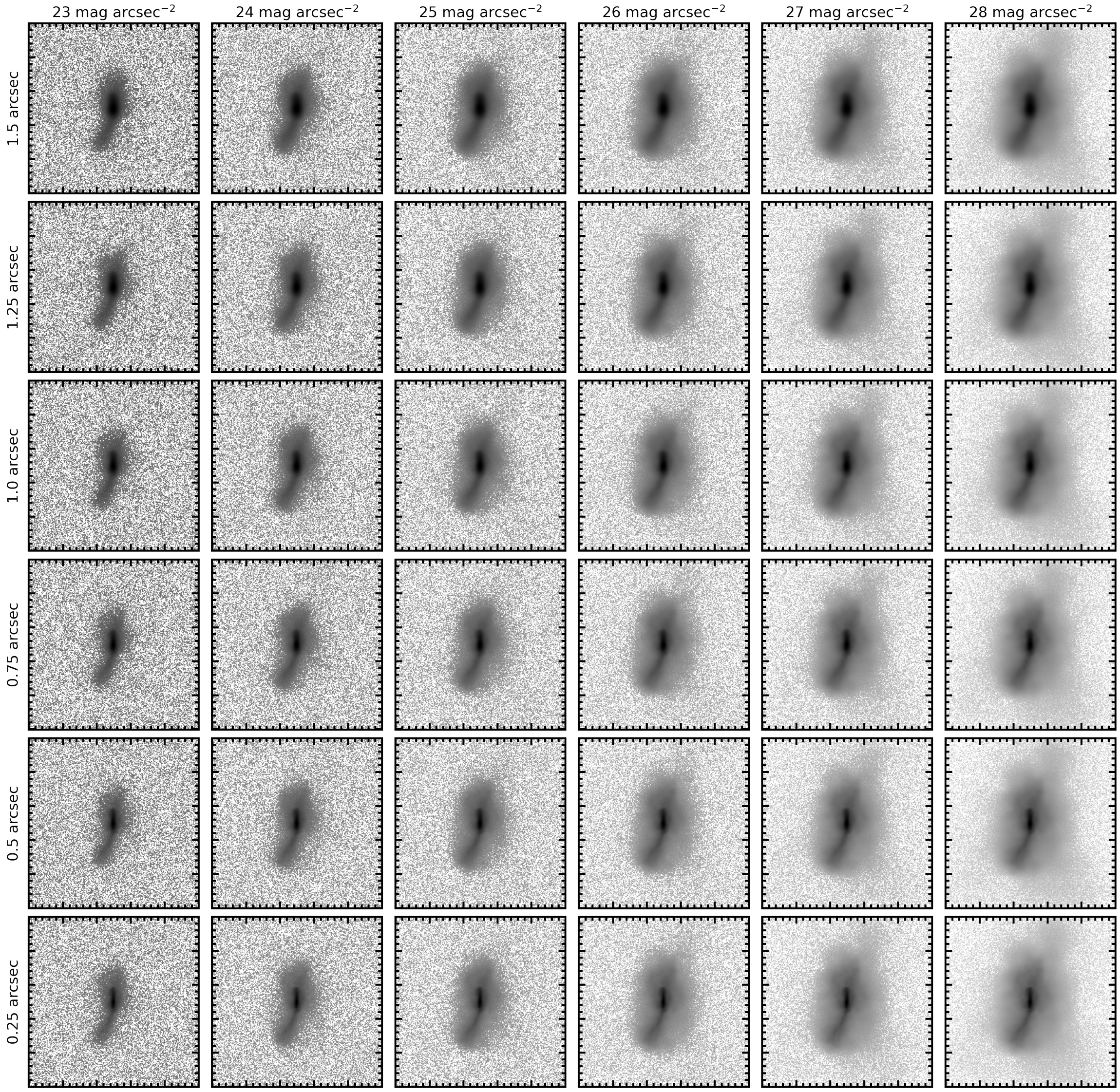

Figure 3.4: Thirty-six degraded images of one idealized synthetic image at one viewing angle. From left to right, the images improve in depth, ranging from 23-28 mag arcsec^{-2}. From top to bottom, the images have reduced atmospheric blurring, ranging from 1.5-0.25 arcsec. Therefore, the worst image quality used in this experiment is in the top left panel and the best is in the bottom right panel. The galaxy is a post-merger drawn from IllustrisTNG100-1 (snapshot 50, subhalo 222023) which has a total stellar mass of $7.4\times10^{10} M_{\odot}$ and a mass ratio of 0.4.

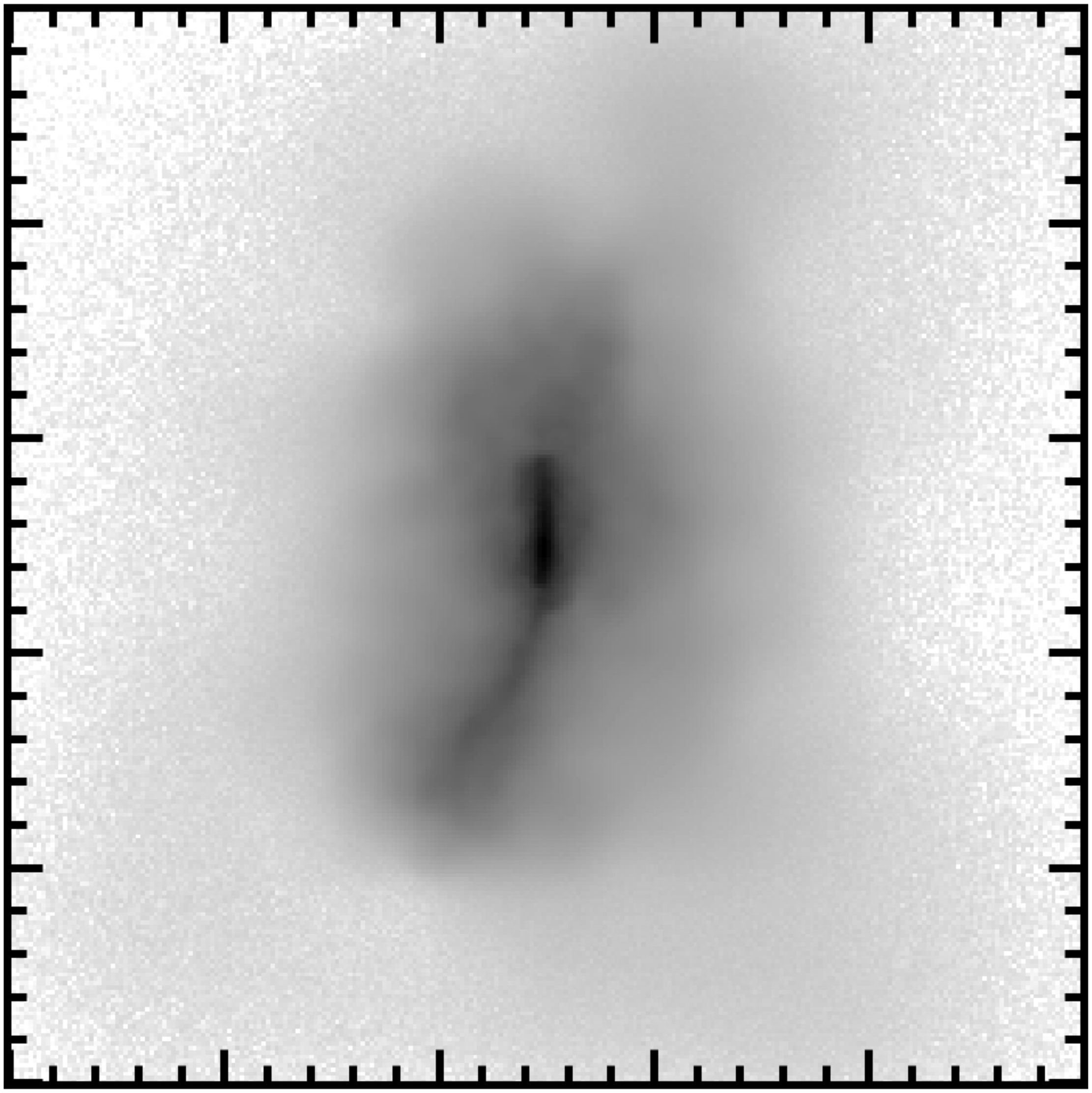

Figure 3.5: The ideal (30 mag arcsec^{-2} sky noise, with no PSF blurring) synthetic image at one viewing angle of the galaxy shown in Figure 3.4. This post-merger drawn from IllustrisTNG100-1 (snapshot 50, subhalo 222023) has a total stellar mass of $7.4{\times}10^{10} M_{\odot}$ and underwent a merger with a mass ratio of 0.4.

necessarily be applicable to subsets of galaxy populations such as a sample of post-starbursts, which will come with their own priors due to additional selection criteria that may make mergers more or less likely (a prior that is not well constrained in the case of post-starbursts!). Beyond that, purity will also depend on the threshold used to identify mergers, the optimization of which would change as a function of image quality. Since the goal of these experiments is to assess the affect of depth and resolution on the ability to detect mergers individually, and not for any specific survey, including these other factors is beyond the scope of this work.

For each quality of imaging shown in Figure 3.4, I measure the non-parametric morphology statistics of the degraded synthetic galaxy images with `statmorph` following the same methods introduced in Section 2.2.1. In this section, I will first present and discuss the completeness results for a single image quality, namely the idealized imaging with a depth of 30 mag arcsec^{-2} and no PSF blurring. Then, I will discuss how those results are affected by the depth and PSF blurring of the images, respectively and in tandem.

3.3.1 Merger Completeness in Ideal Imaging

For each combination of PSF blurring and depth in Figure 3.4 and the ideal imaging, the 8,476 synthetic images of galaxy mergers at that image quality are processed with `statmorph` which provides non-parametric morphology statistics for each of the synthetic images. In Figure 3.6, I present the distributions of four non-parametric morphology statistics useful for identifying galaxy interactions for the 8,476 ideal images of mergers generated from IllustrisTNG100. The ideal imaging represents the best-case-scenario for merger detection. The vertical lines in each panel of Figure 3.6 demarcate the default threshold for each metric above which galaxies are considered detected mergers. The distributions presented here demonstrate that, in the ideal quality images, most mergers have morphologies below the merger threshold of these statistics. This is quantified by the percentage of mergers which are above the default thesholds (i.e. completeness of merger sample) given in each panel. Asymmetry has a completeness of only 12.5% in the ideal imaging. Outer asymmetry and shape asymmetry accomplish higher values of completeness with 36.9% and 25.8%, respectively. The highest completeness is achieved by the Gini-M$_{20}$ merger statistic which successfully identifies 38.7% of mergers. Thus, Figure 3.6 demonstrates that even in ideal imaging, a majority of mergers are undetected by non-parametric morphology statis-

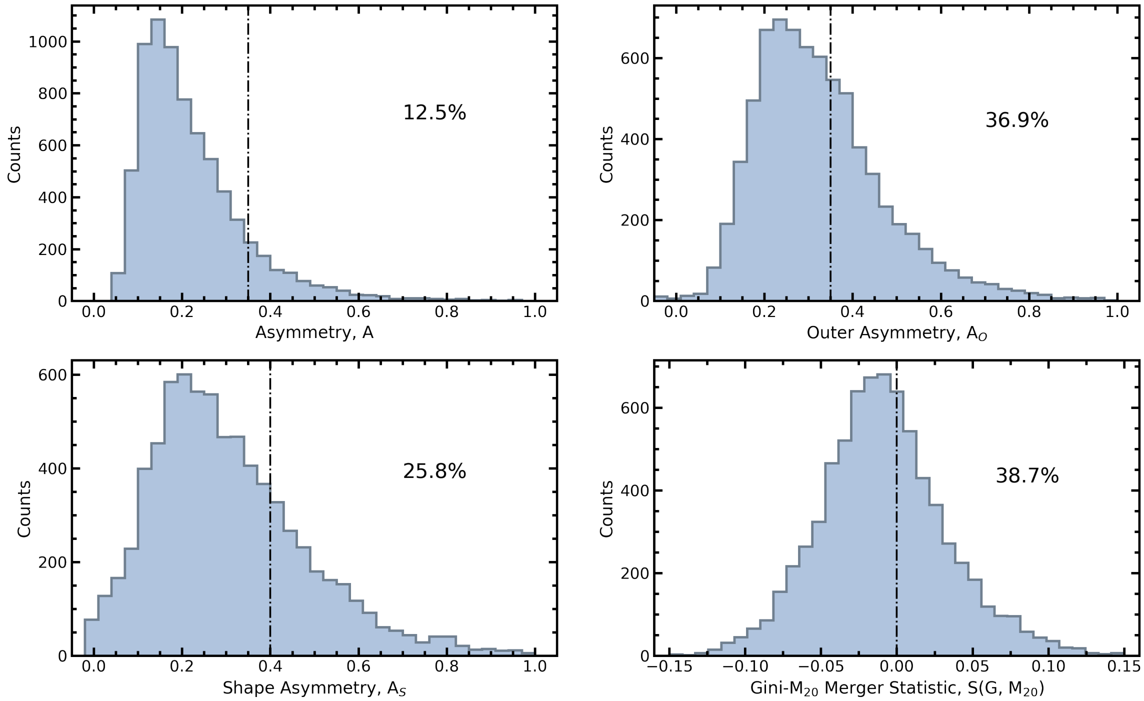

Figure 3.6: The distribution of four non-parametric morphology statistics commonly used to identify mergers as applied to a sample of IllustrisTNG mergers in “ideal” imaging (no atmospheric blurring and a sky noise of 30 mag arcsec^{-2}). The vertical lines demarcate the default merger detection threshold for each statistic, above which a galaxy is considered a merger. The percentage of mergers above each threshold (i.e. the completeness) is given as a percentage on each panel.

tics at their default thresholds. The completeness achieved by the non-parametric morphology statistics in the ideal imaging will act as a benchmark as the effect of image quality on merger completeness is explored in the Section 3.3.2.

3.3.2 Merger Completeness as a Function of Image Quality

Since synthetic images of the entire merger sample are generated for each image quality and processed with `statmorph`, the non-parametric morphology distributions (as in in Figure 3.6) of the entire sample exists for all 36 image qualities. Rather than showing the distributions of the morphology statistics at every image quality, I extract the completeness information from the distributions, so that trends with image quality can be seen in a more compact form. What follows is a detailed description of the observed trends between completeness and image quality for asymmetry, outer asymmetry, shape asymmetry and the Gini-M$_{20}$ merger statistic.

Asymmetry

In Figure 3.7, I present the completeness of the merger sample recovered using the threshold $A > 0.35$ as a function of depth and PSF blurring. The Figure contains three panels. The main panel in the bottom right has depth and PSF FWHM on the x- and y-axes, respectively. At each combination of depth and PSF FWHM, the completeness at that image quality is shown both qualitatively as a colour gradient (white is lowest completeness and dark blue is highest completeness) and quantitatively as a fraction between 0 and 1. The intention of this panel is to showcase the qualitative trends of completeness as a function of image quality and operate as a look-up reference table for other astronomers seeking an estimate of the completeness of their merger sample, given their quality of imaging. Indeed, all of the information in Figure 3.7 is contained within the main panel (bottom right panel). However, the adjacent panels are added to demonstrate the individual trends of completeness with PSF blurring and depth; in general, I find it easier to identify and interpret more subtle features (e.g. exponential increase versus linear increase, plateaus, intersections) of these trends with individual lines rather than as a 2-D gradient. The lines are coloured from red to green with red representing lower quality imaging and green representing higher quality imaging.

At the lowest quality of imaging considered (23 mag arcsec^{-2} sky noise, 1.5 arcsec PSF FWHM) the asymmetry completeness is 0.004, indicating only 0.4% of mergers are correctly identified. The gradient in the bottom right panel of Figure 3.7 shows that as image quality improves, in both resolution and depth, the completeness increases. The highest completeness achieved is 10% at the highest quality imaging considered (28 mag arcsec^{-2} sky noise, 0.25 arcsec PSF FWHM).

A closer look at the top panel of Figure 3.7 shows that the completeness improves with depth monotonically, but the increase in depth begins to have diminishing returns beyond 26 mag arcsec^{-2}. Depth increases the number of mergers recovered because many mergers are asymmetric in their outer regions and including that asymmetric flux in the asymmetry calculation will increase the asymmetry, even if it is given a lower statistical weight than brighter regions. Increasing the depth has diminishing returns at higher depths because any new features identified will be faint and therefore given very low statistical weight and are unlikely to affect the asymmetry measurement significantly.

The left panel of Figure 3.7 shows that completeness increases exponentially as

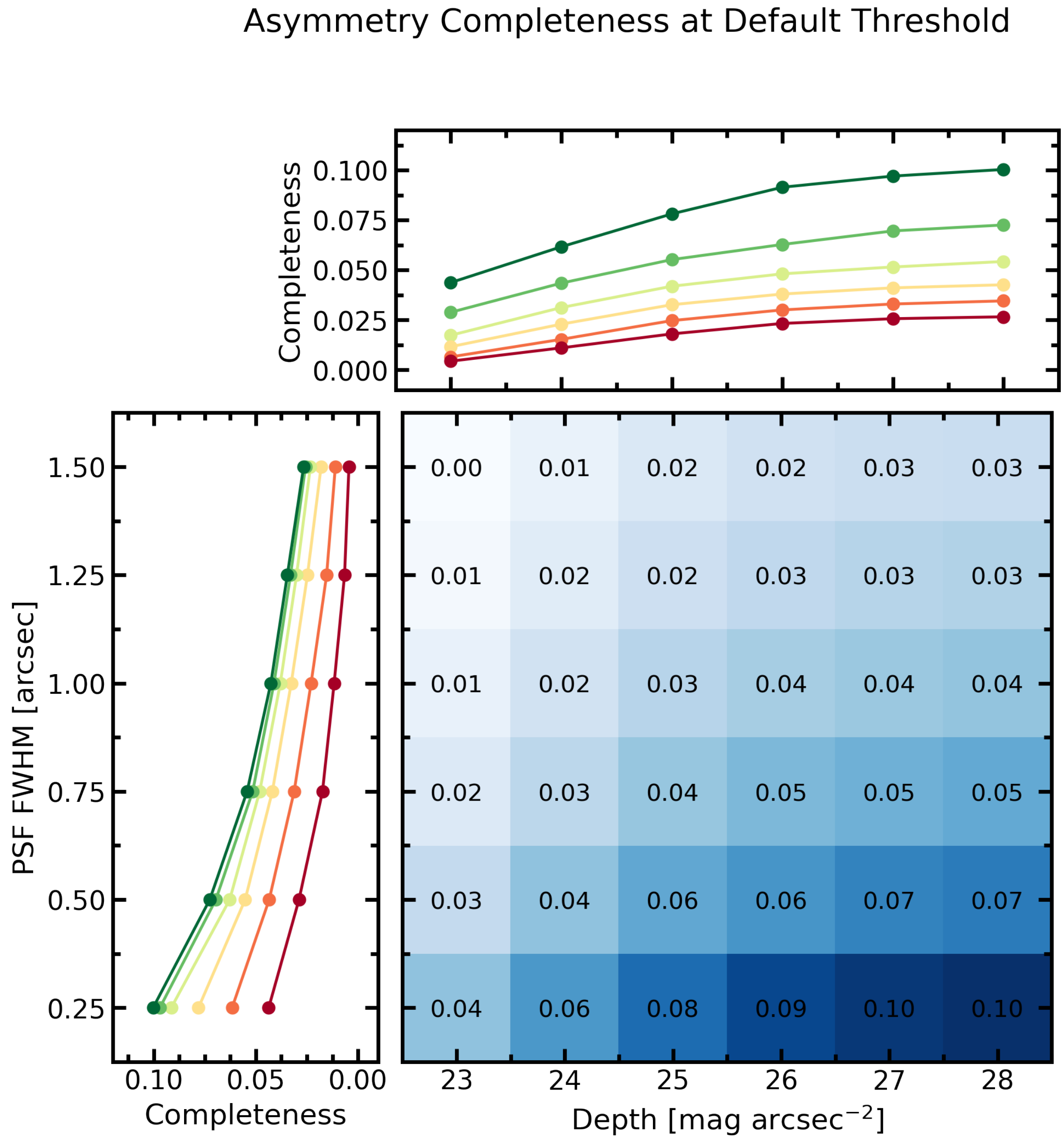

Figure 3.7: The completeness of recovered mergers using asymmetry with the default threshold ($A > 0.35$). In the bottom right panel, the colour gradient shows the completeness as a function of both depth and PSF blurring, with specific completeness values at each image quality reported in the corresponding cell. The top panel shows the relationship between completeness and depth, with each line representing a different PSF FWHM. The lines are coloured from red to yellow to green with red indicating the worst image quality (highest PSF FWHM) and green indicating best image quality (lowest PSF FWHM). The left panel shows the relationship between completeness and resolution, with each line representing a different depth. These lines are also coloured from red to yellow to green with red indicating the worst image quality (lowest depth) and green indicating best image quality (high depth).

the degree of PSF blurring decreases, indicating that asymmetry completeness would continue to improve in higher resolution imaging (i.e. space-based imaging). The bright merger features to which asymmetry is particularly sensitive are often physically small (e.g. double or extended nuclei). Therefore, blurry imaging regularizes and spatially decouples those features, reducing the asymmetry.

Outer Asymmetry

In Figure 3.8, I present the completeness of the merger sample recovered using the threshold $A_O > 0.35$ as a function of depth and PSF blurring. At the lowest image quality, outer asymmetry is approximately twice as effective at identifying mergers as the regular asymmetry metric, with a completeness of 0.9%. However, recovering less than 1% of mergers is still a very low completeness. The completeness increases as image quality improves reaching a maximum of 32% at the highest quality imaging, a factor of ~ 3 higher than asymmetry at the same image quality.

It is immediately apparent from both the outer asymmetry completeness gradient in the bottom right panel of Figure 3.8 and the adjacent panels that the outer asymmetry completeness increases much more strongly with depth than it does with PSF blurring. Since outer asymmetry removes the central region of the galaxy from the asymmetry calculation, more statistical weight is being given to the faint exterior regions of the galaxy. As depth increases, the likelihood of a faint asymmetric feature being observed above the noise of the image increases. However, it is important to note that even in the deepest imaging, there is still a trend of increasing completeness with decreasing PSF blurring (see dark green line of left panel). This indicates that high resolution imaging is still required to identify some of the faint asymmetric features found in the outer regions of the mergers.

Shape Asymmetry

In Figure 3.9, I present the completeness of the merger sample recovered using the threshold $A_S > 0.4$ as a function of depth and PSF blurring. Broadly speaking, shape asymmetry recovers more mergers than its light-weighted asymmetry counterparts A and A_O; the lowest completeness is 20% at a depth of 23 mag arcsec^{-2} and a PSF FWHM of 1.5 arcsec is ~ 20 times higher than that of outer asymmetry. At the best image quality tested, shape asymmetry has a completeness of 26%. This indicates that shape asymmetry produces samples that are always more complete

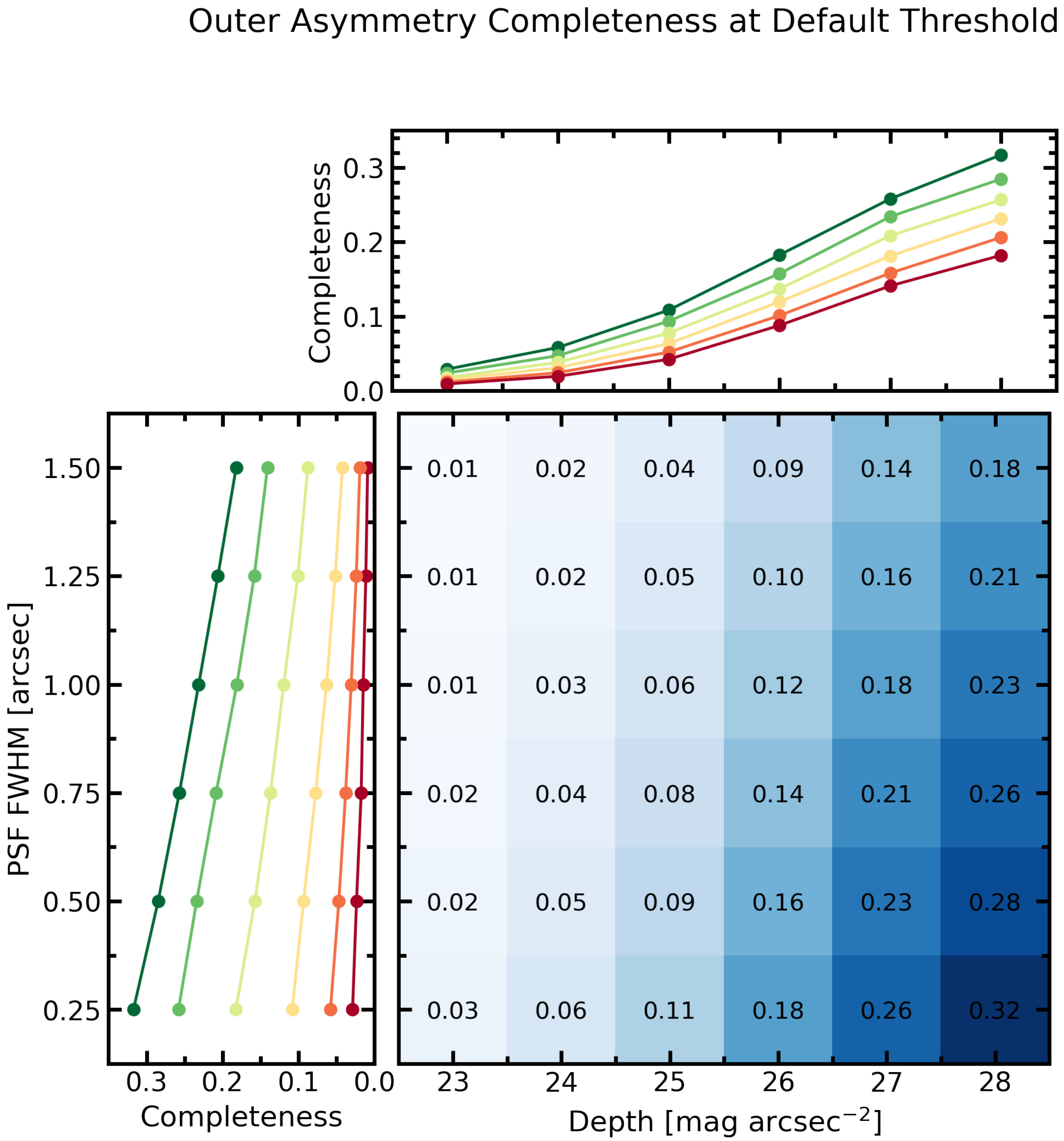

Figure 3.8: The completeness of recovered mergers using outer asymmetry with the default threshold ($A_O > 0.35$). In the bottom right panel, the colour gradient shows the completeness as a function of both depth and PSF blurring, with specific completeness values at each image quality reported in the corresponding cell. The top panel shows the relationship between completeness and depth, with each line representing a different PSF FWHM. The lines are coloured from red to yellow to green with red indicating the worst image quality (highest PSF FWHM) and green indicating best image quality (lowest PSF FWHM). The left panel shows the relationship between completeness and resolution, with each line representing a different depth. These lines are also coloured from red to yellow to green with red indicating the worst image quality (lowest depth) and green indicating best image quality (high depth).

than asymmetry, but at higher depths and resolutions, outer asymmetry identifies more mergers than shape asymmetry. Unlike asymmetry and outer asymmetry, shape asymmetry completeness does not have simple trends with depth and PSF blurring.

The effect of PSF blurring on completeness, depends on whether the imaging is deep or shallow. In relatively deep imaging (25-28 mag arcsec^{-2}), there is no trend between shape asymmetry completeness and the degree of PSF blurring. This is because beyond some level of depth, the shape of a galaxy is dictated primarily by its large-scale structure (i.e. tidal tails, disrupted asymmetric stellar halo) which are fairly robust to changes under a relatively small (for the size of structure) perturbation. In relatively shallow imaging (23-24 mag arcsec^{-2}), PSF blurring has a strong effect on the likelihood of a merger being detected; at a depth of 23 mag arcsec^{-2} the completeness ranges from 20% (the lowest for this metric) to 29% (the highest for this metric) over the span of the PSF FWHM changing from 1.5 arcsec to 0.25 arcsec. The trend with PSF blurring in this depth regime is caused by both the regularization of broad structures and bright internal asymmetric features which dictate the measured shape of the galaxy at low depths. To demonstrate this effect, I show one example of an IllustrisTNG100 post-merger galaxy imaged with low depth (23 mag arcsec^{-2}) and varying degrees of PSF blurring in Figure 3.10. Using the shape asymmetry masks calculated by `statmorph`, one can observe how the PSF blurring causes the post-merger to become undetected at PSF FWHMs higher than 0.75 arcsec due to the regularization of the shape decreasing the shape asymmetry value. However, this trend is not ubiquitous on a galaxy-by-galaxy basis. For example, the galaxy in Figure 3.11 shows that there is some intrinsic stochasticity in which pixels are identified as belonging to the shape asymmetry mask, regardless of the amount of blurring.

Pawlik et al. (2016) states that for galaxies with faint asymmetric features, shape asymmetry will increase with increased depth and will be therefore more likely to be detected as a merger in deeper imaging. However, the results presented in the top panel of Figure 3.9 indicate the relationship between merger completeness and depth of the imaging is not monotonic, but more complicated than previous works would suggest.

My results indicate that the claims made by Pawlik et al. (2016) are correct, but only within a range of image qualities similar to that used in their work (SDSS imaging). At image qualities similar to that of SDSS (PSF FWHMs from 1-1.5 arcsec and sky noise from 23-25 mag arcsec^{-2}) the number of mergers identified by shape

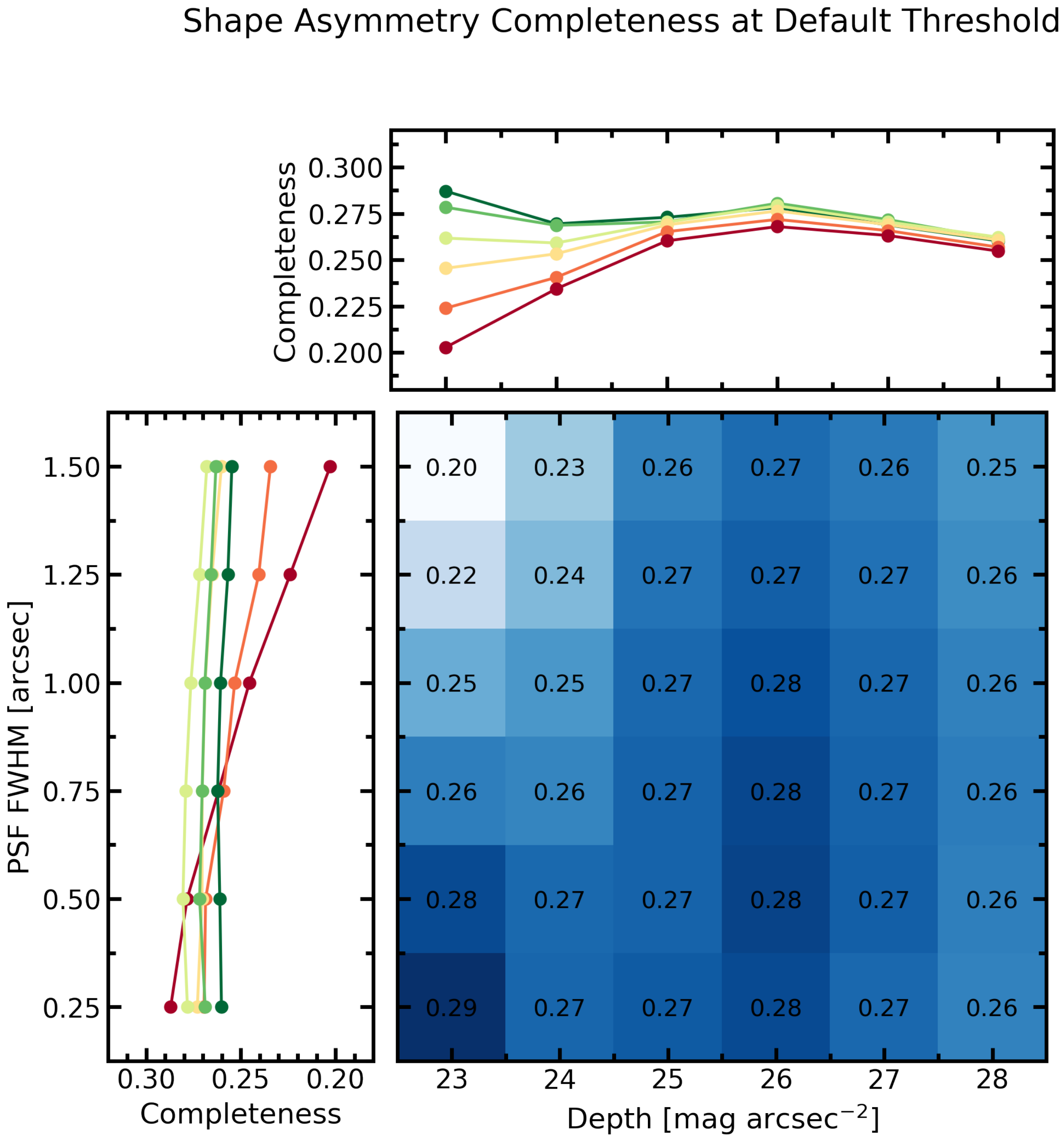

Figure 3.9: The completeness of recovered mergers using shape asymmetry with the default threshold ($A_S > 0.4$). In the bottom right panel, the colour gradient shows the completeness as a function of both depth and PSF blurring, with specific completeness values at each image quality reported in the corresponding cell. The top panel shows the relationship between completeness and depth, with each line representing a different PSF FWHM. The lines are coloured from red to yellow to green with red indicating the worst image quality (highest PSF FWHM) and green indicating best image quality (lowest PSF FWHM). The left panel shows the relationship between completeness and resolution, with each line representing a different depth. These lines are also coloured from red to yellow to green with red indicating the worst image quality (lowest depth) and green indicating best image quality (high depth).

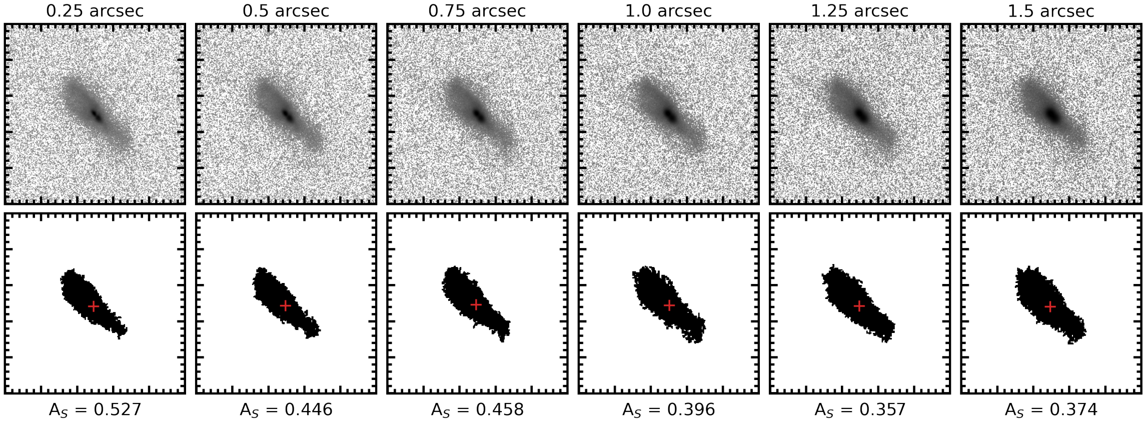

Figure 3.10: Example images and `statmorph`-derived shape asymmetry masks for an IllustrisTNG100 post-merger (snapshot 51, subhalo 206347) imaged at a low depth (23 mag arcsec^{-2}) and varying degrees of PSF blurring (FWHMs of 0.25 arcsec to 1.5 arcsec). The top panels are the 50 arcsec FOV synthetic images passed to `statmorph` with the PSF FWHM listed above. The bottom panels are the shape asymmetry masks computed as an intermediate step by `statmorph` when determining the shape asymmetry which are listed below. The red markers indicate the coordinates around which the shape asymmetry is measured. This example shows that PSF blurring can reduce the values of shape asymmetry.

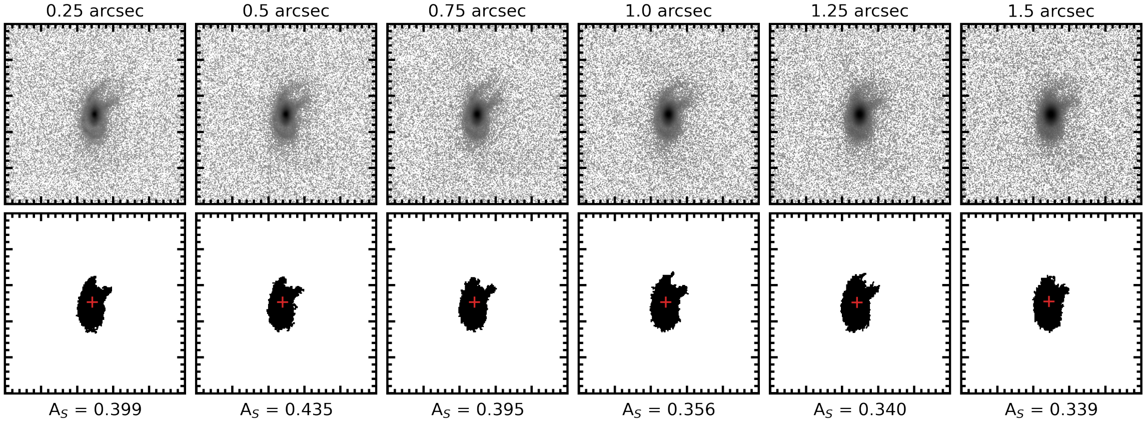

Figure 3.11: Example images and `statmorph`-derived shape asymmetry masks for an IllustrisTNG100 post-merger (snapshot 51, subhalo 264522) imaged at a low depth (23 mag arcsec^{-2}) and varying degrees of PSF blurring (FWHMs of 0.25 arcsec to 1.5 arcsec). The top panels are the 50 arcsec FOV synthetic images passed to `statmorph` with the PSF FWHM listed above. The bottom panels are the shape asymmetry masks computed as an intermediate step by `statmorph` when determining the shape asymmetry which are listed below. The red markers indicate the coordinates around which the shape asymmetry is measured. This example shows that an increase in PSF blurring does not directly correspond to a decrease in shape asymmetry values in all cases, but rather that there is some intrinsic stochasticity to which pixels belong to the galaxy.

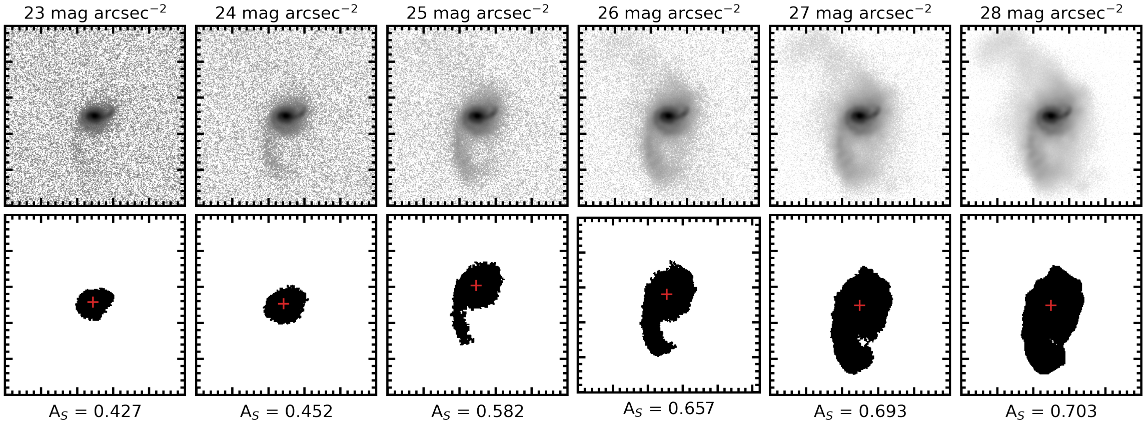

Figure 3.12: Example images and `statmorph`-derived shape asymmetry masks for an IllustrisTNG100 post-merger (snapshot 50, subhalo 277118) imaged with a PSF FWHM of 0.75 arcsec and varying depths from 23-28 mag arcsec^{-2}. The top panels are the 50 arcsec FOV synthetic images passed to `statmorph` with the PSF FWHM listed above. The bottom panels are the shape asymmetry masks computed as an intermediate step by `statmorph` when determining the shape asymmetry which are listed below. The red markers indicate the coordinates around which the shape asymmetry is measured. This example shows that the shape asymmetry measurement of galaxies which exhibit faint asymmetric features *without* stellar halos *increase* as depth is increased.

asymmetry does increase with depth. In this regime, faint large-scale asymmetric structures are being revealed as merger features. In Figure 3.12, I present an example of a merger with faint tidal features that are not included in the shape asymmetry calculation at low depths, but are included at higher depths.

However, given the quality of imaging available to Pawlik et al. (2016), they could not predict that using deeper imaging would decrease the number of mergers detected by shape asymmetry, as indicated by the turnover in completeness at 26 mag arcsec^{-2}. In deep imaging, the number of mergers decreases because many mergers have faint and symmetric stellar halos in addition to tidal tails and internal disturbances which may be picked up in shallower imaging. An example of this effect is presented in Figure 3.13 which shows a galaxy with a tidal tail and a faint stellar halo. As the depth is increased, the symmetric faint stellar halo is revealed and the shape asymmetry decreases.

The results presented in this subsection demonstrate that the relationship between the ability to detect a merger with shape asymmetry and the image quality of the galaxy merger is quite complicated. At different image qualities, different merger

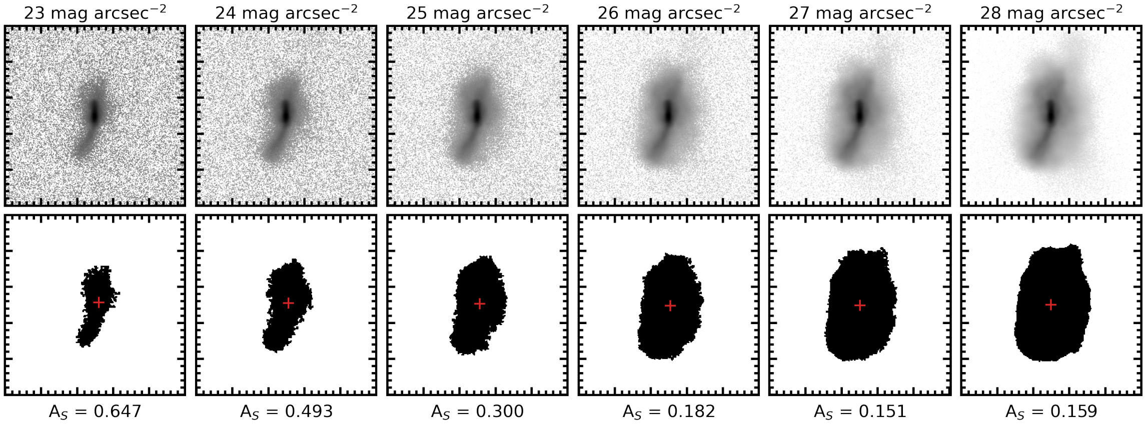

Figure 3.13: Example images and `statmorph`-derived shape asymmetry masks for an IllustrisTNG100 post-merger (snapshot 50, subhalo 222023) imaged with a PSF FWHM of 0.75 arcsec and varying depths from 23-28 mag arcsec^{-2}. The top panels are the 50 arcsec FOV synthetic images passed to `statmorph` with the PSF FWHM listed above. The bottom panels are the shape asymmetry masks computed as an intermediate step by `statmorph` when determining the shape asymmetry which are listed below. The red markers indicate the coordinates around which the shape asymmetry is measured. This example shows that the shape asymmetry measurement of galaxies which exhibit faint asymmetric features *with* stellar halos *decrease* as depth is increased.

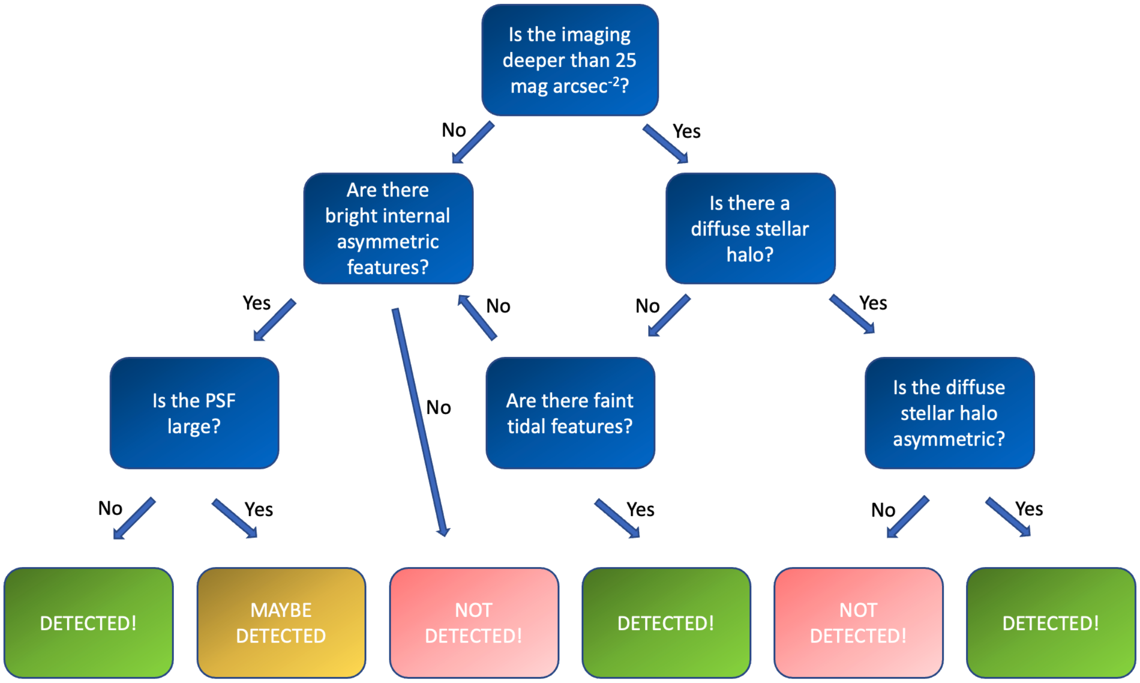

Figure 3.14: A flow chart describing the combination of merger features and image qualities that allow a merger to be detected with shape asymmetry.

features may cause shape asymmetry to detect or not detect the merger. For the readers' reference, I have assembled a series of questions into a flow chart in Figure 3.14 which should help a shape asymmetry user understand what combinations of merger features and imaging properties will allow a merger to be detected.

Gini-M$_{20}$ Merger Statistic

In Figure 3.15, I present the completeness of the merger sample recovered using the threshold $S(G, M_{20}) > 0$ as a function of depth and PSF blurring. It is evident from the gradient in the bottom right panel that there is a strong increasing trend of completeness as PSF blurring is decreased, and a weaker decreasing trend of completeness as depth is increased. As a result, the highest completeness (37%, higher than any other metric at any image quality) occurs at the lowest PSF blurring and the lowest depth. The lowest completeness (8%) occurs at the highest PSF blurring and in the deepest imaging.

The left panel of Figure 3.15 shows that the completeness achieved by the Gini-M$_{20}$ merger statistic increases exponentially as the resolution of the synthetic images

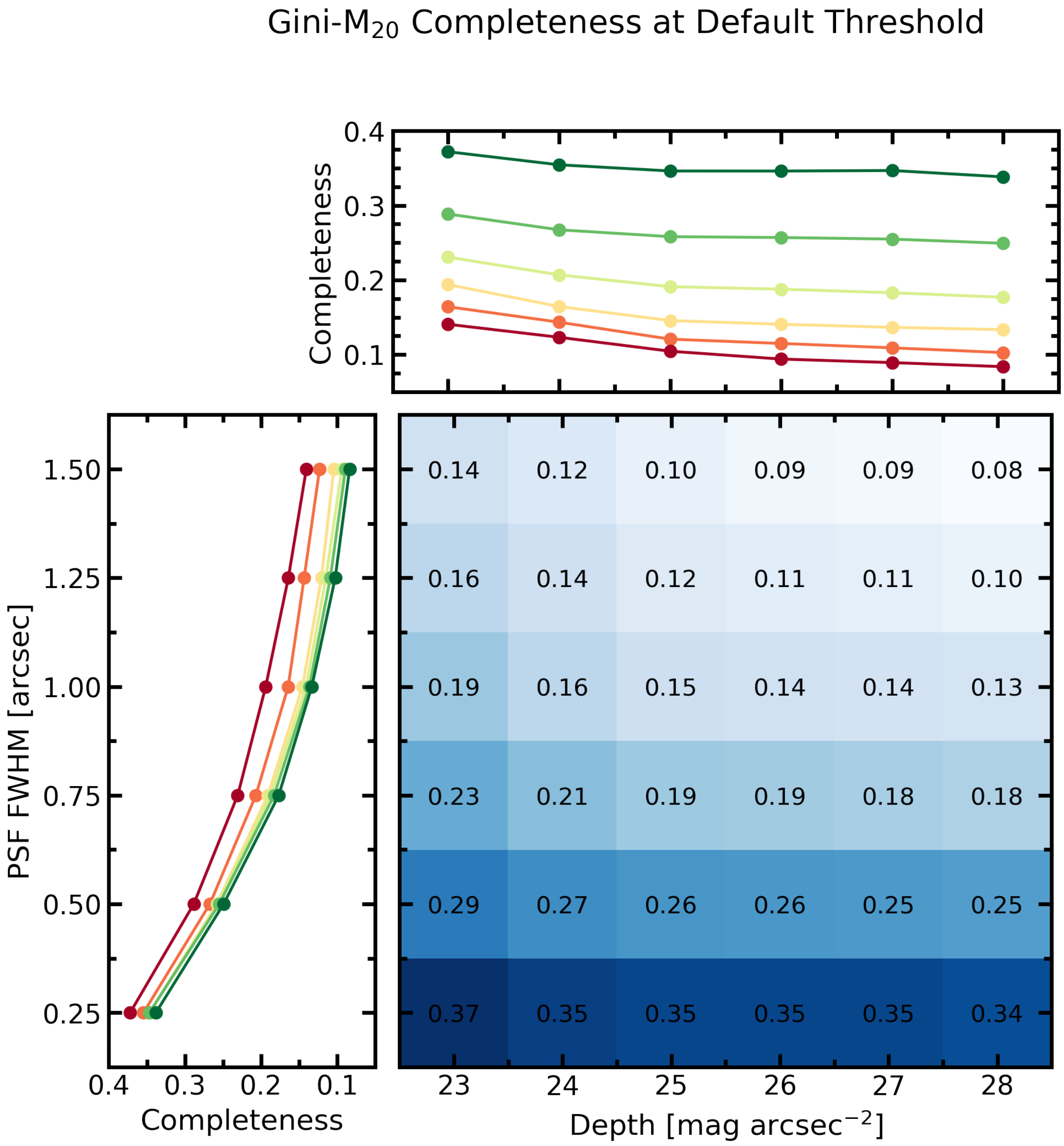

PSF FWHM [arcsec]	23	24	25	26	27	28
1.50	0.14	0.12	0.10	0.09	0.09	0.08
1.25	0.16	0.14	0.12	0.11	0.11	0.10
1.00	0.19	0.16	0.15	0.14	0.14	0.13
0.75	0.23	0.21	0.19	0.19	0.18	0.18
0.50	0.29	0.27	0.26	0.26	0.25	0.25
0.25	0.37	0.35	0.35	0.35	0.35	0.34

Figure 3.15: The completeness of recovered mergers using the Gini-M_{20} merger statistic with the default threshold ($S(G, M_{20}) > 0$). In the bottom right panel, the colour gradient shows the completeness as a function of both depth and PSF blurring, with specific completeness values at each image quality reported in the corresponding cell. The top panel shows the relationship between completeness and depth, with each line representing a different PSF FWHM. The lines are coloured from red to yellow to green with red indicating the worst image quality (highest PSF FWHM) and green indicating best image quality (lowest PSF FWHM). The left panel shows the relationship between completeness and resolution, with each line representing a different depth. These lines are also coloured from red to yellow to green with red indicating the worst image quality (lowest depth) and green indicating best image quality (high depth).

increases. Fewer mergers are identified in blurred images because both Gini and M_{20} decrease due to blurry imaging. Gini will decrease because blurring the image distributes the same amount of flux over a larger number of pixels. M_{20} decreases because it is sensitive to the spatial variance and precise location of the brightest pixels containing 20% of the flux which becomes regularized in the presence of PSF blurring.

The top panel of Figure 3.15 demonstrates that there is a trend, albeit it a very weak one, of decreasing completeness as the depth of the imaging improves. Depth has very little effect on the Gini-M_{20} merger statistic as the statistic is mostly sensitive to the distribution of the brightest pixels in the image. Increasing the depth of the image increases the number of faint pixels detected as belonging to the galaxy. Increasing the number of faint pixels affects the numerator and denominator in the M_{20} equation (see Equation 1.6). The denominator, M_{tot}, will increase slightly as the additional pixels will be faint but highly extended from the centre. The numerator of M_{20} may increase slightly since the 20% of the total flux would become a slightly larger flux and would thus include more pixels in the sum. It is unclear if this would increase or decrease M_{20} and may change on a galaxy-by-galaxy basis. On the other hand, increasing the number of faint pixels will slightly increase the value of Gini since the bright pixels containing most of the flux remain unchanged but now contain more light per pixel relative to the rest of the galaxy.

3.4 How Merger Properties Affect the Completeness of Recovered Mergers

In the previous section, I have critically assessed the completeness of a sample of mergers degraded to various levels of image quality. However, it has been previously observed that other factors such as stellar mass, mass ratio, orbital and dynamic characteristics and gas fraction can also affect the observability of a recent merger (Bell et al. 2006; Lotz et al. 2010a,b; Snyder et al. 2019; Nevin et al. 2019; McElroy et al. 2022). In this section, I break down the merger sample from the previous section into smaller groups based on the mass ratio of the merger (Section 3.4.1) and the stellar mass of the post-merger (Section 3.4.2) to explore how each of these properties affect the merger's likelihood of being detected by each of the non-parametric morphology statistics (and how these properties have contributed to the trends observed in Section

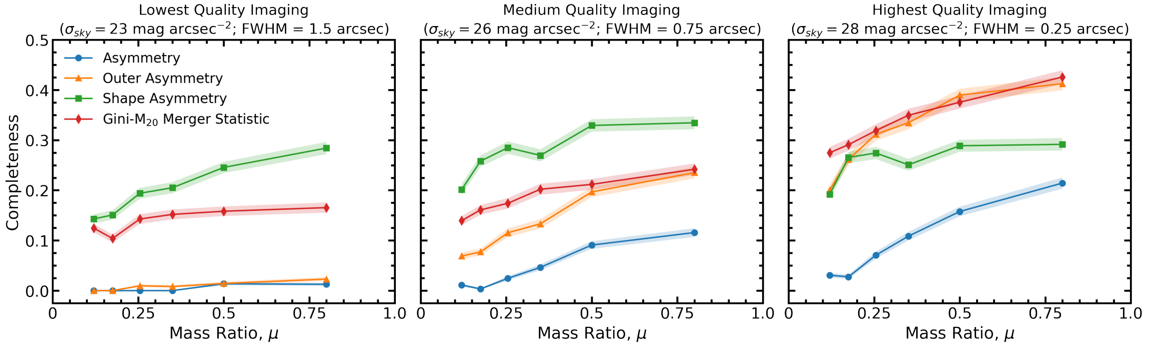
Lowest Quality Imaging (σ_{sky} = 23 mag arcsec^{-2}; FWHM = 1.5 arcsec)
Medium Quality Imaging (σ_{sky} = 26 mag arcsec^{-2}; FWHM = 0.75 arcsec)
Highest Quality Imaging (σ_{sky} = 28 mag arcsec^{-2}; FWHM = 0.25 arcsec)

Figure 3.16: The completeness of the detected mergers using four non-parametric morphology statistics and their default thresholds binned by the mass ratio of the galaxy mergers. The completeness is calculated in an adaptive binning scheme that allows the size of the bins to change in order to maintain equal number of galaxy images (~ 1400) in each bin. The left panel shows the completeness trends for asymmetry (blue circles), outer asymmetry (orange triangles), shape asymmetry (green squares) and the Gini-M_{20} merger statistic (red diamonds) at the lowest image quality tested (23 mag arcsec^{-2} sky noise and 1.5 arcsec PSF FWHM). The same trends are shown in middle panel but for medium image quality (26 mag arcsec^{-2} sky noise and 0.75 arcsec PSF FWHM) and in the right panel for the highest quality imaging tested (28 mag arcsec^{-2} sky noise and 0.25 arcsec PSF FWHM).

3.3).

3.4.1 Mass Ratio of Merger

The mass ratio of the two progenitor galaxies can have a significant impact on the observed morphology and therefore, their ability to be detected as mergers. In general, galaxies with mass ratios closer to one will have more significant and longer lasting morphological disturbances (Lotz et al. 2010b; Casteels et al. 2014b; Ji et al. 2014; Nevin et al. 2019). In Figure 3.16, I present the completeness of the detected merger sample in bins of mass ratio according to each of the non-parametric morphology statistics used for identifying mergers and at three different image qualities. Bins of mass ratio change in size in order to preserve a roughly equal number of galaxies in each bin. The shaded area around each curve corresponds to the standard error in the median, calculated using binomial counting statistics as in Equation 2.4. In general, my results show that *higher mass ratio mergers are more likely to be detected by non-parametric merger indicators immediately after coalescence*. However, the degree to which completeness and mass ratio are correlated depends on the quality of imaging and each individual metric.

In the left panel of Figure 3.16, the completeness of the recovered mergers as determined using each of the four metrics applied to the lowest quality imaging (23 mag arcsec^{-2} depth and 1.5 arcsec PSF FWHM). Too few mergers are identified by either of the light-weighted asymmetry metrics (A and A_O) to observe any trend between completeness and mass ratio. While this is expected given that asymmetry and outer asymmetry had a completeness of less than 1% in Figures 3.7 and 3.8, it is surprising that effectively no mergers, even in the highest mass ratio bin, are detected using these metrics. Gini-M_{20} has a completeness of $\sim$ 10% with no trend with mass ratio at this image quality. Finally, shape asymmetry, which was the best performing metric at low image qualities in Section 3.3, shows a linear trend of increasing completeness with increasing mass ratio. As a result, the major mergers are approximately twice as likely to be identified by shape asymmetry than minor mergers.

In the centre panel of Figure 3.16, I show the completeness of the recovered mergers as determined using each of the four metrics applied to intermediate-quality imaging (26 mag arcsec^{-2} depth and 0.75 arcsec PSF FWHM). In this case, all of the metrics have curves that are higher than in the lower quality imaging, consistent with the trends observed in Section 3.3. Once a baseline quality of imaging is met, all non-parametric morphology indicators exhibit a similar trend of increasing completeness with increasing mass ratio, but with different vertical offsets.

In the right panel of Figure 3.16, the completeness of the recovered mergers as determined using each of the four metrics applied to the highest quality imaging (28 mag arcsec^{-2} depth and 0.25 arcsec PSF FWHM). At high image quality, asymmetry, outer asymmetry and the Gini-M_{20} merger statistic have overall higher completeness (consistent with the results in Section 3.3) and the completeness of these merger indicators is still positively correlated with mass ratio. Asymmetry, outer asymmetry and the Gini-M_{20} merger statistic all have larger slopes in the higher image quality indicating that increase in image quality preferentially enhances the completeness of more major mergers. While asymmetry has higher completeness in all mass ratio bin at this higher image quality relative to the intermediate image quality, it still identified fewer than 5% of minor mergers in the two lowest mass ratio bins. Notably, outer asymmetry and the Gini-M_{20} merger statistic improve and surpass shape asymmetry, identifying a statistically equivalent number of mergers in all mass ratio bins above 0.25. Shape asymmetry decreases its completeness overall (consistent with the results in Section 3.3) and maintains a similar relationship between completeness and mass ratio. The constant relationship indicates the decrease in completeness from increased image quality effects mergers of all mass ratios equally (i.e. major or minor mergers do not preferentially cause specific features like diffuse stellar halos which decrease shape asymmetry in deeper imaging).

3.4.2 Total Stellar Mass of Merger

Another important property of galaxies for measuring morphology and studying galaxy evolution in general is the total stellar mass of the system. In Figure 3.17, I present the completeness of the detected merger sample in bins of total stellar mass of the system according to each of the non-parametric morphology statistics used for identifying mergers and at three different image qualities. Bins of stellar mass are adaptive in order to preserve a roughly equal number galaxies in each bin. The shaded area around each curve corresponds to the standard error in the median, calculated using binomial counting statistics as in Equation 2.4.

Figure 3.17 demonstrates that once a baseline quality of imaging is met, *high mass post-mergers are less likely to be detected than low-mass post-mergers.* This effect is not due to a bias in mass ratio in any of the bins as the mean mass ratio is approximately constant (~ 0.3) and the number of major mergers ($\mu > 0.25$) is actually higher in the highest mass bin than in the lowest mass bin. It could instead be caused by the intrinsic morphology of high mass galaxies, low gas fractions, or orbital dynamics of mergers in cluster environments.

3.4.3 Gas Content of Merger

Another driving property of galaxy morphology and evolution is the availability of star-forming gas (Bell et al. 2006; Lotz et al. 2010a). Star-forming gas content is measured here using the gas fraction, f_{gas}. The gas fraction is defined here, following Equation 1.10, as the total mass of gas particles within twice the half-mass radii[6] divided by the total baryonic mass (gas and stellar mass) within the same radius. In Figure 3.18, I present the completeness of the detected merger sample in bins of gas fraction according to each of the non-parametric morphology statistics used for

---

[6] The half-mass radius is the radius of a sphere around the centre of the subhalo which contains half the total stellar mass of the subhalo. In practice, galaxies in IllustrisTNG100 have significant reservoirs of gas (but not much stellar mass) beyond this radius that are still associated with the subhalo. I do not include this gas mass as I am interested in the gas immediately available to form stars.

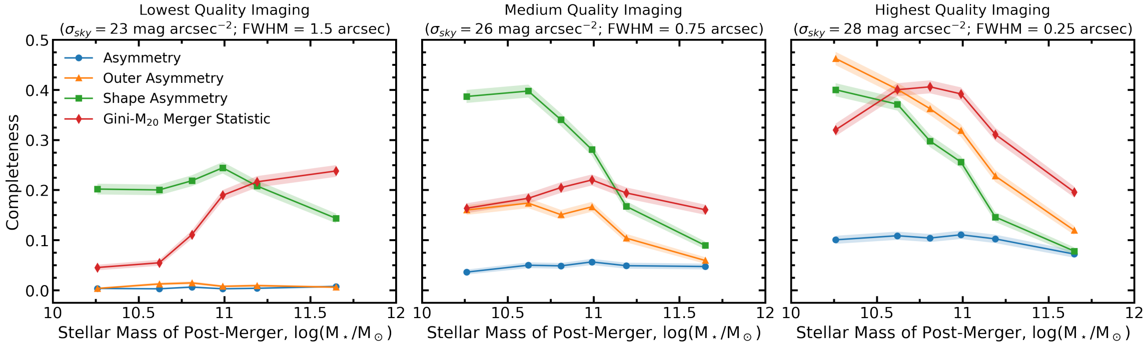

Figure 3.17: The completeness of the detected mergers using four non-parametric morphology statistics and their default thresholds binned by the total stellar mass of the galaxy mergers. The completeness is calculated in an adaptive binning scheme that allows the size of the bins to change in order to maintain equal number of galaxy images ($\sim$ 1400) in each bin. The left panel shows the completeness trends for asymmetry (blue circles), outer asymmetry (orange triangles), shape asymmetry (green squares) and the Gini-M$_{20}$ merger statistic (red diamonds) at the lowest image quality tested (23 mag arcsec^{-2} sky noise and 1.5 arcsec PSF FWHM). The same trends are shown in middle panel but for medium image quality (26 mag arcsec^{-2} sky noise and 0.75 arcsec PSF FWHM) and in the right panel for the highest quality imaging tested (28 mag arcsec^{-2} sky noise and 0.25 arcsec PSF FWHM).

identifying mergers and at three different image qualities. As in Figures 3.16 and 3.17, the bins are adaptive in order to preserve a roughly equal number galaxies in each bin and the shaded area around each curve corresponds to the standard error in the median, calculated using binomial counting statistics as in Equation 2.4.

Figure 3.18 demonstrates that once a baseline quality of imaging is met, *mergers with higher gas contents are more likely to exhibit asymmetric morphologies indicative of a recent merger (as quantified by* A*,* A_S *and* A_O*)*. However, there does not appear to be a strong relationship between gas fraction and the merger completeness using the Gini-M_{20} merger statistic; at all three image qualities presented in Figure 3.18, the Gini-M_{20} merger statistic is comparable in the highest and lowest gas fraction bins within $\sim 5\%$.

The most surprising feature in Figure 3.18 is the Gini-M_{20} merger statistic completeness in the lowest gas fraction bin in varying image quality. In lower and medium quality imaging, the Gini-M_{20} merger statistic completeness in the lowest gas fraction bin (approximately 8% and 17%, respectively) is systematically lower than the higher gas fraction bins. However, in the highest quality imaging, the relationship flips and the highest Gini-M_{20} merger statistic completeness is in the lowest gas fraction bin ($\sim 40\%$), which happens to be roughly double the completeness of shape asymmetry and outer asymmetry at the same image quality and gas fraction bin. This effect is almost certainly related to the fact that more massive galaxies tend to have lower gas fractions (see Figure 3.3) and that the Gini-M_{20} merger statistic was shown to out-perform the other merger identification methods at high mass (see Figure 3.17). Thus, it seems that the Gini-M_{20} merger statistic is particularly potent at identifying massive, gas-poor mergers while the asymmetry statistics are more effective at identifying lower mass, gas-rich mergers. This result is consistent with the findings of (Lotz et al. 2010a) who find the merger observability timescales of Gini-M_{20} to be *shorter* and Asymmetry to be *longer* in mergers with higher gas fractions.

3.5 The Effect of Viewing Angle on Morphology and Completeness

In Figure 3.6, I showed that even in ideal imaging, the maximum completeness using any of the non-parametric morphology statistics 39%. In more realistic imaging, the completeness of detected mergers lower and shown range from 1% to 37% depending

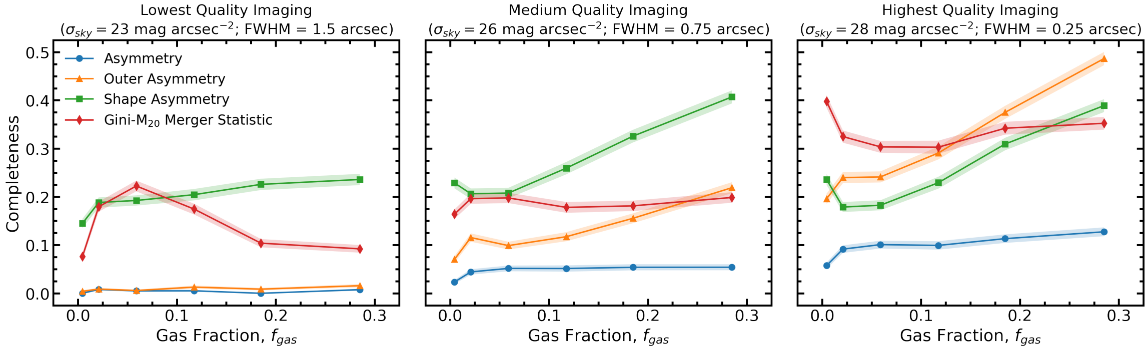

Figure 3.18: The completeness of the detected mergers using four non-parametric morphology statistics and their default thresholds binned by the gas fraction of the merger remnant immediately after coalescence. The completeness is calculated in an adaptive binning scheme that allows the size of the bins to change in order to maintain equal number of galaxy images ($\sim$ 1400) in each bin. The left panel shows the completeness trends for asymmetry (blue circles), outer asymmetry (orange triangles), shape asymmetry (green squares) and the Gini-M$_{20}$ merger statistic (red diamonds) at the lowest image quality tested (23 mag arcsec^{-2} sky noise and 1.5 arcsec PSF FWHM). The same trends are shown in middle panel but for medium image quality (26 mag arcsec^{-2} sky noise and 0.75 arcsec PSF FWHM) and in the right panel for the highest quality imaging tested (28 mag arcsec^{-2} sky noise and 0.25 arcsec PSF FWHM).

on the image quality and merger identification method. To better understand the low values of completeness accomplished by the merger identification methods used in this work, even in the best case scenarios, I explore the dependence of merger observability on the viewing angle from which the imaging is generated. To begin, I generate synthetic imaging for 41 of the 2119 IllustrisTNG mergers following the methods discussed in Section 3.2, but with 648 viewing angles instead of four[7]. The viewing angles are placed 10 degrees apart in inclination (from $-90°$ to $90°$) and azimuth (from $-180°$ to $180°$) for a total of $36 \times 18 = 648$ viewing angles. Unlike the four viewing angles used in the main analysis of this work, the small differences in viewing angle used here are used to show the gradual change in observed morphology. For this test, the images are generated with a PSF FWHM of 0.75 arcsec and depth of 26 mag arcsec^{-2}.

In Figure 3.19 I present the relationship between the measured non-parametric morphology statistics asymmetry, outer asymmetry, shape asymmetry and the Gini-M$_{20}$ merger statistic and the angle from which the galaxy is observed for one example post-merger galaxy. This post-merger (snapshot 50, subhalo 222023) has a total stellar mass of $7.4{\times}10^{10} M_{\odot}$ and has undergone a merger with a mass ratio of 0.4 within the last snapshot of the simulation ($t_{\rm postmerger} \lesssim 162$ Myr). The map in each panel of Figure 3.19 shows a 2-D Aitoff projection of the morphology statistic coloured using Gouraud shading[8]. In each panel, the morphology is shown to vary drastically with viewing angle. At some viewing angles, a morphology statistic is not above the default merger threshold and therefore would not be detected as a merger. Viewing angles for which the morphology statistic is below the merger threshold are indicated by black hatch marks. The number of viewing angles for which this galaxy would be detected as a merger is indicated in the bottom right corner of each panel[9].

Looking at the trends in each panel, it is interesting to note how each morphology statistic is spatially correlated. For example, asymmetry and outer asymmetry (in the first and second panels) both have low asymmetry values in repeating lobes and high asymmetry in a band of inclination (reaching from pole to pole in the case of outer asymmetry) over a relatively narrow window of azimuthal angle. In the case of

---

[7] Repeating this analysis for all 2119 mergers is inhibited by computational resources.

[8] Gouraud shading is built in to the `matplotlib` `pcolormesh` function and determines the colour of each grid point by linearly interpolating from the corners of each grid in the mesh.

[9] Since the viewing angles are evenly spaced in azimuth and inclination, angles at high inclinations subtend less solid angle than those at low inclination. When determining the number of viewing angles above the merger threshold, the viewing angles are weighted by $\cos(\theta)$ to account for the difference in solid angle.

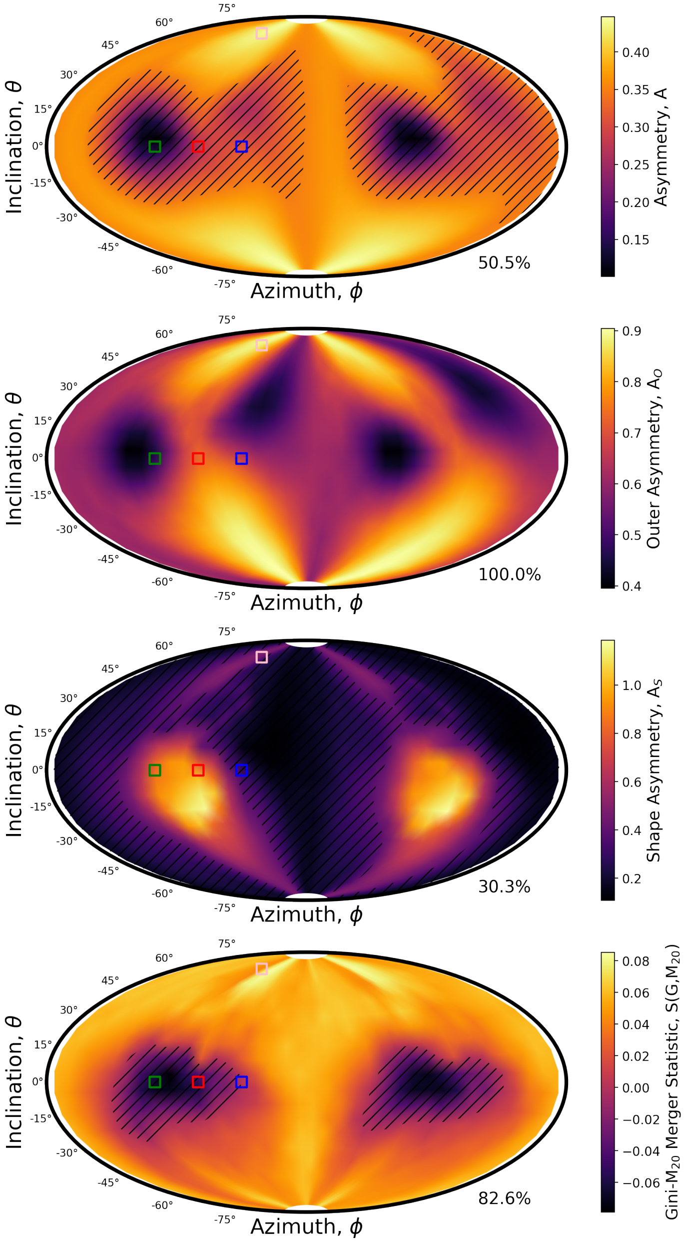

Figure 3.19: An example of the variation of the non-parametric morphology measurements over all viewing angles for one IllustrisTNG100 post-merger (snapshot 50, subhalo 222023). The measurements are made in 10° increments in azimuth and inclination. The maps are generated using an Aitoff projection of a sphere to 2-D and smoothed using Gouraud shading. The asymmetry (first panel), outer asymmetry (second panel), shape asymmetry (third panel) and Gini-M_{20} merger statistic (fourth panel) at each viewing angle is indicated by the colour gradient and quantified by the colour bars on the right of each plot. Viewing angles where the morphology statistic are below the default merger threshold are demarcated by black hatches and the fraction of viewing angles where the morphology statistic is above the default merger threshold is given in the bottom right. Coloured squares denote the viewing angles of the example images in Figure 3.20.

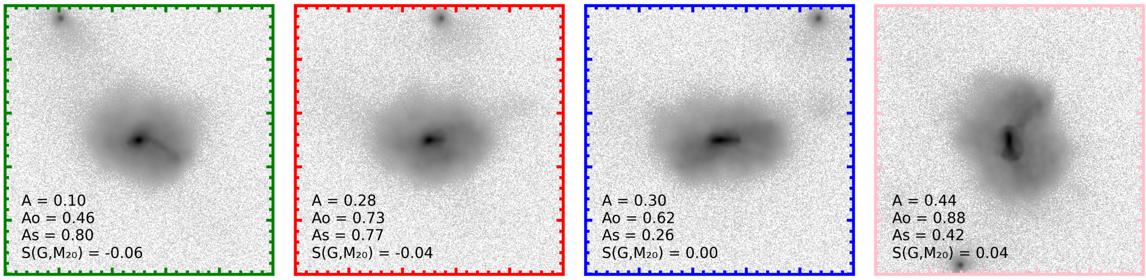

Figure 3.20: Four example images of the same IllustrisTNG100 post-merger from Figure 3.19(snapshot 50, subhalo 222023) taken from four different viewing angles. The colour of the axes surrounding the images corresponds to the colour of the boxes in Figure 3.19 denoting the viewing angle of the galaxy. The green, red, and blue images are at equal inclinations and separated in azimuthal angle by 30° each such that the green and blue images are 60° apart. The pink square is at a similar azimuthal angle as the green square but offset in inclination by 70°. The corresponding morphology statistics are shown in the bottom left corner of each image.

outer asymmetry, the statistic never gets low enough to not be detected as a merger. The repeated trend in azimuthal angle seen in each panel is caused by the fact that viewing a galaxy from opposite sides creates mirror images that are morphologically equivalent. Looking at the bottom panel, the Gini-M_{20} merger statistic is low (indeed, below the default merger threshold) in approximately the same regions as asymmetry and outer asymmetry. In contrast, the third panel shows that at the same viewing angles where asymmetry, outer asymmetry and the Gini-M_{20} merger statistic are at their lowest, shape asymmetry is at its highest and above the default merger threshold. This test, for one example galaxy merger, demonstrates that *the measured morphology of a galaxy, and therefore its detected merger status, is dependent upon the angle from which the merger is viewed.*

In Figure 3.20, I present four example images of the example galaxy tested in Figure 3.19 at a few interesting viewing angles. The colour of the axes around each galaxy images corresponds to the coloured boxes in Figure 3.19 which indicate the orientation of the viewing angle. The red, green, and blue images are at equal inclination and separated in viewing angle by 30° such that the green and blue images are separated by a total of 60°. The pink image is at a similar azimuthal angle as the green image but offset in inclination by 70°. The corresponding morphology statistics are displayed in the lower left corner of each image. For this galaxy, all of the example viewing angles are detected as a merger by at least one method. However, merger features are only obvious in the green and pink examples. In particular, the red example shows almost no merger features and may be misclassified as a non-merger by visual inspection or machine learning methods. Therefore, Figure 3.20 indicates that *there may be an upper limit to the completeness of detected mergers that can be achieved*; if merger features of real galaxies happen to be oriented such that they are not visible from the viewing angle of Earth, those mergers may never be detected.

Thus far in this section, the test results shown in Figures 3.19 and 3.20 are limited to a single IllustrisTNG100 galaxy. Generating 648 synthetic images and processing them with `statmorph` for all mergers drawn from IllustrisTNG100 would be very computationally expensive. However, it is important to understand by how much different viewing angles effect merger detection on a broader statistical scale. For this reason, I repeat the analysis presented in Figure 3.19 for forty other galaxies. In Figure 3.21, I present the fraction of the 648 viewing angles[10] for which the each of the mergers is detected by each stastistic. Each panel of Figure 3.21 represents a different non-parametric morphology statistic and each bar indicates the number of angles each of the forty test galaxies is detected as a merger. The IllustrisTNG100 SubHaloID is used to specify each merger and is given along the x-axis of the bottom two panels. In the top left panel of Figure 3.21 it can be seen that asymmetry frequently detects the mergers in precisely none of the 648 viewing angles. In the cases where the merger is identified in at least one viewing angle, it is generally identified in 30-70% of viewing angles and rarely approaches 100%. In the other three panels, cases where the merger is detect in none of the viewing angles is rare, but the mergers are stil only identified in 30-70% of viewing angles and rarely 100%.

To corroborate the results in Figures 3.19 and 3.21 with an even larger statistical sample, I use the four viewing angles which have already been generated and processed with `statmorph` for all 2119 mergers. While four viewing angles for a single galaxy gives a much less detailed picture of how the morphology changes for a single galaxy, it does allow for a broad understanding of how ubiquitous and widespread the viewing angle limitation is across the entire merger sample. In Figure 3.22, I present the number of mergers which are detected in 0, 1, 2, 3 or 4 of the 4 viewing angles used in Sections 3.3 and 3.4. For the entire sample of IllustrisTNG100 mergers degraded to a depth of 26 mag arcsec^{-2} and PSF FWHM of 0.75 arcsec, asymmetry, outer asymmetry, shape asymmetry and the Gini-M$_{20}$ merger statistic identify mergers on average in 5%, 14%, 28% and 19% of viewing angles, respectively. However, it is apparent in all four panels of Figure 3.22 that a majority of the mergers are detected

---

[10] Weighted by $\cos\theta$.

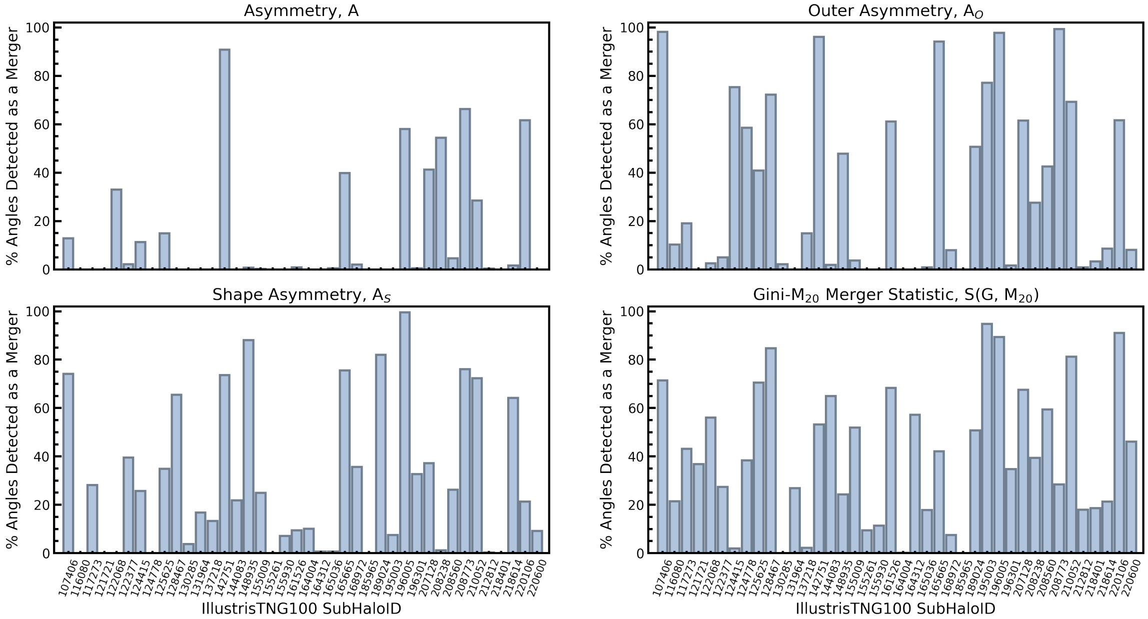

Figure 3.21: The fraction of viewing angles for which a merger is detected, as calculated using 648 viewing angles for forty different IllustrisTNG100 mergers. In each panel, the height of each bar represents the fraction of mergers a given IllustrisTNG100 merger (specified by its SubHaloID along the x-axis of the bottom two panels) is above the default merger threshold of the statistic stated at the top of each panel.

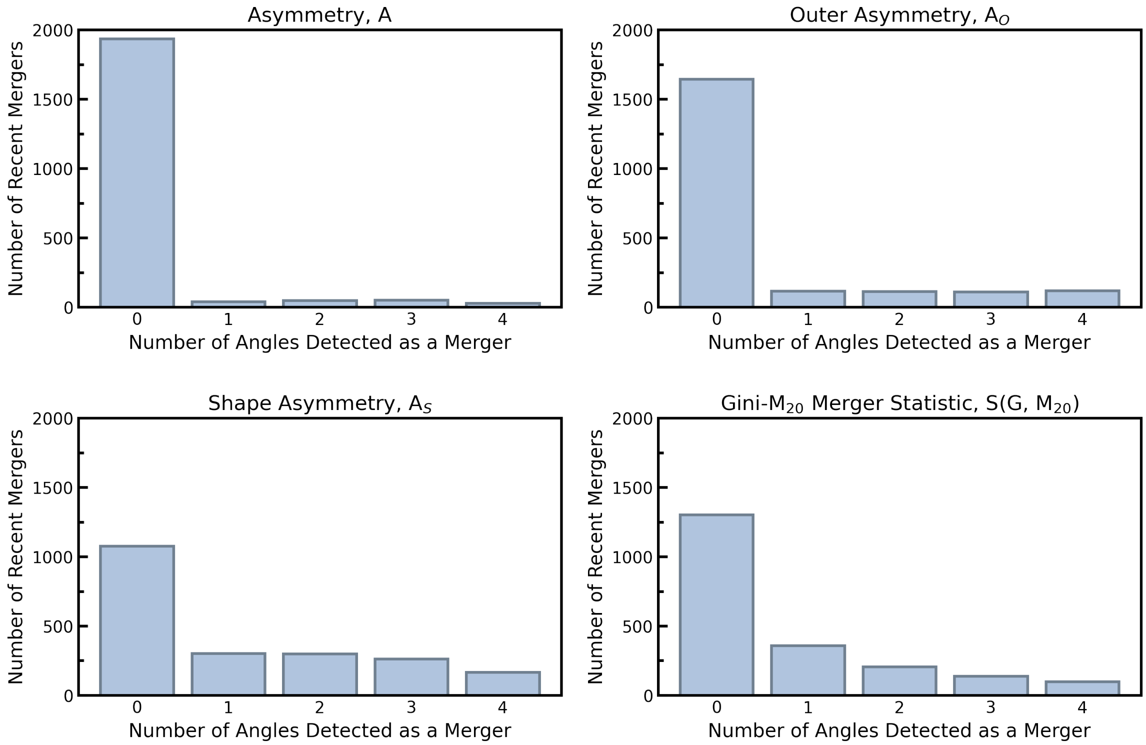

Figure 3.22: A histogram showing the number of IllustrisTNG100 mergers which were detected as a merger in 0, 1, 2, 3, or 4 of the four viewing angles generated for the entire merger sample (see Section 3.2).

in none of the four viewing angles. In mergers where at least one viewing angle is detected as a merger, asymmetry, outer asymmetry, shape asymmetry and the Gini-M_{20} merger statistic identify mergers on average in 60%, 63%, 57% and 49% of viewing angles. Thus, Figure 3.22 demonstrates that *the difference in completeness between different morphology statistics is driven by the ability of each metric to detect the specific type of merger feature present in the galaxy, but when a detectable merger feature is present, all metrics suffer equally from the fact that it may only be visible from a fraction of viewing angles.*

3.6 Chapter Summary

Several non-parametric morphology statistics have been developed for the purpose of identifying mergers (e.g. Conselice 2003; Lotz et al. 2004; Wen and Zheng 2016; Pawlik et al. 2016). Previous works have demonstrated that the measured morphology statistics of galaxies are affected by the quality of imaging used (e.g. Lotz et al.

2008; Pawlik et al. 2016; Thorp et al. 2021). However, the individual relationships between PSF blurring, depth and the number of mergers that are identified using these statistics has not been robustly quantified. In this chapter, I have tested how reliably these statistics can identify mergers using a sample of 2119 known mergers, free from observational degradation, from IllustrisTNG100. In Section 3.2, I describe how the simulation data is used to generate synthetic images of varying image quality. I generate synthetic images for the entire merger sample over a 6×6 grid of PSF blurring and depth, with PSF FWHMs ranging from 0.25-1.5 arcsec with depths ranging from 23-28 mag arcsec^{-2} (see Figure 3.4). The images were processed with `statmorph` and the measured non-parametric morphology statistics are used to quantify the completeness of the recovered merger sample. The main conclusions from this analysis are as follows:

- **In ideal imaging, free of atmospheric blurring and with minimal sky noise, the maximum completeness of the merger sample using non-parametric morphology statistics is 38.7%.** Specifically, asymmetry, outer asymmetry, shape asymmetry and the Gini-M$_{20}$ merger statistic had a completeness of 12.5%, 36.9%, 25.8% and 38.7% in the ideal imaging, respectively (see Section 3.3 and Figure 3.6).

- **Higher quality imaging often (but not always) allows more mergers to be identified, increasing the completeness of the sample.** Over the range of image qualities and morphology statistics tested, the completeness of recovered mergers ranged from 0.4% to 37%. All statistics had an increase in completeness from the lowest quality imaging to the highest quality imaging, but two out of four (shape asymmetry and the Gini-M$_{20}$ merger statistic) achieve the highest completeness at the highest resolution, but lowest depth imaging. This demonstrates that the relationship between the completeness, PSF blurring and depth, respectively, varies depending on the morphology statistic (see Section 3.3 and Figures 3.7-3.15).

- **In high quality imaging, mergers with a high mass ratio, a high gas fraction, and low total stellar mass are more likely to be detected.** This is ubiquitous across all merger identification statistics tested in this work, but the degree to which this relationship is true depends on image quality and the statistic (See Section 3.4 and Figures 3.16-3.18).

- **There is an upper limit on the completeness of recovered mergers caused by merger features not appearing in all viewing angles.** In an intermediate image quality, mergers were only recovered, on average, in 5-28% of viewing angles, depending on the morphology statistic. In cases where a merger was detected in least one viewing angle, only 49-65% of viewing angles could be recovered as mergers (See section 3.5 and Figure 3.19).

Chapter 4

Future Work and Summary

For the purpose of better understanding the mechanisms causing rapid quenching of galaxy in the local Universe, in Chapter 2 I introduced three methods of detecting mergers: non-parametric morphology statistics (asymmetry, outer asymmetry, shape asymmetry, and the Gini-M_{20} merger statistic), CNN classification, and visual inspection. In Chapter 3 the ability of each non-parametric morphology statistic to recover recent mergers (within one snapshot of the simulation) was critically assessed as a function of image quality. There exist three key elements of this analysis that merit further work and development, which will be discussed in this chapter. In Section 4.1, I discuss the construction of experiments yet to be conducted which will explore the effect of image quality on the ability of a CNN classifier and human inspection to detect mergers. In Section 4.2 I discuss the utility of radiative transfer simulations in past and future experiments. Finally, in Section 4.3, I discuss the effect of the elapsed time since coalescence on the likelihood of a galaxy being detected at various image qualities.

4.1 Quantifying the Completeness of CNN- and Visually-Identified Mergers with IllustrisTNG

In Sections 3.3 and 3.4, I presented the relationships between completeness of the recovered merger sample and image quality and characteristics of the merger itself for four non-parametric morphology statistics commonly used to identify mergers. The synthetic imaging of IllustrisTNG100 post-merger galaxies (see Sections 3.1, 3.1.1, and 3.2) also allows for an assessment of the CNN classification and visual inspection methods introduced in Section 2.2. However, an assessment of the CNN and visual inspection methods throughout a range of image qualities requires a more complex and detailed analysis than the non-parametric morphology statistics, which will be discussed in detail in this section.

The Completeness of CNN-identified Mergers in Various Image Qualities

Applying the trained CNN from Bickley et al. (2021) to the synthetic images of IllustrisTNG100 mergers is, in theory, be a relatively trivial exercise. The images would simply need to be down-sampled to a lower resolution to match the input format of the CNN and the CNN would provide a probability of a post-merger prediction with minimal computational expense. The problem with this approach is that the CNN is trained specifically to identify mergers at the image quality of CFIS with real CFIS skies, including survey artefacts, foreground stars and other contaminants. Recent works on the machine learning approach to galaxy merger classification have noted the importance of training the neural network on the specific observational effects expected in your classification experiment to a network's performance (Bottrell et al. 2019; Ćiprijanović et al. 2021). Therefore, assessing the performance of a CNN trained to identify mergers at a range of different image qualities (none of which the network was specifically trained on) cannot be interpreted as the network's capabilities. Consider that at higher image qualities, the galaxies may have more information (shape of diffuse stellar halo) that the network was not trained to identify as (non-)merger features. Similarly, at low image qualities, some fainter merger features may not be observable, but a greater emphasis on internal disturbances during training may allow for better network performance. Thus, regardless of the image quality considered, an accurate interpretation of the network performance requires re-training the CNN following the methods of Bickley et al. (2021) for that image specific quality. While this is deemed outside the scope of this thesis, it is the natural next step of this analysis.

In total, thirty-six independent CNNs will be trained, one for each image quality in the 6×6 grid of PSF FWHM and sky noise. Training each CNN will require the pre-existing 8,476 images of 2,119 mergers viewed along four viewing angles and a non-merger sample of equal size. Three of the four viewing angles of the mergers and non-mergers will be used in training, while the fourth viewing angle will be reserved for the completeness experiment. The CNN architecture will be preserved (as it has been shown to be effective) and, for simplicity of training so many networks, the hyperparameters of the network will kept constant. While the computation time required to train these networks provided the resources available to my research group is non-negligible (on the order of tens of hours to days), the more time consuming aspects will be preparing the data for the network and assessing the learning and performance of the networks. Even with the expertise in my research group, iterating on network training can take time and is not a process that should be rushed. This experiment, once completed, will provide a robust analysis of the relationship between completeness of mergers identified with a proven CNN architecture (and associated hyperparameters) and quality of imaging used. By direct comparison of these results to Figures 3.7-3.15, I will provide the community with an assessment of relative utility between classical non-parametric morphology methods and machine learning methods over a range of image qualities.

The Completeness of Visually-identified Mergers in Various Image Qualities

I also intend to repeat the analysis in Section 3.3 for the visual inspection method of identifying galaxy mergers by conducting an experiment wherein a small group of experts in the field of galaxy evolution are asked to identify the mergers in a sample of mergers and non-mergers. Since the objective of this experiment is to assess the efficacy of the visual inspection method of merger identification, the group of classifiers should reflect those that have conducted or could feasibly conduct merger classification as part of their own research. In practice, this will likely include 5-10 classifiers from my research group, close collaborators, and other graduate students working in my department. The classified merger sample must include a robust sampling of galaxy properties and span a range of PSF FWHMs and depths such that the average completeness achieved by the classifiers can be studied as a function of varying image quality.

Testing the observability of mergers in various image qualities by visual inspection has its own challenges to overcome that automated methods do not. The main problem is that, the statistically robust sample of galaxy mergers used in Chapter 3 is too large for individual human inspection. If four independent viewing angles of the 2119 galaxy mergers were classified at all thirty six image qualities, $4 \times 2119 \times 36 = 305,136$ mergers would have to be individually classified. Furthermore, since visual classification by humans is a subjective process, the mergers to be classified must be intermixed with non-mergers, otherwise the correct classification would be known by default. Therefore, the classification sample must be supplemented by roughly an equal number of non-mergers[1]. Using the same sample as in the analysis of Chapter 3, this would bring the total number of galaxies to be classified to ∼600,000. If a classifier averaged one classification per minute (obvious ones will be quicker than this, but edge-cases may take some time to consider), it would take ∼5000 hours (or ∼636 8-hour work days) to classify all of the galaxies. Clearly, this is not a feasible endeavour.

To make the visual classification experiment more reasonable, I will decrease the number of galaxy mergers classified and reduce the number of image qualities tested. The reasonable number of galaxies I could ask participants to classify is 2000 (including non-mergers and up to ∼1000 mergers). So instead of including the entire merger sample in each point of the grid of image qualities, the merger sample will be decreased from 2119 to ∼1000 and distributed evenly across the the grid of image qualities[2]. To avoid uncertainty in our results accrued by binomial counting statistics, the grid of image qualities will be reduced from 6×6 to 5×5 for this experiment, likely dropping the lowest quality depth and PSF blurring from the experiment. This would distribute ∼40 galaxies into each bin of PSF FWHM and depth, giving a maximum absolute uncertainty in completeness of less than 0.08. Taking the average completeness of recovered mergers in each bin of image quality will allow for a robust assessment of the effect of image quality on researchers' ability to identify mergers.

4.2 Improving Synthetic Imaging with Radiative Transfer Simulations

In Section 3.2, I discussed how previous works (e.g. Rodriguez-Gomez et al. 2019; Guzmán-Ortega et al. 2023) have shown that the visible-light morphologies of IllustrisTNG galaxies and real galaxies are generally comparable, even without the simulation of radiative transfer effects. However, using radiative transfer has been shown to produce morphologies that are, on average, more similar to the distributions of real galaxies (e.g. Rodriguez-Gomez et al. 2019; Guzmán-Ortega et al. 2023) but

---

[1] In practice, the classification sample will include 30-70% non-mergers and the proportion of mergers and non-mergers will not be revealed to the classifying participants.

[2] In practice, this will include only using one viewing angle of each merger and some failsafes in place to ensure an approximately even distribution of masses and mass ratios.

no study has shown the how the morphology of recent mergers, in particular, may be effected on a galaxy-by-galaxy basis.

Since dust grains in the interstellar medium preferentially scatter blue light, starlight travelling through the interstellar medium of the observed galaxy is reddened by regions of high dust content. To determine the exact effects of this process on an observed 2-D image requires resolved co-spatial 3-D information of both the emitters (i.e. stars) and absorbers (i.e. dust) of visible light. For a simulated galaxy in IllustrisTNG, this is fulfilled by the locations of the star and gas particles with a conversion law between the gas density and metallicity and the number of dust particles in a cell (Camps and Baes 2015; Trayford et al. 2017). The amount of light absorbed will vary according to the amount of dust in a region. This calculation can be carried out using a radiative transfer simulation code such as SKIRT[3] (Baes et al. 2011; Camps and Baes 2015).

SKIRT takes as input text files containing the 3-D spatial coordinates of the star and gas particles, along with additional information such as the metallicity and age of the stellar populations. A SKIRT radiative transfer simulation of a given galaxy has four main stages. In the first stage, cells are generated according to the density of the gas in each region such that dense regions can be more accurately rendered. The second stage launches a user-specified number of photon packets per wavelength spanning a user-specified wavelength range from the stellar emission sources and into the 3-D space of the galaxy geometry. Once a photon packet is launched, a Monte Carlo algorithm follows the packets' movement through space and dictates if it is absorbed by a dust grain, scattered by a dust grain or travels through the system without interaction. The third stage, repeats this process but using the dust cells with absorbed photon packets as the emission sources[4]. Finally, when photons hit the camera at a user-specified location, they are recorded according to the user-specified cosmology and distance, field of view, and filter response curve (if broad band imaging is selected). The result is either a broadband image or datacube of flux per wavelength.

In Figure 4.1, I present an example of a recent merger from IllustrisTNG100 (snapshot 50, subhalo 195003) as generated by the "mass map" method outlined in Section 3.2 and using SKIRT. The SKIRT image is generated using Bruzual and

---

[3] The most recent verion of SKIRT is SKIRT9: https://skirt.ugent.be/root/_home.html

[4] In the SKIRT examples presented in Figures 4.1 and 4.2, this third phase is skipped as the light emitted by dust is expected to have little to no effect on the r-band morphology.

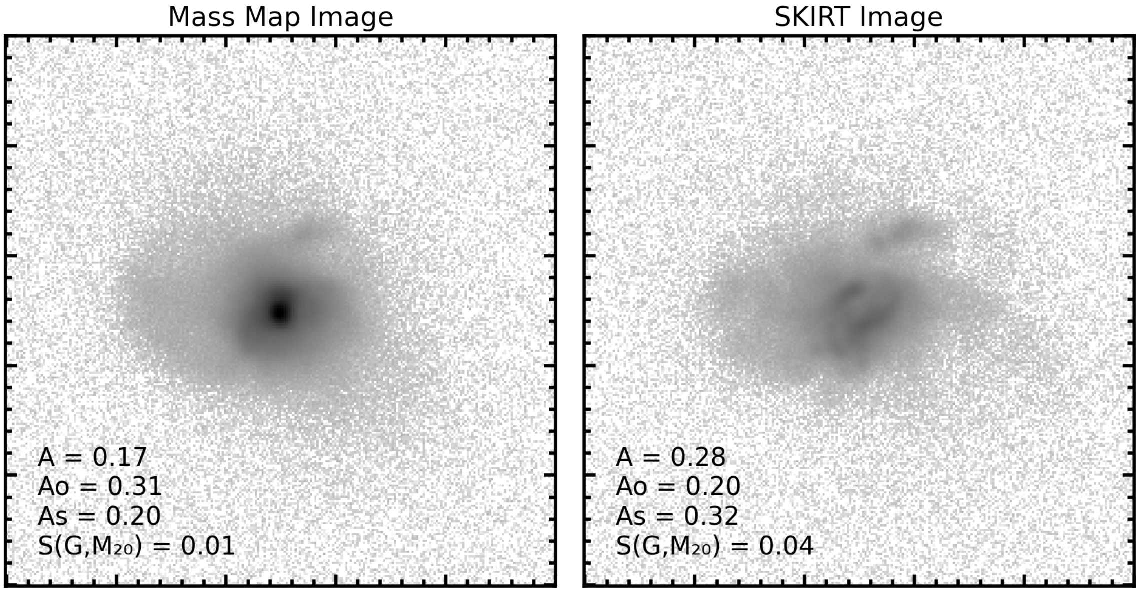

Figure 4.1: Example images of a recent merger from IllustrisTNG100 (snapshot 50, subhalo 195003) as generated by the "mass map" method outlined in Section 3.2 (left panel) and using SKIRT (right panel). The images are degraded with a PSF FWHM of 0.75 arcsec, a sky noise of 26 mag arcsec^{-2}, and to a pixel scale resolution of 0.2 arcsec pix^{-1}. The asymmetry, outer asymmetry, shape asymmetry and Gini-M_{20} merger statistic for each image are given in the bottom left corner of each panel. This figure demonstrates that accounting for dust attenuation with radiative transfer simulations can have a significant effect on the measured morphology of a galaxy.

Charlot (2003) models, the default mixed dust model and the CFHT MegaCam r-band filter response curve. Both r-band images are degraded with a PSF FWHM of 0.75 arcsec, a sky noise of 26 mag arcsec^{-2}, and to a pixel scale resolution of 0.2 arcsec pix^{-1}. Each image is processed with `statmorph` and the results for the four non-parametric morphologies used as merger indicators are displayed in the bottom left corner. Figure 4.1 demonstrates that the morphology of a galaxy merger may be quite different when using radiative transfer simulations to account for dust attenuation in the galaxy.

In Figure 4.2, I present a second example of a recent merger from IllustrisTNG100 (snapshot 51, subhalo 146024) comparing the morphology of the "mass map" method outlined in Section 3.2 and the image generated using SKIRT. In contrast to the example shown in Figure 4.1, the morphological differences between the two methods is minimal and, as a result, the non-parametric morphology statistics are relatively stable. This figure demonstrates that the degree to which radiative transfer may have

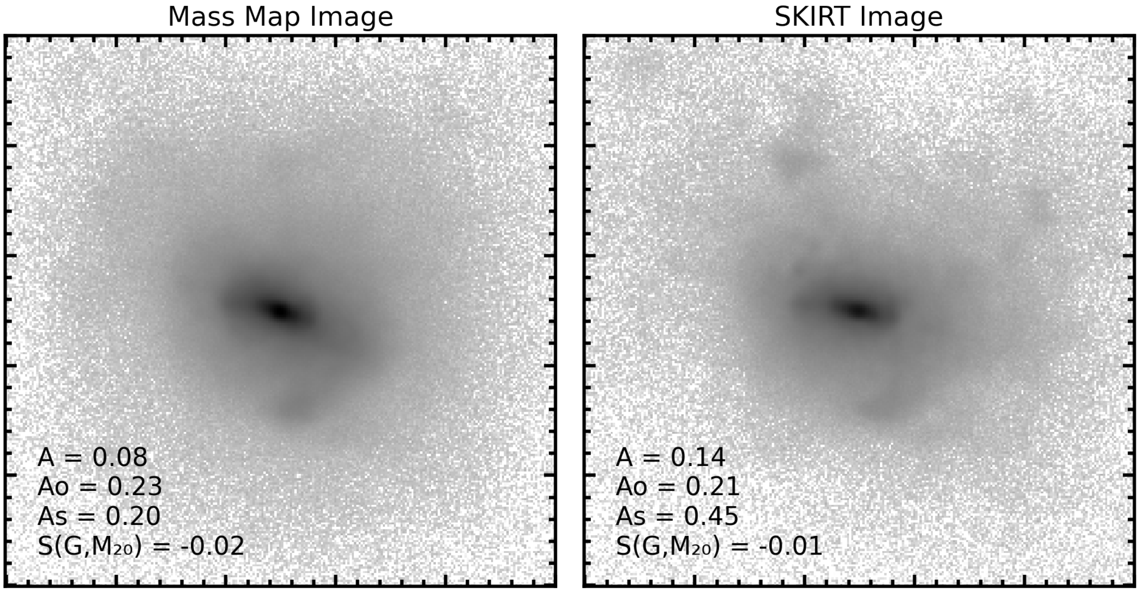

Figure 4.2: Example images of a recent merger from IllustrisTNG100 (snapshot 51, subhalo 146024) as generated by the "mass map" method outlined in Section 3.2 (left panel) and using SKIRT (right panel). The images are degraded with a PSF FWHM of 0.75 arcsec, a sky noise of 26 mag arcsec^{-2}, and to a pixel scale resolution of 0.2 arcsec pix^{-1}. The asymmetry, outer asymmetry, shape asymmetry and Gini-M_{20} merger statistic for each image are given in the bottom left corner of each panel. This figure demonstrates that accounting for dust attenuation with radiative transfer simulations does not always have a significant effect on the measured morphology of a galaxy.

an effect on the observed morphology of a galaxy, can vary from galaxy to galaxy.

In future work, I intend to include the effect of dust attenuation on the measured morphology and therefore merger detectability of mergers in IllustrisTNG and the merger suite introduced in Section 4.3 using SKIRT, as discussed in this section. Before SKIRT is integrated into my synthetic imaging pipeline, I will run statistical tests comparing the distribution of morphologies measured using `statmorph` on SKIRT images and compare them to real galaxy mergers. It is imperative I ensure that the inclusion of radiative transfer recreates the realistic morphologies comparable to that of real merging galaxies.

4.3 Pushing Beyond the Spatial and Temporal Resolution of IllustrisTNG

The analysis presented in Chapter 3 included only very recent mergers in IllustrisTNG100. However, previous works have shown that the observed morphology of galaxies are most disrupted in the first pericentre of the pair phase interaction and immediately after (or coincident with) coalescence (Lotz et al. 2008; Lotz et al. 2010a,b; Pawlik et al. 2018). After coalescence, the merger features have been estimated to fade in as little as 100 Myr (Nevin et al. 2019) and last as long as ∼6 Gyr (Ji et al. 2014) and ∼8 Gyr (Nevin et al. 2019), depending on the orientation, gas fraction, and mass ratio of the mergers (Lotz et al. 2008; Lotz et al. 2010a,b; Ji et al. 2014; Nevin et al. 2019; McElroy et al. 2022). Therefore, one of the most important factors to understanding the completeness of a merger sample, is the time after coalescence in which you observe the mergers. While previous studies have measured the effect of image quality on the morphology of merging galaxies (e.g. Lotz et al. 2004) and the effect of merger properties on the longevity of the merger features (e.g. Lotz et al. 2010a,b), no one has quantified the combined effect of time since coalescence and image quality on the observability of mergers.

In IllustrisTNG, the simulation data is only saved in coarse timesteps such that the time resolution between snapshots is on the order of 160 Myr at $z < 1$ of the simulation. For measuring the effects of time on the observability of features fading on the order of 1-3 snapshots, IllustrisTNG simply does not have sufficient time resolution to explore this effect. Indeed, all large-box cosmological simulations (which allow for a robust sampling of many merger orientations, gas fractions, mass ratios, etc.) are too large to save data in small time increments (e.g. Schaye et al. 2015).

To explore the combined effect of image quality and the time after coalescence of mergers on their observability, in future work I will use a suite of idealized, isolated mergers presented in Blecha et al. (2018). The suite of mergers includes 8 total mergers spanning a range of initial morphologies (in terms of bulge-to-disk ratios), mass ratios, and gas fractions. While the statistical sampling of mergers is much smaller, the time resolution is $\Delta t = 10$ Myr between snapshots, allowing for a more detailed analysis of the observability over time. The mergers are simulated using the galaxy simulation code `GADGET-3` (Springel et al. 2005). Similar to `AREPO`, `GADGET-3` solves the Poisson equation of gravity using the TreePM method, but unlike `AREPO`, `GADGET-3` solves the equations of hydrodynamics using smoothed particle hydrodynamics (SPH). The two codes also differ slightly in the implementation of unresolved sub-grid physics. The simulation suite has a baryonic mass resolution of 2.8×10^{5} $M_{\odot}$, 5× higher than that of IllustrisTNG100.

In Figures 4.3 and 4.4, I present an exploratory exercise regarding the observability of merger features using non-parametric morphologies as function of time before and after coalescence[5] using the merger suite from Blecha et al. (2018). In this example, two pure disk galaxies (i.e. bulge-to-total ratio equal to zero) with stellar masses of 3.9×10^{10} $M_{\odot}$ and 2.0×10^{10} $M_{\odot}$ (and therefore a mass ratio of 0.5) and gas fractions of 0.3 come together first as a pericentric passage and then a second time where the two galaxies coalesce. The morphologies presented in Figure 4.3 are computed using `statmorph` on SKIRT radiative transfer images degraded to an image quality with a depth of 25.4 mag arcsec^{-2} and a PSF blurring of 0.69 arcsec (i.e. CFIS-like imaging). Eight example images of the merger sequence are shown in Figure 4.4. In the three panels of Figure 4.3, you can see that the asymmetry, shape asymmetry, and Gini-M_{20} merger statistic increase above the default merger threshold in two main bouts, once around the time of the first pericentric passage and the second at coalescence (see also the corresponding images in the first column of each row in Figure 4.4). Each metric reaches its maximum value at different times and persists above the merger threshold for different durations of time. For example, shape asymmetry remains above the merger threshold for $\sim$ 500 Myr after coalescence, but asymmetry drops below the merger threshold in 50-150 Myr. However, looking at the second row and third column of Figure 4.4, it appears merger features which are not detected by the non-parametric morphology statistics may persist for more than 600 Myr after coalesce. Applying a CNN to these images, may allow for mergers to be detected for a longer duration. In all morphology statistics, there is stochasticity between the measurement of the metric between 10 Myr snapshots. The degree of stochasticity differs depending on the morphology statistic. The final study will include several viewing angles per snapshot over which the morphology metrics could be averaged and may reduce stochasticity in the measurement.

---

[5] For these mergers, I take the time of coalescence to be the snapshot at which the two black hole particles become one.

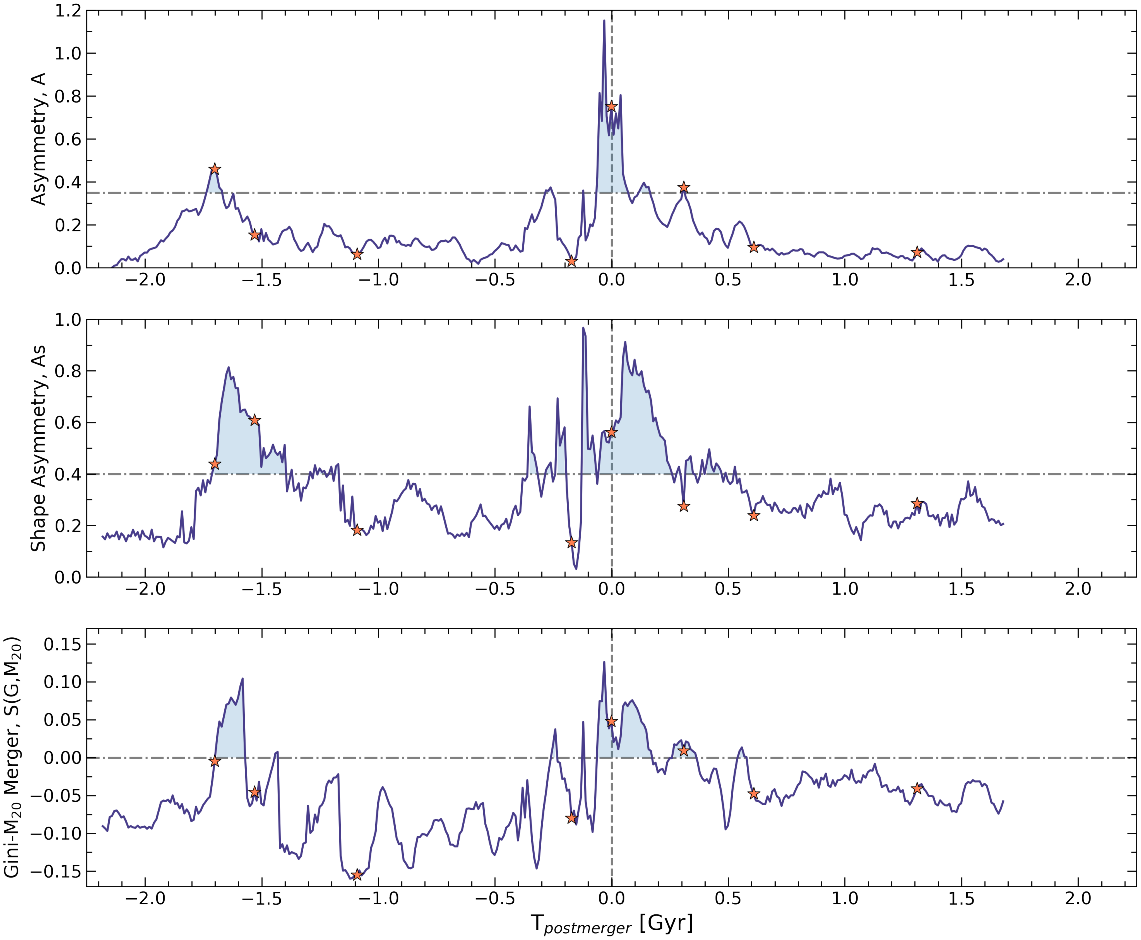

Figure 4.3: The variation of non-parametric morphology statistics indicative of merger calculated in 10 Myr intervals over a duration of ∼2 Gyr before and after coalescence of a major merger. The merger is of two pure disk galaxies with stellar masses of 3.9×10^{10} $M_\odot$ and 2.0×10^{10} $M_\odot$, giving a mass ratio of 0.5. Each have a gas fraction of 0.3 and a bulge-to-disk ratio of 0. Horizontal dot-dashed lines indicate the default merger detection threshold of each morphology statistic such that when the galaxy has a morphology above the line, it is detected as a merger. Shaded regions indicate the snapshots for which the merger is detected. Orange stars indicate snapshots where example images of the merger sequence are shown in Figure 4.4.

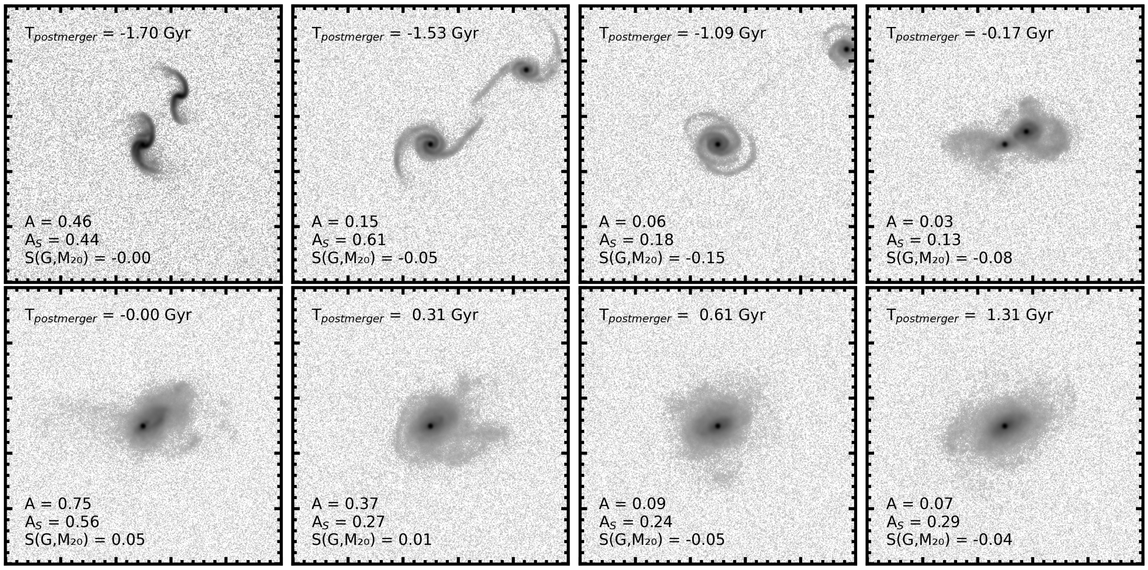

Figure 4.4: Eight example images of the merger sequence shown in Figure 4.3. The time with respect to the time of coalescence (such that negative values are before pre-coalescence) is shown in the top of each panel. The measured asymmetry, shape asymmetry, and Gini-M$_{20}$ merger statistic are shown in the bottom left corner of each panel.

4.4 Summary

In this body of work, I have sought a more accurate quantification of the contribution of galaxy mergers to rapid galaxy evolution in the local Universe. As a probe for rapidly evolving galaxies, I use post-starburst galaxies whose spectral features indicate a recent enhancement in star-formation followed by a prompt truncation of all star-forming activity (Dressler and Gunn 1983; Couch and Sharples 1987). Previous works had shown significant fractions of post-starburst galaxies have disturbed morphologies indicative of a recent merger or interaction (e.g. Zabludoff et al. 1996; Blake et al. 2004; Goto 2005; Yang et al. 2008; Pawlik et al. 2018; Sazonova et al. 2021), but consistently disagree on the precise fraction of post-starbursts with such features (see Figure 1.8). By conducting the most comprehensive assessment of the merger fraction of post-starburst galaxies to date, including a balance between sample size and image quality, a suite of merger identification methods, and a stellar mass- and redshift-matched control sample, I have addressed the weaknesses of previous works.

The results presented in Chapter 2 of this thesis have shown that there is no tension between previous studies at all, but rather that the merger fraction depends on the quality of imaging used to detect mergers, the merger detection technique, and the selection of the post-starburst sample (see Figure 2.16), each of which regularly differs between previous works. A metric that could be compared more reliably between studies is the excess merger fraction compared to a control sample following Equation 2.3, which accounts (to some degree) for the bias in merger identification method by applying it equally to the control sample. However, the excess merger fraction will still be sensitive to how the post-starburst and control samples are selected. Most studies do not compare to a matched control sample (e.g. Zabludoff et al. 1996; Blake et al. 2004; Goto 2005; Yang et al. 2008; Alatalo et al. 2016b) and those that do use controls (Pawlik et al. 2018; Sazonova et al. 2021) have not directly compared them in this way. I address this by reporting an excess merger fraction for each merger identification technique used. Using the ultra-pure, visually inspected CNN-predicted mergers as the positive merger detection criterion, the E+A and PCA PSB samples gives an excess merger fraction of 46 ± 22 and 29 ± 9, respectively. Thus, it is clear that mergers are a prevalent driving mechanism of post-starburst galaxies. However, the fact that merger fractions are less than 100%, opens the door to other causal mechanisms and/or mergers being unidentified due to the quality of imaging.

To test the effect of image quality on the observability of mergers, I turned to the

IllustrisTNG100 cosmological simulation. IllustrisTNG100 happens to include 2119 mergers between z=1 and z=0 of the simulation (see Section 3.1.1) for which there are no observational effects and merger properties are known with certainty (including mass ratio, gas fraction, etc.). Using four viewing angles for each merger, I generated 8,476 synthetic r-band images of the recent mergers drawn from IllustrisTNG100. The synthetic images of the mergers were degraded to various image qualities, adding observational effects such as sky noise and atmospheric blurring. However, since the mergers are selected in the snapshot immediately following coalescence when merger features are typically most evident (Lotz et al. 2008) and additional layers of observational realism (e.g. foreground stars, background galaxies) are not included, these images represent an optimistic best-case-scenario study of merger detection.

My intention here and in future work is to quantify the efficacy of all of the merger identification methods introduced in Section 1.2 and applied in Chapter 2. In Chapter 3, the efficacy of non-parametric morphology statistics used to identify mergers is quantified using the completeness of recovered mergers (see Equation 3.1) as a function of image quality, while the completeness of CNN and visual inspection methods are left for future work. The completeness of recovered mergers is shown to increase with improved image quality. However, even in ideal imaging where there is no atmospheric blurring and minimal sky noise, the maximum completeness of all mergers was shown to be only 39%. As a possible explanation for this, I show that the morphology and thus ability to detect mergers is affected by the viewing angle at which the merger is observed. Therefore, there may be many mergers that can never be detected simply due to the orientation of merger features and the viewing angle from Earth to the galaxy.

The completeness results presented in Chapter 3 (and future work discussed in Chapter 4) will be valuable to future studies attempting to quantify the number of mergers in a given sample of galaxies, as it allows one to estimate the number of missed mergers depending on the merger identification method implemented and quality of the imaging used. For example, comparing the completeness of a merger sample using the $A_S > 0.4$ merger criterion and CFIS-like imaging (25 mag arcsec^{-2} sky noise, 0.75 PSF FWHM), which is 27%, to the merger fraction of E+A PSBs using the same merger criterion in CFIS imaging, (26±3)%, one can see that the measured E+A PSB merger fraction is consistent with a sample of 100% mergers[6]. Furthermore, the lower merger fraction in the PCA PSBs, $f_{A_S} = (19 \pm 2)\%$, may also be consistent with a sample of 100% mergers but at a later post-coalescence epoch in which the merger features are less likely to be detected. This, and much more, will be explored in detail in future work.

---

[6] This statement is only strictly true in the absence of false positives, which I recognize I am neglecting here. As discussed earlier, it would be very challenging to quantify the expected purity of identified mergers if we do not know *a priori* the number of mergers and non-mergers in a PSB sample.

Bibliography

Abazajian, K. N., Adelman-McCarthy, J. K., Agüeros, M. A., Allam, S. S., Allende Prieto, C., An, D., Anderson, K. S. J., Anderson, S. F., Annis, J., Bahcall, N. A., Bailer-Jones, C. A. L., Barentine, J. C., Bassett, B. A., Becker, A. C., Beers, T. C., Bell, E. F., Belokurov, V., Berlind, A. A., Berman, E. F., Bernardi, M., Bickerton, S. J., Bizyaev, D., Blakeslee, J. P., Blanton, M. R., Bochanski, J. J., Boroski, W. N., Brewington, H. J., Brinchmann, J., Brinkmann, J., Brunner, R. J., Budavári, T., Carey, L. N., Carliles, S., Carr, M. A., Castander, F. J., Cinabro, D., Connolly, A. J., Csabai, I., Cunha, C. E., Czarapata, P. C., Davenport, J. R. A., de Haas, E., Dilday, B., Doi, M., Eisenstein, D. J., Evans, M. L., Evans, N. W., Fan, X., Friedman, S. D., Frieman, J. A., Fukugita, M., Gänsicke, B. T., Gates, E., Gillespie, B., Gilmore, G., Gonzalez, B., Gonzalez, C. F., Grebel, E. K., Gunn, J. E., Györy, Z., Hall, P. B., Harding, P., Harris, F. H., Harvanek, M., Hawley, S. L., Hayes, J. J. E., Heckman, T. M., Hendry, J. S., Hennessy, G. S., Hindsley, R. B., Hoblitt, J., Hogan, C. J., Hogg, D. W., Holtzman, J. A., Hyde, J. B., Ichikawa, S.-i., Ichikawa, T., Im, M., Ivezić, Ž., Jester, S., Jiang, L., Johnson, J. A., Jorgensen, A. M., Jurić, M., Kent, S. M., Kessler, R., Kleinman, S. J., Knapp, G. R., Konishi, K., Kron, R. G., Krzesinski, J., Kuropatkin, N., Lampeitl, H., Lebedeva, S., Lee, M. G., Lee, Y. S., French Leger, R., Lépine, S., Li, N., Lima, M., Lin, H., Long, D. C., Loomis, C. P., Loveday, J., Lupton, R. H., Magnier, E., Malanushenko, O., Malanushenko, V., Mandelbaum, R., Margon, B., Marriner, J. P., Martínez-Delgado, D., Matsubara, T., McGehee, P. M., McKay, T. A., Meiksin, A., Morrison, H. L., Mullally, F., Munn, J. A., Murphy, T., Nash, T., Nebot, A., Neilsen, Eric H., J., Newberg, H. J., Newman, P. R., Nichol, R. C., Nicinski, T., Nieto-Santisteban, M., Nitta, A., Okamura, S., Oravetz, D. J., Ostriker, J. P., Owen, R., Padmanabhan, N., Pan, K., Park, C., Pauls, G., Peoples, John, J., Percival, W. J., Pier, J. R., Pope, A. C., Pourbaix, D., Price, P. A., Purger, N., Quinn, T., Raddick, M. J., Re Fiorentin, P., Richards, G. T., Richmond, M. W., Riess, A. G., Rix, H.-W., Rockosi, C. M., Sako, M., Schlegel, D. J., Schneider, D. P., Scholz, R.-D., Schreiber, M. R., Schwope, A. D., Seljak, U., Sesar, B., Sheldon, E., Shimasaku, K., Sibley, V. C., Simmons, A. E., Sivarani, T., Allyn Smith, J., Smith, M. C., Smolčić, V., Snedden, S. A., Stebbins, A., Steinmetz, M., Stoughton, C., Strauss, M. A., SubbaRao, M., Suto, Y., Szalay, A. S., Szapudi, I., Szkody, P., Tanaka, M., Tegmark, M., Teodoro, L. F. A., Thakar, A. R., Tremonti, C. A., Tucker, D. L., Uomoto, A., Vanden Berk, D. E., Vandenberg, J., Vidrih, S., Vogeley, M. S., Voges, W., Vogt, N. P., Wadadekar, Y., Watters, S., Weinberg, D. H., West, A. A., White, S. D. M., Wilhite, B. C., Wonders, A. C., Yanny, B., Yocum, D. R., York, D. G., Zehavi, I., Zibetti, S., and Zucker, D. B. (2009). The Seventh Data Release of the Sloan Digital Sky Survey. *The Astrophysical Journals*, 182(2):543–558.

Abraham, R. G., Valdes, F., Yee, H. K. C., and van den Bergh, S. (1994). The Morphologies of Distant Galaxies. I. an Automated Classification System. *The Astrophysical Journal*, 432:75.

Abraham, R. G., van den Bergh, S., Glazebrook, K., Ellis, R. S., Santiago, B. X., Surma, P., and Griffiths, R. E. (1996). The Morphologies of Distant Galaxies. II. Classifications from the Hubble Space Telescope Medium Deep Survey. *The Astrophysical Journal Supplement Series*, 107:1.

Abruzzo, M. W., Narayanan, D., Davé, R., and Thompson, R. (2018). Identifying Mergers Using Quantitative Morphologies in Zoom Simulations of High-Redshift Galaxies. *arXiv e-prints*, page arXiv:1803.02374.

Alatalo, K., Cales, S. L., Rich, J. A., Appleton, P. N., Kewley, L. J., Lacy, M., Lanz, L., Medling, A. M., and Nyland, K. (2016a). Shocked POststarbust Galaxy Survey. I. Candidate Post-starbust Galaxies with Emission Line Ratios Consistent with Shocks. *The Astrophysical Journals*, 224(2):38.

Alatalo, K., Lisenfeld, U., Lanz, L., Appleton, P. N., Ardila, F., Cales, S. L., Kewley, L. J., Lacy, M., Medling, A. M., Nyland, K., Rich, J. A., and Urry, C. M. (2016b). Shocked POststarburst Galaxy Survey. II. The Molecular Gas Content and Properties of a Subset of SPOGs. *The Astrophysical Journal*, 827(2):106.

Amorín, R. O., Pérez-Montero, E., and Vílchez, J. M. (2010). On the Oxygen and Nitrogen Chemical Abundances and the Evolution of the “Green Pea” Galaxies. *The Astrophysical Journall*, 715(2):L128–L132.

Amorisco, N. C. (2015). On feathers, bifurcations and shells: the dynamics of tidal streams across the mass scale. *Monthly Notices of the Royal Astronomical Society*, 450(1):575–591.

Atkinson, A. M., Abraham, R. G., and Ferguson, A. M. N. (2013). Faint Tidal Features in Galaxies within the Canada-France-Hawaii Telescope Legacy Survey Wide Fields. *The Astrophysical Journal*, 765(1):28.

Baes, M., Nersesian, A., Casasola, V., Bianchi, S., Cassarà, L. P., Clark, C. J. R., De Looze, I., Dobbels, W., Fritz, J., Galametz, M., Galliano, F., Madden, S. C., Mosenkov, A. V., Viaene, S., Trčka, A., and Xilouris, E. M. (2020). Nonparametric galaxy morphology from UV to submm wavelengths. *Astronomy & Astrophysics*, 641:A119.

Baes, M., Verstappen, J., De Looze, I., Fritz, J., Saftly, W., Vidal Pérez, E., Stalevski, M., and Valcke, S. (2011). Efficient Three-dimensional NLTE Dust Radiative Transfer with SKIRT. *The Astrophysical Journals*, 196(2):22.

Baker, W. M., Maiolino, R., Bluck, A. F. L., Lin, L., Ellison, S. L., Belfiore, F., Pan, H.-A., and Thorp, M. (2022). The ALMaQUEST survey IX: the nature of the resolved star forming main sequence. *Monthly Notices of the Royal Astronomical Society*, 510(3):3622–3628.

Baldry, I. K., Glazebrook, K., Brinkmann, J., Ivezić, Ž., Lupton, R. H., Nichol, R. C., and Szalay, A. S. (2004). Quantifying the Bimodal Color-Magnitude Distribution of Galaxies. *The Astrophysical Journal*, 600(2):681–694.

Banerji, M., Lahav, O., Lintott, C. J., Abdalla, F. B., Schawinski, K., Bamford, S. P., Andreescu, D., Murray, P., Raddick, M. J., Slosar, A., Szalay, A., Thomas, D., and Vandenberg, J. (2010). Galaxy Zoo: reproducing galaxy morphologies via machine learning. *Monthly Notices of the Royal Astronomical Society*, 406(1):342–353.

Barbary, K. (2016). Sep: Source extractor as a library. *Journal of Open Source Software*, 1(6):58.

Barnes, J. E. and Hernquist, L. E. (1991). Fueling Starburst Galaxies with Gas-rich Mergers. *The Astrophysical Journall*, 370:L65.

Barton, E. J., Geller, M. J., and Kenyon, S. J. (2000). Tidally Triggered Star Formation in Close Pairs of Galaxies. *The Astrophysical Journal*, 530(2):660–679.

Beck, M. R., Scarlata, C., Fortson, L. F., Lintott, C. J., Simmons, B. D., Galloway, M. A., Willett, K. W., Dickinson, H., Masters, K. L., Marshall, P. J., and Wright, D. (2018). Integrating human and machine intelligence in galaxy morphology classification tasks. *Monthly Notices of the Royal Astronomical Society*, 476(4):5516–5534.

Bekki, K., Couch, W. J., Shioya, Y., and Vazdekis, A. (2005). Origin of E+A galaxies – I. Physical properties of E+A galaxies formed from galaxy merging and interaction. *Monthly Notices of the Royal Astronomical Society*, 359(3):949–965.

Bell, E. F., Naab, T., McIntosh, D. H., Somerville, R. S., Caldwell, J. A. R., Barden, M., Wolf, C., Rix, H.-W., Beckwith, S. V., Borch, A., Häussler, B., Heymans, C., Jahnke, K., Jogee, S., Koposov, S., Meisenheimer, K., Peng, C. Y., Sanchez, S. F., and Wisotzki, L. (2006). Dry Mergers in GEMS: The Dynamical Evolution of Massive Early-Type Galaxies. *The Astrophysical Journal*, 640(1):241–251.

Bendo, G. J. and Barnes, J. E. (2000). The line-of-sight velocity distributions of simulated merger remnants. *Monthly Notices of the Royal Astronomical Society*, 316(2):315–325.

Benitez-Llambay, A. (2015). Py-Sphviewer: Py-Sphviewer V1.0.0. Zenodo.

Benson, A. J. (2010). Galaxy formation theory. *Physics Reports*, 495(2-3):33–86.

Bertin, E. and Arnouts, S. (1996). SExtractor: Software for source extraction. *Astronomy & Astrophysics Supplement Series*, 117:393–404.

Bickley, R. W., Bottrell, C., Hani, M. H., Ellison, S. L., Teimoorinia, H., Yi, K. M., Wilkinson, S., Gwyn, S., and Hudson, M. J. (2021). Convolutional neural network identification of galaxy post-mergers in UNIONS using IllustrisTNG. *Monthly Notices of the Royal Astronomical Society*, 504(1):372–392.

Bickley, R. W., Ellison, S. L., Patton, D. R., Bottrell, C., Gwyn, S., and Hudson, M. J. (2022). Star formation characteristics of CNN-identified post-mergers in the Ultraviolet Near Infrared Optical Northern Survey (UNIONS). *Monthly Notices of the Royal Astronomical Society.*

Bickley, R. W., Ellison, S. L., Patton, D. R., and Wilkinson, S. (2023). AGNs in post-mergers from the ultraviolet near infrared optical northern survey. *Monthly Notices of the Royal Astronomical Society*, 519(4):6149–6161.

Bignone, L. A., Pedrosa, S. E., Trayford, J. W., Tissera, P. B., and Pellizza, L. J. (2020). Non-parametric morphologies of galaxies in the EAGLE simulation. *Monthly Notices of the Royal Astronomical Society*, 491(3):3624–3642.

Bignone, L. A., Tissera, P. B., Sillero, E., Pedrosa, S. E., Pellizza, L. J., and Lambas, D. G. (2017). Non-parametric morphologies of mergers in the Illustris simulation. *Monthly Notices of the Royal Astronomical Society*, 465(1):1106–1122.

Bílek, M., Duc, P.-A., Cuillandre, J.-C., Gwyn, S., Cappellari, M., Bekaert, D. V., Bonfini, P., Bitsakis, T., Paudel, S., Krajnović, D., Durrell, P. R., and Marleau, F. (2020). Census and classification of low-surface-brightness structures in nearby early-type galaxies from the MATLAS survey. *Monthly Notices of the Royal Astronomical Society*, 498(2):2138–2166.

Blake, C., Pracy, M. B., Couch, W. J., Bekki, K., Lewis, I., Glazebrook, K., Baldry, I. K., Baugh, C. M., Bland-Hawthorn, J., Bridges, T., Cannon, R., Cole, S., Colless, M., Collins, C., Dalton, G., De Propris, R., Driver, S. P., Efstathiou, G., Ellis, R. S., Frenk, C. S., Jackson, C., Lahav, O., Lumsden, S., Maddox, S., Madgwick, D., Norberg, P., Peacock, J. A., Peterson, B. A., Sutherland, W., and Taylor, K. (2004). The 2dF Galaxy Redshift Survey: the local E+A galaxy population. *Monthly Notices of the Royal Astronomical Society*, 355(3):713–727.

Blecha, L., Snyder, G. F., Satyapal, S., and Ellison, S. L. (2018). The power of infrared AGN selection in mergers: a theoretical study. *Monthly Notices of the Royal Astronomical Society*, 478(3):3056–3071.

Blumenthal, G. R., Faber, S. M., Primack, J. R., and Rees, M. J. (1984). Formation of galaxies and large-scale structure with cold dark matter. *Nature*, 311:517–525.

Blumenthal, K. A. and Barnes, J. E. (2018). Go with the Flow: Understanding inflow mechanisms in galaxy collisions. *Monthly Notices of the Royal Astronomical Society*, 479(3):3952–3965.

Blumenthal, K. A., Moreno, J., Barnes, J. E., Hernquist, L., Torrey, P., Claytor, Z., Rodriguez-Gomez, V., Marinacci, F., and Vogelsberger, M. (2020). Galaxy interactions in IllustrisTNG-100, I: The power and limitations of visual identification. *Monthly Notices of the Royal Astronomical Society*, 492(2):2075–2094.

Boselli, A., Fossati, M., and Sun, M. (2022). Ram pressure stripping in high-density environments. *Astronomy and Astrophysics Reviews*, 30(1):3.

Bottrell, C., Hani, M. H., Teimoorinia, H., Ellison, S. L., Moreno, J., Torrey, P., Hayward, C. C., Thorp, M., Simard, L., and Hernquist, L. (2019). Deep learning predictions of galaxy merger stage and the importance of observational realism. *Monthly Notices of the Royal Astronomical Society*, 490(4):5390–5413.

Bottrell, C., Hani, M. H., Teimoorinia, H., Patton, D. R., and Ellison, S. L. (2022). The combined and respective roles of imaging and stellar kinematics in identifying galaxy merger remnants. *Monthly Notices of the Royal Astronomical Society*, 511(1):100–119.

Bottrell, C., Simard, L., Mendel, J. T., and Ellison, S. L. (2019). Bulge plus disc and Sérsic decomposition catalogues for 16 908 galaxies in the SDSS Stripe 82 co-adds: a detailed study of the ugriz structural measurements. *Monthly Notices of the Royal Astronomical Society*, 486(1):390–413.

Bournaud, F., Combes, F., and Jog, C. J. (2004). Unequal-mass galaxy merger remnants: Spiral-like morphology but elliptical-like kinematics. *Astronomy & Astrophyics*, 418:L27–L30.

Bournaud, F., Jog, C. J., and Combes, F. (2005). Galaxy mergers with various mass ratios: Properties of remnants. *Astronomy & Astrophyics*, 437(1):69–85.

Boylan-Kolchin, M., Ma, C.-P., and Quataert, E. (2008). Dynamical friction and galaxy merging time-scales. *Monthly Notices of the Royal Astronomical Society*, 383(1):93–101.

Bridge, C. R., Carlberg, R. G., and Sullivan, M. (2010). The CFHTLS-Deep Catalog of Interacting Galaxies. I. Merger Rate Evolution to z = 1.2. *The Astrophysical Journal*, 709(2):1067–1082.

Brinchmann, J., Abraham, R., Schade, D., Tresse, L., Ellis, R. S., Lilly, S., Le Fèvre, O., Glazebrook, K., Hammer, F., Colless, M., Crampton, D., and Broadhurst, T. (1998). Hubble Space Telescope Imaging of the CFRS and LDSS Redshift Surveys. I. Morphological Properties. *The Astrophysical Journal*, 499(1):112–133.

Brinchmann, J., Charlot, S., White, S. D. M., Tremonti, C., Kauffmann, G., Heckman, T., and Brinkmann, J. (2004). The physical properties of star-forming galaxies in the low-redshift Universe. *Monthly Notices of the Royal Astronomical Society*, 351(4):1151–1179.

Brinchmann, J., Charlot, S., White, S. D. M., Tremonti, C., Kauffmann, G., Heckman, T., and Brinkmann, J. (2004). The physical properties of star-forming galaxies in the low-redshift Universe. *Monthly Notices of the Royal Astronomical Society*, 351(4):1151–1179.

Brown, T. M., Tumlinson, J., Geha, M., Simon, J. D., Vargas, L. C., VandenBerg, D. A., Kirby, E. N., Kalirai, J. S., Avila, R. J., Gennaro, M., Ferguson, H. C., Muñoz, R. R., Guhathakurta, P., and Renzini, A. (2014). The Quenching of the Ultra-faint Dwarf Galaxies in the Reionization Era. *The Astrophysical Journal*, 796(2):91.

Bruzual, G. and Charlot, S. (2003). Stellar population synthesis at the resolution of 2003. *Monthly Notices of the Royal Astronomical Society*, 344(4):1000–1028.

Buitrago, F., Trujillo, I., Conselice, C. J., and Häußler, B. (2013). Early-type galaxies have been the predominant morphological class for massive galaxies since only z $\sim$ 1. *Monthly Notices of the Royal Astronomical Society*, 428(2):1460–1478.

Bundy, K., Ellis, R. S., and Conselice, C. J. (2005). The Mass Assembly Histories of Galaxies of Various Morphologies in the GOODS Fields. *The Astrophysical Journal*, 625(2):621–632.

Byrne-Mamahit, S., Hani, M. H., Ellison, S. L., Quai, S., and Patton, D. R. (2023). Interacting galaxies in the IllustrisTNG simulations - IV: enhanced supermassive black hole accretion rates in post-merger galaxies. *Monthly Notices of the Royal Astronomical Society*, 519(4):4966–4981.

Camps, P. and Baes, M. (2015). SKIRT: An advanced dust radiative transfer code with a user-friendly architecture. *Astronomy and Computing*, 9:20–33.

Capelo, P. R., Volonteri, M., Dotti, M., Bellovary, J. M., Mayer, L., and Governato, F. (2015). Growth and activity of black holes in galaxy mergers with varying mass ratios. *Monthly Notices of the Royal Astronomical Society*, 447(3):2123–2143.

Cardamone, C., Schawinski, K., Sarzi, M., Bamford, S. P., Bennert, N., Urry, C. M., Lintott, C., Keel, W. C., Parejko, J., Nichol, R. C., Thomas, D., Andreescu, D., Murray, P., Raddick, M. J., Slosar, A., Szalay, A., and Vandenberg, J. (2009). Galaxy Zoo Green Peas: discovery of a class of compact extremely star-forming galaxies. *Monthly Notices of the Royal Astronomical Society*, 399(3):1191–1205.

Casteels, K. R. V., Bamford, S. P., Skibba, R. A., Masters, K. L., Lintott, C. J., Keel, W. C., Schawinski, K., Nichol, R. C., and Smith, A. M. (2013). Galaxy Zoo: quantifying morphological indicators of galaxy interaction. *Monthly Notices of the Royal Astronomical Society*, 429(2):1051–1065.

Casteels, K. R. V., Conselice, C. J., Bamford, S. P., Salvador-Solé, E., Norberg, P. R., Agius, N. K., Baldry, I., Brough, S., Brown, M. J. I., Drinkwater, M. J., Driver, S. P., Graham, A. W., Bland-Hawthorn, J., Hopkins, A. M., Kelvin, L. S., López-Sánchez, A. R., Loveday, J., Robotham, A. S. G., and Vázquez-Mata, J. A. (2014a). Galaxy And Mass Assembly (GAMA): refining the local galaxy merger rate using morphological information. *Monthly Notices of the Royal Astronomical Society*, 445(2):1157–1169.

Casteels, K. R. V., Conselice, C. J., Bamford, S. P., Salvador-Solé, E., Norberg, P. R., Agius, N. K., Baldry, I., Brough, S., Brown, M. J. I., Drinkwater, M. J., Driver, S. P., Graham, A. W., Bland-Hawthorn, J., Hopkins, A. M., Kelvin, L. S., López-Sánchez, A. R., Loveday, J., Robotham, A. S. G., and Vázquez-Mata, J. A. (2014b). Galaxy And Mass Assembly (GAMA): refining the local galaxy merger rate using morphological information. *Monthly Notices of the Royal Astronomical Society*, 445(2):1157–1169.

Catinella, B., Schiminovich, D., Kauffmann, G., Fabello, S., Wang, J., Hummels, C., Lemonias, J., Moran, S. M., Wu, R., Giovanelli, R., Haynes, M. P., Heckman, T. M., Basu-Zych, A. R., Blanton, M. R., Brinchmann, J., Budavári, T., Gonçalves, T., Johnson, B. D., Kennicutt, R. C., Madore, B. F., Martin, C. D., Rich, M. R., Tacconi, L. J., Thilker, D. A., Wild, V., and Wyder, T. K. (2010). The GALEX Arecibo SDSS Survey - I. Gas fraction scaling relations of massive galaxies and first data release. *Monthly Notices of the Royal Astronomical Society*, 403(2):683–708.

Chambers, K. C., Magnier, E. A., Metcalfe, N., Flewelling, H. A., Huber, M. E., Waters, C. Z., Denneau, L., Draper, P. W., Farrow, D., Finkbeiner, D. P., Holmberg, C., Koppenhoefer, J., Price, P. A., Rest, A., Saglia, R. P., Schlafly, E. F., Smartt, S. J., Sweeney, W., Wainscoat, R. J., Burgett, W. S., Chastel, S., Grav, T., Heasley, J. N., Hodapp, K. W., Jedicke, R., Kaiser, N., Kudritzki, R. P., Luppino, G. A., Lupton, R. H., Monet, D. G., Morgan, J. S., Onaka, P. M., Shiao, B., Stubbs, C. W., Tonry, J. L., White, R., Bañados, E., Bell, E. F., Bender, R., Bernard, E. J., Boegner, M., Boffi, F., Botticella, M. T., Calamida, A., Casertano, S., Chen, W. P., Chen, X., Cole, S., Deacon, N., Frenk, C., Fitzsimmons, A., Gezari, S., Gibbs, V., Goessl, C., Goggia, T., Gourgue, R., Goldman, B., Grant, P., Grebel, E. K., Hambly, N. C., Hasinger, G., Heavens, A. F., Heckman, T. M., Henderson, R., Henning, T., Holman, M., Hopp, U., Ip, W. H., Isani, S., Jackson, M., Keyes, C. D., Koekemoer, A. M., Kotak, R., Le, D., Liska, D., Long, K. S., Lucey, J. R., Liu, M., Martin, N. F., Masci, G., McLean, B., Mindel, E., Misra, P., Morganson, E., Murphy, D. N. A., Obaika, A., Narayan, G., Nieto-Santisteban, M. A., Norberg, P., Peacock, J. A., Pier, E. A., Postman, M., Primak, N., Rae, C., Rai, A., Riess, A., Riffeser, A., Rix, H. W., Röser, S., Russel, R., Rutz, L., Schilbach, E., Schultz, A. S. B., Scolnic, D., Strolger, L., Szalay, A., Seitz, S., Small, E., Smith, K. W., Soderblom, D. R., Taylor, P., Thomson, R., Taylor, A. N., Thakar, A. R., Thiel, J., Thilker, D., Unger, D., Urata, Y., Valenti, J., Wagner, J., Walder, T., Walter, F., Watters, S. P., Werner, S., Wood-Vasey, W. M., and Wyse, R. (2016). The Pan-STARRS1 Surveys. *arXiv e-prints*, page arXiv:1612.05560.

Chandrasekhar, S. (1943). Dynamical Friction. I. General Considerations: the Coefficient of Dynamical Friction. *The Astrophysical Journal*, 97:255.

Chen, Y.-M., Shi, Y., Wild, V., Tremonti, C., Rowlands, K., Bizyaev, D., Yan, R., Lin, L., and Riffel, R. (2019). Post-starburst galaxies in SDSS-IV MaNGA. *Monthly Notices of the Royal Astronomical Society*, 489(4):5709–5722.

Cheng, T.-Y., Conselice, C. J., Aragón-Salamanca, A., Aguena, M., Allam, S., Andrade-Oliveira, F., Annis, J., Bluck, A. F. L., Brooks, D., Burke, D. L., Carrasco Kind, M., Carretero, J., Choi, A., Costanzi, M., da Costa, L. N., Pereira, M. E. S., De Vicente, J., Diehl, H. T., Drlica-Wagner, A., Eckert, K., Everett, S., Evrard, A. E., Ferrero, I., Fosalba, P., Frieman, J., García-Bellido, J., Gerdes, D. W., Giannantonio, T., Gruen, D., Gruendl, R. A., Gschwend, J., Gutierrez, G., Hinton, S. R., Hollowood, D. L., Honscheid, K., James, D. J., Krause, E., Kuehn, K., Kuropatkin, N., Lahav, O., Maia, M. A. G., March, M., Menanteau, F., Miquel, R., Morgan, R., Paz-Chinchón, F., Pieres, A., Plazas Malagón, A. A., Roodman, A., Sanchez, E., Scarpine, V., Serrano, S., Sevilla-Noarbe, I., Smith, M., Soares-Santos, M., Suchyta, E., Swanson, M. E. C., Tarle, G., Thomas, D., and To, C. (2021a). Galaxy morphological classification catalogue of the Dark Energy Survey Year 3 data with convolutional neural networks. *Monthly Notices of the Royal Astronomical Society*, 507(3):4425–4444.

Cheng, T.-Y., Conselice, C. J., Aragón-Salamanca, A., Li, N., Bluck, A. F. L., Hartley, W. G., Annis, J., Brooks, D., Doel, P., García-Bellido, J., James, D. J., Kuehn, K., Kuropatkin, N., Smith, M., Sobreira, F., and Tarle, G. (2020). Optimizing automatic morphological classification of galaxies with machine learning and deep learning using Dark Energy Survey imaging. *Monthly Notices of the Royal Astronomical Society*, 493(3):4209–4228.

Cheng, T.-Y., Huertas-Company, M., Conselice, C. J., Aragón-Salamanca, A., Robertson, B. E., and Ramachandra, N. (2021b). Beyond the hubble sequence - exploring galaxy morphology with unsupervised machine learning. *Monthly Notices of the Royal Astronomical Society*, 503(3):4446–4465.

Cicone, C., Maiolino, R., Sturm, E., Graciá-Carpio, J., Feruglio, C., Neri, R., Aalto, S., Davies, R., Fiore, F., Fischer, J., García-Burillo, S., González-Alfonso, E., Hailey-Dunsheath, S., Piconcelli, E., and Veilleux, S. (2014). Massive molecular outflows and evidence for AGN feedback from CO observations. *Astronomy & Astrophyics*, 562:A21.

Ćiprijanović, A., Kafkes, D., Perdue, G. N., Pedro, K., Snyder, G., Sánchez, F. J., Madireddy, S., Wild, S. M., and Nord, B. (2021). Robustness of deep learning algorithms in astronomy – galaxy morphology studies. *arXiv e-prints*, page arXiv:2111.00961.

Ćiprijanović, A., Snyder, G. F., Nord, B., and Peek, J. E. G. (2020). DeepMerge: Classifying high-redshift merging galaxies with deep neural networks. *Astronomy and Computing*, 32:100390.

Cole, S., Lacey, C. G., Baugh, C. M., and Frenk, C. S. (2000). Hierarchical galaxy formation. *Monthly Notices of the Royal Astronomical Society*, 319(1):168–204.

Conselice, C. J. (2003). The relationship between stellar light distributions of galaxies and their formation histories. *The Astrophysical Journals*, 147(1):1–28.

Conselice, C. J. (2014). The Evolution of Galaxy Structure Over Cosmic Time. *Annual Review of Astronomy and Astrophyics*, 52:291–337.

Conselice, C. J., Bershady, M. A., and Jangren, A. (2000). The asymmetry of galaxies: Physical morphology for nearby and high-redshift galaxies. *The Astrophysical Journal*, 529(2):886–910.

Conselice, C. J., Bundy, K., Trujillo, I., Coil, A., Eisenhardt, P., Ellis, R. S., Georgakakis, A., Huang, J., Lotz, J., Nandra, K., Newman, J., Papovich, C., Weiner, B., and Willmer, C. (2007). The properties and evolution of a K-band selected sample of massive galaxies at z ˜0.4-2 in the Palomar/DEEP2 survey. *Monthly Notices of the Royal Astronomical Society*, 381(3):962–986.

Couch, W. J., Ellis, R. S., Sharples, R. M., and Smail, I. (1994). Morphological Studies of the Galaxy Populations in Distant “Butcher-Oemler” Clusters with HST. I. AC 114 at Z = 0.31 and Abell 370 at Z = 0.37. *The Astrophysical Journal*, 430:121.

Couch, W. J. and Sharples, R. M. (1987). A spectroscopic study of three rich galaxy clusters at zeta=0.31. *Monthly Notices of the Royal Astronomical Society*, 229:423–456.

Cox, T. J., Dutta, S. N., Di Matteo, T., Hernquist, L., Hopkins, P. F., Robertson, B., and Springel, V. (2006). The Kinematic Structure of Merger Remnants. *The Astrophysical Journal*, 650(2):791–811.

Cox, T. J., Jonsson, P., Somerville, R. S., Primack, J. R., and Dekel, A. (2008). The effect of galaxy mass ratio on merger-driven starbursts. *Monthly Notices of the Royal Astronomical Society*, 384(1):386–409.

Curtis, H. D. (1920). Modern Theories of the Spiral Nebulae. *Journal of the Royal Astronomical Society of Canada*, 14:317.

Curtis-Lake, E., McLure, R. J., Dunlop, J. S., Rogers, A. B., Targett, T., Dekel, A., Ellis, R. S., Faber, S. M., Ferguson, H. C., Grogin, N. A., Kocevski, D. D., Koekemoer, A. M., Lai, K., Mármol-Queraltó, E., and Robertson, B. E. (2016). Non-parametric analysis of the rest-frame UV sizes and morphological disturbance amongst L_* galaxies at 4 ¡ z ¡ 8. *Monthly Notices of the Royal Astronomical Society*, 457(1):440–464.

Darg, D. W., Kaviraj, S., Lintott, C. J., Schawinski, K., Sarzi, M., Bamford, S., Silk, J., Andreescu, D., Murray, P., Nichol, R. C., Raddick, M. J., Slosar, A., Szalay, A. S., Thomas, D., and Vandenberg, J. (2010a). Galaxy Zoo: the properties of merging galaxies in the nearby Universe - local environments, colours, masses, star formation rates and AGN activity. *Monthly Notices of the Royal Astronomical Society*, 401(3):1552–1563.

Darg, D. W., Kaviraj, S., Lintott, C. J., Schawinski, K., Sarzi, M., Bamford, S., Silk, J., Proctor, R., Andreescu, D., Murray, P., Nichol, R. C., Raddick, M. J., Slosar, A., Szalay, A. S., Thomas, D., and Vandenberg, J. (2010b). Galaxy Zoo: the fraction of merging galaxies in the SDSS and their morphologies. *Monthly Notices of the Royal Astronomical Society*, 401(2):1043–1056.

Davies, J. J., Pontzen, A., and Crain, R. A. (2022). Galaxy mergers can initiate quenching by unlocking an AGN-driven transformation of the baryon cycle. *Monthly Notices of the Royal Astronomical Society*, 515(1):1430–1443.

Davis, M., Efstathiou, G., Frenk, C. S., and White, S. D. M. (1985). The evolution of large-scale structure in a universe dominated by cold dark matter. *The Astrophysical Journal*, 292:371–394.

Davis, T. A., van de Voort, F., Rowlands, K., McAlpine, S., Wild, V., and Crain, R. A. (2019). Evolution of the cold gas properties of simulated post-starburst galaxies. *Monthly Notices of the Royal Astronomical Society*, 484(2):2447–2461.

De Lucia, G. and Blaizot, J. (2007). The hierarchical formation of the brightest cluster galaxies. *Monthly Notices of the Royal Astronomical Society*, 375(1):2–14.

de Vaucouleurs, G. (1948). Recherches sur les Nebuleuses Extragalactiques. *Annales d'Astrophysique*, 11:247.

Di Matteo, P., Combes, F., Melchior, A. L., and Semelin, B. (2007). Star formation efficiency in galaxy interactions and mergers: a statistical study. *Astronomy & Astrophysics*, 468(1):61–81.

Di Matteo, T., Springel, V., and Hernquist, L. (2005). Energy input from quasars regulates the growth and activity of black holes and their host galaxies. *Nature*, 433(7026):604–607.

Dieleman, S., Willett, K. W., and Dambre, J. (2015). Rotation-invariant convolutional neural networks for galaxy morphology prediction. *Monthly Notices of the Royal Astronomical Society*, 450(2):1441–1459.

Dolag, K., Borgani, S., Murante, G., and Springel, V. (2009). Substructures in hydrodynamical cluster simulations. *Monthly Notices of the Royal Astronomical Society*, 399(2):497–514.

Dressler, A. and Gunn, J. E. (1983). Spectroscopy of galaxies in distant clusters. II. The population of the 3C 295 cluster. *The Astrophysical Journal*, 270:7–19.

Driver, S. P., Allen, P. D., Graham, A. W., Cameron, E., Liske, J., Ellis, S. C., Cross, N. J. G., De Propris, R., Phillipps, S., and Couch, W. J. (2006). The Millennium Galaxy Catalogue: morphological classification and bimodality in the colour-concentration plane. *Monthly Notices of the Royal Astronomical Society*, 368(1):414–434.

Duc, P.-A., Cuillandre, J.-C., Karabal, E., Cappellari, M., Alatalo, K., Blitz, L., Bournaud, F., Bureau, M., Crocker, A. F., Davies, R. L., Davis, T. A., de Zeeuw, P. T., Emsellem, E., Khochfar, S., Krajnović, D., Kuntschner, H., McDermid, R. M., Michel-Dansac, L., Morganti, R., Naab, T., Oosterloo, T., Paudel, S., Sarzi, M., Scott, N., Serra, P., Weijmans, A.-M., and Young, L. M. (2015). The ATLAS^{3D} project - XXIX. The new look of early-type galaxies and surrounding fields disclosed by extremely deep optical images. *Monthly Notices of the Royal Astronomical Society*, 446(1):120–143.

Ellison, S. L., Mendel, J. T., Patton, D. R., and Scudder, J. M. (2013). Galaxy pairs in the Sloan Digital Sky Survey - VIII. The observational properties of post-merger galaxies. *Monthly Notices of the Royal Astronomical Society*, 435(4):3627–3638.

Ellison, S. L., Patton, D. R., Simard, L., and McConnachie, A. W. (2008). Galaxy Pairs in the Sloan Digital Sky Survey. I. Star Formation, Active Galactic Nucleus Fraction, and the Mass-Metallicity Relation. *The Astronomical Journal*, 135(5):1877–1899.

Ellison, S. L., Viswanathan, A., Patton, D. R., Bottrell, C., McConnachie, A. W., Gwyn, S., and Cuillandre, J.-C. (2019). A definitive merger-AGN connection at z ~ 0 with CFIS: mergers have an excess of AGN and AGN hosts are more frequently disturbed. *Monthly Notices of the Royal Astronomical Society*, 487(2):2491–2504.

Ellison, S. L., Wilkinson, S., Woo, J., Leung, H.-H., Wild, V., Bickley, R. W., Patton, D. R., Quai, S., and Gwyn, S. (2022). Galaxy mergers can rapidly shut down star formation. , 517(1):L92–L96.

Ferrari, F., de Carvalho, R. R., and Trevisan, M. (2015). Morfometryka—A New Way of Establishing Morphological Classification of Galaxies. *The Astrophysical Journal*, 814(1):55.

Ferreira, L., Conselice, C. J., Duncan, K., Cheng, T.-Y., Griffiths, A., and Whitney, A. (2020a). Galaxy Merger Rates up to z $\sim$ 3 Using a Bayesian Deep Learning Model: A Major-merger Classifier Using IllustrisTNG Simulation Data. *The Astrophysical Journal*, 895(2):115.

Ferreira, L., Conselice, C. J., Duncan, K., Cheng, T.-Y., Griffiths, A., and Whitney, A. (2020b). Galaxy Merger Rates up to z $\sim$ 3 Using a Bayesian Deep Learning Model: A Major-merger Classifier Using IllustrisTNG Simulation Data. *The Astrophysical Journal*, 895(2):115.

Ferreira, L., Conselice, C. J., Kuchner, U., and Tohill, C.-B. (2022). A Simulation-driven Deep Learning Approach for Separating Mergers and Star-forming Galaxies: The Formation Histories of Clumpy Galaxies in All of the CANDELS Fields. *The Astrophysical Journal*, 931(1):34.

Finkelman, I., Funes, J. G., and Brosch, N. (2012). Polar ring galaxies in the Galaxy Zoo. *Monthly Notices of the Royal Astronomical Society*, 422(3):2386–2398.

Freeman, P. E., Izbicki, R., Lee, A. B., Newman, J. A., Conselice, C. J., Koekemoer, A. M., Lotz, J. M., and Mozena, M. (2013). New image statistics for detecting disturbed galaxy morphologies at high redshift. *Monthly Notices of the Royal Astronomical Society*, 434(1):282–295.

French, K. D. (2021). Evolution Through the Post-starburst Phase: Using Post-starburst Galaxies as Laboratories for Understanding the Processes that Drive Galaxy Evolution. *Publications of the Astronomical Society of the Pacific*, 133(1025):072001.

French, K. D., Yang, Y., Zabludoff, A. I., and Tremonti, C. A. (2018). Clocking the Evolution of Post-starburst Galaxies: Methods and First Results. *The Astrophysical Journal*, 862(1):2.

Genel, S., Vogelsberger, M., Springel, V., Sijacki, D., Nelson, D., Snyder, G., Rodriguez-Gomez, V., Torrey, P., and Hernquist, L. (2014). Introducing the Illustris project: the evolution of galaxy populations across cosmic time. *Monthly Notices of the Royal Astronomical Society*, 445(1):175–200.

Gerhard, O. E. (1981). N-body simulations of disc-halo galaxies - Isolated systems, tidal interactions and merging. *Monthly Notices of the Royal Astronomical Society*, 197:179–208.

Goto, T. (2004). Are e+a galaxies dusty-starbursts?: Vla 20 cm radio continuum observation*. *Astronomy & Astrophysics*, 427(1):125–130.

Goto, T. (2005). 266 E+A galaxies selected from the Sloan Digital Sky Survey Data Release 2: the origin of E+A galaxies. *Monthly Notices of the Royal Astronomical Society*, 357(3):937–944.

Goto, T. (2006). Post-starburst-active galactic nucleus connection: spatially resolved spectroscopy of Hδ-strong active galactic nuclei. *Monthly Notices of the Royal Astronomical Society*, 369(4):1765–1772.

Goto, T. (2007). A catalogue of local E+A (post-starburst) galaxies selected from the Sloan Digital Sky Survey Data Release 5. *Monthly Notices of the Royal Astronomical Society*, 381(1):187–193.

Graham, A. W. and Driver, S. P. (2005). A Concise Reference to (Projected) Sérsic $R^{1/n}$ Quantities, Including Concentration, Profile Slopes, Petrosian Indices, and Kron Magnitudes. *PASA*, 22(2):118–127.

Gunn, J. E. and Gott, J. Richard, I. (1972). On the Infall of Matter Into Clusters of Galaxies and Some Effects on Their Evolution. *The Astrophysical Journal*, 176:1.

Guzmán-Ortega, A., Rodriguez-Gomez, V., Snyder, G. F., Chamberlain, K., and Hernquist, L. (2023). Morphological signatures of mergers in the TNG50 simulation and the Kilo-Degree Survey: the merger fraction from dwarfs to Milky Way-like galaxies. *Monthly Notices of the Royal Astronomical Society*, 519(4):4920–4937.

Gwyn, S. D. J. (2008). MegaPipe: The MegaCam Image Stacking Pipeline at the Canadian Astronomical Data Centre. *Publications of the Astronomical Society of the Pacific*, 120(864):212.

Hani, M. H., Gosain, H., Ellison, S. L., Patton, D. R., and Torrey, P. (2020). Interacting galaxies in the IllustrisTNG simulations - II: star formation in the post-merger stage. *Monthly Notices of the Royal Astronomical Society*, 493(3):3716–3731.

Häußler, B., Bamford, S. P., Vika, M., Rojas, A. L., Barden, M., Kelvin, L. S., Alpaslan, M., Robotham, A. S. G., Driver, S. P., Baldry, I. K., Brough, S., Hopkins, A. M., Liske, J., Nichol, R. C., Popescu, C. C., and Tuffs, R. J. (2013). MegaMorph - multiwavelength measurement of galaxy structure: complete Sérsic profile information from modern surveys. *Monthly Notices of the Royal Astronomical Society*, 430(1):330–369.

Heckman, T. M., Armus, L., and Miley, G. K. (1990). On the Nature and Implications of Starburst-driven Galactic Superwinds. *The Astrophysical Journal Supplement Series*, 74:833.

Hernquist, L. (1992). Structure of Merger Remnants. I. Bulgeless Progenitors. *The Astrophysical Journal*, 400:460.

Hocking, A., Geach, J. E., Sun, Y., and Davey, N. (2018). An automatic taxonomy of galaxy morphology using unsupervised machine learning. *Monthly Notices of the Royal Astronomical Society*, 473(1):1108–1129.

Hogg, D. W., Masjedi, M., Berlind, A. A., Blanton, M. R., Quintero, A. D., and Brinkmann, J. (2006). What Triggers Galaxy Transformations? The Environments of Poststarburst Galaxies. *The Astrophysical Journal*, 650(2):763–769.

Hopkins, P. F., Cox, T. J., Younger, J. D., and Hernquist, L. (2009a). How do Disks Survive Mergers? *The Astrophysical Journal*, 691(2):1168–1201.

Hopkins, P. F., Hernquist, L., Cox, T. J., Di Matteo, T., Robertson, B., and Springel, V. (2006). A Unified, Merger-driven Model of the Origin of Starbursts, Quasars, the Cosmic X-Ray Background, Supermassive Black Holes, and Galaxy Spheroids. *The Astrophysical Journals*, 163(1):1–49.

Hopkins, P. F., Hernquist, L., Cox, T. J., and Kereš, D. (2008). A Cosmological Framework for the Co-Evolution of Quasars, Supermassive Black Holes, and Elliptical Galaxies. I. Galaxy Mergers and Quasar Activity. *The Astrophysical Journals*, 175(2):356–389.

Hopkins, P. F., Somerville, R. S., Cox, T. J., Hernquist, L., Jogee, S., Kereš, D., Ma, C.-P., Robertson, B., and Stewart, K. (2009b). The effects of gas on morphological transformation in mergers: implications for bulge and disc demographics. *Monthly Notices of the Royal Astronomical Society*, 397(2):802–814.

Hubble, E. (1929). A Relation between Distance and Radial Velocity among Extra-Galactic Nebulae. *Proceedings of the National Academy of Science*, 15(3):168–173.

Hubble, E. P. (1925). Cepheids in Spiral Nebulae. *Popular Astronomy*, 33:252–255.

Hubble, E. P. (1926). Extragalactic nebulae. *The Astrophysical Journal*, 64:321–369.

Huertas-Company, M., Aguerri, J. A. L., Bernardi, M., Mei, S., and Sánchez Almeida, J. (2011). Revisiting the Hubble sequence in the SDSS DR7 spectroscopic sample: a publicly available Bayesian automated classification. *Astronomy & Astrophysics*, 525:A157.

Huertas-Company, M., Gravet, R., Cabrera-Vives, G., Pérez-González, P. G., Kartaltepe, J. S., Barro, G., Bernardi, M., Mei, S., Shankar, F., Dimauro, P., Bell, E. F., Kocevski, D., Koo, D. C., Faber, S. M., and Mcintosh, D. H. (2015). A Catalog of Visual-like Morphologies in the 5 CANDELS Fields Using Deep Learning. *The Astrophysical Journals*, 221(1):8.

Huertas-Company, M., Rouan, D., Tasca, L., Soucail, G., and Le Fèvre, O. (2008). A robust morphological classification of high-redshift galaxies using support vector machines on seeing limited images. I. Method description. *Astronomy & Astrophysics*, 478(3):971–980.

Hung, C.-L., Sanders, D. B., Casey, C. M., Lee, N., Barnes, J. E., Capak, P., Kartaltepe, J. S., Koss, M., Larson, K. L., Le Floc'h, E., Lockhart, K., Man, A. W. S., Mann, A. W., Riguccini, L., Scoville, N., and Symeonidis, M. (2013). The Role of Galaxy Interaction in the SFR-M $_*$ Relation: Characterizing Morphological Properties of Herschel-selected Galaxies at 0.2 ¡ z ¡ 1.5. *The Astrophysical Journal*, 778(2):129.

Iono, D., Yun, M. S., and Mihos, J. C. (2004). Radial Gas Flows in Colliding Galaxies: Connecting Simulations and Observations. *The Astrophysical Journal*, 616(1):199–220.

Ji, I., Peirani, S., and Yi, S. K. (2014). Lifetime of merger features of equal-mass disk mergers. *Astronomy & Astrophysics*, 566:A97.

Johnston, K. V., Bullock, J. S., Sharma, S., Font, A., Robertson, B. E., and Leitner, S. N. (2008). Tracing Galaxy Formation with Stellar Halos. II. Relating Substructure in Phase and Abundance Space to Accretion Histories. *The Astrophysical Journal*, 689(2):936–957.

Johnston, K. V., Choi, P. I., and Guhathakurta, P. (2002). Interpreting the Morphology of Diffuse Light around Satellite Galaxies. *The Astronomical Journal*, 124(1):127–146.

Kampczyk, P., Lilly, S. J., Carollo, C. M., Scarlata, C., Feldmann, R., Koekemoer, A., Leauthaud, A., Sargent, M. T., Taniguchi, Y., and Capak, P. (2007). Simulating the Cosmos: The Fraction of Merging Galaxies at High Redshift. *The Astrophysical Journal Supplement Series*, 172(1):329–340.

Kapferer, W., Knapp, A., Schindler, S., Kimeswenger, S., and van Kampen, E. (2005). Star formation rates and mass distributions in interacting galaxies. *Astronomy and Astrophysics*, 438(1):87–101.

Kartaltepe, J. S., Mozena, M., Kocevski, D., McIntosh, D. H., Lotz, J., Bell, E. F., Faber, S., Ferguson, H., Koo, D., Bassett, R., Bernyk, M., Blancato, K., Bournaud, F., Cassata, P., Castellano, M., Cheung, E., Conselice, C. J., Croton, D., Dahlen, T., de Mello, D. F., DeGroot, L., Donley, J., Guedes, J., Grogin, N., Hathi, N., Hilton, M., Hollon, B., Koekemoer, A., Liu, N., Lucas, R. A., Martig, M., McGrath, E., McPartland, C., Mobasher, B., Morlock, A., O'Leary, E., Peth, M., Pforr, J., Pillepich, A., Rosario, D., Soto, E., Straughn, A., Telford, O., Sunnquist, B., Trump, J., Weiner, B., Wuyts, S., Inami, H., Kassin, S., Lani, C., Poole, G. B., and Rizer, Z. (2015). CANDELS Visual Classifications: Scheme, Data Release, and First Results. *The Astrophysical Journal Supplement Series*, 221(1):11.

Katz, N. (1992). Dissipational Galaxy Formation. II. Effects of Star Formation. *The Astrophysical Journal*, 391:502.

Kauffmann, G., Heckman, T. M., Tremonti, C., Brinchmann, J., Charlot, S., White, S. D. M., Ridgway, S. E., Brinkmann, J., Fukugita, M., Hall, P. B., Ivezić, Z., Richards, G. T., and Schneider, D. P. (2003a). The host galaxies of active galactic nuclei. *Monthly Notices of the Royal Astronomical Society*, 346(4):1055–1077.

Kauffmann, G., Heckman, T. M., White, S. D. M., Charlot, S., Tremonti, C., Brinchmann, J., Bruzual, G., Peng, E. W., Seibert, M., Bernardi, M., Blanton, M., Brinkmann, J., Castander, F., Csábai, I., Fukugita, M., Ivezic, Z., Munn, J. A., Nichol, R. C., Padmanabhan, N., Thakar, A. R., Weinberg, D. H., and York, D. (2003b). Stellar masses and star formation histories for 105 galaxies from the Sloan Digital Sky Survey. *Monthly Notices of the Royal Astronomical Society*, 341(1):33–53.

Keel, W. C., Kennicutt, R. C., J., Hummel, E., and van der Hulst, J. M. (1985). The effects of interactions on spiral galaxies. I. Nuclear activity and star formation. *The Astronomical Journal*, 90:708–730.

Kelvin, L. S., Driver, S. P., Robotham, A. S. G., Hill, D. T., Alpaslan, M., Baldry, I. K., Bamford, S. P., Bland-Hawthorn, J., Brough, S., Graham, A. W., Häussler, B., Hopkins, A. M., Liske, J., Loveday, J., Norberg, P., Phillipps, S., Popescu, C. C., Prescott, M., Taylor, E. N., and Tuffs, R. J. (2012). Galaxy And Mass Assembly (GAMA): Structural Investigation of Galaxies via Model Analysis. *Monthly Notices of the Royal Astronomical Society*, 421(2):1007–1039.

Kennicutt, Robert C., J. (1998). The Global Schmidt Law in Star-forming Galaxies. *The Astrophysical Journal*, 498(2):541–552.

Kewley, L. J., Geller, M. J., and Barton, E. J. (2006). Metallicity and Nuclear Star Formation in Nearby Galaxy Pairs: Evidence for Tidally Induced Gas Flows. *The Astronomical Journal*, 131(4):2004–2017.

Knapen, J. H., Cisternas, M., and Querejeta, M. (2015). Interacting galaxies in the nearby Universe: only moderate increase of star formation. *Monthly Notices of the Royal Astronomical Society*, 454(2):1742–1750.

Lacey, C. and Cole, S. (1993). Merger rates in hierarchical models of galaxy formation. *Monthly Notices of the Royal Astronomical Society*, 262(3):627–649.

Lambas, D. G., Tissera, P. B., Alonso, M. S., and Coldwell, G. (2003). Galaxy pairs in the 2dF survey - I. Effects of interactions on star formation in the field. *Monthly Notices of the Royal Astronomical Society*, 346(4):1189–1196.

Lambrides, E. L., Watts, D. J., Chiaberge, M., Tchernyshyov, K., Kirkpatrick, A., Meyer, E. T., Heckman, T., Simons, R., Amram, O., Hall, K. R., Long, A., and

Norman, C. (2021). Merger or Not: Accounting for Human Biases in Identifying Galactic Merger Signatures. *The Astrophysical Journal*, 919(1):43.

Lin, L., Pan, H.-A., Ellison, S. L., Belfiore, F., Shi, Y., Sánchez, S. F., Hsieh, B.-C., Rowlands, K., Ramya, S., Thorp, M. D., Li, C., and Maiolino, R. (2019). The ALMaQUEST Survey: The Molecular Gas Main Sequence and the Origin of the Star-forming Main Sequence. *The Astrophysical Journall*, 884(2):L33.

Lintott, C., Schawinski, K., Bamford, S., Slosar, A., Land, K., Thomas, D., Edmondson, E., Masters, K., Nichol, R. C., Raddick, M. J., Szalay, A., Andreescu, D., Murray, P., and Vandenberg, J. (2011). Galaxy Zoo 1: data release of morphological classifications for nearly 900 000 galaxies. *Monthly Notices of the Royal Astronomical Society*, 410(1):166–178.

Lintott, C. J., Schawinski, K., Slosar, A., Land, K., Bamford, S., Thomas, D., Raddick, M. J., Nichol, R. C., Szalay, A., Andreescu, D., Murray, P., and Vandenberg, J. (2008). Galaxy Zoo: morphologies derived from visual inspection of galaxies from the Sloan Digital Sky Survey. *Monthly Notices of the Royal Astronomical Society*, 389(3):1179–1189.

Lisker, T. (2008). Is the Gini Coefficient a Stable Measure of Galaxy Structure? *The Astrophysical Journals*, 179(2):319–325.

Lotz, J. M., Davis, M., Faber, S. M., Guhathakurta, P., Gwyn, S., Huang, J., Koo, D. C., Le Floc'h, E., Lin, L., Newman, J., Noeske, K., Papovich, C., Willmer, C. N. A., Coil, A., Conselice, C. J., Cooper, M., Hopkins, A. M., Metevier, A., Primack, J., Rieke, G., and Weiner, B. J. (2008). The Evolution of Galaxy Mergers and Morphology at z ¡ 1.2 in the Extended Groth Strip. *The Astrophysical Journal*, 672(1):177–197.

Lotz, J. M., Jonsson, P., Cox, T. J., Croton, D., Primack, J. R., Somerville, R. S., and Stewart, K. (2011). The Major and Minor Galaxy Merger Rates at z ¡ 1.5. *The Astrophysical Journal*, 742(2):103.

Lotz, J. M., Jonsson, P., Cox, T. J., and Primack, J. R. (2008). Galaxy merger morphologies and time-scales from simulations of equal-mass gas-rich disc mergers. *Monthly Notices of the Royal Astronomical Society*, 391(3):1137–1162.

Lotz, J. M., Jonsson, P., Cox, T. J., and Primack, J. R. (2010a). The effect of gas fraction on the morphology and time-scales of disc galaxy mergers. *Monthly Notices of the Royal Astronomical Society*, 404(2):590–603.

Lotz, J. M., Jonsson, P., Cox, T. J., and Primack, J. R. (2010b). The effect of mass ratio on the morphology and time-scales of disc galaxy mergers. *Monthly Notices of the Royal Astronomical Society*, 404(2):575–589.

Lotz, J. M., Primack, J., and Madau, P. (2004). A new nonparametric approach to galaxy morphological classification. *The Astronomical Journal*, 128(1):163–182.

Lotz, M., Dolag, K., Remus, R.-S., and Burkert, A. (2021). Rise and fall of post-starburst galaxies in Magneticum Pathfinder. *Monthly Notices of the Royal Astronomical Society*, 506(3):4516–4542.

Mac Low, M.-M. and Ferrara, A. (1999). Starburst-driven Mass Loss from Dwarf Galaxies: Efficiency and Metal Ejection. *The Astrophysical Journal*, 513(1):142–155.

Malin, D. F. and Carter, D. (1983). A catalog of elliptical galaxies with shells. *The Astrophysical Journal*, 274:534–540.

Marinacci, F., Vogelsberger, M., Pakmor, R., Torrey, P., Springel, V., Hernquist, L., Nelson, D., Weinberger, R., Pillepich, A., Naiman, J., and Genel, S. (2018). First results from the IllustrisTNG simulations: radio haloes and magnetic fields. *Monthly Notices of the Royal Astronomical Society*, 480(4):5113–5139.

Martin, G., Bazkiaei, A. E., Spavone, M., Iodice, E., Mihos, J. C., Montes, M., Benavides, J. A., Brough, S., Carlin, J. L., Collins, C. A., Duc, P. A., Gómez, F. A., Galaz, G., Hernández-Toledo, H. M., Jackson, R. A., Kaviraj, S., Knapen, J. H., Martínez-Lombilla, C., McGee, S., O'Ryan, D., Prole, D. J., Rich, R. M., Román, J., Shah, E. A., Starkenburg, T. K., Watkins, A. E., Zaritsky, D., Pichon, C., Armus, L., Bianconi, M., Buitrago, F., Busá, I., Davis, F., Demarco, R., Desmons, A., García, P., Graham, A. W., Holwerda, B., Hon, D. S. H., Khalid, A., Klehammer, J., Klutse, D. Y., Lazar, I., Nair, P., Noakes-Kettel, E. A., Rutkowski, M., Saha, K., Sahu, N., Sola, E., Vázquez-Mata, J. A., Vera-Casanova, A., and Yoon, I. (2022). Preparing for low surface brightness science with the Vera C. Rubin Observatory: Characterization of tidal features from mock images. *Monthly Notices of the Royal Astronomical Society*, 513(1):1459–1487.

Martin, G., Kaviraj, S., Hocking, A., Read, S. C., and Geach, J. E. (2020). Galaxy morphological classification in deep-wide surveys via unsupervised machine learning. *Monthly Notices of the Royal Astronomical Society*, 491(1):1408–1426.

Mattson, M. P. (2014). Superior pattern processing is the essence of the evolved human brain. *Frontiers in neuroscience*, 8(265):4290–4310.

McElroy, R., Bottrell, C., Hani, M. H., Moreno, J., Croom, S. M., Hayward, C. C., Twum, A., Feldmann, R., Hopkins, P. F., Hernquist, L., and Husemann, B. (2022). The observability of galaxy merger signatures in nearby gas-rich spirals. *Monthly Notices of the Royal Astronomical Society*, 515(3):3406–3419.

Mendel, J. T., Simard, L., Palmer, M., Ellison, S. L., and Patton, D. R. (2014). A Catalog of Bulge, Disk, and Total Stellar Mass Estimates for the Sloan Digital Sky Survey. *The Astrophysical Journals*, 210(1):3.

Meusinger, H., Brünecke, J., Schalldach, P., and in der Au, A. (2017). A large sample of Kohonen selected E+A (post-starburst) galaxies from the Sloan Digital Sky Survey. *Astronomy & Astrophysics*, 597:A134.

Mihos, J. C. (1995). Morphology of Galaxy Mergers at Intermediate Redshift. *The Astrophysical Journall*, 438:L75.

Mihos, J. C. and Hernquist, L. (1996). Gasdynamics and Starbursts in Major Mergers. *The Astrophysical Journal*, 464:641.

Miller, N. A. and Owen, F. N. (2001). Current Star Formation in Post-Starburst Galaxies? *The Astrophysical Journall*, 554(1):L25–L27.

Moore, B., Katz, N., Lake, G., Dressler, A., and Oemler, A. (1996). Galaxy harassment and the evolution of clusters of galaxies. *Nature*, 379(6566):613–616.

Moore, B., Lake, G., and Katz, N. (1998). Morphological Transformation from Galaxy Harassment. *The Astrophysical Journal*, 495(1):139–151.

Moore, J. A., Pimbblet, K. A., and Drinkwater, M. J. (2006). Mathematical Morphology: Star/Galaxy Differentiation & Galaxy Morphology Classification. *Publications of the Astronomical Society of Australia*, 23(4):135–146.

Moreno, J., Torrey, P., Ellison, S. L., Patton, D. R., Bluck, A. F. L., Bansal, G., and Hernquist, L. (2015). Mapping galaxy encounters in numerical simulations: the spatial extent of induced star formation. *Monthly Notices of the Royal Astronomical Society*, 448(2):1107–1117.

Moreno, J., Torrey, P., Ellison, S. L., Patton, D. R., Hopkins, P. F., Bueno, M., Hayward, C. C., Narayanan, D., Kereš, D., Bluck, A. F. L., and Hernquist, L. (2019). Interacting galaxies on FIRE-2: the connection between enhanced star formation and interstellar gas content. *Monthly Notices of the Royal Astronomical Society*, 485(1):1320–1338.

Moster, B. P., Macciò, A. V., Somerville, R. S., Johansson, P. H., and Naab, T. (2010a). Can gas prevent the destruction of thin stellar discs by minor mergers? *Monthly Notices of the Royal Astronomical Society*, 403(2):1009–1019.

Moster, B. P., Somerville, R. S., Maulbetsch, C., van den Bosch, F. C., Macciò, A. V., Naab, T., and Oser, L. (2010b). Constraints on the Relationship between Stellar Mass and Halo Mass at Low and High Redshift. *The Astrophysical Journal*, 710(2):903–923.

Naab, T. and Burkert, A. (2003). Statistical Properties of Collisionless Equal- and Unequal-Mass Merger Remnants of Disk Galaxies. *The Astrophysical Journal*, 597(2):893–906.

Naiman, J. P., Pillepich, A., Springel, V., Ramirez-Ruiz, E., Torrey, P., Vogelsberger, M., Pakmor, R., Nelson, D., Marinacci, F., Hernquist, L., Weinberger, R., and Genel, S. (2018). First results from the IllustrisTNG simulations: a tale of two elements - chemical evolution of magnesium and europium. *Monthly Notices of the Royal Astronomical Society*, 477(1):1206–1224.

Nair, P. B. and Abraham, R. G. (2010). A Catalog of Detailed Visual Morphological Classifications for 14,034 Galaxies in the Sloan Digital Sky Survey. *The Astrophysical Journals*, 186(2):427–456.

Nelson, D., Pillepich, A., Springel, V., Weinberger, R., Hernquist, L., Pakmor, R., Genel, S., Torrey, P., Vogelsberger, M., Kauffmann, G., Marinacci, F., and Naiman, J. (2018a). First results from the IllustrisTNG simulations: the galaxy colour bimodality. *Monthly Notices of the Royal Astronomical Society*, 475(1):624–647.

Nelson, D., Pillepich, A., Springel, V., Weinberger, R., Hernquist, L., Pakmor, R., Genel, S., Torrey, P., Vogelsberger, M., Kauffmann, G., Marinacci, F., and Naiman, J. (2018b). First results from the IllustrisTNG simulations: the galaxy colour bimodality. *Monthly Notices of the Royal Astronomical Society*, 475(1):624–647.

Nelson, D., Springel, V., Pillepich, A., Rodriguez-Gomez, V., Torrey, P., Genel, S., Vogelsberger, M., Pakmor, R., Marinacci, F., Weinberger, R., Kelley, L., Lovell, M., Diemer, B., and Hernquist, L. (2019). The IllustrisTNG simulations: public data release. *Computational Astrophysics and Cosmology*, 6(1):2.

Nevin, R., Blecha, L., Comerford, J., and Greene, J. (2019). Accurate Identification of Galaxy Mergers with Imaging. *The Astrophysical Journal*, 872(1):76.

Nielsen, D. M., Ridgway, S. E., De Propris, R., and Goto, T. (2012). The Current Star Formation Rate of K+A Galaxies. *The Astrophysical Journall*, 761(2):L16.

O'Donnell, J. E. (1994). R v-dependent Optical and Near-Ultraviolet Extinction. *The Astrophysical Journal*, 422:158.

Osterbrock, D. E. and Ferland, G. J. (2006). *Astrophysics of gaseous nebulae and active galactic nuclei*.

Patton, D. R., Qamar, F. D., Ellison, S. L., Bluck, A. F. L., Simard, L., Mendel, J. T., Moreno, J., and Torrey, P. (2016). Galaxy pairs in the Sloan Digital Sky Survey - XI. A new method for measuring the influence of the closest companion out to wide separations. *Monthly Notices of the Royal Astronomical Society*, 461(3):2589–2604.

Patton, D. R., Torrey, P., Ellison, S. L., Mendel, J. T., and Scudder, J. M. (2013). Galaxy pairs in the Sloan Digital Sky Survey - VI. The orbital extent of enhanced star formation in interacting galaxies. *Monthly Notices of the Royal Astronomical Society*, 433(1):L59–L63.

Patton, D. R., Wilson, K. D., Metrow, C. J., Ellison, S. L., Torrey, P., Brown, W., Hani, M. H., McAlpine, S., Moreno, J., and Woo, J. (2020). Interacting galaxies in the IllustrisTNG simulations - I: Triggered star formation in a cosmological context. *Monthly Notices of the Royal Astronomical Society*, 494(4):4969–4985.

Pawlik, M. M., McAlpine, S., Trayford, J. W., Wild, V., Bower, R., Crain, R. A., Schaller, M., and Schaye, J. (2019). The diverse evolutionary pathways of post-starburst galaxies. *Nature Astronomy*, 3:440–446.

Pawlik, M. M., Taj Aldeen, L., Wild, V., Mendez-Abreu, J., Lahén, N., Johansson, P. H., Jimenez, N., Lucas, W., Zheng, Y., Walcher, C. J., and Rowlands, K. (2018). The origins of post-starburst galaxies at z
lt; 0.05. *Monthly Notices of the Royal Astronomical Society*, 477(2):1708–1743.

Pawlik, M. M., Wild, V., Walcher, C. J., Johansson, P. H., Villforth, C., Rowlands, K., Mendez-Abreu, J., and Hewlett, T. (2016). Shape asymmetry: a morphological indicator for automatic detection of galaxies in the post-coalescence merger stages. *Monthly Notices of the Royal Astronomical Society*, 456(3):3032–3052.

Pearson, W. J., Wang, L., Alpaslan, M., Baldry, I., Bilicki, M., Brown, M. J. I., Grootes, M. W., Holwerda, B. W., Kitching, T. D., Kruk, S., and van der Tak, F. F. S. (2019a). Effect of galaxy mergers on star-formation rates. *Astronomy & Astrophyics*, 631:A51.

Pearson, W. J., Wang, L., Trayford, J. W., Petrillo, C. E., and van der Tak, F. F. S. (2019b). Identifying galaxy mergers in observations and simulations with deep learning. *Astronomy & Astrophysics*, 626:A49.

Pei, Y. C. (1992). Interstellar Dust from the Milky Way to the Magellanic Clouds. *The Astrophysical Journal*, 395:130.

Pillepich, A., Nelson, D., Hernquist, L., Springel, V., Pakmor, R., Torrey, P., Weinberger, R., Genel, S., Naiman, J. P., Marinacci, F., and Vogelsberger, M. (2018). First results from the IllustrisTNG simulations: the stellar mass content of groups and clusters of galaxies. *Monthly Notices of the Royal Astronomical Society*, 475(1):648–675.

Pillepich, A., Nelson, D., Springel, V., Pakmor, R., Torrey, P., Weinberger, R., Vogelsberger, M., Marinacci, F., Genel, S., van der Wel, A., and Hernquist, L. (2019). First results from the TNG50 simulation: the evolution of stellar and gaseous discs across cosmic time. *Monthly Notices of the Royal Astronomical Society*, 490(3):3196–3233.

Poggianti, B. M. and Wu, H. (2000). Optical Spectral Signatures of Dusty Starburst Galaxies. *The Astrophysical Journal*, 529(1):157–169.

Pracy, M. B., Croom, S., Sadler, E., Couch, W. J., Kuntschner, H., Bekki, K., Owers, M. S., Zwaan, M., Turner, J., and Bergmann, M. (2013). Stellar population gradients and spatially resolved kinematics in luminous post-starburst galaxies. *Monthly Notices of the Royal Astronomical Society*, 432(4):3131–3140.

Pracy, M. B., Kuntschner, H., Couch, W. J., Blake, C., Bekki, K., and Briggs, F. (2009). The kinematics and spatial distribution of stellar populations in E+A galaxies. *Monthly Notices of the Royal Astronomical Society*, 396(3):1349–1369.

Quai, S., Byrne-Mamahit, S., Ellison, S. L., Patton, D. R., and Hani, M. H. (2023). The interconnection between galaxy mergers, AGN activity, and rapid quenching of star formation in simulated post-merger galaxies. *Monthly Notices of the Royal Astronomical Society*, 519(2):2119–2137.

Quinn, P. J. (1984). On the formation and dynamics of shells around elliptical galaxies. *The Astrophysical Journal*, 279:596–609.

Quintero, A. D., Hogg, D. W., Blanton, M. R., Schlegel, D. J., Eisenstein, D. J., Gunn, J. E., Brinkmann, J., Fukugita, M., Glazebrook, K., and Goto, T. (2004). Selection and Photometric Properties of K+A Galaxies. *The Astrophysical Journal*, 602(1):190–199.

Reichard, T. A., Heckman, T. M., Rudnick, G., Brinchmann, J., and Kauffmann, G. (2008). The Lopsidedness of Present-Day Galaxies: Results from the Sloan Digital Sky Survey. *The Astrophysical Journal*, 677(1):186–200.

Roberts, I. D., Parker, L. C., Gwyn, S., Hudson, M. J., Carlberg, R., McConnachie, A., Cuillandre, J.-C., Chambers, K. C., Duc, P.-A., Furusawa, H., Gavazzi, R., Hill, V., Huber, M. E., Ibata, R., Kilbinger, M., Mei, S., Mellier, Y., Miyazaki, S., Oguri, M., and Wainscoat, R. J. (2022). Ram pressure candidates in UNIONS. *Monthly Notices of the Royal Astronomical Society*, 509(1):1342–1357.

Roberts, I. D., van Weeren, R. J., McGee, S. L., Botteon, A., Ignesti, A., and Rottgering, H. J. A. (2021). LoTSS jellyfish galaxies. II. Ram pressure stripping in groups versus clusters. *Astronomy & Astrophyics*, 652:A153.

Rodriguez-Gomez, V., Genel, S., Vogelsberger, M., Sijacki, D., Pillepich, A., Sales, L. V., Torrey, P., Snyder, G., Nelson, D., Springel, V., Ma, C.-P., and Hernquist, L. (2015). The merger rate of galaxies in the Illustris simulation: a comparison with observations and semi-empirical models. *Monthly Notices of the Royal Astronomical Society*, 449(1):49–64.

Rodriguez-Gomez, V., Snyder, G. F., Lotz, J. M., Nelson, D., Pillepich, A., Springel, V., Genel, S., Weinberger, R., Tacchella, S., Pakmor, R., Torrey, P., Marinacci, F., Vogelsberger, M., Hernquist, L., and Thilker, D. A. (2019). The optical morphologies of galaxies in the IllustrisTNG simulation: a comparison to Pan-STARRS observations. *Monthly Notices of the Royal Astronomical Society*, 483(3):4140–4159.

Rose, C., Kartaltepe, J. S., Snyder, G. F., Rodriguez-Gomez, V., Yung, L. Y. A., Arrabal Haro, P., Bagley, M. B., Calabró, A., Cleri, N. J., Cooper, M. C., Costantin, L., Croton, D., Dickinson, M., Finkelstein, S. L., Häußler, B., Holwerda, B. W., Koekemoer, A. M., Kurczynski, P., Lucas, R. A., Mantha, K. B., Papovich, C., Pérez-González, P. G., Pirzkal, N., Somerville, R. S., Straughn, A. N., and Tacchella, S. (2023). Identifying Galaxy Mergers in Simulated CEERS NIRCam Images Using Random Forests. *The Astrophysical Journal*, 942(1):54.

Rowlands, K., Heckman, T., Wild, V., Zakamska, N. L., Rodriguez-Gomez, V., Barrera-Ballesteros, J., Lotz, J., Thilker, D., Andrews, B. H., Boquien, M., Brinkmann, J., Brownstein, J. R., Hwang, H. C., and Smethurst, R. (2018). SDSS-IV MaNGA: spatially resolved star formation histories and the connection to galaxy physical properties. *Monthly Notices of the Royal Astronomical Society*, 480(2):2544–2561.

Rowlands, K., Wild, V., Nesvadba, N., Sibthorpe, B., Mortier, A., Lehnert, M., and da Cunha, E. (2015). The evolution of the cold interstellar medium in galaxies following a starburst. *Monthly Notices of the Royal Astronomical Society*, 448(1):258–279.

Saintonge, A., Kauffmann, G., Kramer, C., Tacconi, L. J., Buchbender, C., Catinella, B., Fabello, S., Graciá-Carpio, J., Wang, J., Cortese, L., Fu, J., Genzel, R., Giovanelli, R., Guo, Q., Haynes, M. P., Heckman, T. M., Krumholz, M. R., Lemonias, J., Li, C., Moran, S., Rodriguez-Fernandez, N., Schiminovich, D., Schuster, K., and Sievers, A. (2011). COLD GASS, an IRAM legacy survey of molecular gas in massive galaxies - I. Relations between H_2, H I, stellar content and structural properties. *Monthly Notices of the Royal Astronomical Society*, 415(1):32–60.

Salim, S., Rich, R. M., Charlot, S., Brinchmann, J., Johnson, B. D., Schiminovich, D., Seibert, M., Mallery, R., Heckman, T. M., Forster, K., Friedman, P. G., Martin, D. C., Morrissey, P., Neff, S. G., Small, T., Wyder, T. K., Bianchi, L., Donas, J., Lee, Y.-W., Madore, B. F., Milliard, B., Szalay, A. S., Welsh, B. Y., and Yi, S. K. (2007). UV Star Formation Rates in the Local Universe. *The Astrophysical Journals*, 173(2):267–292.

Sazonova, E., Alatalo, K., Rowlands, K., Deustua, S. E., French, K. D., Heckman, T., Lanz, L., Lisenfeld, U., Luo, Y., Medling, A., Nyland, K., Otter, J. A., Petric, A. O., Snyder, G. F., and Urry, C. M. (2021). Are All Post-starbursts Mergers? HST Reveals Hidden Disturbances in the Majority of PSBs. *The Astrophysical Journal*, 919(2):134.

Schaye, J., Crain, R. A., Bower, R. G., Furlong, M., Schaller, M., Theuns, T., Dalla Vecchia, C., Frenk, C. S., McCarthy, I. G., Helly, J. C., Jenkins, A., Rosas-Guevara, Y. M., White, S. D. M., Baes, M., Booth, C. M., Camps, P., Navarro, J. F., Qu, Y., Rahmati, A., Sawala, T., Thomas, P. A., and Trayford, J. (2015). The EAGLE project: simulating the evolution and assembly of galaxies and their environments. *Monthly Notices of the Royal Astronomical Society*, 446(1):521–554.

Schmidt, M. (1959). The Rate of Star Formation. *The Astrophysical Journal*, 129:243.

Scudder, J. M., Ellison, S. L., Torrey, P., Patton, D. R., and Mendel, J. T. (2012). Galaxy pairs in the Sloan Digital Sky Survey - V. Tracing changes in star formation rate and metallicity out to separations of 80 kpc. *Monthly Notices of the Royal Astronomical Society*, 426(1):549–565.

Sérsic, J. L. (1963). Influence of the atmospheric and instrumental dispersion on the brightness distribution in a galaxy. *Boletin de la Asociacion Argentina de Astronomia La Plata Argentina*, 6:41–43.

Shah, E. A., Kartaltepe, J. S., Magagnoli, C. T., Cox, I. G., Wetherell, C. T., Vanderhoof, B. N., Cooke, K. C., Calabro, A., Chartab, N., Conselice, C. J., Croton, D. J., de la Vega, A., Hathi, N. P., Ilbert, O., Inami, H., Kocevski, D. D., Koekemoer, A. M., Lemaux, B. C., Lubin, L., Mantha, K. B., Marchesi, S., Martig, M., Moreno, J., Pampliega, B. A., Patton, D. R., Salvato, M., and Treister, E. (2022). Investigating the Effect of Galaxy Interactions on Star Formation at 0.5 ¡ z ¡ 3.0. *The Astrophysical Journal*, 940(1):4.

Shapley, H. (1919). On the Existence of External Galaxies. *Publications of the Astronomical Society of the Pacific*, 31(183):261.

Sheen, Y.-K., Yi, S. K., Ree, C. H., and Lee, J. (2012). Post-merger Signatures of Red-sequence Galaxies in Rich Abell Clusters at z ¡~0.1. *The Astrophysical Journal Supplement Series*, 202(1):8.

Simard, L., Mendel, J. T., Patton, D. R., Ellison, S. L., and McConnachie, A. W. (2011). A Catalog of Bulge+disk Decompositions and Updated Photometry for 1.12 Million Galaxies in the Sloan Digital Sky Survey. *The Astrophysical Journals*, 196(1):11.

Simmons, B. D., Lintott, C., Willett, K. W., Masters, K. L., Kartaltepe, J. S., Häußler, B., Kaviraj, S., Krawczyk, C., Kruk, S. J., McIntosh, D. H., Smethurst, R. J., Nichol, R. C., Scarlata, C., Schawinski, K., Conselice, C. J., Almaini, O., Ferguson, H. C., Fortson, L., Hartley, W., Kocevski, D., Koekemoer, A. M., Mortlock, A., Newman, J. A., Bamford, S. P., Grogin, N. A., Lucas, R. A., Hathi, N. P., McGrath, E., Peth, M., Pforr, J., Rizer, Z., Wuyts, S., Barro, G., Bell, E. F., Castellano, M., Dahlen, T., Dekel, A., Ownsworth, J., Faber, S. M., Finkelstein, S. L., Fontana, A., Galametz, A., Grützbauch, R., Koo, D., Lotz, J., Mobasher, B., Mozena, M., Salvato, M., and Wiklind, T. (2017). Galaxy Zoo: quantitative visual morphological classifications for 48 000 galaxies from CANDELS. *Monthly Notices of the Royal Astronomical Society*, 464(4):4420–4447.

Smail, I., Morrison, G., Gray, M. E., Owen, F. N., Ivison, R. J., Kneib, J. P., and Ellis, R. S. (1999). HUBBLE SPACE TELESCOPE Near-infrared and Optical Imaging of Faint Radio Sources in the Distant Cluster CL 0939+4713. *The Astrophysical Journal*, 525(2):609–620.

Snyder, G. F., Cox, T. J., Hayward, C. C., Hernquist, L., and Jonsson, P. (2011). K+A Galaxies as the Aftermath of Gas-rich Mergers: Simulating the Evolution of Galaxies as Seen by Spectroscopic Surveys. *The Astrophysical Journal*, 741(2):77.

Snyder, G. F., Lotz, J., Moody, C., Peth, M., Freeman, P., Ceverino, D., Primack, J., and Dekel, A. (2015). Diverse structural evolution at z ¿ 1 in cosmologically simulated galaxies. *Monthly Notices of the Royal Astronomical Society*, 451(4):4290–4310.

Snyder, G. F., Rodriguez-Gomez, V., Lotz, J. M., Torrey, P., Quirk, A. C. N., Hernquist, L., Vogelsberger, M., and Freeman, P. E. (2019). Automated distant galaxy merger classifications from Space Telescope images using the Illustris simulation. *Monthly Notices of the Royal Astronomical Society*, 486(3):3702–3720.

Somerville, R. S. and Davé, R. (2015). Physical Models of Galaxy Formation in a Cosmological Framework. *Annual Review of Astronomy and Astrophysics*, 53:51–113.

Springel, V. (2010). E pur si muove: Galilean-invariant cosmological hydrodynamical simulations on a moving mesh. *Monthly Notices of the Royal Astronomical Society*, 401(2):791–851.

Springel, V., Pakmor, R., Pillepich, A., Weinberger, R., Nelson, D., Hernquist, L., Vogelsberger, M., Genel, S., Torrey, P., Marinacci, F., and Naiman, J. (2017). First results from the IllustrisTNG simulations: matter and galaxy clustering. *Monthly Notices of the Royal Astronomical Society*, 475(1):676–698.

Springel, V., Pakmor, R., Pillepich, A., Weinberger, R., Nelson, D., Hernquist, L., Vogelsberger, M., Genel, S., Torrey, P., Marinacci, F., and Naiman, J. (2018). First results from the IllustrisTNG simulations: matter and galaxy clustering. *Monthly Notices of the Royal Astronomical Society*, 475(1):676–698.

Springel, V., White, S. D. M., Jenkins, A., Frenk, C. S., Yoshida, N., Gao, L., Navarro, J., Thacker, R., Croton, D., Helly, J., Peacock, J. A., Cole, S., Thomas, P., Couchman, H., Evrard, A., Colberg, J., and Pearce, F. (2005). Simulations of the formation, evolution and clustering of galaxies and quasars. *Nature*, 435(7042):629–636.

Springel, V., White, S. D. M., Tormen, G., and Kauffmann, G. (2001). Populating a cluster of galaxies - I. Results at [formmu2]z=0. *Monthly Notices of the Royal Astronomical Society*, 328(3):726–750.

Sreejith, S., Pereverzyev, Sergiy, J., Kelvin, L. S., Marleau, F. R., Haltmeier, M., Ebner, J., Bland-Hawthorn, J., Driver, S. P., Graham, A. W., Holwerda, B. W., Hopkins, A. M., Liske, J., Loveday, J., Moffett, A. J., Pimbblet, K. A., Taylor, E. N., Wang, L., and Wright, A. H. (2018). Galaxy And Mass Assembly: automatic morphological classification of galaxies using statistical learning. *Monthly Notices of the Royal Astronomical Society*, 474(4):5232–5258.

Strateva, I., Ivezić, Ž., Knapp, G. R., Narayanan, V. K., Strauss, M. A., Gunn, J. E., Lupton, R. H., Schlegel, D., Bahcall, N. A., Brinkmann, J., Brunner, R. J., Budavári, T., Csabai, I., Castander, F. J., Doi, M., Fukugita, M., Győry, Z., Hamabe, M., Hennessy, G., Ichikawa, T., Kunszt, P. Z., Lamb, D. Q., McKay, T. A., Okamura, S., Racusin, J., Sekiguchi, M., Schneider, D. P., Shimasaku, K., and York, D. (2001). Color separation of galaxy types in the sloan digital sky survey imaging data. *The Astronomical Journal*, 122(4):1861–1874.

Tacchella, S., Diemer, B., Hernquist, L., Genel, S., Marinacci, F., Nelson, D., Pillepich, A., Rodriguez-Gomez, V., Sales, L. V., Springel, V., and Vogelsberger, M. (2019). Morphology and star formation in IllustrisTNG: the build-up of spheroids and discs. *Monthly Notices of the Royal Astronomical Society*, 487(4):5416–5440.

Thorp, M. D., Bluck, A. F. L., Ellison, S. L., Maiolino, R., Conselice, C. J., Hani, M. H., and Bottrell, C. (2021). Towards robust determination of non-parametric morphologies in marginal astronomical data: resolving uncertainties with cosmological hydrodynamical simulations. *Monthly Notices of the Royal Astronomical Society*, 507(1):886–903.

Thorp, M. D., Ellison, S. L., Simard, L., Sánchez, S. F., and Antonio, B. (2019). Spatially resolved star formation and metallicity profiles in post-merger galaxies from MaNGA. *Monthly Notices of the Royal Astronomical Society*, 482(1):L55–L59.

Tohill, C., Ferreira, L., Conselice, C. J., Bamford, S. P., and Ferrari, F. (2021). Quantifying Non-parametric Structure of High-redshift Galaxies with Deep Learning. *The Astrophysical Journal*, 916(1):4.

Toomre, A. and Toomre, J. (1972). Galactic Bridges and Tails. *The Astrophysical Journal*, 178:623–666.

Trayford, J. W., Camps, P., Theuns, T., Baes, M., Bower, R. G., Crain, R. A., Gunawardhana, M. L. P., Schaller, M., Schaye, J., and Frenk, C. S. (2017). Optical colours and spectral indices of z = 0.1 eagle galaxies with the 3D dust radiative transfer code skirt. *Monthly Notices of the Royal Astronomical Society*, 470(1):771–799.

Tremonti, C. A., Moustakas, J., and Diamond-Stanic, A. M. (2007). The Discovery of 1000 km s^{-1} Outflows in Massive Poststarburst Galaxies at z=0.6. *The Astrophysical Journall*, 663(2):L77–L80.

Vera-Casanova, A., Gómez, F. A., Monachesi, A., Gargiulo, I., Pallero, D., Grand, R. J. J., Marinacci, F., Pakmor, R., Simpson, C. M., Frenk, C. S., and Morales, G. (2022). Linking the brightest stellar streams with the accretion history of Milky Way like galaxies. *Monthly Notices of the Royal Astronomical Society*, 514(4):4898–4911.

Vika, M., Bamford, S. P., Häußler, B., Rojas, A. L., Borch, A., and Nichol, R. C. (2013). MegaMorph - multiwavelength measurement of galaxy structure. Sérsic profile fits to galaxies near and far. *Monthly Notices of the Royal Astronomical Society*, 435(1):623–649.

Vogelsberger, M., Genel, S., Springel, V., Torrey, P., Sijacki, D., Xu, D., Snyder, G., Nelson, D., and Hernquist, L. (2014). Introducing the Illustris Project: simulating the coevolution of dark and visible matter in the Universe. *Monthly Notices of the Royal Astronomical Society*, 444(2):1518–1547.

Vogelsberger, M., Marinacci, F., Torrey, P., and Puchwein, E. (2020). Cosmological simulations of galaxy formation. *Nature Reviews Physics*, 2(1):42–66.

Walmsley, M., Smith, L., Lintott, C., Gal, Y., Bamford, S., Dickinson, H., Fortson, L., Kruk, S., Masters, K., Scarlata, C., Simmons, B., Smethurst, R., and Wright, D. (2020). Galaxy Zoo: probabilistic morphology through Bayesian CNNs and active learning. *Monthly Notices of the Royal Astronomical Society*, 491(2):1554–1574.

Wang, J., Hammer, F., Athanassoula, E., Puech, M., Yang, Y., and Flores, H. (2012). Loops formed by tidal tails as fossil records of a major merger. *Astronomy & Astrophyics*, 538:A121.

Wen, Z. Z. and Zheng, X. Z. (2016). Merging Galaxies with Tidal Tails in COSMOS to z = 1. *The Astrophysical Journal*, 832(1):90.

Werle, A., Poggianti, B., Moretti, A., Bellhouse, C., Vulcani, B., Gullieuszik, M., Radovich, M., Fritz, J., Ignesti, A., Richard, J., Soucail, G., Bruzual, G., Charlot, S., Mingozzi, M., Bacchini, C., Tomicic, N., Smith, R., Kulier, A., Peluso, G., and Franchetto, A. (2022). Post-starburst Galaxies in the Centers of Intermediate-redshift Clusters. *The Astrophysical Journal*, 930(1):43.

Whitaker, K. E., van Dokkum, P. G., Brammer, G., and Franx, M. (2012). The Star Formation Mass Sequence Out to z = 2.5. *The Astrophysical Journall*, 754(2):L29.

White, S. D. M. (1978). Simulations of merging galaxies. *Monthly Notices of the Royal Astronomical Society*, 184:185–203.

White, S. D. M. and Rees, M. J. (1978). Core condensation in heavy halos: a two-stage theory for galaxy formation and clustering. *Monthly Notices of the Royal Astronomical Society*, 183:341–358.

Wild, V., Heckman, T., and Charlot, S. (2010). Timing the starburst–AGN connection. *Monthly Notices of the Royal Astronomical Society*, 405(2):933–947.

Wild, V., Kauffmann, G., Heckman, T., Charlot, S., Lemson, G., Brinchmann, J., Reichard, T., and Pasquali, A. (2007). Bursty stellar populations and obscured active galactic nuclei in galaxy bulges. *Monthly Notices of the Royal Astronomical Society*, 381(2):543–572.

Wild, V., Taj Aldeen, L., Carnall, A., Maltby, D., Almaini, O., Werle, A., Wilkinson, A., Rowlands, K., Bolzonella, M., Castellano, M., Gargiulo, A., McLure, R., Pentericci, L., and Pozzetti, L. (2020). The star formation histories of z $\sim$ 1 post-starburst galaxies. *Monthly Notices of the Royal Astronomical Society*, 494(1):529–548.

Wild, V., Walcher, C. J., Johansson, P. H., Tresse, L., Charlot, S., Pollo, A., Le Fèvre, O., and De Ravel, L. (2009). Post-starburst galaxies: more than just an interesting curiosity. *Monthly Notices of the Royal Astronomical Society*, 395(1):144–159.

Wilkinson, S., Ellison, S. L., Bottrell, C., Bickley, R. W., Gwyn, S., Cuillandre, J.-C., and Wild, V. (2022). The merger fraction of post-starburst galaxies in UNIONS. *Monthly Notices of the Royal Astronomical Society*, 516(3):4354–4372.

Willett, K. W., Lintott, C. J., Bamford, S. P., Masters, K. L., Simmons, B. D., Casteels, K. R. V., Edmondson, E. M., Fortson, L. F., Kaviraj, S., Keel, W. C., Melvin, T., Nichol, R. C., Raddick, M. J., Schawinski, K., Simpson, R. J., Skibba, R. A., Smith, A. M., and Thomas, D. (2013). Galaxy Zoo 2: detailed morphological classifications for 304 122 galaxies from the Sloan Digital Sky Survey. *Monthly Notices of the Royal Astronomical Society*, 435(4):2835–2860.

Willett, K. W., Schawinski, K., Simmons, B. D., Masters, K. L., Skibba, R. A., Kaviraj, S., Melvin, T., Wong, O. I., Nichol, R. C., Cheung, E., Lintott, C. J., and Fortson, L. (2015). Galaxy Zoo: the dependence of the star formation-stellar mass relation on spiral disc morphology. *Monthly Notices of the Royal Astronomical Society*, 449(1):820–827.

Woods, D. F., Geller, M. J., Kurtz, M. J., Westra, E., Fabricant, D. G., and Dell'Antonio, I. (2010). Triggered Star Formation in Galaxy Pairs at z = 0.08-0.38. *The Astronomical Journal*, 139(5):1857–1870.

Wuyts, S., Schreiber, N. M. F., van der Wel, A., Magnelli, B., Guo, Y., Genzel, R., Lutz, D., Aussel, H., Barro, G., Berta, S., Cava, A., Graciá-Carpio, J., Hathi, N. P., Huang, K.-H., Kocevski, D. D., Koekemoer, A. M., Lee, K.-S., Floc'h, E. L., McGrath, E. J., Nordon, R., Popesso, P., Pozzi, F., Riguccini, L., Rodighiero, G., Saintonge, A., and Tacconi, L. (2011). GALAXY STRUCTURE AND MODE OF STAR FORMATION IN THE SFR-MASS PLANE FROMz$\sim$ 2.5 TOz$\sim$ 0.1. *The Astrophysical Journal*, 742(2):96.

Yan, R., Newman, J. A., Faber, S. M., Coil, A. L., Cooper, M. C., Davis, M., Weiner, B. J., Gerke, B. F., and Koo, D. C. (2009). The DEEP2 Galaxy Redshift Survey: environments of post-starburst galaxies at z ˜0.1 and ˜0.8. *Monthly Notices of the Royal Astronomical Society*, 398(2):735–753.

Yang, Y., Zabludoff, A. I., Zaritsky, D., and Mihos, J. C. (2008). The Detailed Evolution of E+A Galaxies into Early Types. *The Astrophysical Journal*, 688(2):945–971.

Yesuf, H. M., Faber, S. M., Trump, J. R., Koo, D. C., Fang, J. J., Liu, F. S., Wild, V., and Hayward, C. C. (2014). FROM STARBURST TO QUIESCENCE: TESTING ACTIVE GALACTIC NUCLEUS FEEDBACK IN RAPIDLY QUENCHING POST-STARBURST GALAXIES. *The Astrophysical Journal*, 792(2):84.

York, D. G., Adelman, J., Anderson, John E., J., Anderson, S. F., Annis, J., Bahcall, N. A., Bakken, J. A., Barkhouser, R., Bastian, S., Berman, E., Boroski, W. N., Bracker, S., Briegel, C., Briggs, J. W., Brinkmann, J., Brunner, R., Burles, S., Carey, L., Carr, M. A., Castander, F. J., Chen, B., Colestock, P. L., Connolly, A. J., Crocker, J. H., Csabai, I., Czarapata, P. C., Davis, J. E., Doi, M., Dombeck, T., Eisenstein, D., Ellman, N., Elms, B. R., Evans, M. L., Fan, X., Federwitz, G. R., Fiscelli, L., Friedman, S., Frieman, J. A., Fukugita, M., Gillespie, B., Gunn, J. E., Gurbani, V. K., de Haas, E., Haldeman, M., Harris, F. H., Hayes, J., Heckman, T. M., Hennessy, G. S., Hindsley, R. B., Holm, S., Holmgren, D. J., Huang, C.-h., Hull, C., Husby, D., Ichikawa, S.-I., Ichikawa, T., Ivezić, Ž., Kent, S., Kim, R. S. J., Kinney, E., Klaene, M., Kleinman, A. N., Kleinman, S., Knapp, G. R., Korienek, J., Kron, R. G., Kunszt, P. Z., Lamb, D. Q., Lee, B., Leger, R. F., Limmongkol, S., Lindenmeyer, C., Long, D. C., Loomis, C., Loveday, J., Lucinio, R., Lupton, R. H., MacKinnon, B., Mannery, E. J., Mantsch, P. M., Margon, B., McGehee, P., McKay, T. A., Meiksin, A., Merelli, A., Monet, D. G., Munn, J. A., Narayanan, V. K., Nash, T., Neilsen, E., Neswold, R., Newberg, H. J., Nichol, R. C., Nicinski, T., Nonino, M., Okada, N., Okamura, S., Ostriker, J. P., Owen, R., Pauls, A. G., Peoples, J., Peterson, R. L., Petravick, D., Pier, J. R., Pope, A., Pordes, R., Prosapio, A., Rechenmacher, R., Quinn, T. R., Richards, G. T., Richmond, M. W., Rivetta, C. H., Rockosi, C. M., Ruthmansdorfer, K., Sandford, D., Schlegel, D. J., Schneider, D. P., Sekiguchi, M., Sergey, G., Shimasaku, K., Siegmund, W. A., Smee, S., Smith, J. A., Snedden, S., Stone, R., Stoughton, C., Strauss, M. A., Stubbs, C., SubbaRao, M., Szalay, A. S., Szapudi, I., Szokoly, G. P., Thakar, A. R., Tremonti, C., Tucker, D. L., Uomoto, A., Vanden Berk, D., Vogeley, M. S., Waddell, P., Wang, S.-i., Watanabe, M., Weinberg, D. H., Yanny, B., Yasuda, N., and SDSS Collaboration (2000). The Sloan Digital Sky Survey: Technical Summary. *The Astronomical Journal*, 120(3):1579–1587.

Zabludoff, A. I., Zaritsky, D., Lin, H., Tucker, D., Hashimoto, Y., Shectman, S. A., Oemler, A., and Kirshner, R. P. (1996). The Environment of “E+A” Galaxies. *The Astrophysical Journal*, 466:104.

Zheng, Y., Wild, V., Lahén, N., Johansson, P. H., Law, D., Weaver, J. R., and Jimenez, N. (2020). Comparison of stellar populations in simulated and real post-starburst galaxies in MaNGA. *Monthly Notices of the Royal Astronomical Society*, 498(1):1259–1277.

Appendix A

Additional Information

A.1 The Effect of Recent Central Starbursts on Asymmetry

In Section 2.4, we show that shape asymmetry, which gives additional weight to low-surface brightness features, detects significant fractions of disturbed morphologies in each of the PSB populations. However, we also found that asymmetry, which is commonly used to identify mergers (Conselice 2003), does not find significant fractions of disturbed morphologies in the PSB samples. In fact, the asymmetry of both PSB samples were suppressed relative to their star-forming controls which are expected to have some asymmetric features like spiral arms, clumpy star formation, and dust obstruction. We argue this is a natural result of our PSB definition; our PSBs are selected on the basis of spectra from fibres placed on the central region of each galaxy[1]. Since our PSB selection uses information only from the central region, these galaxies have had, by definition, a recent burst of central star-formation. A central burst in star formation would create a bright, azimuthally symmetric core which would systematically drive down the asymmetry values which are weighted by each pixel's intensity. To confirm this idea, we explore the concentration and Sérsic index of our PSB samples in relation to their star-forming controls.

The concentration, C, of a galaxy is quantified by Conselice (2003) as:

---

[1] To use the terms from Chen et al. (2019), these PSBs would be considered central PSBs (CPSBs) as opposed to ring PSBs (RPSBs) or irregular PSBs (IPSBs) which can only be identified with spatially resolved spectroscopy.

$$C = 5\log\left(\frac{r_{80}}{r_{20}}\right), \tag{A.1}$$

where r_{20} and r_{80} are the radii of circular apertures containing 20 and 80 per cent of the galaxy's light, respectively. Elliptical galaxies tend to be more concentrated ($C = 4.4 \pm 0.3$) than spiral galaxies ($C = 3.9 \pm 0.5$; Conselice 2003).

Figure A.1 shows that both samples of PSBs have much higher concentrations than their star-forming controls. However, this could be a result of PSBs transitioning elliptical to morphologies, which tend to have both higher concentrations and lower asymmetries, or caused by a recent central starburst increasing the concentration of the stellar light profile.

We can break the degeneracy between elliptical-type morphologies and very bright nuclei using the Sérsic index. A 1-dimensional Sérsic profile (Sérsic 1963) can be used to approximate the intensity of light (as a function of radius) of a galaxy:

$$I(R) = I_e \exp\left\{-b_n\left[\left(\frac{R}{R_e}\right)^{-1/n} - 1\right]\right\} \tag{A.2}$$

where R_e is the radius within which half of the galaxy's light is contained, I_e is the intensity of the light at the radius, R_e, n is the Sérsic index and b_n is a coefficient determined by the Sérsic index (see Graham and Driver 2005).

The Sérsic index, n, describes the rate at which light decreases from its central peak. By this definition a galaxy with a Sérsic index of $n = 1$ has light that drops off as an exponential function and as n increases, the curvature of the light profile tends towards linearity. The curvature of the profile, controlled by the Sérsic index, n, is strongly correlated to the morphological classification of the galaxy; galaxies with Sérsic index $n \sim 1$ tend to be spiral galaxies and galaxies with $2 \lesssim n \lesssim 4$ tend to be elliptical (Sérsic 1963).

Figure A.1 shows that the PCA PSBs exhibit a wide range of Sérsic indices, indicating both disks and ellipticals. In fact, both PSB samples have bimodal Sérsic index distributions, with distinct peaks at $n \sim 1$ and $n \sim 4$. Compare this with the clear unimodal distribution around $n \sim 1$ of their star-forming controls and it is clear that post-starburst galaxies exhibit a wide range of morphological types, not just elliptical. This rules out elliptical morphologies dominating the PSB samples and driving the observed increase in concentration and decrease in asymmetry.

Lastly, more than half of the PSBs in both samples have Sérsic indices much

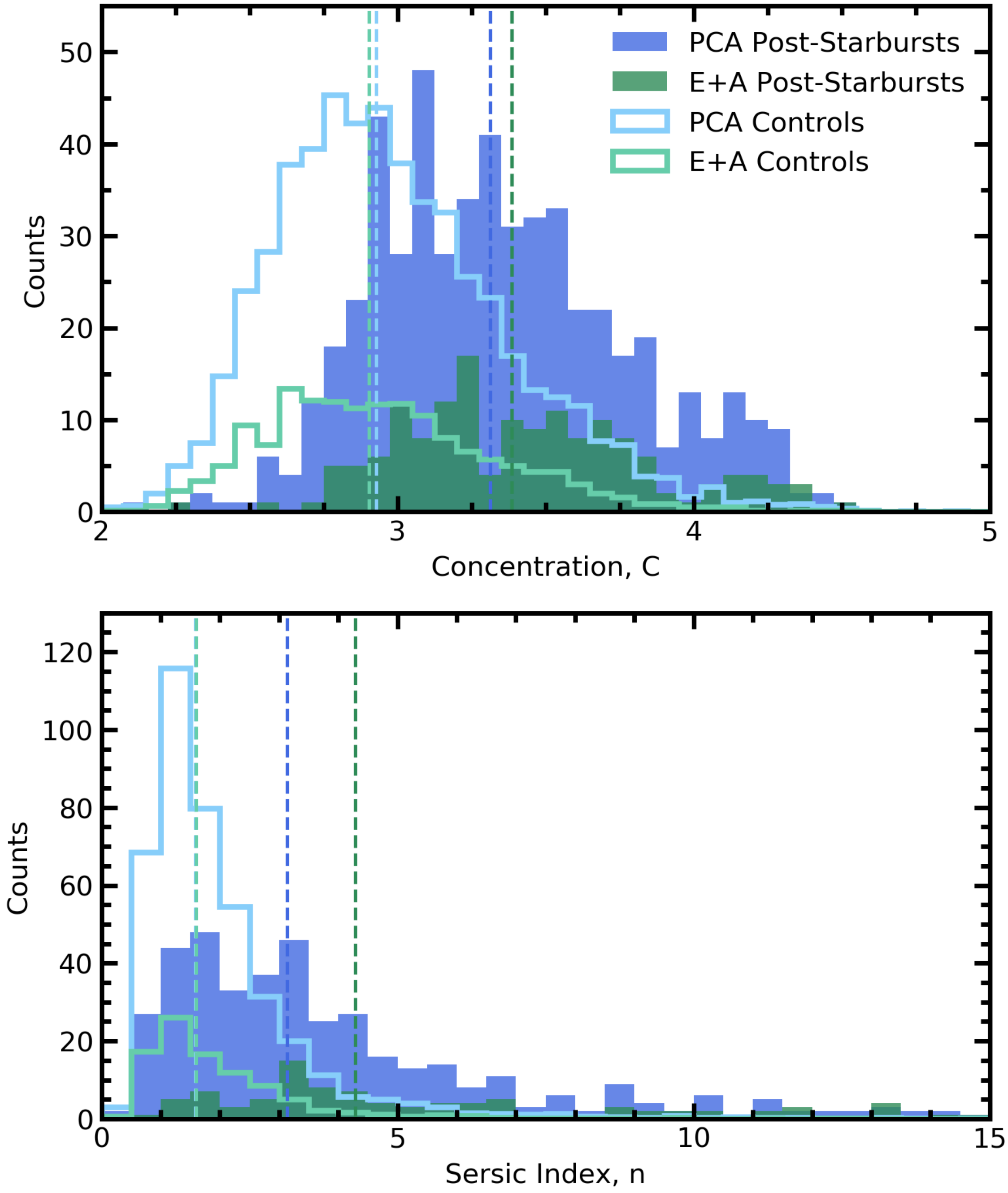

Figure A.1: The distributions of concentration (top) and Sérsic index (bottom) for the PCA PSBs (blue) and their controls (unfilled light-blue) and for the E+A PSBs (green) and their controls (unfilled light green). Note that since there are ten controls for each post-starburst, the histograms of the controls are weighted by a factor of 1/10 so they can be compared directly to the post-starburst distributions and that PSBs and their controls in the lower panel are required to have un-flagged Sérsic fits from `statmorph`.

higher than a typical elliptical galaxy ($n \gtrsim 4$). These high Sérsic indices are a result of trying to fit galaxies with a bright centralized core with a single Sérsic profile. The results presented here are consistent with the results of Goto (2005) who found that PSBs tend to have very bright nuclei based on visual inspection and with the findings of Wuyts et al. (2011) who find higher Sérsic indices for starburst galaxies with enhanced SFR.

A.2 Morphology and Merger Completeness in CFIS- and SDSS-like Imaging

As shown in both Chapters 2 and 3 of this thesis, the quality of imaging can dramatically affect the measured non-parametric morphology statistics, and thus the merger prediction, for a particular galaxy. Indeed, the effect is so pernicious that the same galaxy imaged with two different observing programmes in the same bandpass can have vastly different morphology measurements. In this section, I present an analysis of the effect of image quality on the non-parametric morphologies and the resulting merger completeness with a particular emphasis on comparing the image quality of CFIS to that of SDSS. While this work is peer-reviewed and published in Wilkinson et al. (2022), I moved toward a broader analysis in Chapter 3 of this thesis such that the results may be more universally applicable to other studies. The results presented here are consistent with similar image qualities presented in Chapter 3 except with a little bit higher completeness which I attribute to the lower synthetically observed redshift and higher spatial resolution of the pixels.

A.2.1 Testing Variable Image Quality with IllustrisTNG

To test the sensitivity of S(G, M_{20}), A, and A_S to the quality of imaging (including quality superior to that of CFIS) from which they are derived, I apply my morphology analysis to synthetic galaxy images from the IllustrisTNG simulation. Galaxies from the simulation have no sky noise or atmospheric blurring and have a higher resolution than most imaging systems. From a pristine state free from observational effects, the images can be degraded to varying levels of image quality, including that of CFIS and SDSS, and the variability of the derived morphologies can be tested accordingly.

Synthetic galaxy images are generated from the stellar mass distributions of galaxies in the simulation, used here as a proxy for its stellar light profile. Each synthetic

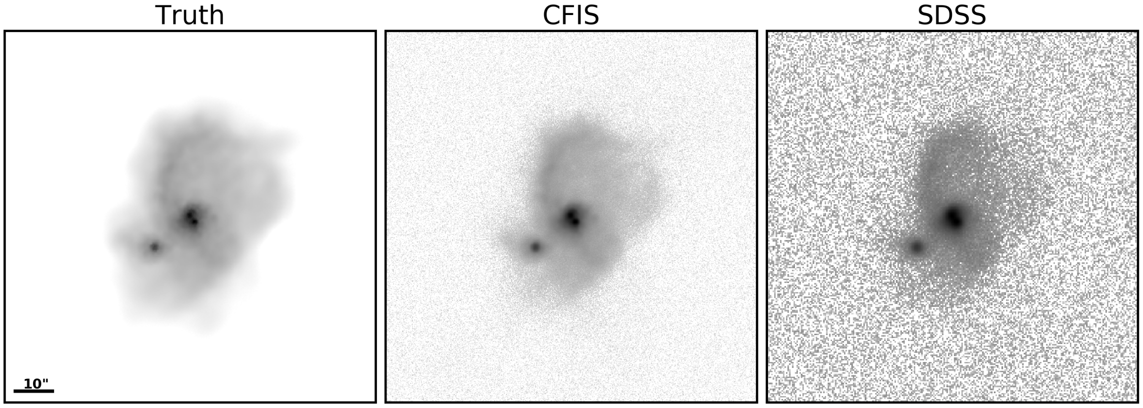

Figure A.2: Example synthetic images for the archetypal post-merger galaxy from the IllustrisTNG simulation described in Section A.2.1. The left panel is the "ground truth" image with no PSF blurring and minimal sky noise. The mock CFIS and SDSS images (middle and right panels) are coadded with sky noise, convolved with a PSF and binned to the pixel scale appropriate for each survey. These synthetic SDSS and CFIS images represent the orange and blue crosses in Figure A.3 and are used in the experiment presented in Section A.2.2. All three images are normalized and displayed on equivalent logarithmic scales.

image is generated at the same field of view as the real CFIS images used in this work and at an "observed" redshift of 0.05. To simulate atmospheric blurring and sky noise, the galaxy profile is convolved with a 2-D Gaussian function with varying FWHMs and is co-added with values drawn from a normal distribution with varying standard deviations. The images are then binned to the pixel scale of CFIS. For a single galaxy, a range of FWHMs from 0.1" to 1.7" and depths from 23.5 mag/arcsec^2 to 25.5 mag/arcsec^2 are combined to form a 9×9 grid of synthetic images with varying quality. An additional 82$^{\text{nd}}$ image is generated at a depth of 30 mag/arcsec^2 and without any blurring effects as a "ground truth" comparison. Each of the 82 images are run through `statmorph` as outlined in Section 2.2.1.

Since I expect the dependence of non-parametric morphology metrics on depth and atmospheric blurring to differ between galaxies, I present a case study of one archetypal post-merger galaxy in IllustrisTNG. The 3.51×10^{10} M$_\odot$ galaxy in question is at $z = 0.33$ of the simulation and has undergone a merger with a mass ratio of $\mu = 0.553$ within the last snapshot of the simulation ($t_{\text{post-merger}} \lesssim 162$ Myr). In Figure A.2, I display the "ground truth" image of this archetypal galaxy with minimal realism applied as well as the degraded synthetic images at the image quality CFIS and SDSS. Several late-stage merger features are present including faint, extended, asymmetric tidal tails, a double-nucleus, and a diffuse stellar halo. As a result, the ground truth shape asymmetry ($A_S \sim 0.76$) and Gini-M_{20} merger statistic ($S(G, M_{20}) \sim 0.06$) are each well above their respective merger thresholds and thus the galaxy would be classified as a merger by both metrics. However, the ground truth asymmetry is only moderately high ($A \sim 0.28$) placing it below the Conselice (2003) merger threshold of 0.35. In Figure A.3, I show how each of the morphology metrics deviate from the ground truth as the image quality varies across the 9×9 grid of synthetic images.

The top panel of Figure A.3 shows that the calculated asymmetry value decreases from the ground truth by a maximum of -0.208 at the lowest quality imaging. However, at the maximal depth and minimal atmospheric blurring considered, the difference from the ground truth is minimized to less than 0.003. The diagonal trend indicates that asymmetry tends to be affected equally by atmospheric blurring and image depth, consistent with asymmetry being sensitive to both asymmetric tidal features and high spacial frequency internal disturbances (Sazonova et al. 2021). For additional context, Figure A.3 indicates the typical image quality of CFIS and SDSS images with the blue and orange crosses, respectively. For this post-merger galaxy, the asymmetry in CFIS is ~0.1 higher (36% closer to the true value) than if it were measured using SDSS imaging. However, this post-merger galaxy would not be considered a merger in either of the surveys as the ground truth galaxy profile is simply not asymmetric enough to surpass the merger threshold.

In the middle panel of Figure A.3, I repeat the comparison of true and observed metrics, but now for shape asymmetry. The left-to-right trend evident in the deviation from ground truth of the shape asymmetry indicates that the variation in the shape asymmetry is driven largely by the depth of the imaging rather than the atmospheric blurring. This is consistent with shape asymmetry being sensitive to asymmetric low surface brightness features (Pawlik et al. 2016) and neglecting internal disturbances. As the depth of the imaging improves, the shape asymmetry increases to a value ~0.16 *higher* than the ground truth before decreasing again to be within 0.02 of the ground truth, on average, in the column of highest depth images. As a result, the shape asymmetry of this galaxy would be higher in SDSS than in CFIS. In this case, the shape asymmetry decreases at higher depths because the binary segmentation map begins to include the ultra faint diffuse halo which happens to be more symmetric than the less faint tidal tails. Nonetheless, this galaxy's shape asymmetry exceeds the nominal merger threshold of 0.4 and thus would be classified as a merger regardless of the image quality used in my experiment.

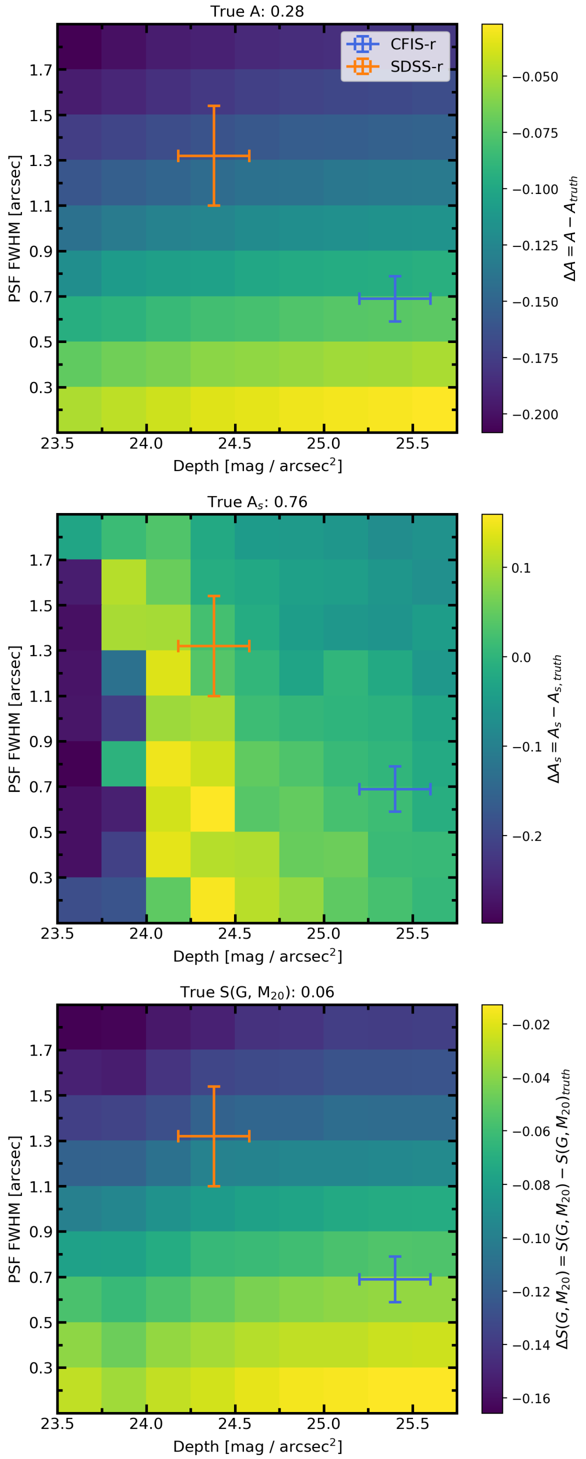

Figure A.3: The asymmetry (top), shape asymmetry (middle) and Gini-M_{20} merger statistic (bottom) of a simulated post-merger from IllustrisTNG convolved with a Gaussian PSF with varying FWHM and coadded with sky noise at various depths. Each grid is coloured by the resulting difference from the ground truth morphology of the galaxy, as defined at a depth of 30 mag/arcsec^2 and no PSF blurring. Orange and blue crosses portray typical image quality of SDSS and CFIS, respectively. All images are binned to the pixel scale of CFIS: 0.187 arcsec/pixel.

Finally, in the lower panel of Figure A.3, I assess the impact of image quality on S(G, M_{20}). In contrast to shape asymmetry, S(G, M_{20}) changes dramatically with atmospheric blurring but is less affected by a change in image depth. I attribute this to atmospheric blurring distributing the flux of the bright nuclei over more pixels, reducing G and increasing M_{20}, and the additional depth having little influence on the brightest pixels in the image. In the range of CFIS image quality, this galaxy would be marginally considered a merger, but in SDSS the image has been degraded to a degree that it would not be classified as a merger.

With this test, I have shown that the sensitivity of S(G, M_{20}), A, and A_S to the depth and atmospheric blurring of the imaging differs between each metric. However, I have repeated this experiment on many galaxies and found that the magnitude of each metric's sensitivity depends on the morphological features inherent to the galaxy in question. For example, the shape asymmetry of a galaxy with asymmetric tidal features is expected to increase with increased depth as more asymmetric features are detected, while a galaxy without such features will exhibit minimal change in its shape asymmetry with increased depth (see also Pawlik et al. 2016).

A.2.2 The Fraction of Undetected Mergers in CFIS and SDSS

In the previous subsection, I have established that a post-merger galaxy may be given a different merger classification depending on the morphology statistic implemented and the quality of the imaging used. In the case described in Section A.2.1, the asymmetry suggests the example post-merger galaxy is a non-merger at both CFIS and SDSS image quality, the shape asymmetry indicates it is a recent post-merger for the entire range of image qualities, and the Gini-M_{20} merger statistic classified it as a merger in CFIS imaging but not SDSS. I now assess how image quality representative of SDSS and CFIS will affect my ability to identify mergers from a statistical sample of simulated post-merger galaxies.

I use a sample of 2332 recent IllustrisTNG post-mergers at $z < 1$ of the simulation[2]. To be considered, the merger must have been significant ($\mu > 0.1$) and the post-merger remnant galaxy must have a mass between 10^{10} $M_\odot$ and 10^{12} $M_\odot$. Each post-merger is observed from four distinct viewing angles; each viewing angle provides a new stellar light distribution of a post-merger event, effectively enhancing

---

[2] The merger sample presented here used the mass ratio definition in Hani et al. (2020) while the main body of the thesis uses the mass ratio definition from Quai et al. (2023). For this reason the merger sample presented here is a little bit larger.

the post-merger sample by a factor of four to 9328. The 9328 post-merger images are scaled in angular size as if they were at an observed redshift of 0.05 and then degraded to the pixel scale resolution and typical atmospheric blurring and depth of CFIS and SDSS (see Section 2.1) before being processed by `statmorph` as described in Section 2.2.1. 7971 of these galaxies have flag-free morphologies for both the mock SDSS and CFIS images.

With 7971 mock-observed post-mergers in hand, I can assess the ability of A, A_S and S(G, M_{20}) to identify recent post-merger galaxies using merger thresholds of 0.35, 0.4 and 0.0, respectively. For each of the three metrics, the number of simulated post-mergers that would be identified as such is shown in Table A.1. Only 6.8% of the post-merger sample was identified as a merger based on their mock-observed CFIS asymmetries. However, this is an improvement over the 2.5% that would have been identified using SDSS imaging. S(G, M_{20}) recovers 30% of post-mergers when using CFIS-realistic imaging, an improvement over the 21% recovered using SDSS imaging. Shape asymmetry appears to be equally effective as S(G, M_{20}) at identifying recent mergers, identifying 30% with CFIS-realistic imaging and 28% with SDSS-realistic imaging.

CFIS imaging allows for a greater number of post-mergers to be detected using non-parametric morphologies. However, *more than 70% of galaxies that have undergone a merger within the last ∼200 Myr do not exhibit the features necessary to be detected using non-parametric morphology merger indicators.* By the time a post-merger galaxy that goes on to rapidly reduce its star formation rate and would be considered a post-starburst ($\gtrsim$ 500 Myr later), the merger features will likely have faded further and even fewer post-mergers would be recovered. Thus, based on the results presented in Section 2.4.1, I cannot exclude the possibility that the entire PSB sample is of merger origin.

	A > 0.35	$A_S > 0.4$	S(G, M_{20}) > 0
SDSS realism	2.5%	28%	21%
CFIS realism	6.8%	30%	30%

Table A.1: The fraction of recent post-merger galaxies from the IllustrisTNG simulation that would be detected as a merger using automated non-parametric morphology metrics. Realistic observational effects such as atmospheric blurring, pixel scale resolution and sky noise tuned to typical CFIS and SDSS imaging are applied to the synthetic images of 7971 simulated post-mergers.